

# **Breach Growth in Clay-Dikes**



# Breach Growth in Clay-Dikes

Proefschrift

ter verkrijging van de graad van doctor  
aan de Technische Universiteit Delft,  
op gezag van de Rector Magnificus Prof. dr. ir. J.T. Fokkema,  
voorzitter van het College voor Promoties,  
in het openbaar te verdedigen

op maandag 25 september 2006 om 10:00 uur

door

Yonghui ZHU  
civil engineer, Hohai University  
geboren te Hunan, China

Dit proefschrift is goedgekeurd door de promotor:

Prof. drs. ir. J.K. Vrijling

Toegevoegd promotor:

Dr. ir. P.J. Visser

Samenstelling promotiecommissie:

Rector Magnificus	Voorzitter
Prof. drs. ir. J.K. Vrijling	Technische Universiteit Delft, promotor
Dr. ir. P.J. Visser	Technische Universiteit Delft, toegevoegd promotor
Prof. dr. V.P. Singh	Louisiana State University, United States
Prof. dr. ir. F.B.J. Barends	Technische Universiteit Delft, GeoDelft
Prof. dr. ir. H.J. de Vriend	Technische Universiteit Delft, WL Delft Hydraulics
Dr. ir. J.S. Ribberink	University of Twente
Dr. ir. H.L. Fontijn	Technische Universiteit Delft
Prof. dr. ir. M.J.F. Stive	Technische Universiteit Delft, reservelid

Prof. Wu Zhongru (Hohai University, China) has provided valuable support and suggestions in the preparation of this thesis.

Front cover: breach in the dike of Menggang River in Jiangxi, China, 2006

Back cover: dike built in the DUT laboratory experiments

breach growth in the laboratory experiments conducted at HR  
Wallingford in the UK under the EC IMPACT Project

ISBN-10: 90-9020964-6

ISBN-13: 978-90-9020964-7

Copyright © 2006 by Yonghui Zhu

All rights reserved. No part of this book may be reproduced in any form, by print, copy or in any other way without prior written permission from the author.

Printed by PrintPartners Ipskamp BV, the Netherlands





## Summary

Numerous flood disasters occur every year worldwide, mostly resulting from failure of dikes, some with catastrophic outcomes. Examples are the dike failures along the Yangtze River in China in 1931 due to heavy rainstorms and those in the Netherlands in 1953 due to a storm surge at the North Sea. Both floods induced many deaths and enormous economic losses. The consequences of a flood induced by a dike burst can vary strongly and depend mainly on the speed and rate of inundation of the polder. This inundation speed and rate depend strongly on the flow rate through the breach, which in its turn depends on the development of the breach in time. Comprehension of the breach development process, and the mathematical translation of this process into a model, is of great importance to the design method of dikes based on a risk-approach. It is also important for the development of early warning systems for dike failures and evacuation plans of people at risk.

Regrettably, the significance of modeling the breach growth in dikes was not emphasized until recently, not only in the Netherlands but worldwide. The knowledge of the breach erosion process in dikes is still poor and the state-of-the-art of dike breach modeling technology is far from advanced. So far mainly the breach growth in dikes of granular soils (i.e. soils without cohesion, e.g. sand) was studied, see, for instance, the model developed by Visser (1998). In addition, available prototype as well as experimental data of dike failures, which are of high importance for model calibration and validation, are scarce.

In this thesis a mathematical model is developed for the process of breach growth in dikes built of cohesive soil (here named clay-dikes throughout the thesis) and for the flow rate through the breach. The model is based on the mechanism of breach development as observed in various tests in the laboratory and the field. Due to the complexity of the dike breaching process, the present study is restricted to homogeneous clay-dikes. Furthermore, possible effects of protection layers on the surface of the dike are not included, except those of a toe protection on the outer slope. Effects of waves are also not taken into account.

It is assumed that the breaching process starts with a small initial breach in the crest of the dike. Five stages are distinguished in the breach development process in clay-dikes, similar to the breaching process in sand-dikes as described by Visser (1998). In

Stage I, erosion occurs along the inner slope and, depending on the flow velocity, possibly also along the dike crest, resulting in a decrease of the width and the height of the dike in the breach. Then in Stages II and III, the dike body in the breach is further eroded through a combination of (1) flow shear erosion, (2) fluidization of the surface of the slope, (3) impinging jet scour of dike foundation and (4) discrete headcut slope mass failure, until at the end of Stage III the dike body in the breach has been washed away completely. In the following Stages IV and V, the breach grows further mainly laterally due to principally flow shear erosion along the side-slopes of the breach and the resulting discrete side-slope instability. The breach growth in vertical direction in these two stages relies mainly on the erodibility of the dike foundation, the presence and, if any, strength of a toe protection on the outer slope of the dike, and the presence and, if any, erodibility of a relatively high foreland. The flow through the breach is decelerated by the rising inner water in the polder in Stage V, consequently also the breach growth. This flow ultimately stops when either the inner and outer water levels equal or the outer water level drops below the breach bottom.

Laboratory experiments were conducted in a flume at Delft University of Technology (DUT) to improve the understanding of the physics of the breach erosion process in clay-dikes and to provide data for the model calibration and validation. Altogether five tests were performed, one with a sand-dike, four with clay-dikes constructed with different mixtures of fine sand, silt and clay. Much attention was paid to get proper sand-silt-clay mixtures. In all the tests water levels and flow velocities both upstream and downstream of the dike were measured. The process of dike breaching was recorded by both digital video cameras and digital cameras. The evolution of the dike profile was determined from the videos and photographs. When the clay-dikes were overflowed, generally erosion occurred first at locations close to the toe of the dike. The larger erosion rate at the lower part of the downstream slope of the dike induced steepening of the slope in time. This slope evolved gradually into a headcut. Headcut erosion then played an important role in the breach growth. The cohesiveness of the dike material affected remarkably the breach erosion process: the sand-dike test had a much faster erosion rate than the others, and higher clay proportions in the soil mixtures led to lower erosion rates.

The model has been calibrated against the data of two DUT laboratory experiments and two EC IMPACT Project laboratory experiments on breach growth in clay-dikes.

For modeling of breach growth in dikes, the key problem is the description of the rate of erosion of the dike by the flow, and more for dikes built of cohesive soil than for those built of non-cohesive soil. Erosion of cohesive soil is a complicated process and its mathematical description is still not satisfactory. The crucial soil erodibility coefficient  $M_e$  used in existing erosion formulae is often stated as an experimentally or empirically determined constant. Therefore, based on the calibration results of the four laboratory experiments, an expression has been developed for the calculation of

---

$M_e$  according to relevant soil properties. With this expression, the validation of the model against the data of the other two DUT laboratory experiments on clay-dike breaching yields reasonable agreement between the model predictions and the measurements.

Finally, the model has been confronted with a prototype dike failure in China in 1998. The predicted final breach width of 274 m is about 40% smaller than the observed 390 m. The predicted  $5.6 \times 10^8 \text{ m}^3$  of diverted floodwater volume is very close to the investigation-based estimation of  $5.2 \times 10^8 \text{ m}^3$ .



## Samenvatting

Wereldwijd vinden jaarlijks vele overstromingen plaats, meestal als gevolg van dijkdoorbraken, sommige met rampzalige gevolgen. Voorbeelden hiervan zijn de dijkdoorbraken langs de rivier Yangtze in China in 1931 als gevolg van zware regenval en de dijkdoorbraken in Nederland in 1953 als gevolg van een stormvloed op de Noordzee. Beide overstromingen hadden vele doden en een enorme economische schade tot gevolg. De gevolgen van een overstroming na een dijkdoorbraak kunnen zeer sterk variëren en zijn vooral afhankelijk van het inundatieverloop van de polder. Dit inundatieverloop wordt vooral bepaald door het debiet dat de polder instroomt, en daarmee door de ontwikkeling van de bres in de dijk. Kennis van het proces van bresgroei in dijken, en de mathematische beschrijving van dit proces in een model, is van belang voor de ontwerpmethodiek van dijken op basis van een inundatie-risico benadering. Het is tevens van belang voor de ontwikkeling van waarschuwings-systemen voor dijkdoorbraken en van evacuatieplannen voor bewoners van gebieden met een overstromingsrisico.

Het belang van het kunnen modeleren van het bresgroeiproces werd tot voor kort helaas niet onderkend, niet alleen in Nederland maar wereldwijd. De kennis van het bresgroeiproces is daardoor nog tamelijk beperkt en de bestaande bresgroeimodellen zijn nog allesbehalve geavanceerd. Tot dusverre is vooral gekeken naar het proces van bresgroei in dijken opgebouwd met loskorrelige grond (dus zonder cohesie, bijvoorbeeld zand); een voorbeeld hiervan is het model ontwikkeld door Visser (1998). Hier komt nog eens bij dat er weinig gegevens beschikbaar zijn van zowel prototype dijkdoorbraken als van dijkdoorbraakproeven, terwijl deze van groot belang zijn voor de calibratie en validatie van modellen.

In dit proefschrift wordt een mathematisch model ontwikkeld voor het proces van bresgroei in dijken opgebouwd van cohesieve grond (hier in het gehele proefschrift klei genoemd) en voor het verloop van het debiet door de bres. Het model is gebaseerd op het bresgroeiemechanisme als waargenomen in verscheidene laboratoriumexperimenten en veldproeven. Door de complexiteit van het bresgroeiproces is de studie beperkt tot homogene kleidijken. Verder worden mogelijke effecten van taludbekledingen niet meegenomen, behalve mogelijke effecten van een teenconstructie op het buitentalud. Effecten van mogelijk aanwezige golven worden ook verwaarloosd.

Er wordt verondersteld dat het bresgroeiproces begint met een relatief kleine initiële bres in de kruin van de dijk. Vijf stadia worden onderscheiden in het proces van bresgroei in kleidijken, vergelijkbaar met de bresontwikkeling in zanddijken als beschreven door Visser (1998). In Stadium I vindt erosie plaats langs het binnentalud en, afhankelijk van de stroomsnelheid, mogelijk ook aan de kruin van de dijk, waarbij geleidelijk de breedte en de hoogte van de dijk afnemen. Vervolgens nemen in de Stadia II en III de breedte en de hoogte van de dijk in de bres verder af door een combinatie van (1) erosie t.g.v. de bodemschuifspanning, (2) fluïdisatie van het oppervlak van het binnentalud, (3) ontgronding van de ondergrond van de dijk door de overstromende waterstraal en (4) discrete afkalving van brokken grond t.g.v. zogenaamde ‘headcut erosion’, tot aan het eind van Stadium III de dijk in de bres volledig is verdwenen. In de volgende Stadia IV en V groeit de bres verder, vooral in de breedte, hoofdzakelijk als gevolg van erosie door bodemschuifspanningen langs de dijkkoppen in de bres en de resulterende discrete instabiliteit van de zijhellingen. De bresgroei in verticale richting in deze twee stadia is vooral afhankelijk van de erosiegevoeligheid van de ondergrond van de dijk, van de eventuele aanwezigheid en sterkte van een teenconstructie op het buitentalud en van de hoogte en erosiegevoeligheid van een eventueel aanwezig voorland. De stroming door het stroomgat vertraagt in Stadium V door de stijgende waterstand in de polder, en als gevolg daarvan vertraagt ook de snelheid van de bresgroei. De stroming door de bres stopt uiteindelijk wanneer de binnen- en buitenwaterstand gelijk zijn geworden of wanneer de buitenwaterstand lager wordt dan de bodem van het stroomgat.

Laboratoriumexperimenten zijn uitgevoerd in een goot van de Technische Universiteit Delft (DUT) met als doel het bresgroeiproces beter te begrijpen en om data te verkrijgen voor de kalibratie en validatie van het model. In totaal zijn vijf proeven gedaan, één met een zanddijk, vier met kleidijken opgebouwd met verschillende mengsels van fijn zand, silt en klei. Er is veel aandacht besteed aan het verkrijgen van de beoogde zand-silt-klei mengsels. In alle proeven werden metingen verricht van waterstanden en stroomsnelheden, zowel bovenstrooms en benedenstrooms van de dijk. De ontwikkeling van het dwarsprofiel van de dijk werd opgenomen met zowel digitale videocamera’s als digitale fotocamera’s. Nadat de kleidijken in de goot overstroonden begon het erosieproces nabij de teen van het benedenstroomse talud. Als gevolg van de snellere erosie onder aan het binnentalud versteilde dit talud in de tijd. Geleidelijk ontwikkelde zich een zogenaamde ‘headcut’, waarna ‘headcut erosion’ een belangrijke rol ging spelen in het bresgroeiproces. De cohesie van de grond waarmee de dijk was opgebouwd had een grote invloed op het bresgroeiproces: de zanddijk erodeerde veel sneller dan de kleidijken, en een groter kleigehalte in het zand-silt-klei mengsel leidde tot een langzamere erosie.

Het model is gekalibreerd met de data van twee DUT gootproeven en twee laboratoriumexperimenten van het EC IMPACT Project aan bresgroei in kleidijken.

Het sleutelprobleem voor de modelering van bresgroei in dijken is de beschrijving van de mate van erosie van de dijk in de bres, voor dijken opgebouwd van cohesief materiaal in nog sterkere mate dan voor dijken opgebouwd van loskorrelig materiaal. Erosie van cohesieve grond is een ingewikkeld proces en de mathematische beschrijving hiervan is nog steeds niet voldoende nauwkeurig. De belangrijke erosiecoëfficiënt  $M_e$  van de grond in bestaande erosieformules wordt vaak empirisch bepaald. Met het oog hierop is uit de resultaten van de modelkalibratie met de vier laboratoriumproeven een formule afgeleid voor de erosiecoëfficiënt  $M_e$  als functie van relevante grondeigenschappen. Deze formule is toegepast in de validatie van het model met de data van de twee andere DUT laboratoriumproeven, resulterend in een redelijke overeenkomst tussen de modelvoorspellingen en de meetresultaten.

Ten slotte is het model geconfronteerd met een prototype dijkdoorbraak in China in 1998. De berekende uiteindelijke bresbreedte van 274 m is ongeveer 40% kleiner dan de waargenomen 390 m. Het berekende totale volume aan geïndundeerd water van  $5.6 \times 10^8 \text{ m}^3$  is vrijwel gelijk aan het (door middel van een schatting verkregen) waargenomen volume van  $5.2 \times 10^8 \text{ m}^3$ .



# Contents

<b>Summary</b>	<b>vii</b>
<b>Samenvatting</b>	<b>xi</b>
<b>Contents</b>	<b>xv</b>
<b>Chapter 1 Introduction</b>	<b>1</b>
1.1 China and the Netherlands, two countries with a long history of flood defence -----	1
1.1.1 Flooding history of the Netherlands.....	1
1.1.2 Flooding history of China .....	3
1.2 Present and future design standards for flood defences in the Netherlands ---	5
1.2.1 Present approach.....	5
1.2.2 Future approach .....	5
1.3 Necessities for modeling breach growth in dikes -----	6
1.4 Past efforts to model dike breaching-----	6
1.5 Objective of the present study-----	7
1.6 Arrangement of dissertation-----	7
<b>Chapter 2 Review of embankment breach modeling</b>	<b>9</b>
2.1 Introduction -----	9
2.2 Mathematical modeling of earth dam breaching-----	10
2.2.1 Developments in mathematical modeling .....	10
2.2.2 Discussion .....	18
2.3 Mathematical modeling of dike breaching-----	19
2.4 Experiments on embankment breaching -----	22
2.4.1 Introduction .....	22
2.4.2 Fuse plug dam field tests in China .....	23
2.4.3 Zwin'94 field experiment in the Netherlands .....	24
2.4.4 The Nordland field experiments in Norway .....	26
2.4.5 The HERU large-scale experiments in the United States .....	28
2.5 Headcut erosion during embankment breaching -----	29

2.5.1	Introduction .....	29
2.5.2	Experiments on headcut erosion.....	31
2.5.3	Headcut migration prediction.....	35
2.5.4	Discussion .....	36
2.6	Discussion -----	37
<b>Chapter 3</b>	<b>Erosion of cohesive and non-cohesive sediment</b>	<b>39</b>
3.1	Introduction -----	39
3.2	Incipient motion of sediment-----	40
3.3	Erosion of non-cohesive sediment -----	41
3.4	Erosion of cohesive sediment -----	42
3.4.1	Introduction .....	42
3.4.2	Properties of cohesive soil .....	42
3.4.3	Erodibility of cohesive soil.....	47
3.4.4	Erosion rate of cohesive sediment.....	52
3.5	Discussion -----	58
<b>Chapter 4</b>	<b>Breach growth process in clay-dikes</b>	<b>59</b>
4.1	Introduction -----	59
4.2	Five stages of the breach erosion process in clay-dikes-----	60
4.3	Initiation of erosion in Stage I-----	61
4.4	Breach development in Stage I -----	64
4.5	Breach development in Stage II-----	66
4.5.1	Introduction .....	66
4.5.2	Classifications of headcut .....	67
4.5.3	Headcut erosion during dike breaching.....	68
4.6	Breach development in Stage III-----	73
4.7	Breach enlargement in the dike crest in Stages I, II and III-----	75
4.8	Breach development in Stage IV -----	77
4.9	Breach development in Stage V -----	85
4.10	Discussion -----	85
<b>Chapter 5</b>	<b>Mathematical model</b>	<b>87</b>
5.1	Introduction -----	87
5.2	Breach development in Stage I -----	88
5.2.1	The breach flow.....	88
5.2.2	Breach erosion in Stage I .....	90
5.2.3	Steepening of dike inner slope in Stage I.....	91
5.3	Breach development in Stage II-----	94
5.3.1	Introduction .....	94
5.3.2	Trajectory of impinging jet of the breach flow .....	95

5.3.3	Jet scour of dike foundation and headcut undermining.....	96
5.3.4	Slope instability .....	100
5.4	Breach development in Stage III-----	103
5.5	Breach enlargement in the dike crest in Stages I, II and III-----	105
5.6	Breach development in Stage IV-----	107
5.6.1	Development of a Type A breach .....	107
5.6.2	Development of a Type B breach .....	110
5.6.3	Development of a Type C breach .....	113
5.7	Breach development in Stage V-----	114
5.8	Input and output data-----	115
5.9	Discussion-----	116
<b>Chapter 6</b>	<b>Experiments for verification</b>	<b>119</b>
6.1	Introduction-----	119
6.2	DUT laboratory experiments-----	119
6.2.1	Introduction .....	119
6.2.2	Set-up of the laboratory experiments .....	120
6.2.3	Experimental results .....	127
6.3	EC IMPACT Project laboratory experiments-----	134
6.4	Discussion-----	137
<b>Chapter 7</b>	<b>Model calibration and validation</b>	<b>141</b>
7.1	Introduction-----	141
7.2	Model calibration with tests $T_1$ , $T_2$ , $T_{10}$ and $T_{12}$ -----	141
7.2.1	Model calibration with tests $T_1$ and $T_2$ .....	141
7.2.2	Model calibration with tests $T_{10}$ and $T_{12}$ .....	147
7.2.3	Establishment of a relationship between $M_e$ and soil properties.....	152
7.3	Model validation with tests $T_3$ and $T_4$ -----	153
7.4	Sensitivity of the model to $M_e$ -----	157
7.5	Model applied to a prototype dike failure-----	159
7.5.1	Description of polder and 1998 floods .....	159
7.5.2	Model prediction .....	161
7.6	Discussion-----	162
<b>Chapter 8</b>	<b>Conclusions and recommendations</b>	<b>165</b>
8.1	Introduction-----	165
8.2	Conclusions-----	165
8.3	Recommendations-----	167
<b>References</b>		<b>171</b>
<b>Appendix A</b>	<b>Data of laboratory experiments</b>	<b>181</b>

---

A.1	Introduction -----	181
A.2	Main characteristics of Millisil M10, Polwhite E Kaolin and Illite-----	181
A.3	Results of water level and flow velocity measurements, the DUT tests ----	184
A.4	Measured water level and breach flow rate, the IMPACT Project tests-----	197
<b>Appendix B Height limitation of a headcut</b>		<b>201</b>
B.1	Introduction -----	201
B.2	Circular surface analysis -----	201
B.3	Planar surface analysis -----	202
B.4	Lateral earth pressure analysis -----	204
B.5	Examples -----	205
<b>List of main symbols</b>		<b>207</b>
<b>Acknowledgments</b>		<b>211</b>
<b>Curriculum Vitae</b>		<b>213</b>

# Chapter 1

## Introduction

### 1.1 China and the Netherlands, two countries with a long history of flood defence

#### 1.1.1 Flooding history of the Netherlands

As long as mankind remembers, the Netherlands is a sinking country bordering the rising sea. Approximately 25% of its surface is below mean sea level. The lowest point, north-east of Rotterdam, is 6.7 m below mean sea level. In the absence of dunes and dikes more than 65% of the country would be flooded at high sea and high river levels (see Figure 1.1, see also Van de Ven, 1993 and Huisman et al., 1998). This situation makes the Netherlands very vulnerable to storm surges and river floods. During an extreme heavy storm on the North Sea, the difference between the lowest land and the level of the nearby seawater could well exceed 10 m.

The history of the Netherlands is full of stories dealing with floods. People living in the Frisian counties started to build dwelling mounds (in Dutch “terpen”) as early as 500 BC to protect themselves and their properties against flooding (Van de Ven, 1993; Visser, 1998). From AD 800 to 1250 a considerable drop in the ground level was caused by drainage of peat areas for cultivation. Accordingly these settled areas were threatened by floods from the sea. This made the construction of dikes around the inhabited areas unavoidable in the 12th and 13th century. However, the strength of the dikes was not always sufficient. At least 150 known cases of dike breaching and flooding occurred in the next six centuries, some of which caused big disasters.

The storm surge of 1 February 1953 in the coastal provinces Zeeland and South Holland, led to one of the biggest natural disasters in the Dutch history. This storm surge damaged 800 km of dikes and breached these dikes in about 900 places, causing inundation of 2000 km<sup>2</sup> of land, mostly with salt water. More than 3000 houses were destroyed and 43000 were damaged, 72000 people had to be evacuated and 1835

people lost their lives. The disaster caused a direct economic loss of about 14% of the Dutch GDP. Later this disaster led to the world famous Delta Works, aiming at damming up the estuaries and strengthening dikes in the southwestern part of the Netherlands (Van de Ven, 1993; Huisman et al., 1998).

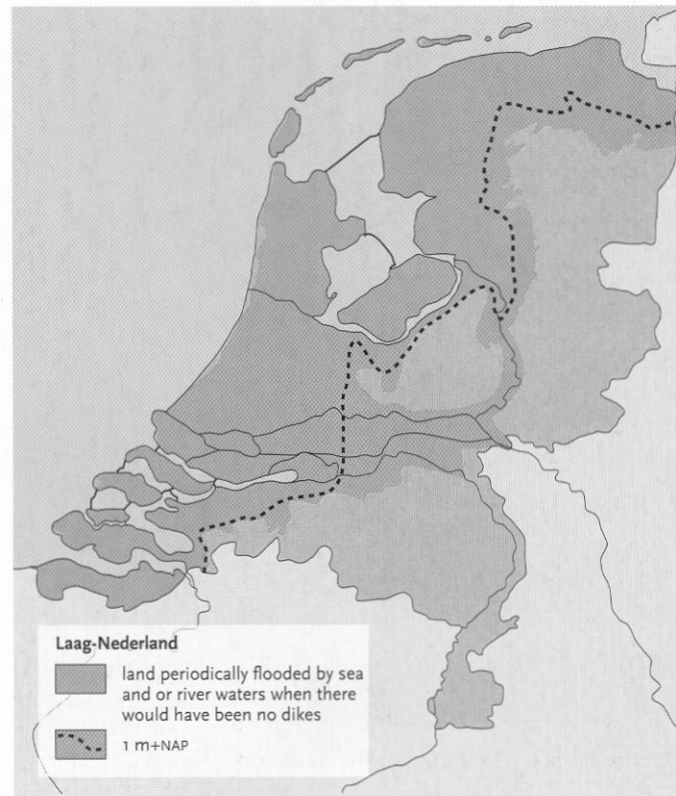


Figure 1.1 The vulnerability of the Netherlands to flooding (Van de Ven, 1993).

However, the risk of flooding arises not only from the sea, but also from rivers, as proved in 1926 and 1995. In 1926 high discharges of the rivers Rhine and Meuse breached some river dikes, inundating large areas. In 1995 heavy rainfall during several weeks produced high river discharges, threatening the river dikes. It forced the authorities to evacuate more than 250000 people (and millions of livestock) within 36 hours. Fortunately the dikes held.

Today, the dike ring is the basis of the Dutch flood defence policy. The country is divided into 53 so-called dike ring areas. Each dike ring consists of flood defences as dikes, dunes, ship locks, sluices and storm surge barriers. Safety levels (in terms of return period or frequency of design water levels) are specified for each dike ring.

### 1.1.2 Flooding history of China

In China, flooding is considered as one of the severest natural disasters. The historical records with respect to flooding go back at least 4000 years. During the period from 770 to 221 BC, dikes were built widely to defend the land against flooding in the lower reach of the Yellow River. From 256 to 251 BC, the world famous Dujiangyan Project was built in the Minjiang River, a tributary of the upper reach of the Changjiang (i.e. Yangtze) River. This large project was mainly composed of diversion works, spillways and desilting works, with functions of irrigation, flood control, navigation and water supply, among others, and is still in service at present.

Countless floods occurred in the long history of China, some of which caused big disasters. Despite the incomplete statistics, hundreds of floods in the history are found in literature (see Table 1.1), and as shown in the table, the average frequency of flood occurrence became higher as time went by.

Table 1.1 Statistics of flood disasters in the Chinese history (after OSFCDRH/NIHWR, 1997).

Dynasty	Period	Number of years	Number of flood recorded	Yearly frequency (%)
The Han Dynasty	206 BC – AD 220	425	76	17.9
The Wei & Jin Dynasties	220 – 420	200	56	28.0
The South & North Dynasties	420 – 581	161	77	47.8
The Sui & Tang Dynasties	581 – 907	326	120	36.8
The Five Dynasties	907 – 960	53	11	20.8
The Song Dynasty	960 – 1271	311	193	62.1
The Yuan Dynasty	1271 – 1368	97	92	94.8
The Ming Dynasty	1368 – 1644	276	196	71.0
The Qing Dynasty	1644 – 1911	267	192	71.9
	1911 – 1936	26	24	92.3

The Changjiang (i.e. Yangtze) River, the largest river in China, flowing over a distance of 6300 km from the Qinghai-Tibet Plateau to the East China Sea, is most vulnerable to flood at its middle and lower reaches due to the very low and flat topography. Three extreme floods happened in the 20th century in the Changjiang River, each resulting in huge damages. In 1931, a catastrophic flood occurred in the whole drainage basin. Along the main dikes more than 300 places were breached, with 38000 km<sup>2</sup> farmland inundated, 145000 human deaths, 1.78 million houses destroyed. Hankou City (the second largest trade centre in China then) was flooded for 3 months. The direct economic loss was enormous. Yet, even more extreme flooding

took place in 1954. This time the flood caused huge damage to 123 cities in 5 provinces: 61 breaches occurred along the Changjiang River main dikes and the lower reach of the Hanjiang River (one of the main tributaries of the middle reach of the Changjiang River), 32000 km<sup>2</sup> farmland inundated, 30000 people died, and the Beijing to Guangzhou railway, which was crucial for Chinese economy, was interrupted for 100 days. It had a gigantic negative influence on the life of the people and the development of the country. Most recently, in 1998, due to the intensive and long rainfall in the Changjiang River basin, severe flooding occurred again with water levels in some reaches of the river surpassing the highest historical values. Fortunately, the damage was reduced to a certain low level, as a result of the incessant construction and strengthening of the dikes and the hard defence against floods by the government and the people. Nevertheless, one breach in the main dike occurred near Jiujiang City, and hundreds of larger and smaller polders were inundated because of dike breaching. The total inundated area amounted to 3200 km<sup>2</sup>, among which 60% is farmland, and 1562 people died in this big flood (MWR, 1999).

The Yellow River, the second longest river (5464 km) in China, is well-known as a sediment-laden river (its name refers to the muddiness of the water). Although the drainage basin of the Yellow River is regarded as the "Cradle of Chinese Civilization", frequent severe floods arising from the Yellow River made it known as "China's Sorrow" in the past. For instance, in mid-June of 1855 a big flood occurred in the lower reach of the Yellow River (Chien, 1990). The flooding water began overflowing the levee on 19 June at Tongwaxiang, Henan Province. Flow scoured the soil at the breach very quickly. The breach was enlarged so fast that only one day later the river channel was entirely relocated with no more water flowing through its original downstream channel. The flow of the Yellow River entered the Daqing River channel and the flow was so large that the channel could not carry it. Both banks were overflowed and a vast area outside the river was inundated. A part of the floodwater flowed further and reached the Tuhai River and others, bursting their levees at several places.

Apart from the numerous flood disasters arising from the rivers, the more than 18000 km long coastline of China does not bring only benefits but also the risk of flooding. According to elementary statistics, in the 1846 years from AD 66 to 1911, altogether 1687 storm surges occurred along the East China Sea, average out at once per 1.1 years. From AD 798 to 1949, in altogether 1152 years 1440 storm surges can be found in literature along the Yellow Sea, average out at more than once per year. Most of these storm surges resulted in huge losses in both human lives and economic properties, some with tens of thousands of deaths (OSFCDRH/NIHWR, 1997).

After the 1998 big floods, flood defence and flood mitigation have been strongly emphasized by both the government and the ordinary people in China. Large amounts of money were invested in these fields. Dikes along rivers were constructed, reconstructed and strengthened. Unreliable and aged reservoirs and dams were

inspected and repaired. Management of flood storage and detention basins were improved. It is also expected that the Three Gorges Project after its completion will contribute to the safety against flooding of people living downstream of it.

## **1.2 Present and future design standards for flood defences in the Netherlands**

### **1.2.1 Present approach**

In the Netherlands, the present design method of sea and river dikes is the same as the one in China, primarily based on frequency of exceedance of the design water levels. The crest height of a dike is achieved by adding a certain extra height to this level. For instance, based on analysis of the economic values protected, a design water level with a return period of 10000 years was fixed for Central Holland. The Commission on River Dykes of the Netherlands recommended a design standard of 1/1250 per year for river dikes in 1977 (CUR/TAW, 1990 and 1991). As a reference here, the design standard of the Yangtze River main dike in China is based on the water level of the 1954 big floods.

In the present Dutch approach, the required dimensions of the dike cross-section are determined per section of dike. No correlations between the different dike sections are considered. This means that for a dike ring its total length has no influence on the design; however, a longer dike ring implies more potential weak points. Furthermore, the various sections and elements of the dike ring do not necessarily have the same safety degree, therefore it is certain that the weakest spot will determine the overall safety of the dike ring (CUR/TAW, 1990).

Since 1980 the awareness has grown that the probability of exceedance of the design water level cannot satisfactorily predict the probability of flooding (Vrijling, 2001). A possible catastrophic water level could be higher than the design level, i.e. the dike could well stand the design level with a certain margin of safety. However, on the other hand the dike could fail due to other failure mechanisms (e.g. seepage and piping, slope sliding) at levels below the design level. Recent experiences in Wilnis (the Netherlands) and New Orleans (USA) showed that sliding can cause a breach. In short, with the present design method the real probability of inundation of the region protected by a dike ring is not clearly known.

### **1.2.2 Future approach**

In order to understand the overall probability of failure of a flood defence system, a new design philosophy named risk analysis approach has been proposed (see Vrijling, 2001). In this new design method the contribution of all elements of the system and

of all failure mechanisms of each element to the probability of flooding is taken into account. Furthermore, not only the probability of failure is included, but also the consequences of the failure. Risk ( $R$ ) is defined as the result of the probability of failure ( $P_f$ ) times the expected damage ( $D_a$ ) caused by the failure (Kraak et al., 1995):

$$R = P_f \cdot D_a \quad (1.1)$$

Kraak et al. (1995) distinguished the following steps to evaluate risk:

- estimation of the probability of failure of the flood defence system;
- estimation of the inundation process in case of failure;
- analysis of the expected damage (material and immaterial) in case of inundation.

To assess a risk, according to Equation (1.1), the damage of inundation should be treated carefully. This damage depends heavily on the inundation process, according to CUR/TAW (1990), including the inundation speed, the inundation depth and the inundation duration.

### 1.3 Necessities for modeling breach growth in dikes

Dikes are of large benefit to people in many countries. However, it is clear from Section 1.1 that breaching of dikes can lead to huge losses in both human lives and economic properties. No matter how high the adopted design standard is and how solid the dike looks, the risk of failure of the dike can never be eliminated.

Yet, the magnitude and extent of the losses depend highly on the rate of the breaching of dikes, which determines the discharge through the breach and the speed and rate of inundation of the polder. Therefore, modeling of breach evolution in dikes, predicting the breach parameters (e.g. depth, width) and the breach flow rate, is of significant interest for damage assessment and risk analysis. It is also important for the development of early warning system for dike failures and evacuation plans of people at risk.

### 1.4 Past efforts to model dike breaching

Despite numerous dike failures occurring every year in the world, some with catastrophic outcomes (e.g. those described in Section 1.1 and the recent levee breaches in New Orleans, USA, due to Hurricane Katrina), the importance of modeling the breach development in dikes was not emphasized until fairly recently. So far mainly the breach growth in dikes of granular soils (i.e. soil without cohesion, e.g. sand) was studied, for instance, the models developed by Visser (1998), and by Steetzel and De Vroeg (1998), see also Section 2.3.

Various studies have also been done elsewhere in the world on the breaching of earth dams, which is similar to that of dikes (for a comparison of these two processes, see Section 2.3), e.g. Fread (1988a and b), Singh and Scarlatos (1988), Bechteler and Broich (1991) and Mohamed et al. (2002), see Chapter 2 for a detailed review.

In spite of the numerous studies conducted and the considerable progress achieved, understanding of the breach erosion process in embankments (here including both dikes and earth dams) is still unsatisfactory and the state-of-the-art of embankment breach modeling technology is far from mature. In addition, available experimental as well as prototype data of dike failures, which is of significant importance for the model calibration and verification, is exiguous (see Chapter 2).

## 1.5 Objective of the present study

The general objective of this study is

- to investigate the physics of the breach erosion process in clay-dikes (i.e. dikes constructed with cohesive soil);
- to develop a mathematical model for this process, which is capable of predicting the breach growth in clay-dikes and the flow rate through the breach;
- to verify the model against data of laboratory experiments on dike breaching and a prototype dike failure.

Due to the large complexities expected, the present study aims only at homogeneous clay-dikes. Furthermore, possible effects of dike surface protection layers (e.g. vegetation cover) on the breaching process are not included, except those of a toe protection on the outer slope. Also effects of waves are not taken into account.

## 1.6 Arrangement of dissertation

Chapter 2 holds a literature review of the breach modeling of embankments (including both earth dams and dikes). Both experimental studies and mathematical modeling are covered. Because of the high complexities involved with erosion of cohesive soil and its key role in the breaching of clay-dikes, a literature study on the erosion of cohesive soil was made; the main results of this study are given in Chapter 3. In Chapter 4 a qualitative description of the breach erosion process in clay-dikes is presented. The mathematical model for this process is then given in Chapter 5. Experiments on the breach erosion of clay-dikes were conducted in the laboratories of Delft University of Technology (DUT) as well as HR Wallingford in the UK. These experiments are described in Chapter 6. The calibration and validation of the model against the data of the two series of experiments and the confrontation of the model

with one prototype dike failure are described in Chapter 7. Finally in Chapter 8 conclusions from this study are drawn and recommendations for further research are given.

## Chapter 2

# Review of embankment breach modeling

### 2.1 Introduction

As described in Chapter 1, devastating disasters can occur if an embankment fails. Two very painful instances of earth dam failure are given here: in 1889, overtopping of the South Fork Dam, Pennsylvania, USA, caused over 2200 deaths and large property losses (Singh, 1996); in August 1975, the uncommonly heavy rainstorms (maximum 6-hour rainfall 830 mm) in central China caused disastrous failure of the Banqiao Reservoir Dam and the Shimantan Reservoir Dam with 26000 deaths (Pan, 2000). Brown and Graham (1988) analysed twenty-four historical dam failures and flash floods reported by the U.S. Bureau of Reclamation. Their result indicated that loss-of-life varies from 0.0% to 0.2% (averaged 0.04%) of the population-at-risk with more than 90 minutes of warning time. However, the ratio ranges from 1.4% to 100% (averaged 13%) when less than 90 minutes of warning time was available. Therefore, extensive research has recently been done to model the breach erosion process in embankments and to predict the breach parameters (e.g. rate of breach development and outflow hydrograph).

Unfortunately, breach simulation and breach parameter prediction are considered by many investigators (e.g. Wurbs, 1987) to contain the largest uncertainty of all aspects of embankment breach flood forecast. The breach growth in embankments is believed to be dependent on various factors including the causes for the breach, the type of material composing the embankments, and the shape and dimensions of the embankments, etc. These factors vary greatly from case to case.

Nevertheless, despite the many difficulties encountered in the modeling of embankment breaching, considerable progress has already been made (Zhu et al., 2004b). A variety of mathematical models have been developed in the last forty years for simulation of the breach erosion process in embankments. In addition, many large-

or small-scale experiments have been carried out in order to gain more insight into the mechanism of embankment breaching.

Generally, the mathematical models developed can be classified as parametric based or physically based models. Parametric based models frequently use key parameters (e.g. final breach geometry and breach formation duration) to simulate the breach growth as a simplified time-dependent process (e.g. linear increase of breach dimensions). Some parametric models contain various regression equations to compute the peak breach outflow and time of failure using parameters like the reservoir volume and the dam height, etc. Good reviews of these models were made by Wahl (1998) and Xie (1993), with the latter particularly for those developed by Chinese investigators and institutes. The majority of these regression equations were developed on the basis of the assumption of an instantaneous dam breaching, which certainly leans to the conservative and safe side. Sudden and instantaneous breaching is, however, generally the fashion of concrete dam failure; embankments constructed with soils (cohesive or non-cohesive) will breach gradually in a certain relatively long period. In short, parametric based models are generally simple and easy to use. However, on the other hand, these models do not have a solid foundation and their accuracy of prediction could be questionable (Zhu et al., 2004b).

Physically based embankment breach models use principles of for instance, hydraulics, sediment transport and soil mechanics to simulate the breach growth process and the breach outflow hydrograph. This category includes models, e.g. Ponce and Tsivoglou (1981), Fread (1988b), Singh and Scarlatos (1988), Bechteler and Broich (1991), Steetzel and De Vroeg (1998), Visser (1998), and Wang and Bowles (2005a). Physically based models are more complicated in structure and possess the potential to model in more detail and more accurately the embankment breaching process, although they are restricted by the degree of understanding of the embankment breaching mechanism.

## **2.2 Mathematical modeling of earth dam breaching**

### **2.2.1 Developments in mathematical modeling**

Wahl (1998) indicated that the two main tasks of dam breach analysis are the prediction of the outflow hydrograph through the breach and the routing of that hydrograph through the downstream valley. Prediction of the outflow hydrograph can be further subdivided into prediction of the breach characteristics (e.g. breach shape, width, depth, rate of development), and routing of the reservoir storage and outflow through the breach.

During the last forty years, particularly since the 1980's, considerable progress has been made in mathematical modeling of earth dam breaching and consequently also

in flood forecasting. Many numerical models are now available for the simulation of breach growth in earth dams. Table 2.1 summarizes the main characteristics of various mathematical models for the breach growth in earth dams. Among these models, Cristofano (1965), Ponce and Tsivoglou (1981), Giuseppetti and Molinaro (1989), Havnø et al. (1989), SMPDAM, BEED, Peviani (1999), Tingsanchali and Chinnarasri (2001), Coleman et al. (2002), and Wang and Bowles (2005a) deal with earth dam breaching due to overflowing; Renard and Rupro study only piping failure of earth dams; and BRDAM, DAMBRK, BREACH, DEICH, Loukola and Huokuna (1998) and Mohamed et al. (2002) take both overflowing and piping into account. The tailwater effect is considered in the models like BRDAM, DAMBRK, Havnø et al. (1989), BEED and BREACH. The BREACH model, BEED model, Peviani (1999) and Mohamed et al. (2002) also contain the breach side-slope stability analysis. Almost all the models describe the breach flow with broad-crested weir formula when dam overflowing is concerned.

According to Singh (1996), Cristofano (1965) was "perhaps the first to have simulated gradual dam breach erosion". In his model a trapezoidal breach with constant bottom width was assumed. The side-slopes of the breach were fixed to the angle of repose of the material. Brown and Rogers (1981) developed their model BRDAM, which was applicable to both overtopping and piping induced breaches. The model was tested against the failure of the Teton Dam (Idaho, USA, 1976, see Eikenberry et al., 1977) with a good agreement between computed and estimated peak flow.

As will be described below, the failure of the Teton Dam has been utilized by many investigators to calibrate or validate their models (e.g. DAMBRK; BREACH; BEED; Giuseppetti and Molinaro, 1989; Loukola and Huokuna, 1998; Coleman et al., 2002; Mohamed et al., 2002; and Rozov, 2003). However, available data of this dam failure is limited, and as illustrated in Table 2.2, these few available data from different data sources contradict each other. This definitely undermines the model calibration or validation.

Ponce and Tsivoglou (1981) assumed in their model that a breach initiates at some low or weak point of the dam crest and downstream face when overtopped. Manning's equation was used to describe the resistance of the breach channel bottom. The breach top width was initially assumed to remain constant, and later the breach width was related to the flow rate by a specified relation. The model was tested against the failure of the natural embankment formed by earthquake-generated landslide in central Peru in 1974. The simulated flood characteristics agree well with the estimated actual values. However, the channel friction, sediment transport and channel geometry parameters were adjusted in the calculation.

The DAMBRK model is a dam break flood routing model (one dimensional Saint-Venant equations) developed by Fread in 1977 with the latest version released in 1988. The failure duration and the final shape and dimensions of the breach are required as input for the model. The breach is initiated at the dam crest and grows at a linear

rate over the failure duration to the ultimate breach dimensions. The model was tested on five historical dam failures and one laboratory scale dam-break modeling performed in 1961 by the U.S. Corps of Engineers. For the simulation of the Teton Dam failure and the Buffalo Creek coal-waste dam collapse (West Virginia, USA, 1972), the computed breach flow volumes are in agreement with the estimated values in magnitude and timing. Estimated peak discharges along the downstream valleys were well reproduced by the model (Fread, 1988a).

Table 2.1 Summary of the main characteristics of earth dam breach models (to be continued).

Model and time developed	Flow	Sediment transport	Breach geometry	Input parameters
Cristofano (1965)	broad-crested weir flow	empirical formula	trapezoidal	soil properties, others
BRDAM (Brown and Rogers, 1981)	broad-crested weir flow	Schoklitsch (1934) bed-load formula	parabolic	soil properties, tailwater, others
Ponce and Tsivoglou (1981)	full hydrodynamic system	Meyer-Peter and Müller (1948) bed-load formula	constant peak flow width	initial breach geometry, soil properties, others
DAMBRK (Fread, 1988a)	broad-crested weir flow, orifice flow	linear predetermined erosion	rectangular, triangular, trapezoidal	final breach shape, failure time, others
BREACH (Fread, 1988b)	broad-crested weir flow, orifice flow	Meyer-Peter and Müller formula, DuBoys relation	rectangular, trapezoidal	soil properties, dam geometry, others
BEED (Singh and Scarlatos, 1988)	broad-crested weir flow	Einstein-Brown (1950) bed-load formula	rectangular, trapezoidal	soil properties, initial breach, others
Giuseppetti and Molinaro (1989)	similar broad-crested weir flow	Englund's formula, Smart (1983)	triangular	soil properties, others
Havnø et al. (1989)	-	linear predetermined erosion/Engelund and Hansen (1967), Meyer-Peter and Müller (1948)	trapezoidal	soil properties, dam geometry, others
SMPDBK (Wetmore and Fread, 1991)	broad-crested weir flow	-	rectangular, trapezoidal	final breach shape, failure time, others

Table 2.1 Summary of the main characteristics of earth dam breach models (continued).

Model and time developed	Flow	Sediment transport	Breach geometry	Input parameters
DEICH (Bechteler and Broich, 1991)	broad-crested weir flow	Meyer-Peter and Müller formula, Smart (1984) and Cristofano (1965) formulae	varies in time	soil properties, others
Renard/Rupro (reported by Paquier et al., 1998)	orifice flow	Meyer-Peter and Müller formula	circular $\Rightarrow$ half circular (lower) + rectangular (upper) / rectangular	soil properties, dam geometry, others
Loukola and Huokuna (1998)	broad-crested weir flow, orifice flow (Fread 1988a and b)	Meyer-Peter and Müller (1948) formula	trapezoidal	dam geometry, soil properties, hydrological data, others
Peviani (1999)	broad-crested weir flow	Di Silvio and Peviani (1989)	trapezoidal	soil properties, sediment transport formula coefficients, others
Tingsanchali and Chinnarasri (2001)	1D shallow water equations	Smart (1984)	rectangular	soil properties, dam geometry, others
Coleman et al. (2002)	empirical formula	empirical formula	parabolic	soil properties, dam geometry, others
Mohamed et al. (2002)	broad-crested weir flow, orifice flow	Yang (1979), Visser (1998), and Chen and Anderson (1986)	rectangular	soil properties, initial breach, others
Rozov (2003)	broad-crested weir flow	Voinich-Syanojensky (1972)	rectangular	soil properties, dam geometry, others
Wang and Bowles (2005a)	gradually varied flow, 2D shallow water equations	Chen and Anderson (1987), and Smart (1984)	-	soil properties, dam geometry, others

Table 2.2 Summary of contradicting data on the Teton Dam failure from different data sources.

Items		Data sources			
		Wahl (1998)	Fread (1988b)	Havnø et al. (1989)	Singh (1996, page 98)
Dam slope	upstream (H:V)	3:1	2.5:1	2.5:1	3:1
	downstream (H:V)	2.5:1	2:1	2:1	2.5:1
Reservoir capacity ( $10^6 \text{ m}^3$ )		356	308	-	308
Peak outflow ( $10^4 \text{ m}^3/\text{s}$ )		6.5	4.7~7.9	4.5~8.0	4.67
Breach height (m)		86.9	-	91.5	79.0
Breach side-slopes (H:V)		1:1	-	0.75:1	-
Breach width	bottom (m)	-	-	55.0	46.0
	top (m)	-	-	192.0	-
	averaged (m)	151.0	-	-	-

The BREACH model was developed by Fread in 1984 and later revised in 1988 (see Fread, 1988b). The model is capable of simulating earth dam failure due to either overtopping or piping. The dam may be homogeneous or otherwise consists of two materials: an outer zone and an inner core with different material properties. Flow through the breach is determined by orifice or weir formulas. The breach is initially assumed to be rectangular-shaped. The sides of the breach channel collapse when the depth of the breach reaches a critical value and then the breach is transformed to a trapezoidal-shaped channel (see Figure 2.1). Erosion is assumed to occur equally along the bottom and sides of the breach channel except when the breach sides collapse. The model was tested on failure of four dams (man made or landslide-formed dams, including the Teton Dam). The predicted outflow hydrograph and breach size and shape agree well with the estimated prototype values (Fread, 1988b).

The BEED model was developed to simulate earth dam breach development, flood routing and sediment routing (Singh and Scarlatos, 1988). The breach is assumed to be trapezoidal and behave as a broad-crested weir. The Einstein-Brown (1950) formula is utilized to compute the rate of flow erosion. After a certain amount of erosion has taken place at the breach section, the side-slopes become unstable and instability occurs eventually. The BEED model was tested against four historical earth dam failures (see Singh, 1996): South Fork Dam, Pennsylvania, 1889; Buffalo Creek Dam, West Virginia, 1972; Teton Dam, Idaho, 1976; and Huaccoto Natural Dam, Peru, 1976. For all the cases, according to Singh (1996), "some of the input parameters were assumed to be such that the corresponding results coincided with

those observed at the site, although keeping physical values as close as possible". Figure 2.2 shows the breach evolution predicted by the model for the South Fork Dam. The calculated values for the peak discharge and breach formation time were in good agreement with the observed values. However, notable discrepancies were seen between those of the breach top width.

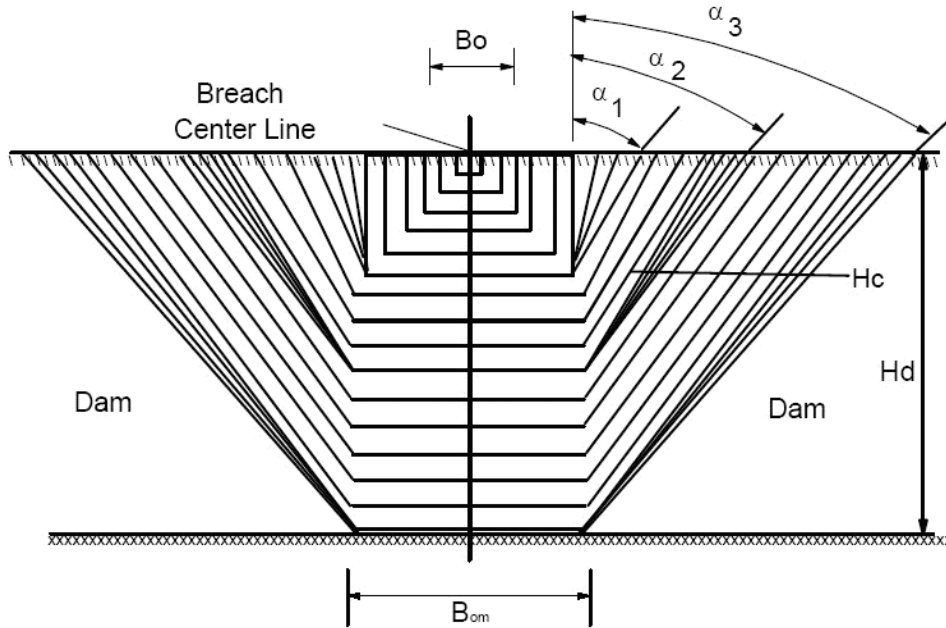


Figure 2.1 Front view of a dam with sequence of breach formation predicted by the BREACH model (Fread, 1988b).

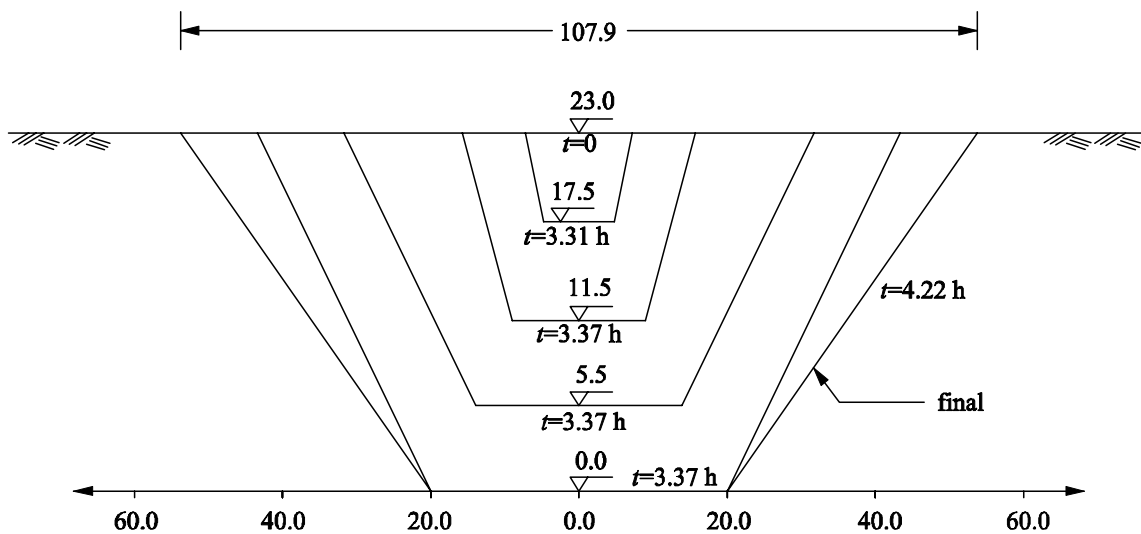


Figure 2.2 Breach evolution for the South Fork Dam simulated by the BEED model (all dimensions are expressed in m, after Singh, 1996).

Giuseppetti and Molinaro (1989) proposed a model to simulate the breach development in an earth dam due to overtopping. The cross-section of the dam is assumed to be of triangular shape with equal upstream and downstream slopes. The granular material composing the dam is assumed to be homogeneous and of constant diameter. The model was applied to two prototype dam failures, one of the Teton Dam, and the other of the rockslide-formed Val Pola natural dam in 1987 in Italy. Reasonable results were obtained by the model for both cases.

In the model developed by Havnø et al. (1989) either a linear failure mechanism or an erosion based formulation can be selected to model the breach development; the linear failure approach follows that of the DAMBRK model of Fread (1988a). For both modes, limits on the final breach width and level need to be specified. The model was applied to the Teton Dam failure. Good agreements were achieved between the model predictions and the estimated prototype values.

The SMPDBK model is a simplified version of the DAMBRK model and was developed by Wetmore and Fread in 1983 for quick prediction of downstream flooding caused by a dam breach. The breach is assumed to have a rectangular shape, however, a trapezoidal breach can also be analysed by specifying a rectangular breach width equal to the average width of the trapezoidal breach. Partial breaching and breach without reaching the bottom of the reservoir can also be analysed. According to Wetmore and Fread (1991), the SMPDBK model compares well with the DAMBRK model when applied to the failure of the Teton Dam, the Buffalo Creek coal waste dam, and to numerous theoretical dam failures. Wetmore and Fread (1991) stated a few limitations of the model, e.g. because the model assumes normal, steady flow at the peak, backwater effects cannot be considered and may substantially affect the prediction accuracy for the peak flood level.

Bechteler and Broich (1991) developed a model called DEICH for the simulation of earth dam breaching caused by either overtopping or piping. When applied to a homogeneous physical dam model build of granular material, good agreement was achieved between the model results and the measured data concerning the peak outflow and the shape of the hydrograph.

Paquier et al. (1998) reported two models, one used by Electricité de France (the Renard model) and one by Cemagref, France (the Rupro model). These two models are based on nearly the same assumptions and are capable of providing the discharge hydrograph due to piping failure of embankment dams. The pipe is supposed to initiate at the bottom of the valley. When the pipe diameter reaches two thirds of the dam height, the vault of the pipe is assumed to fail and a channel forms through the dam body, with its width increasing due to erosion of the walls. These two models apply numerous simplifications and do not precisely describe the physical erosion process. However, the peak discharges obtained from the models are close to the ones acquired by a statistical analysis of real dam failures (see Paquier et al., 1998).

Loukola and Huokuna (1998) proposed a numerical erosion model for embankment dam failure due to either overtopping or piping. Development and calibration of the model were based to large extent on the observations on fuse plug breach tests in China (see Pan and Loukola, 1993, see also Section 2.4). The failure of the Teton Dam has been used for verification of the model. However, it is a pity that the result of the model verification was not presented in the paper. The model was applied for hazard analysis of two embankment dams in Finland together with a 1D flow model.

Peviani (1999) developed a 1D mathematical model for simulating the overtopping process of a natural (landslide-formed) dam. The model was first applied to a hypothetical case of the Spriana landslide in Valmalenco Valley (Italy), checking the sensitivity of the model to some physical and computational parameters (e.g. sediment properties, coefficients of the sediment transport formula). Then application of the model to the "La Josefina" landslide (Paute River, Ecuador, March 1993) reproduced the erosive process and the outflow hydrograph well.

The 1D numerical model developed by Tingsanchali and Chinnarasri (2001) is for simulating of non-cohesive dam failure due to flow overtopping. The model consists of three modules: a module of unsteady flow over steep bed slopes, a dam surface erosion module, and a (dam downstream) slope sliding failure module. Model calibration and validation was done by use of laboratory experimental data. The model was also applied to the failure of the Buffalo Creek Dam. The computed peak breach outflow and the time to peak agree well with the estimated prototype values. However, it should be noted that during this application the value of one of the model parameters was not the calibrated one.

Based on flume experiments on breaching of small-scale non-cohesive homogeneous embankments, Coleman et al. (2002) developed a set of empirical formulations to describe the breach geometry, rate of erosion and breach flow. After being formulated together with sediment transport expressions into a numerical model, it was applied to the Teton Dam failure with reasonable results compared with the estimated data. Coleman et al. (2002) concluded that the model must be quantitatively limited to small-amplitude non-cohesive homogeneous embankments with large upstream reservoirs, otherwise the model predictions are principally qualitative.

The model developed by Mohamed et al. (2002) is aiming at simulation of breach formation through embankment dams due to either overtopping or piping. The structure of the dam can be either homogeneous or containing a clay core. For overtopping, the breach enlargement is the result of continuous erosion combined with discrete side-slope instability. The continuous erosion of the breach is calculated through a sediment transport formula to determine the volume of the sediment transported. In case of piping, the pipe is assumed to enlarge uniformly along its length according to the volume of eroded sediment. This volume is gained as the product of the sediment transport rate and the selected time step. Initiation of the piping has not been included. Mohamed et al. (2002) applied three cases to test

different aspects of the model. These cases are a laboratory experiment carried out at the Federal Armed Forces University in Munich, the fuse plug dam field test at Yahekou, China (see Section 2.4), and the Teton Dam failure. The model calculation results are in reasonably good agreement with the measured or estimated data. However, Mohamed et al. (2002) stated that uncertainty still remains in some aspects of the parameterization of the model. In addition, no description of the erosion along the embankment downstream slope has been included in the model.

Rozov (2003) developed a model to simulate the washout of dams. The model assumes an initial breach in the dam with its bottom reaching the base of the dam. Therefore the dam washout process is considered only after formation of the initial breach. The breach shape is assumed to be rectangular. The rate of erosion is generally assumed to be proportional to the sediment transport rate. The model was calibrated with laboratory and field experimental data. Application to ten historical dam failures yielded reasonable results for peak breach flow rate, final breach width and time of reservoir depletion (see Rozov, 2003).

Wang and Bowles (2005a) developed a model for the breaching of non-cohesive earth dams induced by overtopping. Gradually varied flow was used to simulate the overland flow at the beginning of the breach. A numerical scheme was proposed to solve the 2D shallow water equations for simulating the breach outflow through the breach channel. The formula proposed by Chen and Anderson (1987) was applied to calculate the erosion rate, and the method of Smart (1984) was used for sediment transport capacity calculation. The dam foundation was assumed to be non-erodible. Slope stability along the main flow direction in the breach channel was checked using Bishop's simplified method. The model was tested against Test 3 of the Nordland field experiments in Norway in 2002 (see Section 2.4.4). The calculated peak breach outflow and final breach width agreed well with those measured (see Wang and Bowles, 2005b). The calculation for a hypothetical long dam yielded consistent results for peak breach outflow with those obtained from historical-data-based empirical formulae.

### 2.2.2 Discussion

Considerable progress has been achieved on the mathematical modeling of earth dam breaching over the last forty years, especially since the 1980's, despite the complicated process involved. Yet, understanding so far of the mechanism of earth dam breaching is still unsatisfactory, and the state-of-the-art of the breach modeling technology is far from advanced. For instance, almost all of the mathematical models available now are limited to the breach in homogeneous earth dams due to overtopping and/or piping. The formation of the initial opening in the dam, the composite dam structure, and the effect of dam slope protective layers are neglected in the models. Besides, most of the earth dam breach models available so far do not distinguish the flow sediment

transport capacity and the flow erosion rate of soil material from the dam, despite the significant difference in physical meaning of the two concepts (Zhu et al., 2004b). For modeling of the breach growth in embankments, the key problem is the description of the rate of erosion of the embankment by the flow, and more for embankments built of cohesive soil than for those built of non-cohesive soil.

Wahl (2004) and Hanson et al. (1999) stated that the primary weakness of the available earth dam breach models is their use of tractive stress-based erosion models. Based on laboratory experiments and observations of real embankment failures, Ralston (1987), Dodge (1988), Powledge et al. (1989), Hanson et al. (1999) and Wahl (2004) proposed that most embankment breaches are dominated by headcut erosion. Flow shear erosion may still take place to a certain extent, however, erosion due to headcutting is often the dominant mechanism determining breaching. A headcut here means a vertical or near vertical drop or discontinuity on the flow-bed (see Figure 2.9 in Section 2.5), and headcutting means the upstream migration of a headcut due to flow erosion and soil mechanical slope instability (see Figure 2.10 in Section 2.5). A review of literature on headcut erosion research is given in Section 2.5.

During the literature study it is also found that the available data on the numerous historical earth dam failures in the world are limited and rough, and are mostly based on eye-witness reports. Many dam breaching processes have not been recorded or have not been recorded accurately and in detail. Sometimes contradictions are found between different sources of data on the same dam failure cases (see e.g. Table 2.2). On the other hand however, prototype data of good quality is of great importance for the calibration and validation of the earth dam breach models. It is a big surprise to discover that most of the available models use the same few limited prototype dam failure cases (e.g. the Teton Dam breach) for their calibration and validation (Zhu et al., 2004b).

## 2.3 Mathematical modeling of dike breaching

Compared with the progress made in earth dam breach modeling, efforts dedicated to dike breach simulation have been launched later. The status quo of the dike breach modeling is in a preliminary stage.

In general the physics of breach erosion in dikes and in earth dams have a lot in common, however, there are still some significant differences between the two processes, e.g.

- Earth dams generally have a much larger ratio of embankment height to length than dikes do. This implies that the breach enlargement process before reaching to the embankment foundation is relatively more important for earth dams than for dikes. In respect to the inundation rate and depth of the polder protected by

the dike, the breach enlargement (mainly widening) after the dike foundation is reached is more significant.

- The head differences between upstream and downstream of earth dams are generally considerably larger than those of dikes, making a dam breach hold a more destroyable potential than a dike failure.
- After an earth dam breaching is initiated, it is normally impossible to stop it during the process, however, it may be feasible for dike failures (e.g. the dike breach near Jiujiang City during the big floods in the Yangtze River in 1998 has been closed after 5 days of development when the flood stage in the river was still high).
- For sea dikes, the breach erosion will be a repeating in- and outflow process due to the influence of tides.
- For river dikes, the direction of the main flow in the river is usually more or less parallel to the breach opening; while for earth dams, the flow direction in front of the dam is normal to the opening. That is, the breach flow is a side outflow of the river for river dikes, however is the mainstream of the river for dams.

Mathematical models available so far for dike breaching are few. Two models, BRES (developed by Visser since 1986 with latest update in 1998, see Visser, 1998) and BREACH (developed by Steetzel in 1996 with latest update in 1998 by Steetzel and De Vroeg, see Steetzel and De Vroeg, 1998) have been specifically developed for the breach growth in sand-dikes. The main characteristics of these two models are summarized in Table 2.3.

The BRES model is based on the mechanism of breach erosion as observed in various tests in the laboratory and the field (Visser, 1998). It is assumed that the dike was constructed with sand and that the clay-layers and revetments on the slopes do not decelerate the erosion process. A relatively small initial breach is assumed in the top of the dike that is so large that water flows through it starting the breach erosion process. Visser (1998) divided the breach erosion process into five stages. In the first three stages the initial breach cuts itself into the dike until at the end of Stage III the dike in the breach has been completely washed out. Then in the following Stages IV and V three types of breaches can be distinguished depending on the geometrical and material conditions of the dike. For the entrainment of the dike material and its transportation through the breach, a simplified version of Galappatti's (1983) description for the pick up of sediment is applied. The sediment transport formulae of Engelund-Hansen (1967), Van Rijn (1984a, b), Wilson (1987) and Bagnold-Visser (1989) can be selected in each of the five stages. The model was calibrated with the data of the Zwin'94 field experiment and validated against the data of a laboratory experiment (see Visser, 1998, for the Zwin'94 field experiment, see also Section 2.4). A good agreement between the model predictions and the data of the two experiments was obtained. Confrontation of the model with the failure of the Noord Dike in the Netherlands in 1953 achieved a more or less agreement with a rough eye-witness report.

Table 2.3 Main characteristics of the BRES and BREACH models.

Items	BRES (Visser, 1998)	BREACH (Steetzel and De Vroeg, 1998)
Time developed	first edition in 1986 with latest update in 1998	first edition in 1996 with latest update in 1998
Function	modeling of breach growth in sand-dikes	modeling of breach growth in sand-dikes
Breach flow discharge	broad-crested weir flow	product of specific discharge and breach width
Sediment transport	Bagnold-Visser (1989), Engelund and Hansen (1967), Van Rijn (1984a,b), and Wilson (1987)	Bagnold-Visser (1989)
Breach geometry	trapezoidal	rectangular
Erosion initiation	initial breach in the dike crest	initial breach in the dike crest
Number of stages divided	5	5
Scour hole formation	no	no
Input	geometry of dike and initial breach, material properties, hydraulic conditions, polder, etc.	geometry of dike and initial breach, material properties, hydraulic conditions, polder, etc.
Validation data	laboratory tests, field tests, and prototype dike failure	laboratory tests, field tests, and prototype dike failure

The BREACH model was first developed by Steetzel in 1996 as an effort for prediction of breach growth in sand-dikes. Later it was extended, tested and validated by Steetzel and De Vroeg (1998). The sand-dike breach erosion process is divided into five stages too, with the first three dominated by weakening of the dike body and the last two by breach widening. The erosion of the breach in vertical direction is directly derived from the computed transport gradient in the breach. The sediment transport rate is computed by use of Bagnold-Visser (1989) formula. The model was validated against a series of laboratory and field tests of sand-dikes. A reasonable agreement has been achieved for the majority of the predicted items (see Steetzel and De Vroeg, 1998).

Busnelli (2001) described numerical simulation of breach growth in sand-dikes. A 3D hydrodynamic model was used to compute the flow velocities in the breach. The model was tested with the data of the Zwin'94 experiment (see Visser, 1998, see also Section 2.4). The simulated maximum velocity in the breach and the Froude number for the maximum velocity agree with the measured values. A 1D morphological model was applied to simulate the vertical erosion in the early stages of the breach growth. For the sediment transport the formula of Meyer-Peter and Müller (1948) was chosen. The laboratory experiment on sand-dike breaching carried out in 1996 at Delft Uni-

versity of Technology (see Visser, 1998) was taken as an example to check the potential of the 1D model.

Liang et al. (2002) developed a model for the simulation of breaching of the dikes along the Yellow River. The 2D shallow water equations were applied to simulate the river flow. The sediment transport during dike breaching was described by formulae for non-equilibrium sediment transport and riverbed deformation. The method for riverbank stability analysis of Osman and Thorne (1988) was adopted to calculate breach widening. The model was first tested against a hypothetical idealized rectangular dam-break event and then against a laboratory experiment on dike breaching along the Yellow River, with predicted hydraulic characteristics for the latter in reasonable agreement with the experimental data. The model was also applied to a hypothetical prototype breach in the dikes of the Yellow River.

Due to the large ratio of dam height to length, most of the mathematical models for earth dam breaching (as been reviewed in Section 2.2) do not include the breach widening after the dam is broken through (i.e. the breach reaches the dam foundation). These models can be roughly considered to contain only the first three stages of the dike breach growth models (see e.g. Visser, 1998 and Chapters 4 and 5).

## 2.4 Experiments on embankment breaching

### 2.4.1 Introduction

Breach formation and development in embankments is a complicated process with still little understanding. Experiments on the breaching of embankments are therefore, at least for the moment, very valuable and irreplaceable for gaining more insight into the process, and for the development, calibration and validation of the mathematical models.

It is found from the literature that various experiments on breaching of embankments have been performed during the last several decades, particularly since the end of 1980's (Zhu et al., 2004b). These experiments include both large-scale tests in the field and small-scale tests in the laboratory. The latter include numerous flume and wave basin embankment breach tests, which can be found in e.g. Powledge and Dodge (1985), Fujita and Tamura (1987), Steetzel and Visser (1992, 1993), Pan and Loukola (1993), De Looff et al. (1997), Visser (1998), Andrews et al. (1999), Hahn et al. (2000), Tingsanchali and Chinnarasri (2001), Rozov (2003), Mohamed et al. (2004) and Zhu et al. (2006c). Almost all of these laboratory-tested embankments have less than 1 m height. However, the height of embankments is important because scale effects sometimes may interpret an unreal mechanism of breach erosion.

Accordingly, large-scale experiments in the field are preferable when possible. Relevant tests have been carried out in many countries such as China, the

Netherlands, the United States, the United Kingdom, Norway and Germany. For details on these tests readers are referred to Pan and Loukola (1993), Visser et al. (1991, 1996), Visser (1998), Temple and Hanson (1998), Hahn et al. (2000), Chen and Anderson (1987), Meadowcroft et al. (1996), Höeg et al. (2004), and De Vroeg et al. (1998). A few of these tests are shortly described below.

### 2.4.2 Fuse plug dam field tests in China

Since the end of the 1970's, large-scale fuse plug dam model tests have been carried out in situ in many projects in China, e.g. the tests for the Dahuofang Reservoir, for the Nanshan Reservoir, and for the Yahekou Reservoir (see Pan and Loukola, 1993). Here a fuse plug dam refers to an auxiliary or emergency spillway comprising a low embankment designed to be eroded away during exceptionally large flood. Table 2.4 gives a brief summary of the main characteristics of the fuse plug dam model tests for these three reservoirs.

Table 2.4 Characteristics of the fuse plug dam model tests conducted in China.

	Dahuofang Reservoir fuse plug dam test	Nanshan Reservoir fuse plug dam test	Yahekou Reservoir fuse plug dam test
Time of test	-	March 25, 1978	March 1982
Location of test dam	tailrace	chute of main spillway	chute of spillway
Dam type	inclined clay core gravel fill dam	inclined clay core gravel fill dam	clay core sand fill dam
Dam height (m)	3.0	2.5	5.6 <sup>1</sup>
Dam length (m)	15.4	13.5	30.5
Dam crest width (m)	-	1.0	4.0
Dam upstream slope	-	1:1	1:3
Dam downstream slope	-	1:1.5	1:2.5
Pilot channel depth (m)	0.63	0.5	1.3
Pilot channel width (m)	-	2.0	1.5
Model reservoir capacity (m <sup>3</sup> )	7000	1900	46000
Dam break period (min)	19.5/34.25 <sup>2</sup>	37	33

<sup>1</sup> A series of fuse plug dam model tests were performed for the Yahekou Reservoir with 5.6 m being the highest one.

<sup>2</sup> The two time periods correspond respectively to two different reservoir water levels (2.80 m/2.56 m).

Figure 2.3 shows the scouring time-contours of one of the fuse plug dam tests for the Yahekou Reservoir. The whole process of the dam breach took 33 min, of which 22'40" were taken for the formation of pilot scouring opening, and 10'20" for lateral erosion.

The main conclusions drawn from these fuse plug dam model tests include (Pan and Loukola, 1993):

- Pilot scouring type fuse plug dam seemed to be feasible and effective as an emergency spill facility.
- The erosion process of a fuse plug dam can approximately be distinguished into three phases: downstream slope erosion, denudation of the inclined core and the collapse of the inclined core (drawn from the Nanshan Reservoir test).
- In addition to the water head, the main factors affecting the erosion rate were the type and the thickness of the core (drawn from the Nanshan and Yahekou Reservoir tests).
- The average velocity at the opening for a fuse plug dam about 1.0 to 5.6 m high is generally larger than the critical scouring velocity (below which no scouring occurs) of soil or soft rock base. Therefore, great attention should be paid to the protection of the foundation if a fuse plug dam has to be built on such foundation (drawn from the Yahekou Reservoir tests).

### 2.4.3 Zwin'94 field experiment in the Netherlands

The Zwin'94 field experiment on embankment breach erosion was performed in 1994 in the Zwin Channel, a tidal inlet at the Dutch-Belgian border (see Visser et al., 1996 and Visser, 1998). This experiment was preceded by an experiment in 1989 at the same location aimed at observing the breach development process rather than measuring the process (see Visser et al., 1991).

In the Zwin'94 experiment a sand-dam 2.6 m high was built with local sand. Figure 2.4 shows the cross-section of the sand-dam. A small trapezoidal pilot channel, 0.8 m deep, 1.0 m wide at the breach bottom and 3.6 m wide at the embankment crest was made in the upper part of the dam to induce the breaching. Water levels and flow velocities upstream and downstream of the breach were measured continuously during the experiment; the increase of the breach width was both video-taped and photographed; and the breach development under water after the formation of a breach in the sand-dam was detected by use of 40 vibration probes entrenched in the channel sandy bottom (see Visser, 1998).

Figure 2.5 displays the results of observations of the breach width growth in time in the Zwin'94 experiment. The Zwin'94 experiment clearly confirms the five-stage breach erosion mechanism described by Visser (1998), see also Chapter 4.

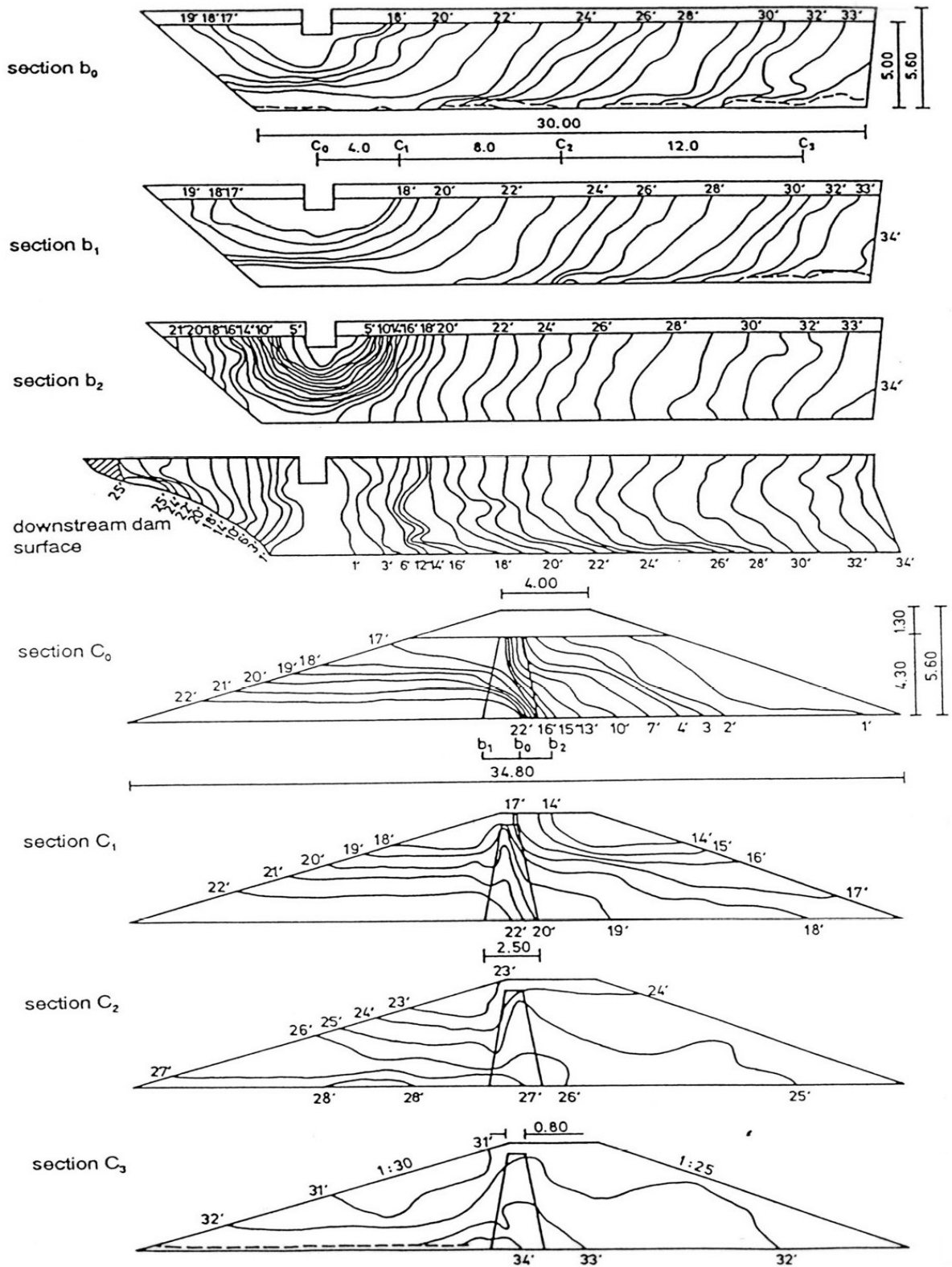


Figure 2.3 Scouring time-contours of one of the Yahekou Reservoir tests (after Pan and Loukola, 1993).

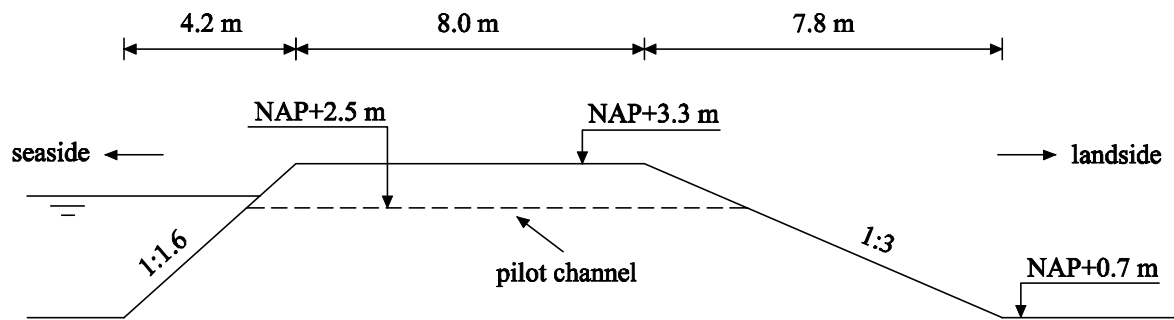


Figure 2.4 Cross-section of the sand-dam in Zwin'94 experiment (with NAP being the reference mean sea level in the Netherlands, after Visser, 1998).

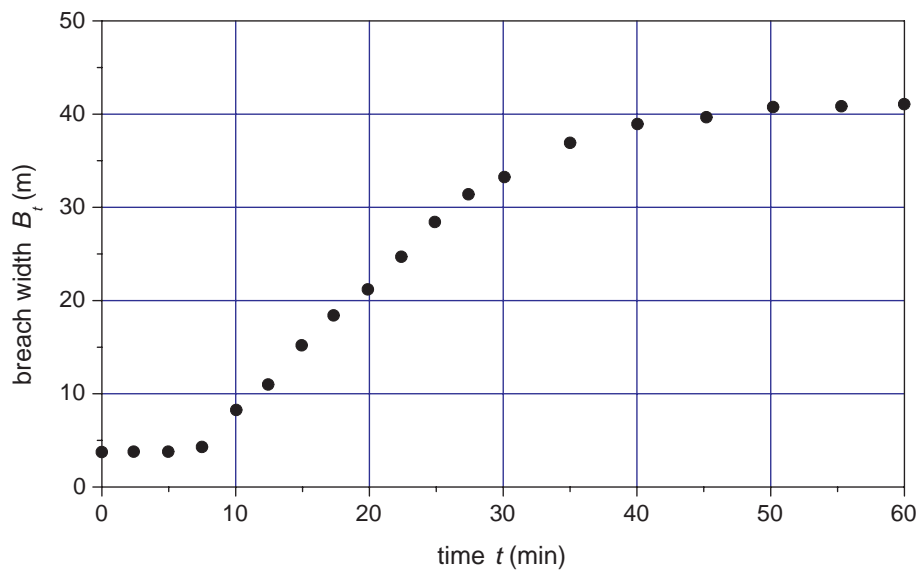


Figure 2.5 Increase of breach width in Zwin'94 experiment (observed at dam crest, after Visser, 1998).

#### 2.4.4 The Nordland field experiments in Norway

Altogether 7 field embankment breach tests were performed in Nordland in Norway in 2002 and 2003, with 5 of them as part of the EC IMPACT Project<sup>1</sup> (see Höeg et

<sup>1</sup> IMPACT Project: Investigation of Extreme Flood Processes and Uncertainty. EC Project Reference No.: EVG1-CT2001-00037.

al., 2004 and Vaskinn et al., 2004). The test site is about 600 m downstream of the Rössvatn dam. The Rössvatn spillway gates feed directly into the test reservoir with a capacity of  $450 \text{ m}^3/\text{s}$ , capable of maintaining a constant reservoir level during the dam breaching.

According to Höeg et al. (2004), among the 7 tests, in Test 1 a homogeneous rockfill dam was tested, in Test 2 a homogeneous clay fill dam, in Test 3 a homogeneous gravel dam, and in Test 4 a homogeneous rockfill dam with smaller crest width and coarser rockfill than those in Test 1. Test 5 concerns a rockfill dam with a central moraine core, Test 6 a rockfill dam with a central moraine core, and Test 7 a homogeneous dam made of moraine. Except for Tests 6 and 7 in which the dams failed due to piping, in all the other tests the dams were breached by overtopping. The test dams are 36 m long, and most of them are 6 m high. Figure 2.6 shows the cross-section of Test 2.

During the tests, inflow and outflow, pore water pressures in the dam body, breach initiation, formation and progression were monitored and relevant data recorded. The preliminary findings showed that the erosion along the downstream slope due to overtopping was slow and gradual (see Höeg et al., 2004). However, when the "scour and unravelling" reached the dam upstream slope, the breaching was rapid and dramatic. The breach was first enlarged vertically till the dam foundation was reached, before it expanded laterally. The breach side-slopes were discovered to be very steep, almost vertical. The phenomena described above generally hold for all the three materials (i.e. rockfill, gravel and clay). For Test 6, the internal erosion initiated at the defects built into the moraine core developed very slowly, even without filters between the moraine core and the downstream rockfill. Breaching of the dam did not occur until the erosion reached the crest and then the dam failed by overtopping as in Test 5, however, the breach was not as wide (Höeg et al., 2004).

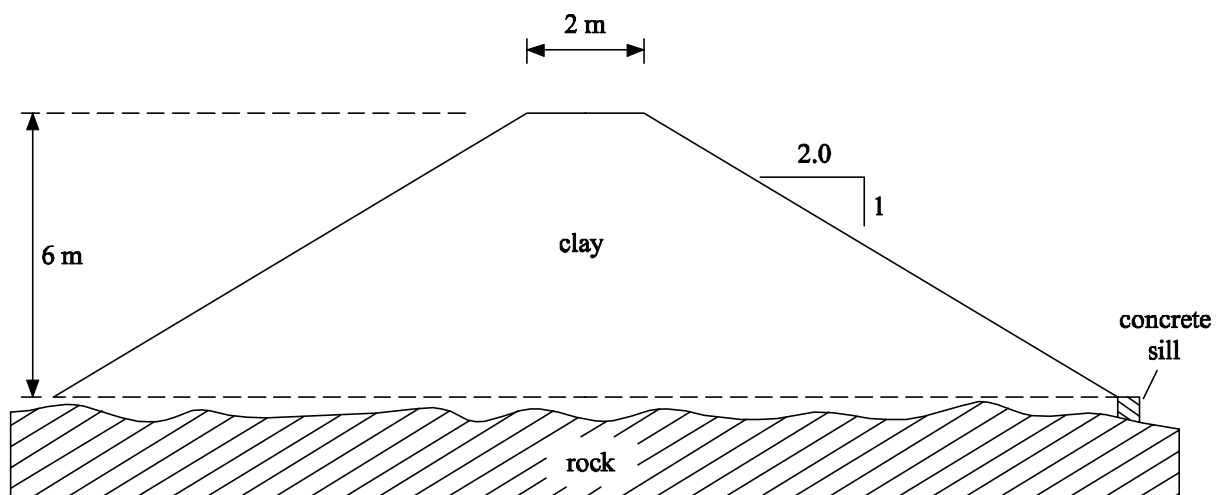


Figure 2.6 Cross-section of embankment of field Test 2 (after Höeg et al., 2004).

#### 2.4.5 The HERU large-scale experiments in the United States

The Hydraulic Engineering Research Unit (HERU) of the United States Department of Agriculture (USDA) at Stillwater, Oklahoma, has recently performed some large-scale embankment (2.3 m or 1.5 m high) overtopping and breaching tests (see Temple and Hanson, 1998; Hahn et al., 2000). Three different materials, two non-plastic silty sand materials and one lean clay material were used to build the embankments, respectively. Based on test observations and recorded data on bed profiles and breach cross-sections during testing, the mechanism of embankment overtopping erosion was described (see Hahn et al., 2000). First rill and micro-rill erosion on the downstream slopes of the embankments were initiated by the overland sheet flow (see Figure 2.7b). The erosion eventually developed a network of rills that gradually developed into a master rill(s) (i.e. gully). This dominant channel initially consisted of multiple cascading overfalls (see Figure 2.7c) that in time migrated upstream while simultaneously widened, until only a single large headcutting channel remained (see Figure 2.7d). The headcut eventually migrated to the upstream end of the embankment crest, from then on any further upstream migration of the headcut resulted in a crest lowering (see Figure 2.7e) and increased the discharge from the reservoir. This progression finally led to a full breach (see Figure 2.7f).

The gully widening and the headcut upstream migration were believed to be due to the turbulence and hydraulic stresses surrounding the jet impingement area just downstream of the headcut (Hahn et al., 2000). The hydraulic stresses eroded the base of the headcut, causing the wall to become unstable and ultimately producing mass failure. As a result the breach was widened and the headcut moved backwards.

Figure 2.8 shows the centerline profile of one of the HERU tests indicating the process of headcut migration during testing.

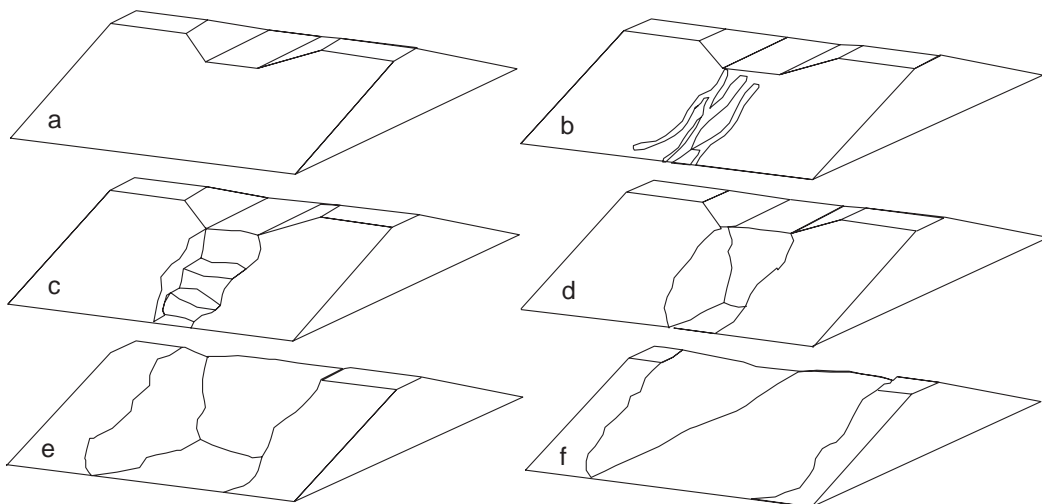


Figure 2.7 Observed breaching process during embankment overtopping tests (after Hahn et al., 2000).

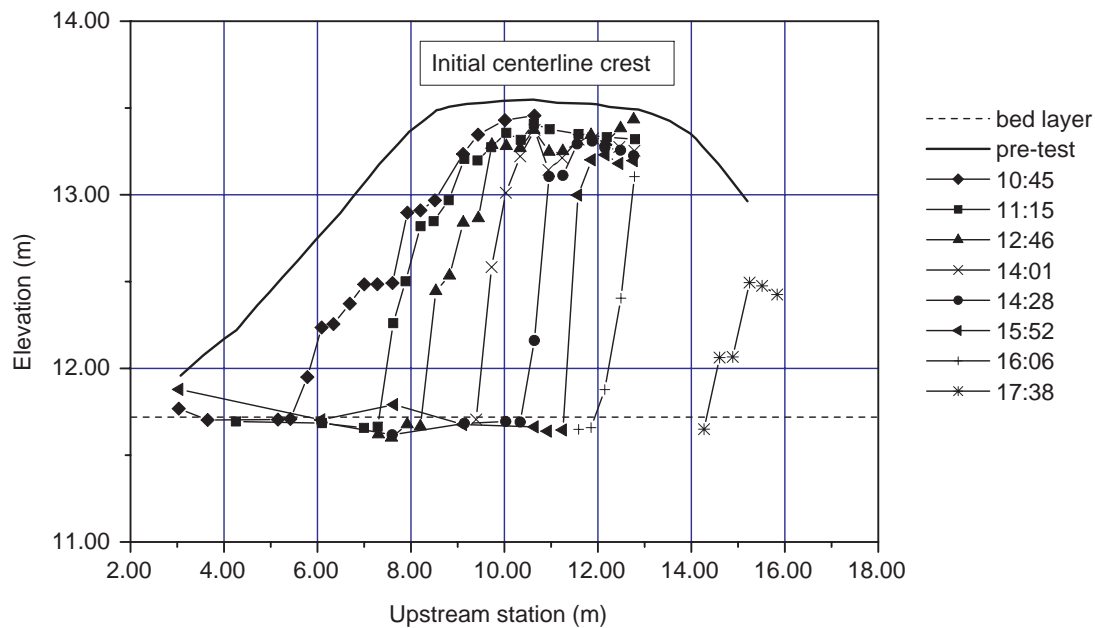


Figure 2.8 Centerline profile of Test 3, FS#2 (after Hahn et al., 2000).

## 2.5 Headcut erosion during embankment breaching

### 2.5.1 Introduction

When water flows over an abrupt drop in a bed elevation, the impinging jet may attack the downstream bed and create a reverse roller (see Figure 2.9). This reverse rolling water exerts hydraulic shear stress to the bottom and the near vertical slope of the overfall (Robinson, 1992), causes deepening of the bed and undermining of the near vertical slope, resulting in soil mechanical slope instability and accordingly retreat of the overfall (see Figure 2.10). The overfall or abrupt drop in the bed elevation is called headcut.

As stated earlier in Section 2.2, based on laboratory experiments and observations of real embankment failures, a new view on the mechanism of embankment erosion during overtopping has been put forward recently. Headcut erosion is regarded as the predominant mode of failure for most cohesive embankments (see e.g. Ralston, 1987; Dodge, 1988; Powledge et al., 1989; Hanson et al., 1999; Wahl, 2004).

Ralston (1987) presented a description of the mechanics of embankment erosion. He argued that for cohesive embankments, breaching takes place by headcutting rather than tractive stress erosion. Sometimes a series of stair-step headcuts form on the downstream slope of the dam after initiation of erosion. Seepage through the

embankment that exits the eroding face will increase the rate of erosion. This effect has also been noted by Powledge et al. (1989).

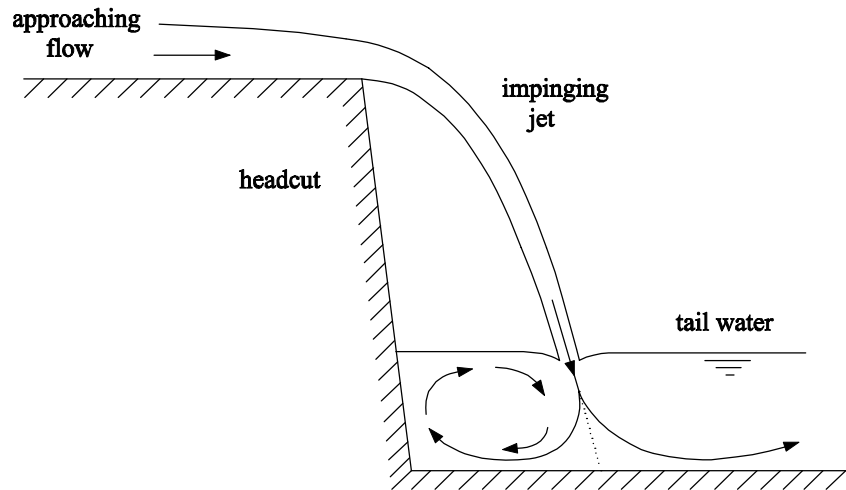


Figure 2.9 Sketch of a headcut.

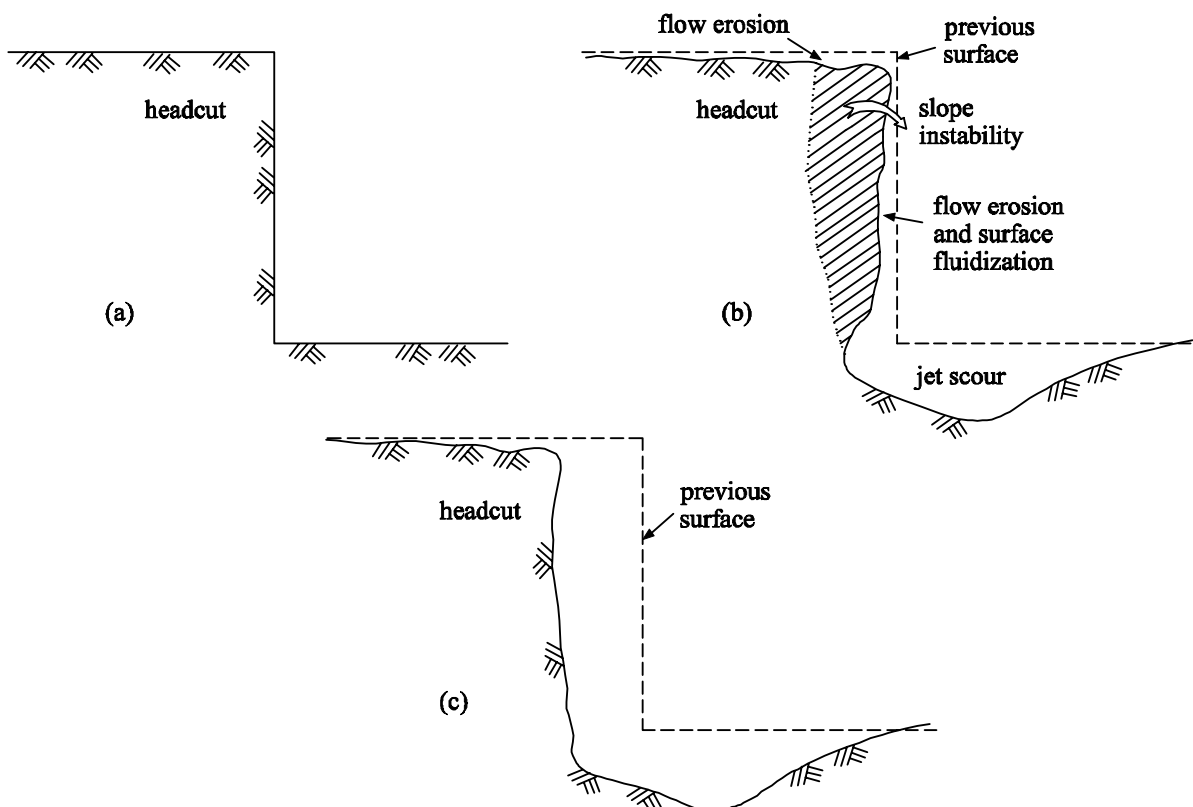


Figure 2.10 Erosion at a headcut (flow is not drawn): (a) intact headcut; (b) flow erosion and soil mechanical slope instability; and (c) migration of headcut.

Similar mechanisms are also important in the erosion of earth and rock spillways (Wahl, 1998). According to Temple and Hanson (1994), headcut formation and migration is part of the erosion process in vegetated earth (soil and rock) auxiliary or emergency spillways. Mathewson et al. (1998) concluded from post-flow field inspections of eroded spillway channels that once erosion was initiated at some geometric anomaly, the principal erosion mechanism was either boundary shear or headcutting.

In this section a review of literature on experimental (Section 2.5.2) and mathematical (Section 2.5.3) research on headcut erosion is given.

### 2.5.2 Experiments on headcut erosion

Robinson (1996) presented the results of ten large-scale headcut erosion tests with either red sandy clay or silty sand. The red sandy clay exhibited 25% clay, 40% silt and 35% sand, and the silty sand had 13% clay, 30% silt and 57% sand (according to the Unified Classification System, see Chapter 3). The outdoor flume used is 1.8 m wide and 29 m long with 2.4 m high sidewalls. Discharge (approximately 1.55 m<sup>3</sup>/s), headcut height (1.2 m) and backwater level (either 0.3 m or 1.0 m) were held constant while altering soil properties in the tests. The headcut migration rate decreased as the average density and average unconfined compressive strength increased (see Figure 2.11). The influence of an underlying sand layer was also examined (Robinson, 1996). The sand layer did not appear to influence the rate of advance significantly when the overlying material was very erodible, however, it accelerated the advance rate greatly due to undercutting when the overlying material was more erosion resistant. Tension cracks and mass failures are typically the failure mechanisms for tests with an underlying sand layer. A similar phenomenon was also observed by Okagbue (1989) in the erosion process along Ekole Creek bank between Yenaka and Ayama in the Niger Delta.

The same flume was also used to investigate the headcut advance with multiple headcut heights (from 0.91 m to 1.58 m) and discharges (from 0.72 m<sup>3</sup>/s to 2.43 m<sup>3</sup>/s) for the same red sandy clay, see Robinson (1996). Eleven tests were conducted in total. It was observed that the headcut migration rate was not greatly affected by the headcut height and discharge over the tested range. The soil properties overshadowed the effects of the headcut height and discharge when headcut migration rate was concerned. The headcuts were found to erode with both sloping and vertical faces. The headcuts in tests with lower moisture content were more likely to proceed with a sloping face, while the higher moisture tests exhibited erosion along a vertical face. A typical plot of the headcut migration versus time is shown in Figure 2.12 for Test 27.

The influence of the backwater level on the rate of headcut migration was also studied through experiments in the flume (Robinson, 1996). The discharge (1.6 m<sup>3</sup>/s), headcut height (1.2 m), and soil type (red sandy clay) were held constant and the

backwater level was varied. Totally four tests were performed with four backwater levels per test. It was found that the maximum advance rate occurred at a backwater to headcut height ratio of approximately 0.8 (Robinson, 1996). This agreed well with predicted stresses on the vertical headcut face, which also peak at the same backwater to headcut height ratio (see Robinson, 1992). Based on laboratory experiments, Robinson (1992) proposed expressions for the maximum time-averaged stress on the horizontal floor below the headcut and on the vertical wall.

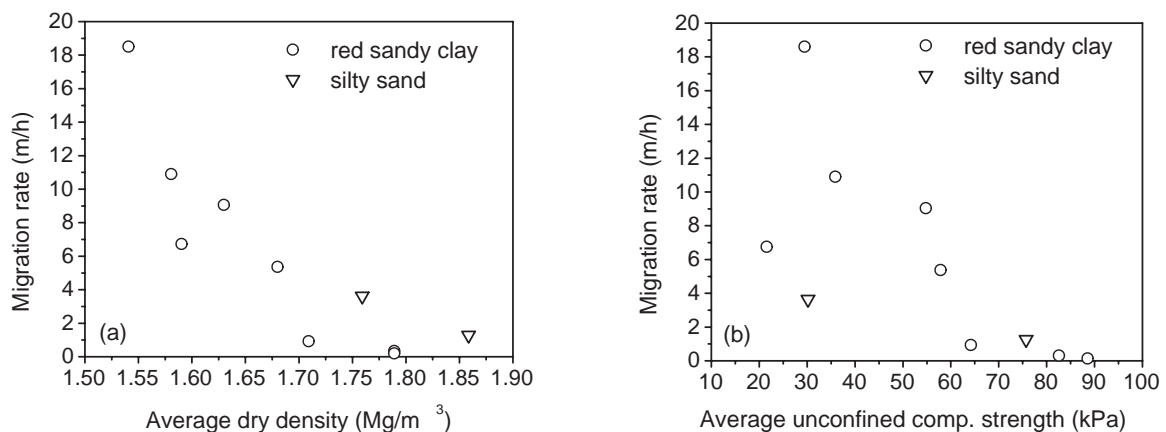


Figure 2.11 Headcut migration rate vs. average dry density (a) and migration rate vs. unconfined compressive strength (b) (after Robinson, 1996).

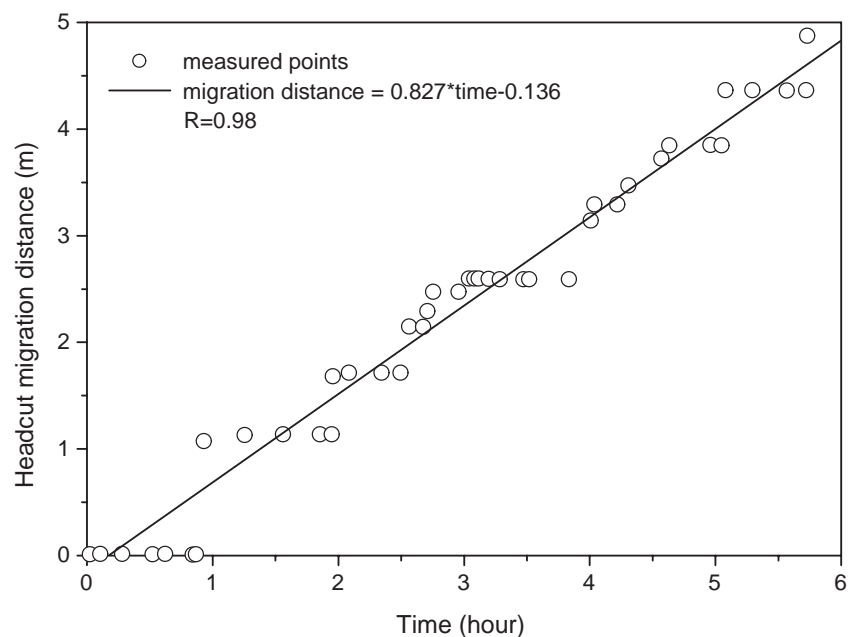


Figure 2.12 Headcut migration distance vs. time for Test 27 (after Robinson, 1996).

Robinson et al. (2000) measured the velocity field downstream of a large straight drop headcut (1.2 m high) in the same flume as described above in this section. The velocities were measured for six combinations of backwater levels and flow rates. Upstream of the nappe entry point into the backwater pool, a reverse roller was observed to circulate in a clockwise direction. Downstream of this nappe entry point, a large area of counterclockwise circulation was observed: the flow exited downstream along the bottom and returned upstream at the surface.

In the tests performed in the same flume as described above with a stable, non-migrating headcut (0.6 m high, see Bennett et al., 2000b), the flow varied from 0.2 to 2.5 m<sup>3</sup>/s. The tests showed that erosion occurred both along the approach bed due to turbulent shear and downstream of the headcut due to nappe impingement. The erosive potential of the nappe increased when the relative backwater height decreased, and the erosion rate downstream of the headcut decreased obviously with high backwater levels (i.e., when the headcut nappe floated). Highest rates of erosion in the area of nappe impingement were observed when flow discharge was high and backwater level was low.

Stein and LaTray (2002) reported nine headcut retreating experiments (numbered CL1-CL9) with stratified structure: the so-called F-70 Ottawa sand provided the base layer, and pure kaolinite clay the surface layer. The experiments were performed in a flume made of plexiglas with a length of 241 cm, a width of 15.2 cm and a depth of 61 cm. The height of the headcuts varied from 1.3 cm to 4.3 cm. Due to preparation failure of the required headcut in three experiments, only six useable data sets were yielded. During the tests, a scour hole developed just downstream of the headcut in the exposed sand layer. The hole developed quickly in vertical and horizontal directions, undermining and causing a cantilevered condition of the clay layer, eventually followed by a mass failure and upstream migration of the headcut. This process repeated from then on. Figure 2.13 presents the measured headcut migration distance as a function of time.

Bennett et al. (2000a) reported experiments on headcut growth and migration performed in a non-recirculating, 5.5 m long flume. The soil material used in the study is a sandy loam to sandy clay loam texture. It consists of 20.0% clay, 2.9% silt and 77.1% sand, with the  $D_{50}$  of the sand component being 0.26 mm. A pre-formed headcut 2.5 cm high was made before testing. Altogether nine runs of experiments were performed with differences in, e.g. soil bulk density and flow discharge. Scour hole development downstream of the headcut and headcut upstream migration were observed and recorded. Headcut growth and development were found to be the same for all runs. After an initial period of bed adjustment, a steady condition was reached in which scour hole geometry, migration rate and sediment yield remained unchanged. It was concluded from the experiments that increased flow discharge caused a larger scour hole.

Bennett and Casallí (2001) conducted experiments to examine the effect of the initial step height on headcut development in upland concentrated flows in the same flume as reported in Bennett et al. (2000a). The material used is a sandy loam to sandy clay loam texture, commonly found in the southeastern USA. Ten different heights were used: 5, 10, 15, 20, 25, 30, 35, 40, 45, and 50 mm. The overland flow discharge was about 69.6 l/min, the average upstream flow depth was about 14 mm, and the average upstream flow velocity was about 0.57 m/s. Bennett and Casallí (2001) found that as the initial step height increased, the headcut migration rate increased (not statistically significant), the jet entry angle and maximum scour depth ( $S_D$ , the vertical distance from the headcut brink to lowest point within the scour hole) increased, and the length to maximum scour depth ( $S_L$ , the horizontal distance from the headcut brink to  $S_D$ ) decreased (see Figure 2.14). The ratio  $S_L/S_D$  decreased as the initial step height increased.

The very small scale of the experiments described by Stein and LaTray (2002), Bennett et al. (2000a) and Bennett and Casallí (2001) makes them susceptible to measuring inaccuracies and other interferential factors (e.g. nonuniformity of density and moisture content).

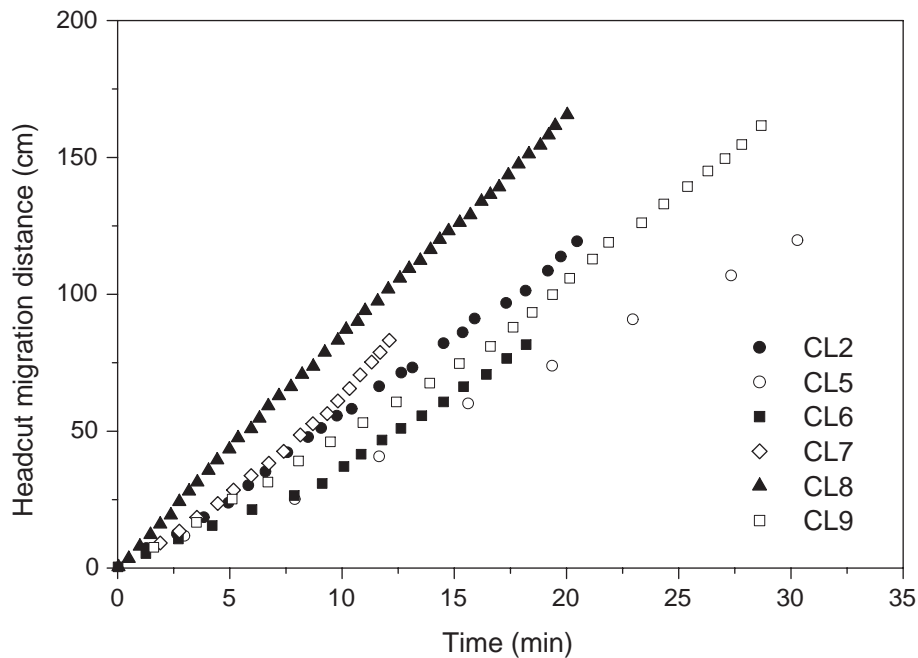


Figure 2.13 Measured headcut migration distance vs. time (after Stein and LaTray, 2002).

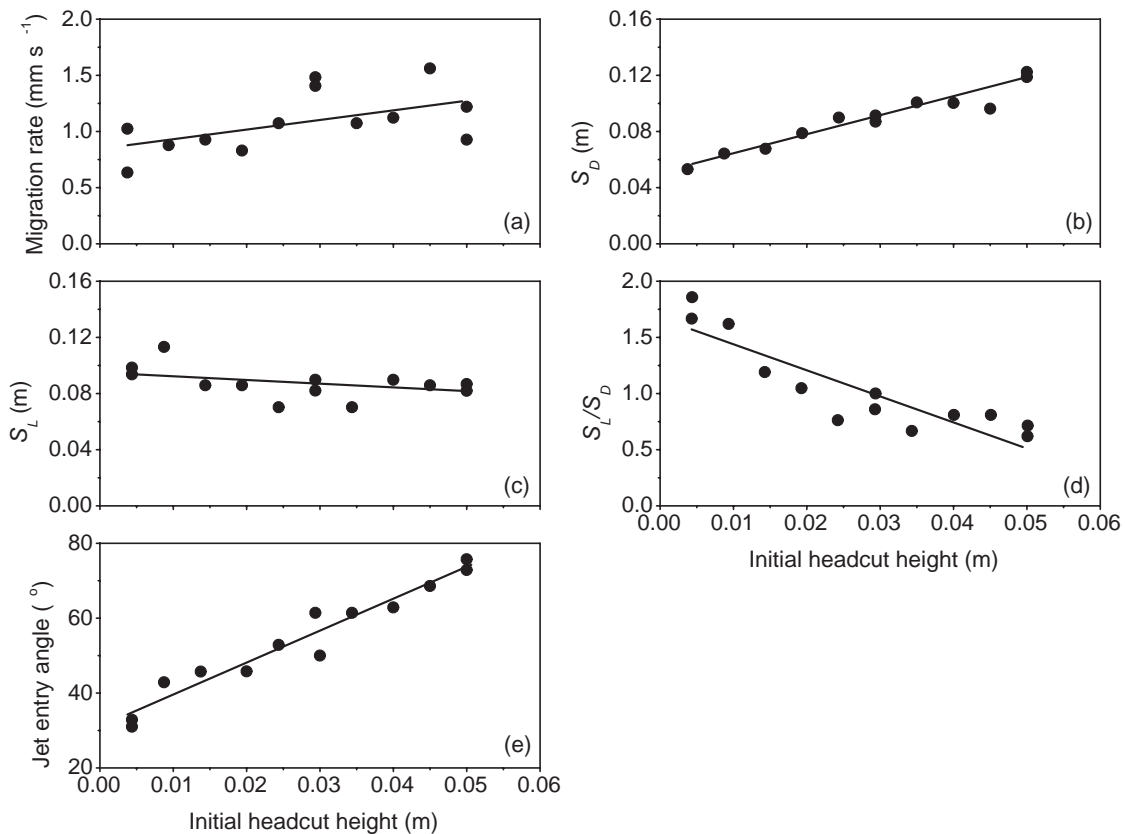


Figure 2.14 Variation of steady state headcut parameters with initial headcut height (after Bennett and Casalí, 2001).

### 2.5.3 Headcut migration prediction

Predicting headcut migration is an intricate problem. The process of headcut migration may involve scour of jet impingement to the downstream bed, mass failure and/or shear erosion from the headcut slope surface, erosion along the approaching bed and removal of the failed material from the scour hole. There is presently no generally accepted model for prediction of the headcut migration (Zhu et al., 2004a, 2004b and 2005a). However, recently some simplified approaches have been proposed to calculate the rate of headcut migration (e.g. De Ploey, 1989; Temple, 1992; Robinson and Hanson, 1994; Temple and Moore, 1997; Wu et al., 1999; Hanson et al., 2001; Alonso et al., 2002; Stein and LaTray, 2002; Zhu et al., 2004a and 2005a). De Ploey (1989), Temple (1992), Temple and Moore (1997) and Hanson et al. (2001) are simple equations that generally link the headcut migration rate with the energy at the headcut by a material dependent factor. The others listed above are relatively more complicated models with more factors taken into account. Table 2.5 lists the simple equations, and Table 2.6 summarizes the main characteristics of the other relative more complicated models.

Table 2.5 Summary of the equations predicting headcut migration (after Zhu et al., 2004b).

Model and time developed	Equation	Explanation
De Ploey (1989)	$R_h = Cq \left[ g + U_b^2 / (2H_b) \right]$	$R_h$ = rate of headcut migration; $C$ = a material dependent factor; $q$ = unit discharge; $g$ = gravity acceleration; $U_b$ = flow velocity at headcut brink; $H_b$ = headcut height;
Temple (1992)	$R_h = Cq^m H_b^n$	
Temple and Moore (1997)	$R_h = C \left[ (q\gamma H)^{1/3} - E'^a \right]$	$\gamma$ = unit weight of water; $H$ = the change in elevation of the energy grade line through the headcut; $E'$ = threshold energy required to generate headcut migration;
Hanson et al. (2001)	$R_h = \frac{TE}{E_v}$	$T$ = average retreat distance at each mass failure; $E$ = soil detachment rate; and $E_v$ = the amount of erosion required into the vertical wall to induce failure.

### 2.5.4 Discussion

Based on laboratory experiments and observations of prototype embankment failures, headcut erosion was recently proposed to be dominant in most embankment breaches by some investigators (e.g. Ralston, 1987; Dodge, 1988; Powledge et al., 1989; Hanson et al., 1999; Wahl, 2004).

During the literature review, however, it has been found that research on headcut erosion for embankment breaching is only in a preliminary phase (Zhu et al., 2004b). Little information exists on the variation of scour hole morphology and the headcut migration dynamics. Understanding of the headcut formation and migration is not complete and far from mature to be described mathematically. Although there are already some models trying to predict the migration rate of headcut, most of them are empirical and simplified.

In addition, the experiments conducted so far on headcut erosion (as described in Section 2.5.2) generally concern relatively small headcut heights. The stability of the headcut and the morphology of the headcut erosion are not only dependent on the soil properties and the hydraulic conditions, but also on the height (dimensions) of the headcut (see Chapter 4 and Appendix B).

Table 2.6 Summary of the main characteristics of the other mentioned headcut migration models.

Model and time developed	Flow	Foundation scour and headcut undermining	Seepage	Headcut migration distance
Robinson and Hanson (1994)	experimental data fitted equation for jet flow	Robinson (1992) and an excess stress equation	not considered	assumed half of the headcut height
Wu et al. (1999)	the flow model of FAST3D.river code	the sediment transport model of FAST3D.river code	not considered	the maximum of those induced by vertical surface shear erosion and toe scour
Alonso et al. (2002)	theoretically calculated jet flow	based on the analytical development of Stein et al. (1993)	not considered	steady migration rate equation
Stein and LaTray (2002) <sup>1</sup>	development of Alonso et al. (2002)	based on the analytical development of Stein et al. (1993)	not considered	calculated through mechanical method
Zhu et al., (2004a and 2005a)	theoretically calculated jet flow	a. erodible foundation: based on the analytical development of Stein et al. (1993); b. non-erodible foundation: Robinson (1992) and an excess stress equation	considered	calculated through mechanical method

<sup>1</sup> This model is developed for the specific case of a relatively erosion-resistant soil layer overlying a deep, relatively erosive base soil, see Stein and LaTray (2002).

## 2.6 Discussion

Modeling of embankment breaching is essential in estimation and minimization of the consequences of embankment failures. The breach model together with the flood routing model can give a prediction of the breach development and the outflow hydrograph and then the propagation of the breach-induced flood wave, with its arriving time to a certain place and the velocity and water depth as functions of time.

These calculations provide vital information for the embankment failure early warning system, emergency evacuation plan and rescue action, etc.

Considerable progress in the modeling technology of embankment breaching has been achieved over the last forty years, particularly since the 1980's (Zhu et al., 2004b). Various experiments on the breaching of embankments have been performed during the last several decades both in situ and in the laboratory. Many tools are now available for analysis of embankment failures and the resulting floods. These models can be generally classified into two categories: parametric based and physically based. Nevertheless, understanding of the mechanism of embankment breaching so far is still unsatisfactory, and the state-of-the-art of the breach modeling technology is far from advanced. There is presently no widely accepted model for embankment breach modeling. Most of the available models use tractive stress analysis and sediment transport process. This philosophy however, is considered by some investigators (e.g. Wahl, 1998) only to be appropriate for non-cohesive embankment breaches. Laboratory experiments and field observations of prototype embankment failures have indicated that headcutting is the predominant mode of failure for most cohesive embankments or rockfill embankments with a cohesive core.

For some mathematical models, the final breach parameters (i.e. final dimensions of the breach) are provided as input data, the development of the breach is then simulated using a linear increase in breach dimensions over the breach formation period. The final breach parameters are often estimated through case study-based predictive equations relating the breach parameters to features of the embankment and reservoir. Accuracy of the model simulation is therefore controlled by the quality of these equations which suffer from scattering of the available case study data.

In comparison with the developments in earth dam breach modeling, efforts dedicated to the simulation of breach growth in dikes initiated much later. Models available so far for dike breach erosion specifically are mostly limited to the simplest case of homogeneous sand-dikes.

Remarkably, data on the many historical prototype embankment failures, which are of great importance for the model verification, are found during the study to be limited and of poor quality (Zhu et al., 2004b). These data were usually collected after a failure and very often based on human observations rather than instrumentation. Such information is subjective and sometimes conflicting for the same event between different data sources (see e.g. Table 2.2).

To better model the breach growth in embankments, more research including both desktop work as well as experiments need to be conducted in the future. Experiments, especially full-scale or large-scale tests in the field are significant for better understanding of the physics of embankment breach growth and for the improvement in predictive accuracy of breach models. Professional collection and preserving of data on prototype embankment failures should be emphasized.

## Chapter 3

# Erosion of cohesive and non-cohesive sediment

### 3.1 Introduction

Generally, sediment can be classified as cohesive or non-cohesive. The two sediment categories differ enormously in performance when erosion by flow is concerned. For a long time various kinds of classification have been used according to the size of sediment particles. Table 3.1 summarizes the most widely accepted classification systems: the system used in the hydraulic engineering field in China (Technical Standard SL 42-92), the British Standard system (BS), the system of the American Society for Testing and Materials (ASTM), the system of the United States Department of Agriculture (USDA) and the Unified Soil Classification System (USCS).

For cohesive sediment, the resistance to erosion by flow depends heavily on the strength of the cohesive bond binding the particles. Cohesion may far surpass the influence of the physical characteristics of the individual particles (Simons and Sentürk, 1992). Contrarily, the reaction to fluid forces of non-cohesive sediment and their movement is mainly affected by the physical properties of the particles such as size, shape, density, porosity and fall velocity.

This chapter starts with a short description of the incipient motion of sediment (Section 3.2) and the erosion of non-cohesive sediment (Section 3.3). Because non-cohesive sediment is not the focus of this study and at the same time numerous good reference books are available on the erosion and transportation of non-cohesive sediment, these two sections give only very brief and basic information. Features of cohesive sediment, including the composition, structure, settling and deposition, consolidation, compaction, mechanical properties and erodibility, together with the rate of erosion by flow are presented in Section 3.4. Finally Section 3.5 hosts a discussion on the erosion of cohesive sediment.

Table 3.1 Classification of sediment according to particle size.

ASTM	clay	silt			sand			gravel			cobble	boulders			
					fine	medium	coarse								
	0.005	0.075	0.425	2	4.75	75	300								
BS	clay	silt			sand			gravel			cobble	boulders			
		fine	medium	coarse	fine	medium	coarse	fine	medium	coarse					
	0.002	0.006	0.02	0.06	0.2	0.6	2	6	20	60	200				
CHINA	clay	silt			sand			gravel		cobble		boulders			
		0.004	0.062	2	16	250									
USDA	clay	silt			sand			gravel			cobble	boulders			
		0.002	0.05	2	76	250									
USCS	clay	silt			sand			gravel		cobble					
					fine	medium	coarse	fine	coarse						
	0.001	0.002	0.01	0.075	0.1	0.425	1	2	4.75	10	19	75	100	300	1000
	Particle size (mm)														

### 3.2 Incipient motion of sediment

The incipient motion of a sediment particle on the streambed is due to the resultant effect of the flow disturbing forces on the particle becoming larger than the stabilizing forces such as gravity and cohesion.

The disturbing forces are highly related to the local near-bed velocities. In turbulent flow conditions the velocities are fluctuating in space and time. Together with the randomness of particle size, shape and position, this causes the initiation of motion having a statistical aspect (Van Rijn, 1993). Thus, even for uniform sediment, particles do not start to move simultaneously. For non-uniform sediment, conditions are much more complicated. Therefore, the incipient of motion is difficult to define, and different investigators have derived different criteria for the incipient motion of sediment from either a shear stress or a velocity approach or a flow power way.

Apart from depending on the definition of initiation of motion, the critical bed shear stress for incipient motion is also influenced by many other factors, such as particle shape, gradation, bed slope, and the form of the bed. When the bed consists of cohesive materials, cohesive forces between the sediment particles become important. These forces increase the strength of the sediment against flow erosion distinctly.

### 3.3 Erosion of non-cohesive sediment

The erodibility of non-cohesive sediment relies primarily on its particle size distribution, density and particle shape, etc. The main resistance to erosion by flow is offered by the submerged weight of the particles, i.e. gravitational forces.

Van Rijn (1984) performed flume experiments to determine the pick-up rate of particles in the range of 130 to 1500  $\mu\text{m}$ . An empirical pick-up function has been proposed based on the analysis of the experimental data (Van Rijn, 1984):

$$E = 0.00033\rho_s [(s-1)gD_{50}]^{0.5} D_*^{0.3} T_\tau^{1.5} \quad (3.1)$$

in which  $E$  is the pick-up rate in mass per unit area and time ( $\text{kg/s}\cdot\text{m}^2$ ),  $\rho_s$  is the density of sediment ( $\text{kg/m}^3$ ),  $s = \rho_s/\rho$ ,  $\rho$  is the density of water ( $\text{kg/m}^3$ ),  $g$  is the gravitational acceleration ( $\text{m/s}^2$ ),  $D_{50}$  is the median particle diameter (m) and  $D_*$  and  $T_\tau$  are given by, respectively

$$D_* = D_{50} [(s-1)g/\nu^2]^{1/3} \quad (3.2)$$

$$T_\tau = (\tau_b - \tau_{b,cr})/\tau_{b,cr} \quad (3.3)$$

in which  $\nu$  is the kinematic viscosity coefficient ( $\text{m}^2/\text{s}$ ),  $\tau_b$  is the bed shear stress ( $\text{N/m}^2$ ), and  $\tau_{b,cr}$  is the critical bed shear stress according to Shields ( $\text{N/m}^2$ ).

Different pick-up functions have been proposed by other investigators, e.g. Yalin (1977), and Nagakawa and Tsujimoto (1980). A good review has been given by Van Rijn (1993).

Once the non-cohesive sediment particles have been picked up by flow, three kinds of motion are distinguished depending on the size of the sediment particles and the flow conditions: rolling and sliding motion; saltation motion; and suspended particle motion (Van Rijn, 1993). Usually, the transport of particles by rolling, sliding and saltating is called the bed load transport. The suspended load may also contain some wash load, which is governed by the upstream supply rate.

Many methods for calculation of suspended load and bed load transport have been proposed to date. Here these methods will not be discussed specifically. For an overview the reader is referred to the many good reference books on sediment transport, e.g. Chien and Wan (1999), Simons and Sentürk (1992) and Van Rijn (1993).

## 3.4 Erosion of cohesive sediment

### 3.4.1 Introduction

Partheniades (1986) stated that cohesive sediments are characterized by two important properties, cohesion and plasticity, both due to the fine parts, usually of a settling diameter less than 5 micrometers, and of sufficiently large specific area for the surface physico-chemical forces to dominate the weight of the individual particles.

The behaviour of cohesive sediment is highly complicated during erosion with many influential factors involved (Mehta, 1986; Mirstkhoulava, 1991; Teisson et al., 1993; Mitchener and Torfs, 1996). In the last few decades, numerous studies have been done on the erodibility and erosion rate of cohesive sediment (e.g. Partheniades, 1965; Arulanandan, 1975; Kamphuis and Hall, 1983; Mei et al., 1997; Whitehouse et al., 2000; Winterwerp and Van Kesteren, 2004; Schaaff et al., 2006). As a result substantial progresses have been made in these fields.

Nevertheless, despite these studies and progresses, so far no general predictive models of cohesive sediment erosion exist. Available models are generally empirical and site-specific. From the present literature study it is found that the erosion of compacted cohesive soil (e.g. the soil composing a dike or earth dam) is not well documented, probably due to the following reasons: the high complexity of the erosion of cohesive soil and the non-quantitative description of the influence of compaction on the erodibility of cohesive soil. The literature mentioned in this chapter mostly focuses on soft cohesive sediment or mud. However, in Sections 3.4.2 and 3.4.3 the properties of both soft cohesive sediment and cohesive soil are described.

### 3.4.2 Properties of cohesive soil

#### *Composition*

Soil composition is one of the most important properties determining the erodibility of the soil. It is referred to as the mineral type, clay percentage by weight, organic matter and pore fluid composition, etc.

Generally, soil consists of particles composed of clay and non-clay mineral components and organic material. Clay particles are generally finer than a few micrometers and in water possess the characteristics of plasticity, thixotropy and adsorption (Van Olphen, 1977). The most abundant types of clay minerals are kaolinite, montmorillonite and illite. The non-clay minerals consist of quartz, carbonates, etc. The organic material appears either as discrete particles of wood, leaf matter, spores, etc., or it may be present as organic molecules adsorbed on the surface of the clay mineral particles (Murthy, 2003). The organic material present in cohesive soil may have a high compressibility and low strength and therefore can influence considerably the performance of soil during erosion.

The clay mineral composition affects to a large extent the properties of the soil. However, studies of cohesive soil erosion have hitherto considerably ignored the types of clay minerals in the soil. In some publications even no clear mention of the clay mineral type has been given when the erosion rate of cohesive soil is described. Kaolinite consists of a structure based on a single sheet of silica tetrahedrons combined with a single sheet of alumina octahedrons (see Figure 3.1a). The combined silica-alumina sheets are held together fairly tightly by hydrogen bonding and are not easily penetrated by water. The mineral is therefore stable and exhibits relatively low water absorption, small compressibility and plasticity, and low susceptibility to shrinkage and swelling under variations in water content (Berry and Reid, 1987; Qian and Yin, 1995). The structural arrangement of montmorillonite is composed of two silica tetrahedral sheets with a central alumina octahedral sheet. These combined sheets are linked together by very weak bonding of adsorbed water molecules and (exchangeable) cations (see Figure 3.1c). Montmorillonite therefore readily breaks down into very small particles and exhibits very high water absorption, very high shrinkage and swelling characteristics, very high compressibility and plasticity (Berry and Reid, 1987; Qian and Yin, 1995). The basic structural unit of illite is similar to that of montmorillonite except the combined sheets are linked together by rather weak bonding (however stronger than between montmorillonite sheets) due to non-exchangeable potassium ions held between them (see Figure 3.1b). Illite, accordingly, possesses properties between kaolinite and montmorillonite.

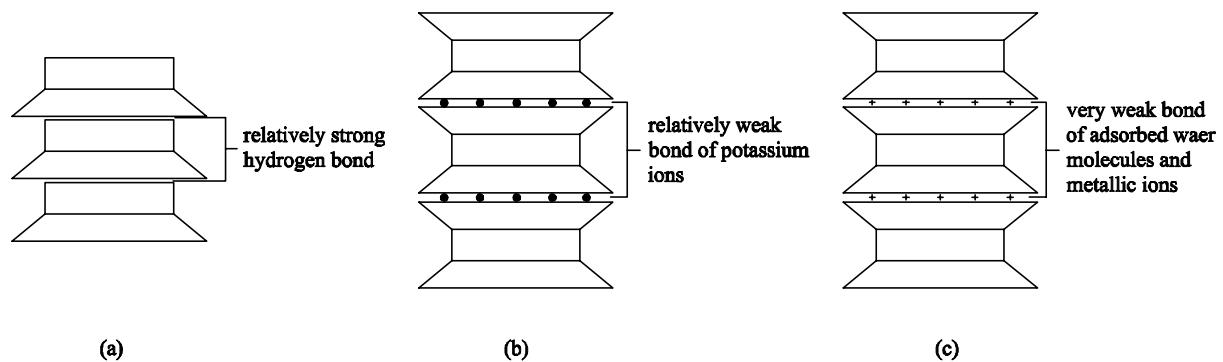


Figure 3.1 Clay mineral structure (a) kaolinite, (b) illite, (c) montmorillonite (after Berry and Reid, 1987).

The pore fluid exerts a significant impact on the erosion resistance of soil by salinity, pH, sodium absorption ratio (SAR), cation/anion composition, etc. The experimental results of Kelly and Gularte (1981) showed that the soil critical shear stress for erosion increases with an increasing salinity. That is, the salinity increases the erosion resistance of the soil. The same conclusion was drawn by Parchure and Mehta (1985). Arulanandan (1975) found that at high SAR values, the soil critical shear stress for erosion decreases with increasing cation exchange capacity (CEC). At low SAR values,

higher critical shear stress is required to detach particles and this increases with rising CEC value. However, Ariathurai and Arulanandan (1978) described conflicting results: for both high and low SAR values, the erosion rates decrease when CEC increases. Despite the many studies performed already, quantification of the effects of the multiple factors from the pore fluid on the erodibility of cohesive soil needs more research.

### ***Structure***

The term soil structure refers to the orientation and distribution of particles in a soil mass and the force between adjacent soil particles (Lambe and Whitman, 1969). The structure was found to strongly affect the entire bed erosion resistance. The clay particles in the soil are very small and the majority of which possess a large specific area. Thus the inter-particle forces are comparable or even dominant to the gravitational forces in certain conditions and affect the structure and properties of the soil during settling and deposition.

The relationship between clay particles and water molecules is governed by inter-particle electrochemical forces. Grimshaw (1971) addressed that the different configurations and groupings as well as electric charges of clay particles affect their association with water molecules.

Inter-particle forces are the result of the relative strengths of the attractive and repulsive forces. The attractive forces are mostly Van der Waals forces and are only significant when the particles are very close together. The repulsive forces are due to ion clouds of similar charge repelling each other, and are increasing in an exponential fashion with decreasing particle separation. A rise in the salinity will cause a drop in the magnitude of the repulsive forces (Van Rijn, 1993; Hayter et al., 1995).

Under the influence of their attractive inter-particle forces, the clay particles may attract each other driven by either Brownian motion or the surrounding turbulence and then flocculate. Under large shearing forces the flocs can break up into particles again when the forces are larger than the strength of the flocs (Van Rijn, 1993). Dispersed particles have lower resistance to erosion than flocculated ones.

### ***Settling and deposition***

For cohesive sediment, the cohesive property results in the formation of flocs during settling. Usually, at moderate concentration, an increase of the settling velocity with concentration can be observed as a result of the flocculation effect. Nevertheless, very high concentration suspensions are subjected to hindered settling effect and settling velocity decreases with increasing concentration (Mehta, 1986; Van Rijn, 1993; Chien and Wan, 1999).

Flocculation is affected by a large number of factors including organic-inorganic composition, grain size, density, salinity, turbulence, pH and grain mineralogy

(Kranck, 1986). Therefore, the factors governing flocculation will also influence settling. For coagulated sediment particles, Van Rijn (1993) put forward that the settling velocity depends on the size and density of the aggregates, the salinity, the sediment concentration, the water depth and the flow velocity.

Deposition has been defined to occur when the bed shear stress is not high enough to resuspend sediment material that settles onto and bonds with the bed surface (Hayter et al., 1995). Deposition is governed by the bed shear stress, turbulence structure above the bed, settling velocity, type of sediment, depth of flow, suspension concentration and ionic constitution of the suspending fluid, etc. For a freshly deposited cohesive bed, usually a stratified bed profile is formed with density and shear strength increase along depth (see e.g. Parchure and Mehta 1985; Zreik et al., 1998). Further, the strength increases in time after deposition.

### *Consolidation*

Consolidation is defined as the gradual reduction in volume of a soil under a certain pressure (e.g. self-weight) with a simultaneous expulsion of pore water and a gain in strength. Coarse sediment particles like sand, gravel do not further consolidate once they settle down onto the riverbed. However, for cohesive sediment, the new deposits have a loose honeycomb-like texture with high water content and low density (Chien and Wan, 1999). Under the action of self-weight or other external force, the weak connection among the deposits breaks, and the texture of the deposits changes progressively into denser and denser state (Chien and Wan, 1999). Obviously, properties like density, cohesion, and shear resistance of the deposits increase, and their resistance to erosion increases accordingly. The critical shear stress for erosion is found to increase also with consolidation pressure, see Figure 3.2, see also Kamphuis and Hall (1983) and Hanson (1993).

### *Compaction*

Craig (1997) defined the soil compaction as the process of increasing the density of a soil by packing the particles closer together with a reduction in the volume of air, however, without significant change in the volume of water in the soil. In general the higher the degree of compaction the higher the shear strength will be and the lower the compressibility and permeability of the soil will be. Soil compaction is generally affected by factors like soil type (cohesive or non-cohesive), soil gradation, water content and compaction energy (Qian and Yin, 1995; Shroff and Shah, 2003). For instance, the water content of soil is an important parameter in soil compaction. The water content at which the soil obtains a maximum value of dry density for a given compaction energy is defined as the optimum water content. Moreover, usually the larger the compaction energy applied to the soil is, the denser the soil will be.

In the construction of dikes or earth dams, loose soil is placed in layers and compacted to a certain designed density by means of rollers, vibrators or rammers. There is no doubt that the degree of compaction strongly affects the erosion resistance of the soil. However, in the literature little information can be found which quantitatively describes the relationship between the compaction degree and the soil erodibility.

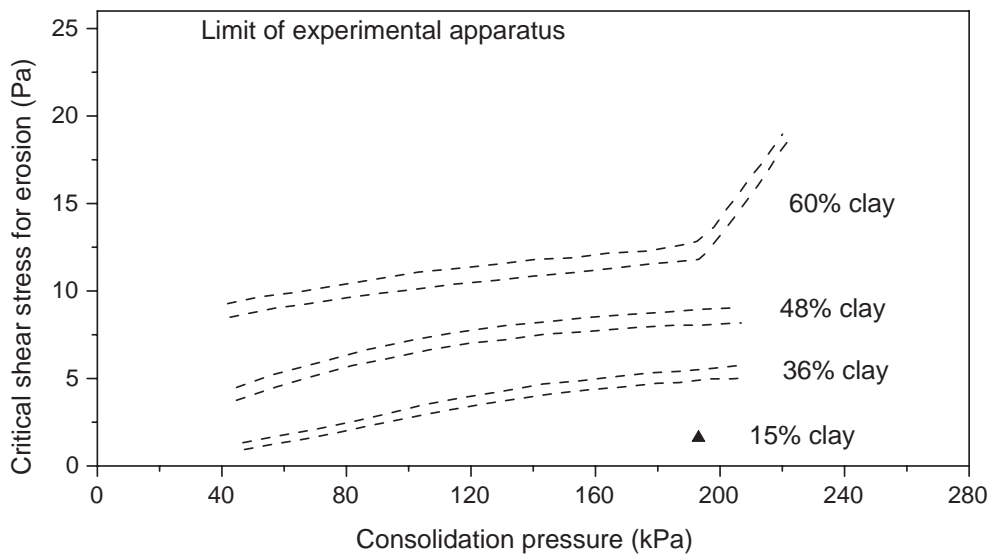


Figure 3.2 Critical shear stress as a function of consolidation pressure for various clay proportions (after Kamphuis and Hall, 1983).

### *Mechanical properties*

The mechanical properties of cohesive soil can be expressed as its performance under compression and shear. The relationship between the shear strength ( $\tau_s$ ) and the normal stress ( $\sigma$ ) is as follows:

$$\tau_s = c + \sigma \tan \phi \quad (3.4)$$

in which  $c$  is the cohesion of the soil also termed yield stress,  $\phi$  is the internal friction angle. The cohesion of cohesive soil is closely related to its resistance to erosion. It is revealed by many experimental studies that an increase in the shear strength generates a decrease in the erosion rate, see e.g. Shaikh et al. (1988) and Kamphuis and Hall (1983).

Various factors can impact the soil shear strength, including the clay mineral type, soil gradation, water content, consolidation time, stress history, degree of sample

disturbance, void ratio, anisotropy and drainage condition, see e.g. Murthy (2003), and Qian and Yin (1995).

Cohesive soil also has a character of plasticity, which represents the property to undergo unrecoverable deformation at constant volume without cracking or crumbling (Craig, 1997). Kamphuis and Hall (1983) concluded from laboratory experiments that the resistance of cohesive soil to erosion increases with the plasticity index.

### 3.4.3 Erodibility of cohesive soil

For cohesive soil, its erodibility depends on various interacting and inter-related factors (see e.g. Mehta 1986; Mirstkhoulava, 1991). These factors include the amount and type of clay fraction, organic matter and other cementing agents, composition of the pore fluid, grain size distribution, structure, density, temperature, water content, and composition of the eroding fluid, etc. For instance, it is quite common that the clay content is used as an indicator of the soil erodibility, Morgan (1995) addressed that the clay particles combine with organic matter to form soil aggregates or clods and it is the stability of these which determines the erosion resistance of the soil. An increasing clay proportion induces a decrease in the soil erodibility, as indicated in Figure 3.2.

Partheniades (1965) stated that erosion of cohesive soil occurs whenever the shear stress induced by fluid flow over the bed is large enough to break the electrochemical inter-particle bonds. Van Rijn (1993) pointed out that sediment particles, flocs or lumps of the bed surface (including fluid mud layers) will be eroded when the applied current-induced or wave-induced bed shear stress ( $\tau_b$ ) exceeds the critical value for erosion ( $\tau_c$ ). The factors that affect this critical bed shear stress are type and amount of clay, chemical composition of pore and eroding fluids, presence of organic matter and stress history, etc.

Mirstkhoulava (1991) described the scouring process of cohesive beds in detail. Loosening and washing away of dispersed particles and aggregates (separates) marks the initial stage. This process leads to a rougher surface with increased drag and lift forces. Higher pulsating drag and lift forces increase the vibration and dynamic action on protruding aggregates. As a result the bonds between aggregates are destroyed little by little until the aggregate is instantaneously torn out of the surface and carried away by the flow.

Generally two modes of erosion by flow can be classified for cohesive sediment<sup>2</sup>. When erosion takes place by removal of individual sediment particles and/or aggregates, it is defined as surface erosion; another type is the erosion of clusters or lumps of aggregates which is referred to as mass erosion. The former is what usually is

---

<sup>2</sup> Note that also other distinctions of erosion modes can be found in the literature, e.g. Winterwerp and Van Kesteren (2004).

represented in experiments. However, during the erosion of overtopped cohesive-soil dikes, mass erosion is often observed. The mathematical description of mass erosion so far is not much and often simplistic with many assumptions. De Vroeg et al. (2002) addressed that in structured cohesive soil separate lumps of clay can be eroded, and the size of and the interaction between lumps may be more important than the interaction between soil particles, for the critical velocity for erosion. It should be noted here that the principle to determine the size of and the interaction between the eroded lumps is complicated and not clear yet.

From three disparate examples studied in the field and the laboratory, Kamphuis (1990) found that the presence of sand in the eroding flow lowers the critical shear stress for erosion of cohesive sediment, increases the erosion volume and erosion rate, and determines where erosion takes place, i.e. at the protrusions of the bed instead of the depressions. Erosion was most rapid when the sand in the eroding flow saltated. The increase in erosion by sand in the eroding flow for constant shear stress is proposed to be explained by abrasion.

Many efforts have been made to relate the critical shear stress for erosion to the basic soil parameters as plasticity index, voids ratio, water content, cohesion and others. However, generally accepted relationships are not available. Hanson (1996) investigated the potential of initial soil strength indices and stress-strain characteristics for characterising the erosion resistance of two compacted soils. It is indicated from the results that one should not depend solely on soil strength for prediction of soil erodibility, and the stress-strain features should be included in future research when developing relationships between soil erodibility and other soil parameters.

The effect of salt concentration in the eroding fluid was studied by Arulanandan (1975) and Mehta (1986), among others. Arulanandan (1975) concluded from erosion tests that the erodibility of soil decreases with increasing salt concentration. He explained that when the salt concentration is higher in the soil pore fluid than in the eroding fluid, the osmotic potential of the eroding fluid is less than that of the soil solution and thus swelling will occur, resulting in weakening of inter-particle bonds.

Kelly and Gularte (1981) carried out experiments on erosion of remoulded illite clay at different temperatures. They found that when temperature increases, an increase of the soil erodibility is yielded. This result has also been described by Ariathurai and Arulanandan (1978), Mirskhoulava (1991) and Zreik et al. (1998).

According to Simon and Collison (2001), the entrainment and erosion of cohesive bed material is affected by the magnitude and distribution of positive and negative pore-water pressures. Upward-directed seepage forces within cohesive streambeds promote the entrainment of flocculated aggregates. On the contrary, suction caused by negative pore-water pressures is found to increase the shear strength of unsaturated cohesive bed.

Hanson (1992) described jet index tests conducted on compacted soil in the laboratory. These studies were conducted to observe the influence of compaction water content  $\omega$  and dry unit weight  $\gamma_{dry}$  on erosion resistance for soil in a controlled laboratory setting. Erosion resistance was observed to increase with  $\omega$  and  $\gamma_{dry}$  for soil compacted at less than 100% saturation. For soil compacted at 100% saturation erosion resistance was found to increase with increased  $\gamma_{dry}$  and to decrease with increased  $\omega$ . However, Grissinger (1966) observed that both increase and decrease in erosion resistance could occur with increases in  $\omega$ , depending on the specific situation.

Considerable work has been done to determine the critical bed shear stress for erosion ( $\tau_c$ ) of cohesive soil. An increase in (dry) bed density generally increases the number of bonds between the soil particles (flocs), accordingly increases bed strength (Winterwerp and Van Kesteren, 2004; Houwing, 1999; Aberle et al., 2004). The  $\tau_c$  for consolidating beds is related to the dry sediment density ( $\rho_{dry}$ ) as follows according to several researchers:

$$\tau_c = K_1 (\rho_{dry})^{K_2} \quad (3.5)$$

Given  $\tau_c$  in N/m<sup>2</sup> and  $\rho_{dry}$  in kg/m<sup>3</sup>, Owen (1975, see Mehta, 1986) experimentally obtained  $K_1 = 6.85 \times 10^{-6}$  and  $K_2 = 2.44$  for statically deposited bed of Avonmouth mud. Thorn and Parsons (1980) determined  $K_1 = 5.42 \times 10^{-6}$  and  $K_2 = 2.28$  based on tests on mud from Brisbane, Grangemouth and Belawan in saline water, see Figure 3.3.

Through erosion tests on artificially mixed (mud/sand) sediment which include under-consolidated deposited beds and more consolidated blended beds at higher densities, Mitchener and Torfs (1996) proposed a relationship between  $\tau_c$  and the soil bulk density ( $\rho_s$ ) as follows:

$$\tau_c = 0.015 (\rho_s - 1000)^{0.73} \quad (3.6)$$

The density gradients in the bed (bed profile) also have an important influence on the erosion, see e.g. Figure 3.4. Torfs (1997) described that for uniform beds, the erosion rate will be constant if the discharge is constant (constant bed shear stress higher than  $\tau_c$ ). While if the bed density is increasing with depth, the erosion rate will decrease in time under a constant bed shear stress, until a layer is reached with such a density that the applied shear stress is lower than the critical shear stress for that density.

Based on experiments performed on natural mud in a 7 m long, 150 mm wide and 50 mm high pipe, Otsubo and Muraoko (1988) proposed formulae for the critical shear stress for surface erosion ( $\tau_{c,1}$ ) and mass erosion ( $\tau_{c,2}$ ) as function of the mud yield stress  $c$ :  $\tau_{c,1} = 0.27c^{0.56}$  and  $\tau_{c,2} = 0.79c^{0.94}$ .

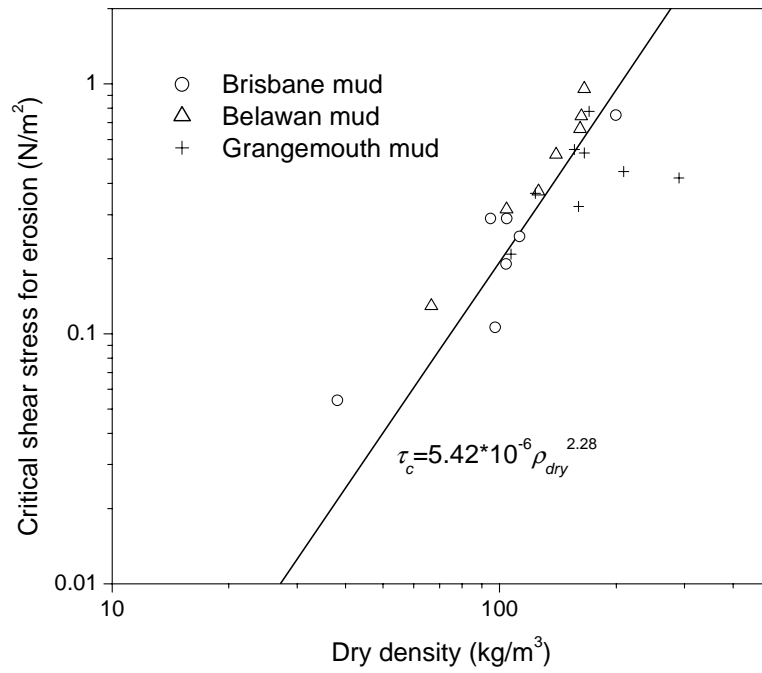


Figure 3.3 Critical shear stress for erosion vs. dry bed density (after Thorn and Parsons, 1980).

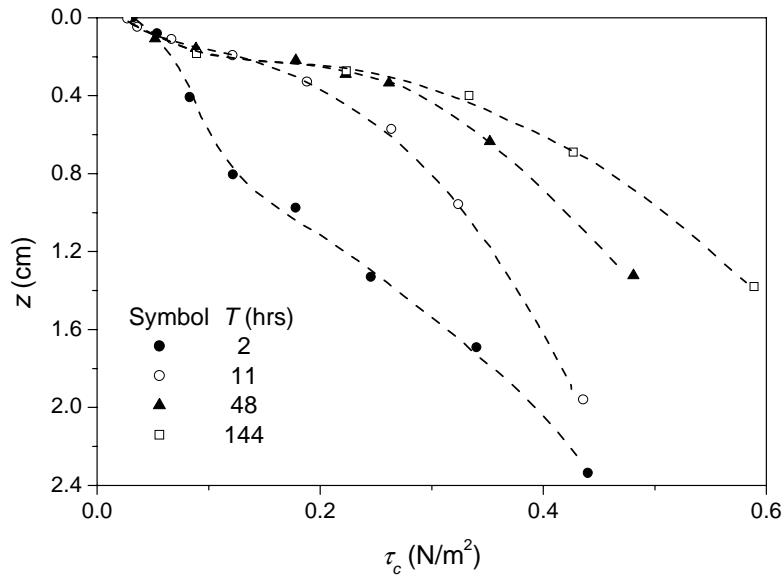


Figure 3.4 Variation of critical shear stress for erosion with depth  $z$  for kaolinite bed in tap water for various consolidation times  $T$  (after Mehta and Partheniades, 1983)

For the critical velocity of incipient motion for cohesive sediment that has been consolidated recently, Chien and Wan (1999) summarized the formulae proposed in China by some researchers and institutes, see Table 3.2. This critical velocity refers to the highest value of flow velocity at which the particles are not scoured to move. Chien and Wan (1998) compared these formulae with the experimental data from tests with a water depth of 15 cm and the specific density of sediment of 2.65 g/cm<sup>3</sup>. The results showed that for fine sediment, these formulae agreed fairly well with the experimental data. But for coarse sediment ( $D > 5$  mm), the data tended to scatter.

Table 3.2 Incipient velocity formulae in consideration of the cohesion among grains (after Chien and Wan, 1999).

Author	Form of formula	Remarks
G.R. Dou (1960)	$\frac{U_{ci}^2}{gD} = \frac{\gamma_s - \gamma}{\gamma} \left( 6.25 + 4.16 \frac{h}{h_a} \right) + \left( 111 + 740 \frac{h}{h_a} \right) \frac{h_a \delta}{D^2}$	$h_a$ : atmospheric pressure measured by height of water column, $\delta$ : thickness of water molecule (= $3 \times 10^{-8}$ cm)
Y.Q. Sha (1965)	$U_{ci} = R^{1/5} \sqrt{\left( 1520 \frac{D^{5/3}}{\omega^{4/3}} + 194D \right) (f \cos \theta - \sin \theta)}$	all length in m, $\omega$ : fall velocity of grains, $f$ : friction coefficient = $1.42D^{1/8}$ , $\theta$ : inclination of river bed
WIHEE (1960)	$U_{ci} = \left( \frac{h}{D} \right)^{0.14} \left( 17.6 \frac{\gamma_s - \gamma}{\gamma} D + 0.000000605 \frac{10 + h}{D^{0.72}} \right)^{1/2}$	-
C.B. Tang (1964)	$U_{ci} = \frac{h^{1/m}}{D} \frac{m}{m+1} \left[ 3.2 \frac{\gamma_s - \gamma}{\gamma} gD + \left( \frac{\gamma_b}{\gamma_{b0}} \right)^{10} \frac{C}{\rho D} \right]^{1/2}$	$m = 4.7(h/D)^{0.06}$ (flume data) or $m = 6$ (natural river), $C = 2.9 \times 10^{-4}$ g/cm

Kamphuis and Hall (1983) found (through a literature review) in four studies for approximately similar cohesive sediment conditions, a variation in the critical shear stress with a factor about 200. They conjectured the variation to be the result of experimental error, variation in experimental techniques, an overly simplistic interpretation of sediment properties, and further of the difference in criteria defining the initiation of erosion by different investigators. Sandford and Maa (2001) indicated that at least three different interpretations of  $\tau_c$  can be found in the literature: some

investigators define it as the stress at which initiation of motion first occurs; some define it as the stress at which significant erosion first occurs; and some define it by extrapolating erosion rate vs. stress data back to zero erosion. These differences in definitions can induce considerable differences in the results even under the same experimental conditions (Sandford and Maa, 2001). The studies of Kamphuis and Hall (1983) and Sandford and Maa (2001) clearly revealed the large complexities and difficulties in determination of the erodibility of cohesive sediment.

#### 3.4.4 Erosion rate of cohesive sediment

When erosion of cohesive soil starts, the erosion rate is dependent on the erodibility of the soil and the features of the flow over the bed.

Presently various devices and methods can be used to measure the erosion rate of cohesive sediment in experiments (Winterwerp and Van Kesteren, 2004). However, considerable variance (sometimes even by orders of magnitude) in results can be generated between different devices (see e.g. Tolhurst et al., 2000). These experiments are often performed in steps (see e.g. Parchure and Mehta, 1985; Johansen et al., 1997; Tolhurst et al., 2000). During each step the bed shear stress is kept constant. After each step the suspended sediment concentration ( $c_s$ ) reaches a constant value and the erosion rate is then determined from the variation of  $c_s$  at the beginning of each step (Johansen et al., 1997).

Based on data from experiments conducted in an 18 m (60 feet) long rectangular flume (see Figure 3.5), Partheniades (1965) proposed a formula for the erosion rate ( $E$ ) of cohesive sediment as follows

$$E = \frac{KD_s\gamma_s}{t^{(\tau_b)}} \left[ 1 - \frac{1}{\sqrt{2\pi}} \int_{\frac{-c}{k\eta_b\bar{\tau}_b} \frac{1}{\eta_b}}^{\frac{c}{k\eta_b\bar{\tau}_b} \frac{1}{\eta_b}} \exp\left\{-\frac{\xi^2}{2}\right\} d\xi \right] \quad (3.7)$$

in which  $K$  and  $k$  are dimensionless coefficients,  $D_s$  denotes the average diameter of eroded clay particles or clay clusters,  $\gamma_s$  is the unit weight of solids,  $t^{(\tau_b)}$  is the time required for breaking of a particle acted on by a shear stress  $\tau_b$ ,  $c$  is the cohesion due to inter-particle forces,  $\bar{\tau}_b$  is the mean value of  $\tau_b$ ,  $\eta_b$  is a constant number and  $\xi$  is a dummy variable.

Shaikh et al. (1988) performed some experiments on erosion of unsaturated compacted Na-montmorillonite clays in a rectangular flume 15.5 cm wide, 11 cm deep, and 250 cm long with an adjustable slope. They found a linear relationship between the erosion rate and the shear stress:

$$E = C_E \tau_b \quad (3.8)$$

in which  $E$  is the erosion rate in  $\text{N}/\text{min}\cdot\text{m}^2$ ,  $\tau_b$  is the bed shear stress in  $\text{N}/\text{m}^2$ , and  $C_E$  is an erosion-rate coefficient that can be expressed as  $C_E = 4.14 (\% \text{clay})^{-0.91}$ . This erosion rate formula indicates a zero value of the critical shear stress.

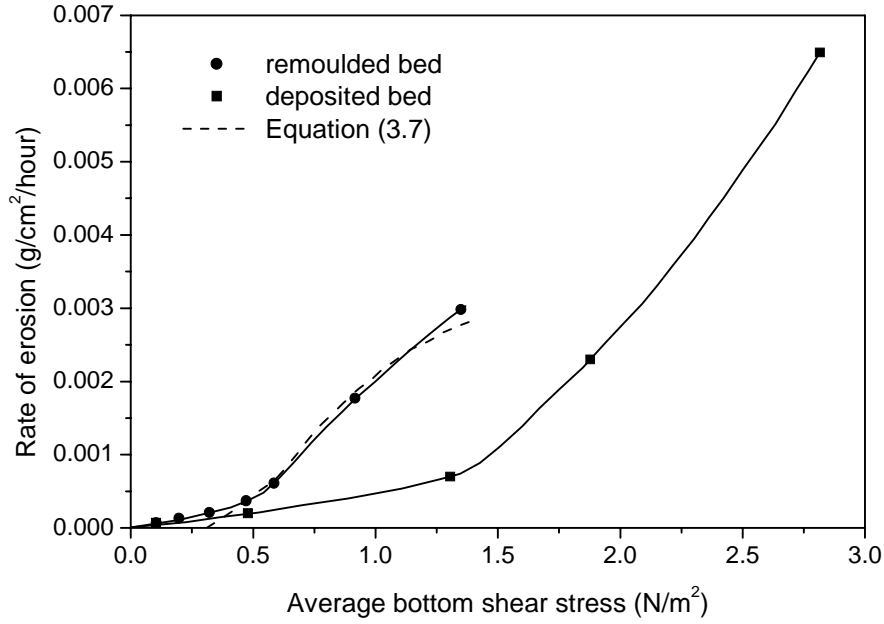


Figure 3.5 Erosion rate measured by Partheniades (after Partheniades, 1965).

Verheij (2001, see De Vroeg et al., 2002) proposed a formula for the erosion rate as:

$$E = 0 \quad \text{for } \tau_b < \tau_c \quad (3.9)$$

$$E = C_E \tau_b \quad \text{for } \tau_b \geq \tau_c \quad (3.10)$$

in which

$$C_E = \frac{1.85 \times 10^{-4}}{\tau_c} \quad (3.11)$$

$$\tau_c \approx 4U^2 \quad (3.12)$$

When the bed properties are relatively uniform over depth, the frequently used excess shear stress equation representing the detachment process of cohesive sediment is (see e.g. Sheng, 1986; Mitchener and Torfs, 1996; Mei et al., 1997):

$$E = M (\tau_b - \tau_c)^a \quad (3.13)$$

in which  $E$  is the erosion rate in mass of sediment per unit time per unit area ( $\text{kg/s-m}^2$ ),  $\tau_b$  is the local bed shear stress in  $\text{N/m}^2$ ,  $M$  is the soil erodibility coefficient in  $\text{s/m}$ , and  $a$  is an exponent (often assumed = 1).

The  $M$  and  $\tau_c$  terms are soil parameters whereas  $\tau_b$  is a hydraulic parameter. The value of  $M$  is very sensitively dependent on the soil properties. Figure 3.6 shows the rate of erosion as a function of the excess shear stress ( $\tau_b - \tau_c$ ) for cohesive sediments from different sites tested at HR Wallingford (Whitehouse et al., 2000). The solid line shows Equation (3.13) with  $M = 0.002 \text{ s/m}$ . The range of the experimental scatter shown in the figure indicates considerable variation in the erodibility ( $M$ ) among the tested sediments.

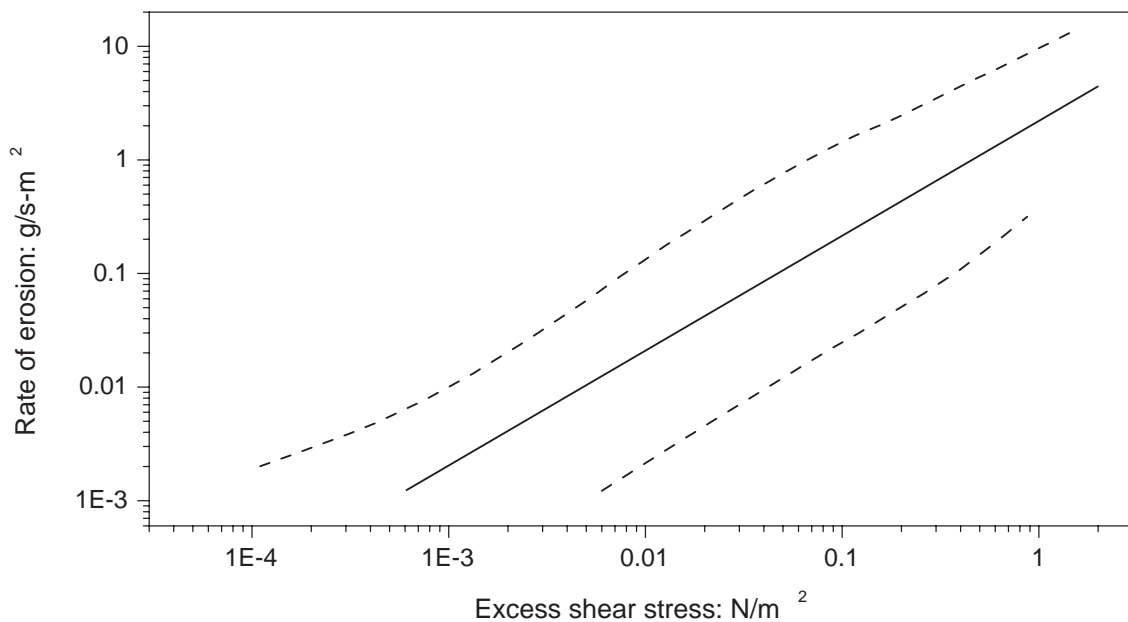


Figure 3.6 Rate of erosion as a function of excess bed shear stress (from Delo, 1988, see Whitehouse et al., 2000). The dashed line indicates the limits of scatter in the experimental data, and the solid line shows Equation (3.13) with  $M = 0.002 \text{ sm}^{-1}$ .

In the literature not much quantitative information on  $M$  has been found. It is often claimed that  $M$  is an empirically or experimentally determined constant. In addition, most of the reported values are for soft cohesive sediment or mud. Table 3.3 lists typical values of  $M$  for a large number of different mud tested at HR Wallingford (Whitehouse et al., 2000), with  $E$  specifically defined as the dry mass of mud eroded per unit area per unit time.

Winterwerp and Van Kesteren (2004) proposed the following formula connecting  $M$  with properties of sediment for the surface erosion of mud:

$$M = \frac{c_v \phi_{s,0} \rho_{dry}}{10D_{50} \tau_s} \quad (3.14)$$

in which  $c_v$  is the sediment consolidation coefficient,  $\tau_s$  is the sediment shear strength, and  $\phi_{s,0}$  is described by

$$\phi_{s,0} = \frac{1}{1 + \omega \rho_{solid} / \rho} \quad (3.15)$$

in which  $\omega$  is the water content and  $\rho_{solid}$  is the density of sediment particles.

To the best of the author's knowledge, this is the only mathematical relationship available so far in literature aiming at quantification of  $M$  based on the relevant sediment properties. This formula was tested against data of experiments on mud taken from Lake Ketel and the Port of IJmuiden in the Netherlands, and from the Kembs Reservoir in France, with favourable agreement between data and predictions achieved (see Winterwerp and Van Kesteren, 2004).

Table 3.3 Soil erodibility coefficient  $M$  and characteristics of the mud tested at HR Wallingford (after Whitehouse et al., 2000).

Mud type	$M$ (s/m)	Silt: $\leq 63\mu\text{m}$ (%)	Organics (%)	Mineralogy	Bulk density ( $\text{kg/m}^3$ )
Grangemouth	0.0005-0.0014	80-90	4.7-5.5	quartz 18% clays 82%	1370
Harwich	0.0007	88-95	2.2-2.7	quartz 24% clays 76%	1250
Hong Kong	0.0006-0.0015	65-80	6.9-9.6	quartz 20% clays 80%	-
Ipswich	0.0009-0.003	-	-	quartz 17% clays 83%	1320
Kelang	0.0002-0.0009	65-80	-	quartz 17% clays 83%	-
Kingsnorth	0.0007	64	4.8	quartz 17% clays 83%	1375
Medway	0.0007	80	2.7-2.9	quartz 21% clays 79%	1220
Mersey eastham	0.0005	80	8.6	-	1140
Poole	0.0007-0.0014	80-85	2.2-2.3	quartz 30% clays 70%	1500
Tees Seal Sands	0.0002-0.0014	75	4.0-4.5	quartz 19% clays 81%	1550
Tees dredged	0.0005-0.0018	75	10.1-11.1	quartz 22% clays 78%	1430

Hanson (1993) argued through open channel erodibility tests that the erosion rate results could be described adequately, assuming that  $\tau_c$  was assumed zero, thus Equation (3.13) ( $a$  is assumed to be 1) will give the similar form as Equations (3.8) and (3.10):

$$E = M\tau_b \quad (3.16)$$

This assumption will result in significant difference in  $E$  when  $\tau_b$  is just exceeding  $\tau_c$ .

Another frequently used relationship for the erosion rate of cohesive sediment with relatively uniform properties over depth has the following form (see e.g. Ariathurai and Arulanandan, 1978; Parchure and Mehta, 1985):

$$E = M' \left( \frac{\tau_b - \tau_c}{\tau_c} \right) \quad (3.17)$$

in which  $M'$  is a material-dependent coefficient. For a given  $\tau_b$ ,  $E$  is constant, since  $\tau_c$  does not change with depth. Parchure and Mehta (1985) stated that the value of  $M'$  does not uniquely correlate with soil mechanical indices such as the Atterberg limits, but also relies on physico-chemical parameters characterising the inter-particle bond strength. Equation (3.17) is essentially the same as Equation (3.13).

Divided by the soil density ( $\rho_s$ ) with  $a$  assumed equal to 1, Equation (3.13) can be transformed into:

$$E = M_e (\tau_b - \tau_c) \quad (3.18)$$

in which  $E$  is the erosion rate in length per unit time (m/s), and  $M_e = M/\rho_s$  is the soil-dependent coefficient describing the soil erodibility in s-m<sup>2</sup>/kg.

Equations (3.13), (3.17) and (3.18) have one irrationality in common, i.e. both the soil erodibility coefficient ( $M/M'/M_e$ ) and the critical shear stress for erosion ( $\tau_c$ ) in those equations are functions of the soil properties.

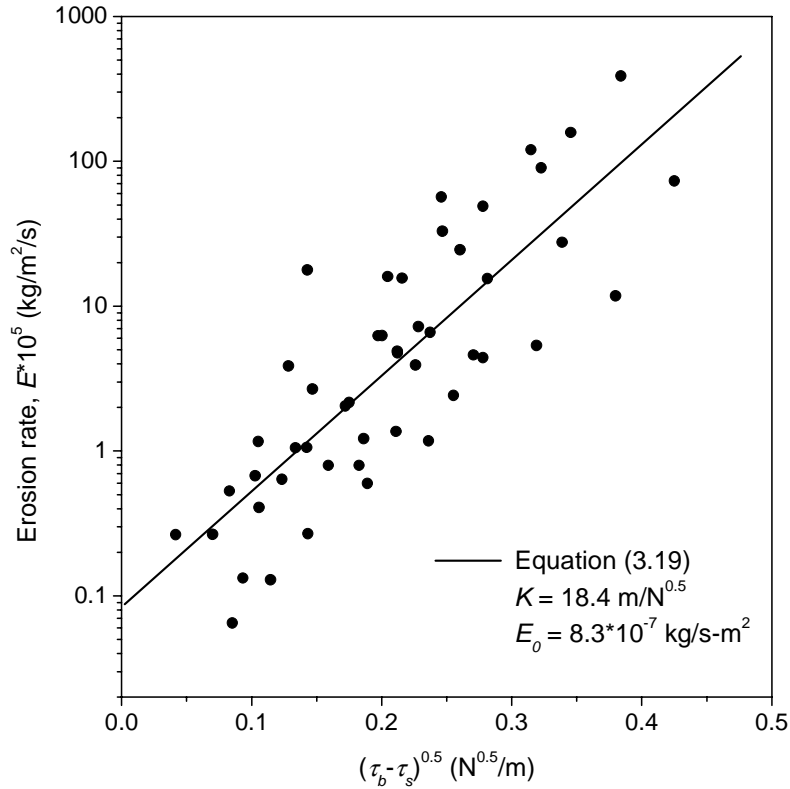
For beds possessing an increasing density with depth ( $z$ ), Parchure and Mehta (1985) proposed a relationship for the erosion rate of the form:

$$E = E_0 \exp \left[ K (\tau_b - \tau_c)^{0.5} \right] \quad (3.19)$$

The  $E_0$  value (in kg/s-m<sup>2</sup>) is defined as the value for  $\tau_b = \tau_c$  (at the surface  $z = 0$ ) and can be determined by extrapolation from a plot of  $E$  against  $\tau_b - \tau_c$ . Values for  $E_0$  and  $K$  obtained by various investigators based on laboratory experiments are given in Table 3.4. As an example, a plot for the experiments with kaolinite in tap water is shown in Figure 3.7. The large diversity of the values listed in Table 3.4 for  $E_0$  and  $K$  indicates that these two parameters are very sensitive to the properties of the sediment.

Table 3.4 Values for the coefficients in Equation (3.19).

	Material	$E_o$ (kg/s-m <sup>2</sup> )	$K$ (m/N <sup>0.5</sup> )
Parchure and Mehta (1985)	kaolinite in tap water	$8.3 \times 10^{-7}$	18.4
	kaolinite in salt water	$2.3 \times 10^{-6}$	17.2
	lake mud in salt water	$5.3 \times 10^{-6}$	13.6
	bay mud (Partheniades, 1965)	$6.7 \times 10^{-8}$	8.3
	lake mud (Lee, 1979)	$7.0 \times 10^{-7}$	8.3
	estuarial mud (Thorn and Parsons, 1977)	$7.0 \times 10^{-7}$	8.3
	estuarial mud (Thorn and Parsons, 1979)	$3.1 \times 10^{-6}$	4.2
	kolinite (Dixit, 1982)	$1.0 \times 10^{-6}$	25.6
Amos et al. (1992)	mud from the bay of Fundy	$5.1 \times 10^{-5}$	1.62
Chapalain et al. (1994)	deposited kaolinite	$1.6 \times 10^{-5}$	14.3

Figure 3.7 Variation of erosion rate  $E$  with  $(\tau_b - \tau_c)^{0.5}$  for kaolinite in tap water (after Parchure and Mehta, 1985).

It is clear from the above literature review that almost all these equations for the erosion rate of cohesive sediment are simplistic and most of them only include one or two parameters. The large number of factors affecting the cohesive sediment erosion performance has very often been accounted for by one empirical coefficient (e.g.  $M$  in Equation (3.13)). The role each factor plays in the erosion process is not embodied specifically and respectively. In addition, the value of  $M$  can usually only be determined experimentally or empirically. To the best of the author's knowledge, presently only one mathematical relationship (Equation (3.14)) is available (for mud) that connects  $M$  to the sediment properties. For a wide application, further testing of this relationship against more experiments with a wider range of cohesive sediment types is highly needed. It should also be noted that all those erosion rate equations were generally derived for the soil surface erosion. Little quantitative data is, however, available on the soil mass erosion.

### 3.5 Discussion

Taking one with another, both the erosion processes of cohesive and non-cohesive sediment are actually complicated. However, the erosion mechanism of cohesive sediment is far more intricate than that of non-cohesive sediment. The erosion resistance of cohesive sediment is controlled by many factors. Identification of all these factors and the respective roles they play in the erosion process is incomplete and not well understood, and therefore can hardly be satisfactorily described mathematically. Conflicting results were sometimes found even for similar experimental conditions (e.g. the effect of SAR of the pore fluid on the soil erodibility).

Despite the many studies conducted as yet on the erosion of cohesive sediment, no model has been generally accepted. The existing empirical erosion models are usually based on laboratory studies and are simplistic and more or less case specific. The erodibility coefficient (e.g.  $M$  in Equation (3.13)) in these models, to which the erosion rate is greatly sensitive, usually can only be determined experimentally or empirically.

For a comprehensive description of the erosion process of cohesive sediment, hydraulics as well as soil mechanics have to be combined. Further studies, especially experimental research are needed to survey the main factors that influence the rate of erosion, and to determine the quantitative dependence of the erosion rate on these factors. Furthermore, development of a uniform criterion defining the initiation of erosion among different investigators, unification and improvement of experimental devices and methods will certainly help to reduce the scatter among experimental results under similar conditions and benefit a better understanding and better mathematical modeling of the erosion of cohesive sediment.

## Chapter 4

### Breach growth process in clay-dikes

#### 4.1 Introduction

In general, various causes can be identified for the failure of a dike, e.g. overflowing and wave overtopping, seepage and piping, cracking through the dike body, erosion of the dike outer slope, sliding of the dike inner slope and/or outer slope. Among the rest, overflowing and wave overtopping, piping and seepage are the most common and serious causes. This is particularly true for the dikes in China. During the 1998 big flooding in the Changjiang (i.e. Yangtze) River drainage basin, altogether 495 dikes (of polders all with areas larger than 67 ha) failed due to breaching of the dikes, according to the statistics of The Ministry of Water Resources (MWR) of China and The Changjiang Water Resources Commission (CWRC) (MWR/CWRC, 2002). Among these 495 dike failures, as much as 64% was caused by overflowing and wave overtopping, and another 9% by piping and seepage.

Diverse dike failure mechanisms can form an initial breach in the dike crest. Overflowing and wave overtopping can result in such an initial breach due to erosion. In the case of piping, the pipe through the dike body may collapse at a certain time when it is enlarged adequately; accordingly a breach is formed in the dike crest. In addition, combinations of different failure mechanisms are also possible. These mechanisms will result in an initial breach, in general irregularly shaped, small or medium-sized or large. In the present study, it is assumed that the initial breach is relatively small and located in the top of the dike. The flow of water through the small initial breach starts the dike breach erosion process. Nevertheless, the formation of the initial breach in the dike crest is not the topic of this research and therefore it is not investigated further.

In this chapter, a qualitative description of the breach erosion process in clay-dikes is presented. Firstly, the general division of the whole breach erosion process (into five stages) is outlined in Section 4.2. The breach flow regime and the initiation of breach

erosion in Stage I is then described in Section 4.3. The breach erosion process in Stages I, II and III are elaborated in Sections 4.4, 4.5 and 4.6, respectively. Section 4.7 deals mainly with the process of breach enlargement in the first three stages due to the flow erosion; the process of further breach growth in Stages IV and V is described in Sections 4.8 and 4.9, respectively. Finally a discussion on the breach erosion process in clay-dikes is given in Section 4.10.

## 4.2 Five stages of the breach erosion process in clay-dikes

It is assumed that the initial breach in the dike crest possesses a trapezoidal cross-section with a side-slope angle  $\gamma$ . As stated above, the flow of water through this initial breach launches the erosion process at  $t = t_0$ .

The influence on the breach erosion process of the protection layers on the dike surface, such as vegetation cover and/or revetment, is not taken into account in the present study due to the high complexities involved, though it may affect the dike breach erosion process (especially the initiation of erosion) to a considerable degree under certain circumstances. For the same reason, the effect of waves is also kept out of consideration for the moment.

Similar to the division made by Visser (1998) for the sand-dikes, generally the whole breach erosion process in clay-dikes can also be distinguished into five stages. However, as distinct from sand-dikes, headcut erosion can play a very important role in the breaching of clay-dikes. The five stages are summarized as follows (see Figure 4.1).

Stage I ( $t_0 \leq t < t_1$ ): Floodwater flows through the initial breach in the dike crest and starts the breach growth process at  $t = t_0$  by eroding soil away from the inner slope of the dike and, depending on the flow velocity, possibly also from the dike crest in the breach. Both flow shear erosion as well as small-scale headcut erosion can occur along the inner slope in Stage I. Generally, the erosion rate close to the toe of the inner slope is larger than that on the upper part. This uneven rate of erosion induces steepening in time of the inner slope. By the end of Stage I at  $t = t_1$  the gradient of the inner slope of the dike increases from an initial value  $\beta_0$  to a critical value  $\beta_1$ , which is a function of the properties of the dike material.

Stage II ( $t_1 \leq t < t_2$ ): The steepened inner slope of the dike holds the critical slope angle  $\beta_1$  throughout Stage II and acts like a headcut during the erosion process owing to its large steepness. The dike body in the breach is further eroded through a combination of breach flow shear erosion, fluidization of the surface of the slope, scour of the dike foundation and headcut undermining, and discrete headcut slope mass failure, until at  $t = t_2$  the headcut retreats to the outer slope of the dike and Stage II ends. The erosion along the dike crest lowers the height of the dike in the breach and increases the breach flow gradually.

Stage III ( $t_2 \leq t < t_3$ ): In Stage III the headcut still maintains the critical slope angle  $\beta_1$ . The various erosion mechanisms described for Stage II hold also for Stage III, except that the remaining dike body in Stage III is thinner and weaker so that the rate of erosion is faster. The breach enlarges rapidly, accordingly also the breach flow rate, which in turn accelerates the breach erosion process in the dike. At  $t = t_3$  the dike body in the breach has been washed away completely down to the dike foundation or to the toe protection on the dike outer slope, if any, and then Stage III is finished.

Stage IV ( $t_3 \leq t < t_4$ ): Breach erosion takes place mainly laterally in Stage IV, with flow shear erosion along the side-slopes of the breach and the resulting discrete side-slope instability being the main mechanisms for the breach enlargement. Vertical erosion in this stage relies mainly on the geometrical and material features of the dike. Visser (1998) distinguished three types of breaches for Stage IV (and the following Stage V) for sand-dikes. This division is followed here for clay-dikes as well. Along with the discharge flowing into the polder through the breach, the inner water level (i.e. water level in the polder) rises gradually and begins to influence the breach flow after  $t = t_4$ .

Stage V ( $t_4 \leq t < t_5$ ): The breach erosion in Stage V is similar to that in Stage IV: mainly laterally with vertical erosion relying chiefly on the geometrical and material conditions of the dike. Due to the growing obstructive effect of the rising inner water level, a gradual decrease of the breach flow velocity is brought on, accordingly of the rate of breach erosion as well. At the end of Stage V at  $t = t_5$  the velocity of the breach flow is reduced to such an extent that it can no longer erode away soil material from either the dike body or the dike foundation, hence the breach growth process stops. However, the breach inflow to the polder continues until at  $t = t_6$  when either the outer water level (water level of the river or sea) and the inner water level equals, or the outer water level drops below the breach bottom.

### 4.3 Initiation of erosion in Stage I

During the breach erosion process in dikes, the breach flow is often approximated as broad-crested weir flow. The regime of the breach flow in Stage I can be generally divided into two conditions (see Figure 4.2): firstly, the breach flow on the dike crest is critical, or subcritical but achieves the critical flow condition at the downstream end of the dike crest; and then over the inner slope of the dike the breach flow becomes supercritical, considering the large steepness of the inner slope from a hydraulic point of view. In case of a high inner water level, a hydraulic jump can be formed acting as a transition between the supercritical flow along the slope and the subcritical flow in the polder. The division of the breach flow regime shown in Figure 4.2 is generally in agreement with that described by Powledge et al. (1989).

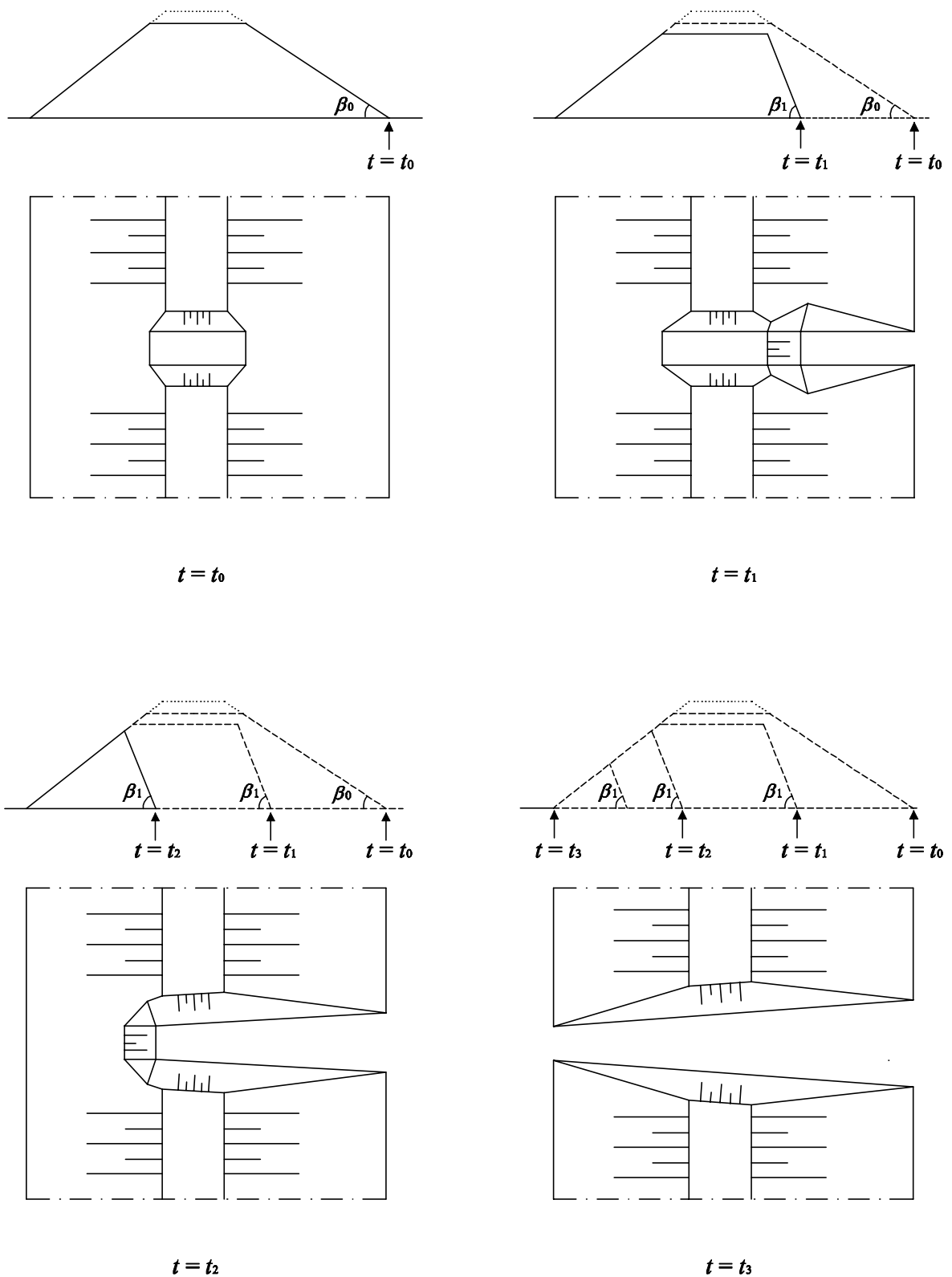


Figure 4.1 Sketch of breach development process in clay-dikes (to be continued).

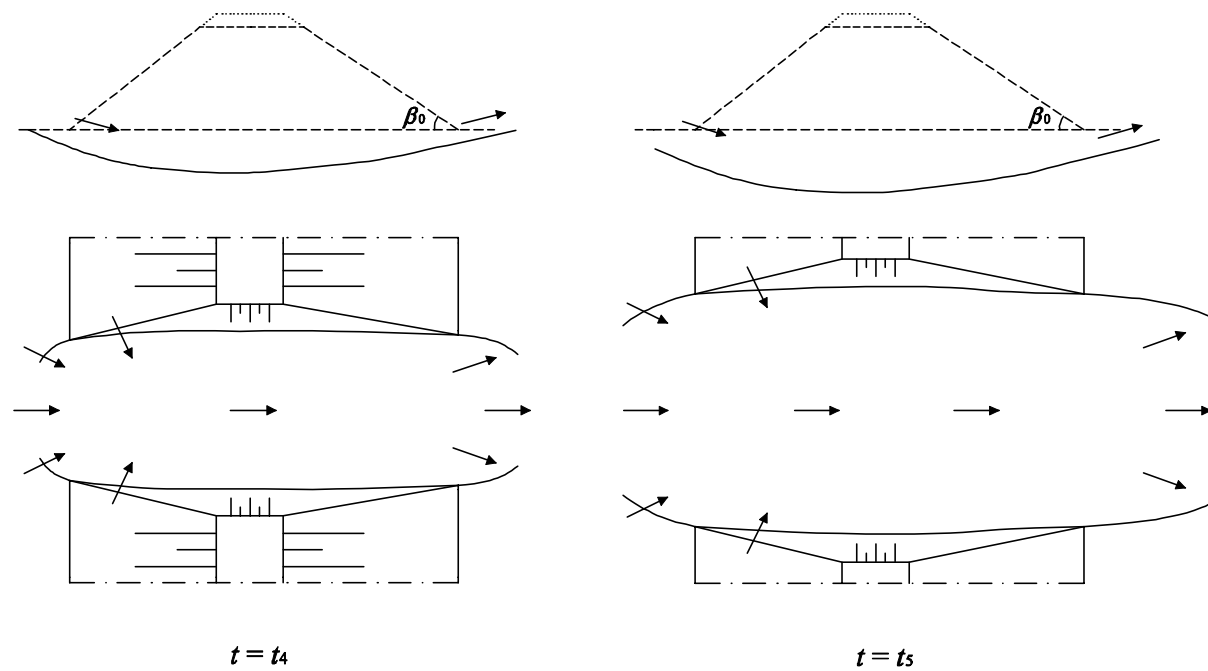


Figure 4.1 Sketch of breach development process in clay-dikes (continued).

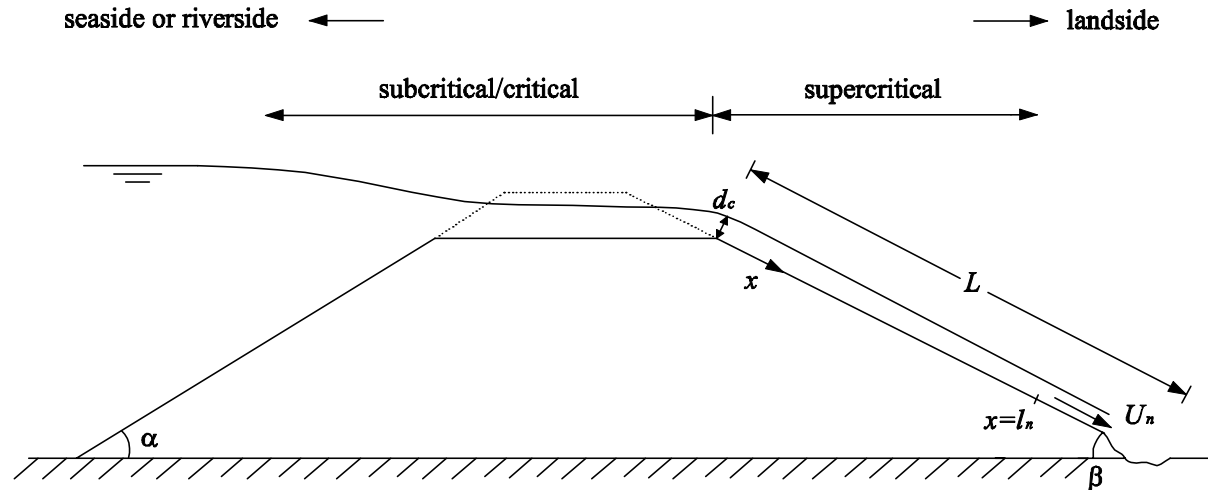


Figure 4.2 Breach flow regime in Stage I.

In Stage I, water flows down and accelerates along the inner slope of the dike, getting more and more erosive. It achieves the normal flow velocity at the point of  $x = l_n$  on the inner slope of the dike if the slope is sufficiently long (i.e.  $L > l_n$ , see Figure 4.2);  $x$  is the coordinate along the inner slope and originates from the top end of the slope; and  $L$  is the length of the inner slope. The symbol  $l_n$  is called the adaptation length of the flow on the inner slope, over which the breach flow approaches the normal flow velocity (see Visser, 1998). Beyond  $x = l_n$ , the breach flow remains uniform. It can therefore be concluded that, in Stage I the breach flow attains its largest erosion

potential in the vicinity of the toe of the dike, unless the inner slope is very long, longer than the adaptation length of the sediment transport.

In reality, in case of water overflowing a dike, the initial point of erosion can be anywhere on the dike surface, depending on the specific situation. However, Powledge et al. (1989) suggested that this initial point is often associated with topography anomaly on the dike surface, such as discontinuities, cracks and voids. In addition, in the author's opinion, the erosion initiation may also be associated with the weak points in strength, if any, as observed in test  $T_4$  of the laboratory experiments on clay-dike breaching conducted at Delft University of Technology (DUT), see Chapter 6. Considering the dramatic slope change at the toe of the dike, where turbulence intensity is fiercely strengthened nearby and where the breach flow achieves its largest erosive potential, it can be expected that the dike breach erosion should often initiate close to the toe of the dike (see Figure 4.2, as observed in tests  $T_1$ ,  $T_2$  and  $T_3$  of the DUT laboratory experiments, see Chapter 6). Later as time goes on, the erosion extends to the entire inner slope as well as the dike crest, steepening the slope and lowering the height of the dike in the breach.

#### 4.4 Breach development in Stage I

In Stage I, the breach erosion occurs along the inner slope and, also along the dike crest if the flow velocity at the dike crest is large enough to cause erosion there.

Over the dike crest, flow shear erosion is the dominant erosion mechanism with the controlling hydraulic factor being the breach flow velocity. The breach flow imposes shear stress on the boundary of the breach and gradually erodes soil material away. As a result the cross-section of the breach in the dike crest is enlarged (see Figure 4.3). The breach enlargement subsequently induces an increase of the breach flow rate, which in turn accelerates the breach erosion.

Two types of erosion are possible to occur along the inner slope of the dike in Stage I (Zhu et al., 2005b). Firstly, the overtopping water flows down along the inner slope and the flow velocity increases, causing shear erosion along the slope with the largest erosion rate close to the toe of the dike. Secondly, it is observed from experiments (e.g. the HERU large-scale embankment breach tests, see e.g. Hanson et al., 1999) that along with the breach flow shear erosion, some small-scale headcuts may also appear on the inner slope of the dike in continuous or separate manner at places such as discontinuities and cracks (see Figure 4.4). The appearance of these small-scale headcuts strengthens the flow turbulence nearby and leads to intensified local scour there. This local scour occurs mainly by small-scale jet impingement as well as some shear erosion, followed by discrete mass failure from the small-scale headcuts (Zhu et al., 2005b). The random characteristics of these small-scale headcuts, however, bring

along large complexities and uncertainties to the breach erosion along the inner slope in Stage I.

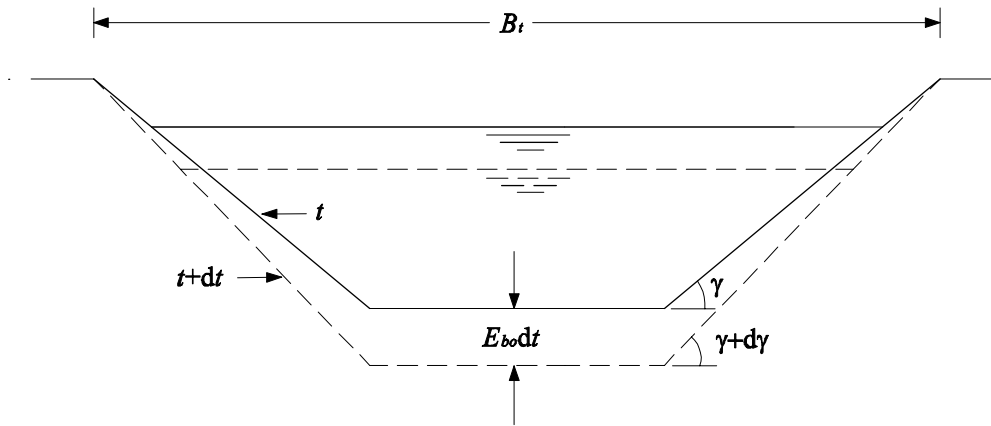


Figure 4.3 Breach enlargement in the dike crest in Stage I.

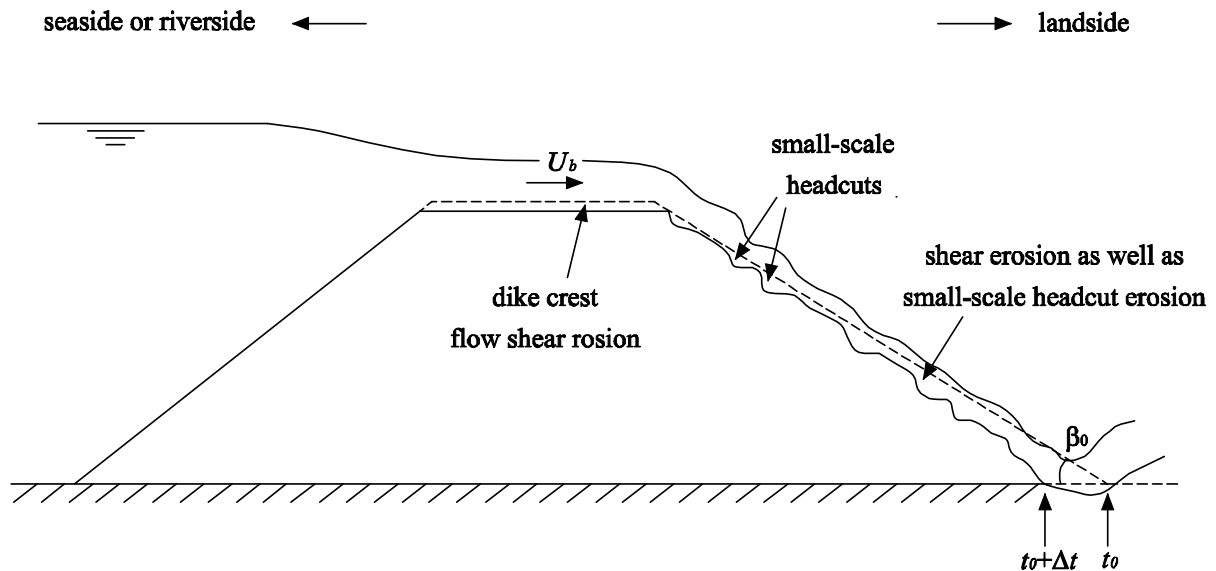


Figure 4.4 Breach erosion in Stage I.

As described earlier in this chapter, in Stage I the breach flow accelerates along the inner slope of the dike and achieves the largest flow velocity at  $x = l_n$  (if  $l_n \leq L$ ), or at the toe of the dike (i.e.  $x = L$ , if  $L < l_n$ ), consequently the rate of flow erosion also reaches the largest value there (see Figure 4.5). Therefore it can be concluded that in

Stage I the rate of breach erosion is completely determined by the rate of erosion at  $x = l_n$  (when  $l_n \leq L$ , or at  $x = L$  if  $l_n > L$ ) together with that at the dike crest.

In case of a small breach flow velocity at the dike crest which is not sufficient to erode dike material away there, or when the erosion at the dike crest is neglectable compared with that occurring close to the toe of the dike, the rate of erosion (along the inner slope of the dike) in Stage I is totally controlled by the erosion near the toe of the dike (i.e.  $x = l_n$  if  $l_n \leq L$ , or  $x = L$  if  $l_n > L$ ).

Due to the larger erosion rate close to the toe of the dike than that on the upper part of the inner slope, the slope becomes steeper and steeper as time goes on in Stage I. When a certain critical slope angle  $\beta_1$  is achieved at  $t = t_1$  by the inner slope, Stage I ends and Stage II starts (see Figures 4.1 and 4.5);  $\beta_1$  is a function of the soil properties of the dike (see Chapter 5).

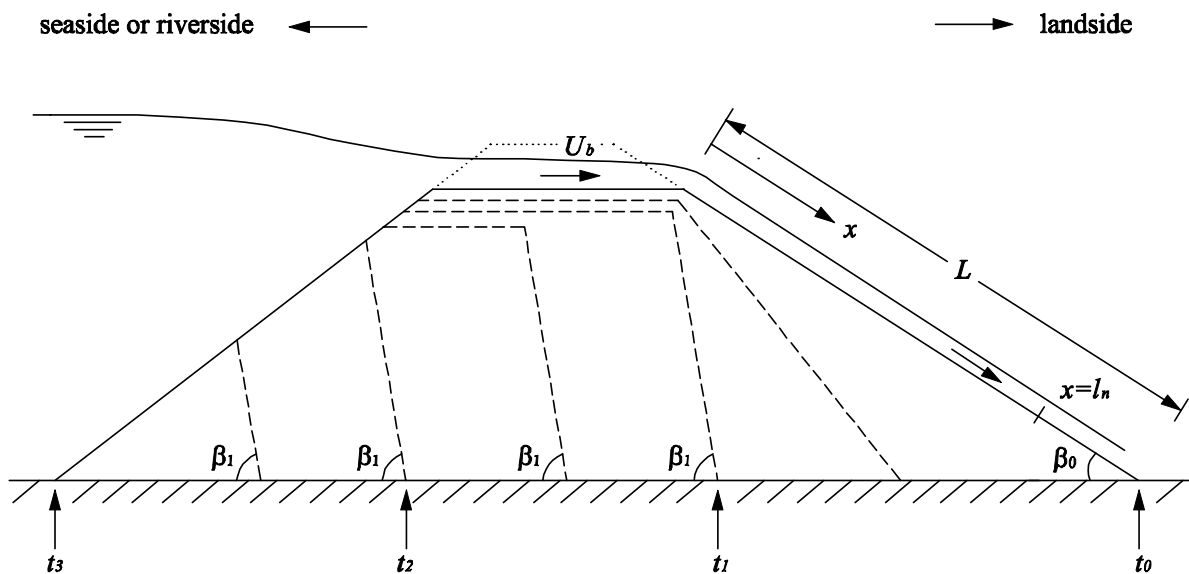


Figure 4.5 Sketch of dike profile evolution in Stages I, II and III.

## 4.5 Breach development in Stage II

### 4.5.1 Introduction

Stage II commences after the inner slope of the dike arriving at the critical value  $\beta_1$ . This gradient (i.e.  $\beta_1$ ) is maintained later on throughout Stage II (and also the following Stage III), see Figures 4.1 and 4.5. The steepened inner slope of the dike acts as a headcut in Stage II due to its large steepness.

In this section a classification of headcuts based on two criteria (i.e. shape of the headcut and erodibility of the headcut foundation) is made first (see Section 4.5.2), then the mechanism of soil erosion at different types of headcut is investigated (Section 4.5.3).

#### 4.5.2 Classifications of headcut

Classification of headcut can be made based on various criteria, e.g. Stein and Julien (1993) discerned two modes of headcut according to different evolving characteristics during migration: rotating headcut that tends to flatten as it migrates, and stepped headcut that tends to retain nearly vertical faces. In the present study headcut is classified on the basis of its shape and the erodibility of the foundation (see also Zhu et al., 2006a). It will be illustrated later in this chapter that different types of headcut based on these classifications show different erosion features.

According to the shape of the headcut, generally two categories of headcuts can be distinguished, i.e. single-step headcuts and multi-step headcuts (see Figure 4.6). The height of a headcut is limited by slope stability conditions (basic soil mechanics theory, see Appendix B). In other words, there is a height limitation for the headcut, which depends mainly on the soil properties (e.g. soil cohesion and internal friction angle). Therefore, in a relatively high headcut, usually several steps can be observed.

However, in some very dynamic processes like dike breaching or earth dam breaking, the headcut height could well exceed the soil mechanical height limitation and the high steep slope can stand stable for a certain period before it collapses. This has been shown in some prototype dike breaching and earth dam breaking events, for instance, the breaking of the 93 m high embankment Teton Dam in the United States in 1976.

When the erodibility of the headcut foundation is concerned, headcuts can be simply classified as headcuts with erodible foundation and headcuts with non-erodible foundation (see Figure 4.7), which display different erosion characteristics as will be shown later (in Figures 4.9 and 4.10). Table 4.1 summarizes the classifications of headcut as presented above.

Table 4.1 Summary of headcut classification.

Criterion	Classification
Shape of headcut	single-step
	multi-step
Erodibility of headcut foundation	non-erodible foundation
	erodible foundation

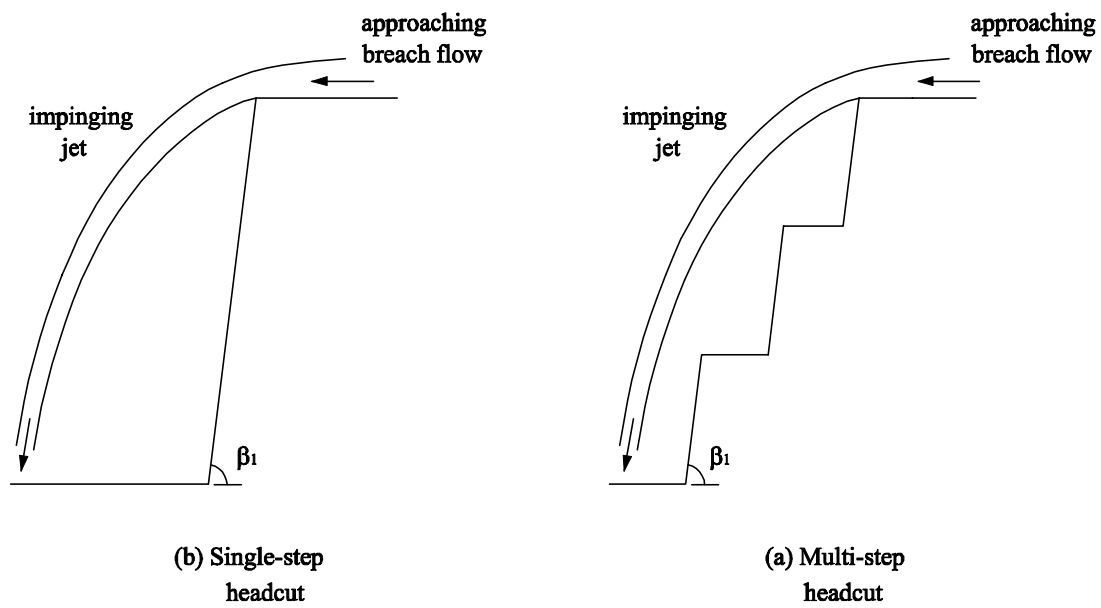


Figure 4.6 Sketch of single-step and multi-step headcuts.

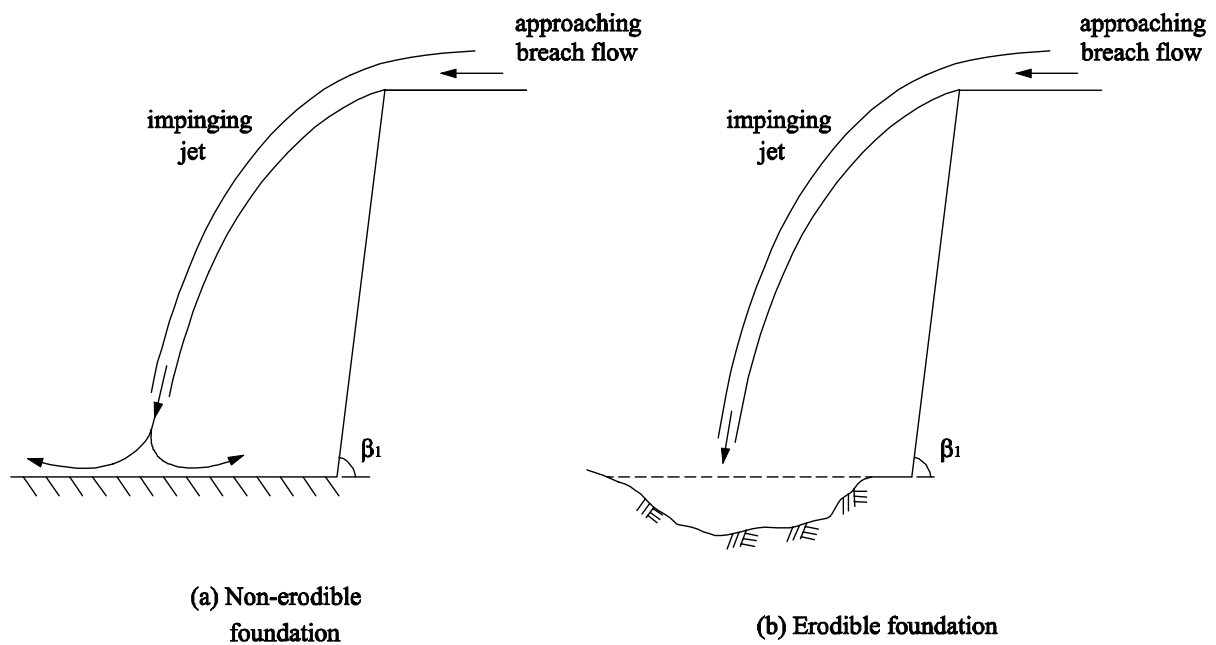


Figure 4.7 Sketch of single-step headcuts with non-erodible and erodible foundation.

### 4.5.3 Headcut erosion during dike breaching

As the breach discharge flows over the headcut, due to the large steepness of the headcut slope, it is very likely that the breach discharge flees away from the headcut

at the headcut brink and falls down as a jet. In case of a multi-step headcut, the falling jet impinges on the first lower horizontal platform when the flow velocity is not large enough, causing significant scour of the horizontal platform and potential undermining of the first headcut step (see Figure 4.8a). Then the nappe continues to fall down from this platform, impinging on the next lower one, until finally it attacks the dike foundation. On each of the horizontal platforms, characteristics of both the flow and the scour in the jet action area are complicated and case-specific.

The breach flow will flee further away from the headcut if the flow velocity at the headcut brink is increasing. It can therefore be expected that when the velocity of the breach flow is sufficiently large at the top of the headcut (i.e. the dike crest in the breach), the falling jet will fly over all the horizontal platforms in between and impinge directly on the downstream dike foundation as shown in Figure 4.8b. In this case the jet scour can only take place in the dike foundation, forming a hole in the foundation when it is erodible. This scour hole enlarges gradually and undermines the toe of the headcut, causing soil mechanical slope mass failure from the headcut. Under these circumstances the multi-step headcut evolves eventually into a single-step headcut.

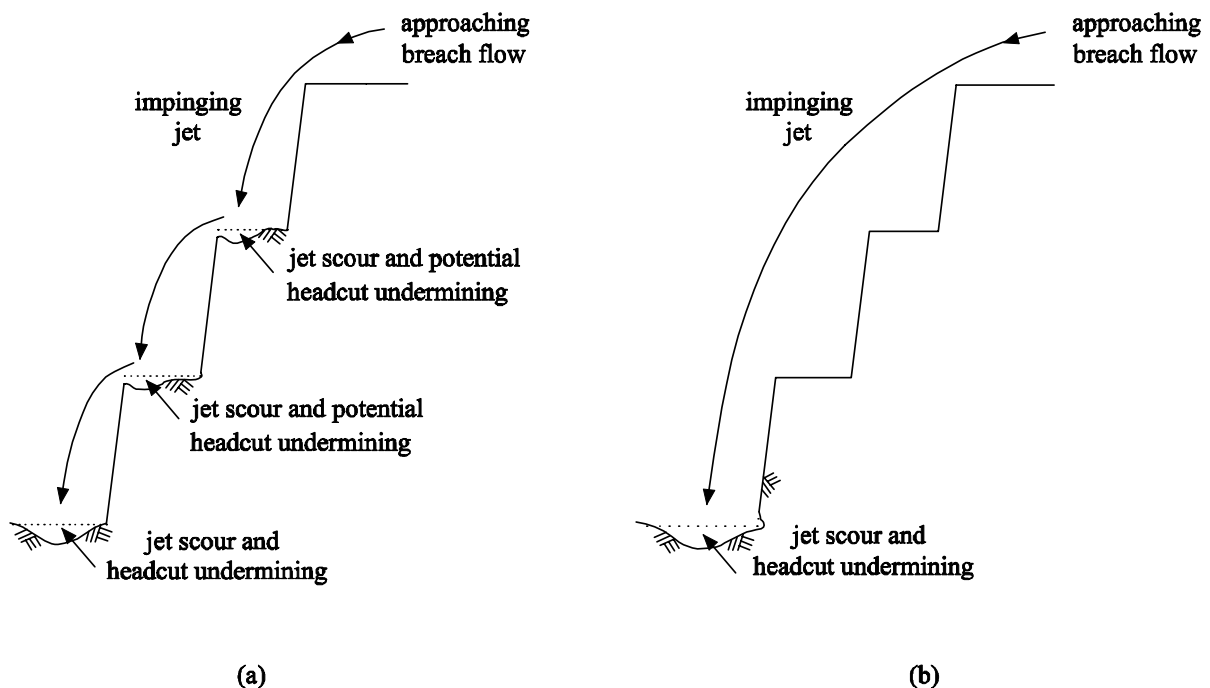


Figure 4.8 Erosion at a multi-step headcut: (a) falling jet impinges on the horizontal platforms in between; (b) falling jet impinges directly on the dike foundation.

Because of the large complexities involved in the erosion process at a multi-step headcut, only the erosion at a single-step headcut during dike breaching with either erodible or non-erodible foundation is going to be elaborated and modeled later on in Chapter 5.

Generally four types of erosion are likely to occur at the headcut in Stage II (and in the following Stage III as well) during the breach erosion process of clay-dikes (Zhu et al., 2005a and 2005b). Figure 4.9 shows the erosion at the headcut with an erodible dike foundation, and Figure 4.10 with a non-erodible dike foundation. The first type of erosion at the headcut is the breach flow shear erosion along the approaching headcut top surface, gradually lowering the height of the dike (see ① in Figures 4.9 and 4.10, see also Figure 2.10). The second one is the erosion along the headcut slope surface (indicated as ② in Figures 4.9 and 4.10). This erosion consists of two possible contributions: one is the shear erosion along the headcut slope due to the hydraulic shear stress imposed by the falling flow; the other is the failure of the surface soil layer due to fluidization. The third type of erosion at the headcut is the jet scour of the dike foundation (if any) and the headcut undermining, see ③ in Figures 4.9 and 4.10. The impinging nappe attacks the downstream dike foundation, causing intensive turbulence in the impingement region and imposes considerable erosive forces on both the foundation and the toe of the headcut. As a result, a scour hole is formed in the foundation if it is erodible. The scour hole is enlarged both vertically and horizontally in time and starts to undermine the headcut from a certain moment. For a headcut with non-erodible foundation, the jet is deflected in the region close to the foundation, causing curving of the streamlines that partly rush towards the headcut slope and undermine the headcut. Finally, when the headcut undermining has developed to a certain critical degree, the headcut becomes unstable under the action of gravity and seepage forces, and soil mechanical slope mass failure occurs from the headcut (④ in Figures 4.9 and 4.10, see also Figure 2.10).

The failure block CDFE of the slope mass failure in Figures 4.9 and 4.10 is assumed to collapse by overturning around point E rather than sliding down. After the occurrence of each slope mass failure, the headcut retreats a distance of the width of the failure block, subsequently the impinging jet readjusts its entry point to the plunge pool and starts a new cycle of erosion as shown in Figures 4.11 and 4.12 (see also Zhu et al., 2005a and 2005b).

Depending on the specific situations (e.g. the status of the erosion and the flow conditions at the dike crest), the respective roles played by each of the four erosion mechanisms in Stage II are of different significance for the process of the dike breach growth. If the breach flow velocity at the headcut brink ( $U_b$ ) is sufficiently large, the breach flow flees relatively far away from the headcut, and then the second type of erosion, i.e. erosion along the headcut slope surface, is relatively insignificant for the breach erosion in Stage II. On the contrary, the other three types of erosion dominate the headcut backwards migration and the lowering of the dike height in Stage II.

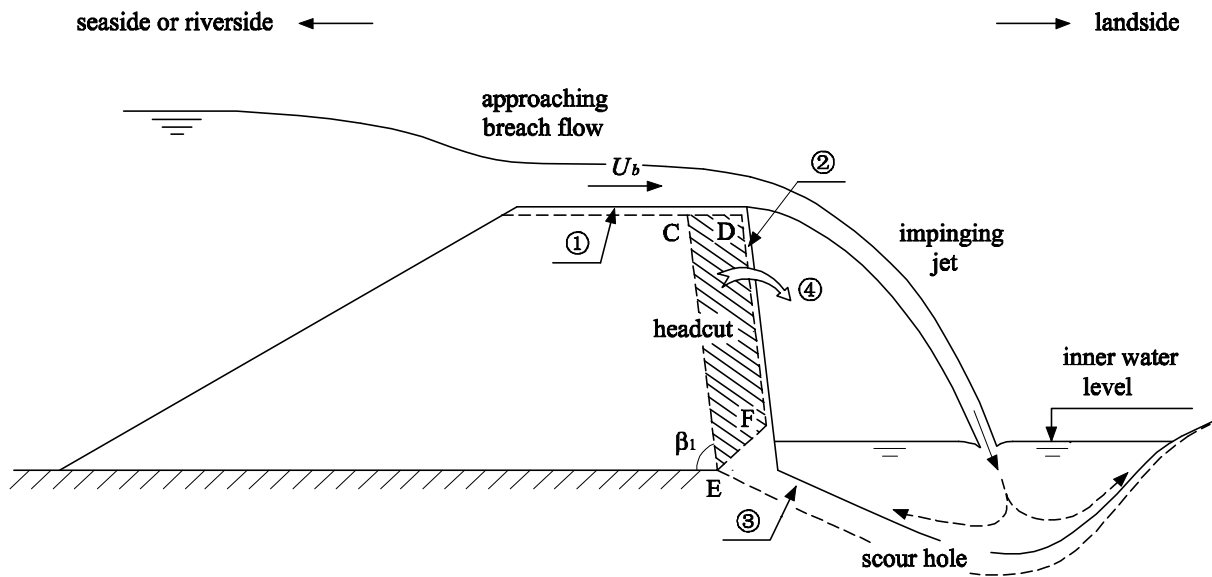


Figure 4.9 Erosion at the headcut during dike breaching with an erodible foundation: ① shear erosion along headcut top surface; ② erosion along headcut slope; ③ jet scour of foundation and headcut undermining and ④ slope mass failure.

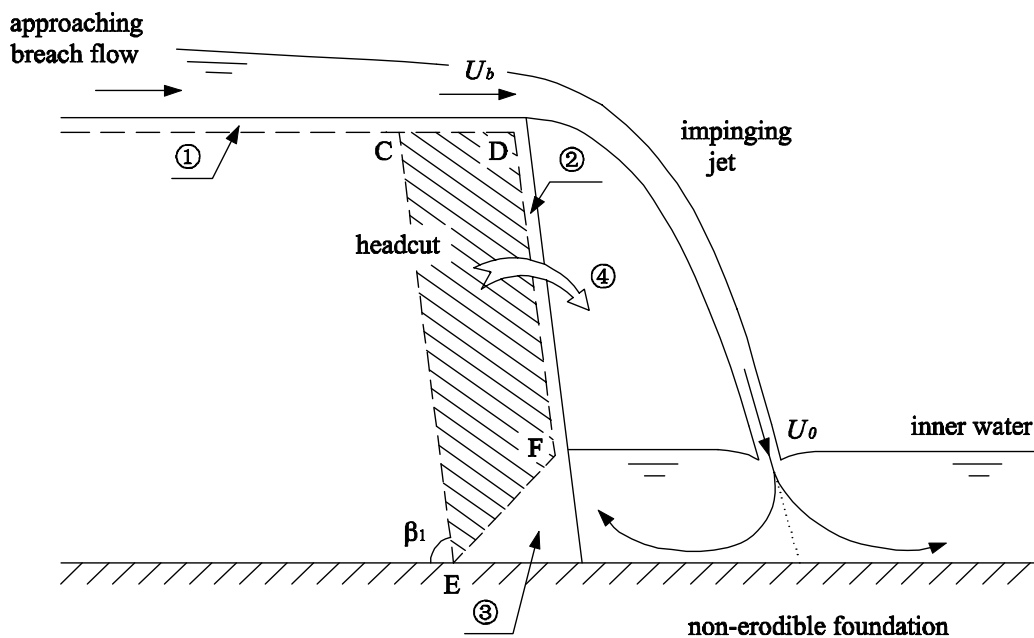


Figure 4.10 Erosion at the headcut during dike breaching with a non-erodible foundation: ① shear erosion along headcut top surface; ② erosion along headcut slope; ③ headcut undermining and ④ slope mass failure.

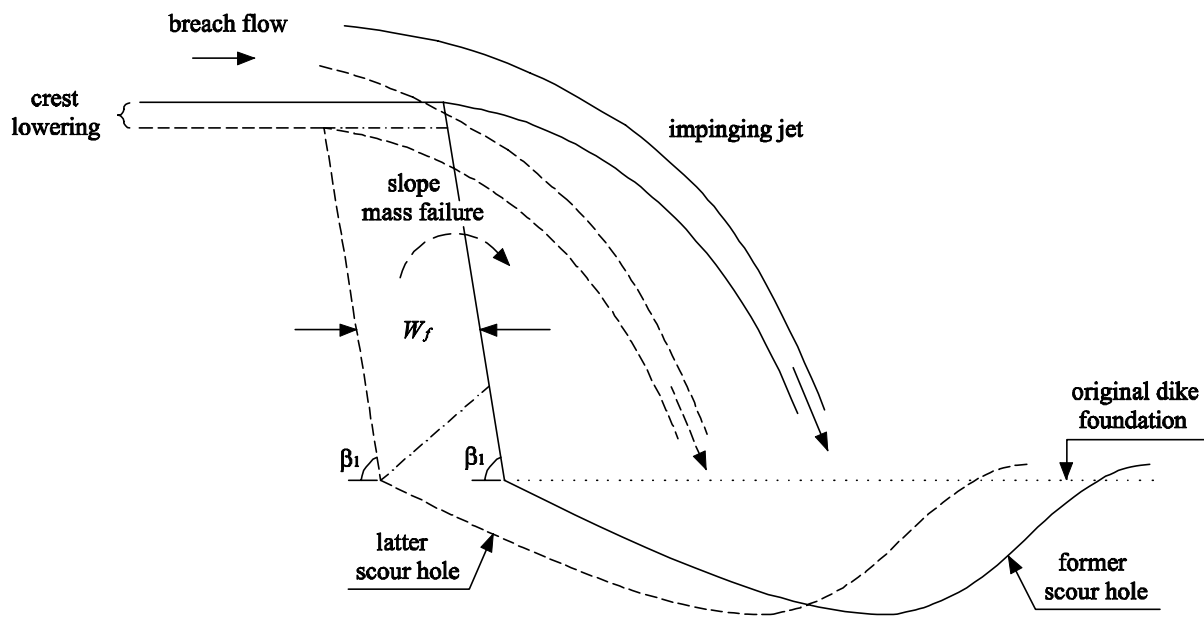


Figure 4.11 Headcut slope mass failure and jet entry point relocation.

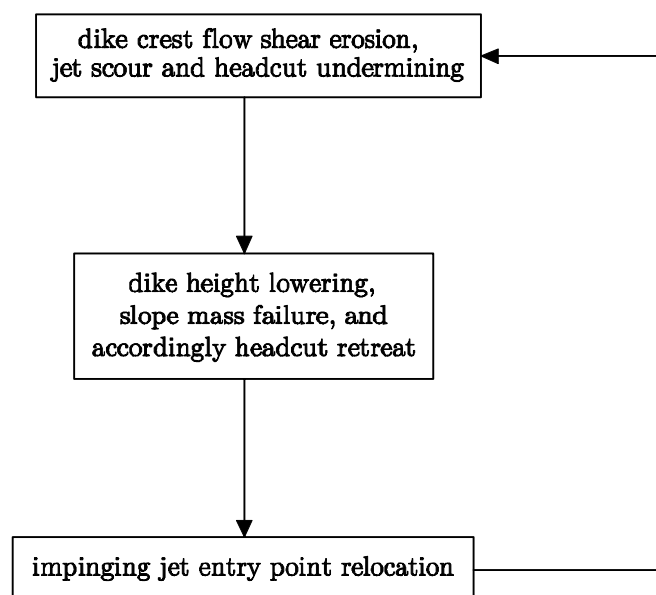


Figure 4.12 Cycle of erosion in Stage II.

On the contrary, sometimes the transition area between the dike crest and the steepened inner slope is eroded into a rounded angle. Then the breach flow may not flee away from the headcut at the top, instead it rushes down along the slope and probably detaches from the slope at a certain lower point (as observed occasionally in the DUT laboratory experiments, see Chapter 6). In addition, when the breach flow velocity at the headcut brink is small, the breach flow is also likely to flow down

along the steepened inner slope (i.e. the headcut slope) rather than fleeing away as an impinging jet. In these instances the breach flow exerts far less attack momentum on the downstream dike foundation compared with the jet impingement situation. However, the role played by the flow shear erosion along the headcut slope surface is strengthened.

The fluidization of the headcut slope surface due to diffused falling water in Stage II (and also later in Stage III) reduces the soil mechanical strength of the surface layer and speeds up the erosion process (as observed in the DUT laboratory experiments, see Chapter 6). However, quantitative consideration of this influence on the breach erosion is difficult.

Noticeably, for prototype dikes, a possible weak layer(s) (in strength) might be hidden among the dike foundation and is able to accelerate the backward migration speed of the headcut dramatically. That is, a more erodible layer underlying a less erodible layer in the dike foundation can remarkably accelerate the breach erosion process by undermining the less erodible layer and then the headcut (see e.g. Robinson, 1996, see also Section 2.5). Besides, the weak layer is likely to increase the potential of piping through the dike foundation, which can also speed up the breach erosion process. Nevertheless, most of the descriptions on this issue so far are qualitative, while a universal mathematical description of it is hard because of the large diversity of the dike foundations in reality. More research is required to gain better insight into this phenomenon.

As a result of the aforementioned four erosion mechanisms, the headcut (i.e. the steepened inner slope of the dike) migrates upstream unevenly but ceaselessly as time goes by in Stage II, the width of the dike crest in the breach decreases accordingly. At the same time the height of the dike in the breach decreases due to the flow erosion over the crest. At the end of Stage II the headcut moves backwards to the outer slope of the dike and at  $t = t_2$  the dike crest in the breach has disappeared completely (see Figure 4.1).

## 4.6 Breach development in Stage III

In the beginning of Stage III at  $t = t_2$ , the headcut has migrated to the outer slope of the dike and the cross-section of the residual dike body becomes triangular-shaped (see Figures 4.1, 4.5 and 4.14). The headcut maintains the critical slope angle  $\beta_1$  throughout Stage III.

The thin tip of the remaining dike body can hardly stand the water forces (both hydrostatic and hydrodynamic) from the river (or sea) and is therefore washed (pushed) away very quickly down to a certain height (see Figure 4.13), resulting in a rapid breach enlargement and an increase of the breach flow (Zhu et al., 2005b).

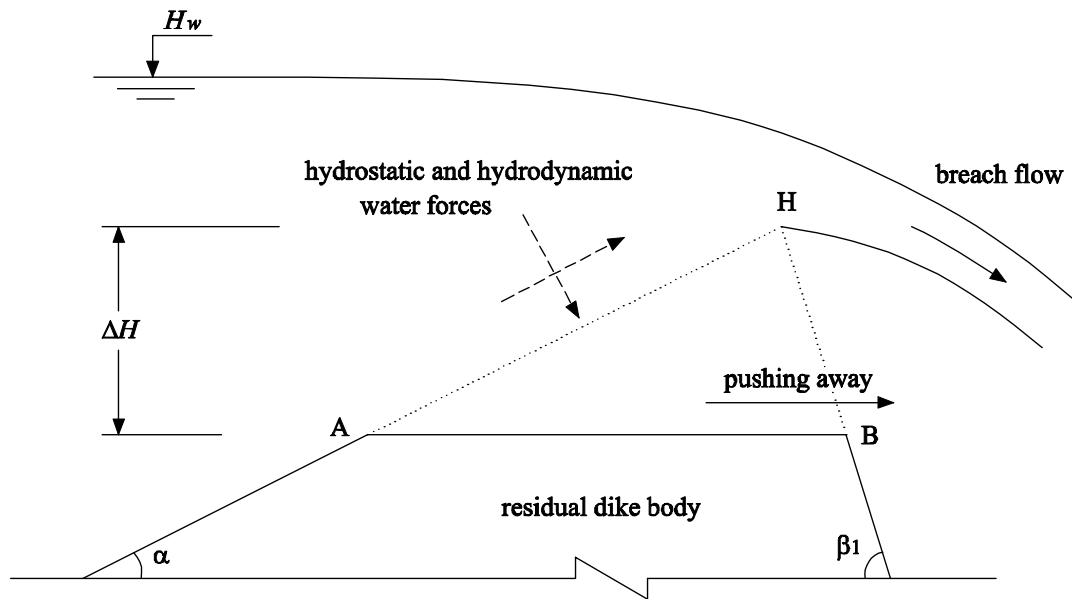


Figure 4.13 Pushing away of the thin tip of the residual dike body soon after  $t = t_2$ .

In Stage III still four types of erosion are likely to occur at the headcut, similar to those described for Stage II, i.e. flow shear erosion along the headcut top surface (see ① in Figure 4.14), erosion along the headcut slope (see ② in Figure 4.14), dike foundation scour (if any) and headcut undermining (see ③ in Figure 4.14), and the resultant soil mechanical slope mass failure (see ④ in Figure 4.14).

Due to the above-mentioned erosion in Stage III (see Figure 4.14) the headcut continues to migrate backwards and the height of the dike in the breach decreases rapidly, as a result the breach flow increases very fast, which in its turn accelerates the breach erosion process greatly.

It should be kept in mind that occasionally the lowering of the dike body in the breach and the enlargement of the breach in Stage III is not only determined by the flow shear erosion along the breach boundary. To be clear, at the time of slope mass failure the width of the failure block (i.e. length of CD in Figure 4.14) is possibly larger than the width of the dike crest in the breach (i.e. length of GD), which means that in Figure 4.14 the point C is possibly at the upstream side of the point G. Under these circumstances the headcut slope mass failure contributes to the breach enlargement and dike lowering as well. Soon after the slope mass failure occurrence the thin tip of the newly-formed triangular-shaped dike body is again quickly washed or pushed away to a certain height, initiating a new cycle of dike breach erosion in Stage III.

It should also be pointed out that, along with the reduction of the height of the dike in the breach in Stage III, the role played by the headcut slope mass failure is about to decline, on the contrary, the role played by the flow shear erosion to the breach boundary is about to increase, due to the increase of the breach flow rate.

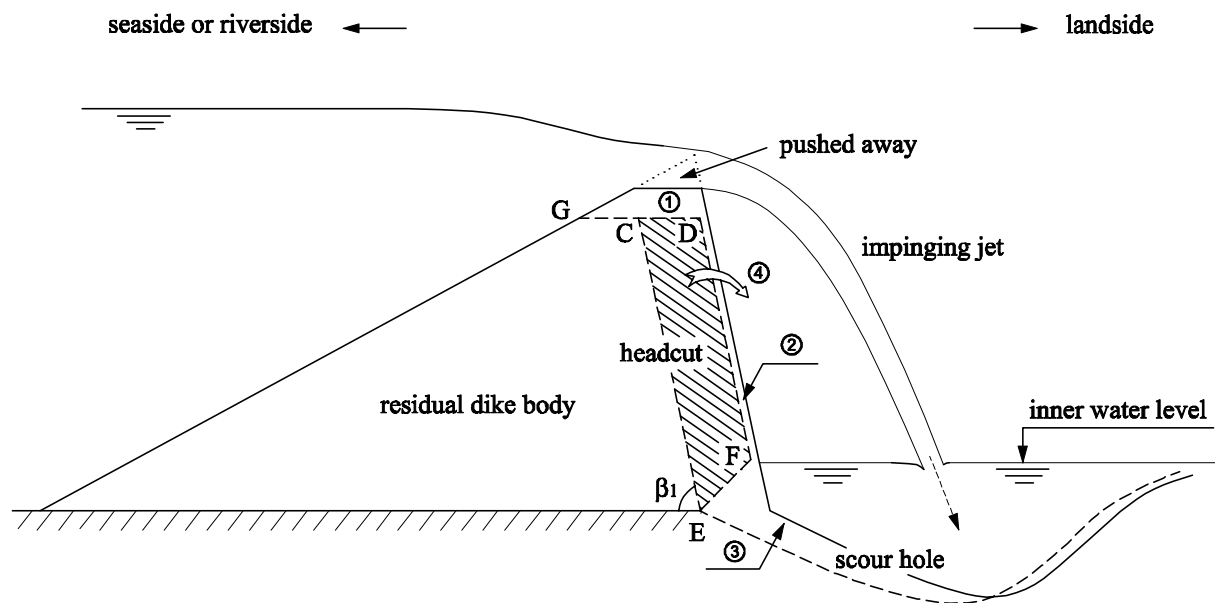


Figure 4.14 Schematic illustration of breach erosion in Stage III (with an erodible foundation): ① shear erosion along headcut top surface; ② erosion along headcut slope; ③ jet scour of foundation and headcut undermining and ④ slope mass failure.

## 4.7 Breach enlargement in the dike crest in Stages I, II and III

As stated before, the initial breach in the dike crest is assumed to have a trapezoidal cross-section with an initial side-slope angle  $\gamma$ . This initial breach is enlarged in time due to the breach flow erosion during Stages I, II and III. The process of this breach enlargement in the dike crest in these three stages is described qualitatively in this section.

When the initial breach in the dike crest is overflowed by the flooding water at  $t = t_0$ , flow shear erosion occurs along the breach bottom as well as the breach side-slopes (see Figure 4.15a), provided that the flow velocity in the breach is large enough to erode dike material away. Due to the larger flow velocity at the breach bottom, the erosion rate there is also larger than that along the breach side-slopes. Similarly the erosion rate at lower parts of the breach side-slopes is larger than that at the upper parts. Therefore the breach side-slopes become steeper in time along with the flow shear erosion, and accordingly the inclination angle of the side-slopes increases (see Figure 4.15a).

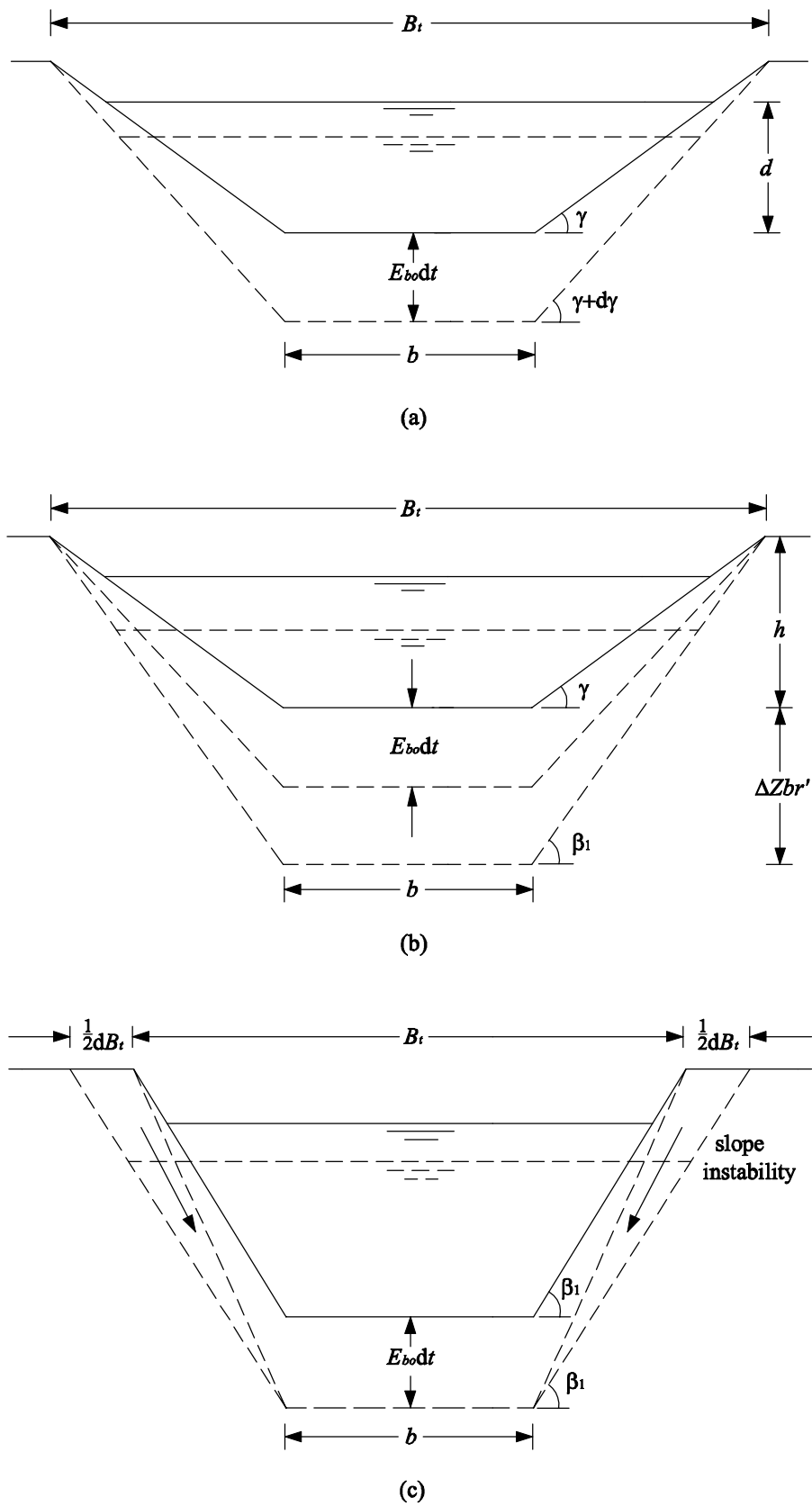


Figure 4.15 Process of breach enlargement in the dike crest in Stages I, II and III: (a) steepening of breach side-slopes; (b) reaching of  $\beta_1$  by the side-slope gradient; (c) breach widening after  $\beta_1$  is reached.

After some time in the erosion process, the gradient of the steepened breach side-slopes has reached the critical slope angle  $\beta_1$  (see Figure 4.15b). From observations of various experiments on the breaching of embankments (e.g. the EC IMPACT Project laboratory experiments in UK, the HERU large-scale experiments in USA and the Nordland field experiments in Norway, see Mohamed et al., 2004, Hahn et al., 2000 and Vaskinn et al., 2004, respectively), it is found that both the downstream slope of the embankment and the side-slopes of the breach can become very steep during the breach erosion process. It is assumed here that the critical slope angle of the breach side-slopes is the same as that of the inner slope of the dike in the breach, for the sake of simplicity.

The depth ( $\Delta Z_{br}'$ ) at the breach bottom that is required to erode down in order to reach  $\beta_1$  along the entire breach side-slopes is

$$\Delta Z_{br}' = \frac{h \sin(\beta_1 - \gamma)}{\sin \gamma \cos \beta_1} \quad (4.1)$$

in which  $h$  is the depth of the initial breach (see Figure 4.15b).

From then on, any further erosion in the breach always results in the exceeding of  $\beta_1$  of the gradient of the breach side-slopes and leads to over-steepness and instability of the breach side-slopes. Collapsing of the breach side-slopes is then expected with an increase in the width of the breach (see Figure 4.15c). After the occurrence of the side-slope instability, the slope gradient returns to  $\beta_1$  and a new cycle of flow shear erosion and side-slope instability repeats.

It will be shown later (see Section 4.8) that the breach side-slope instability is considered to be the main mechanism of breach widening in the subsequent Stages IV and V as well. The only principal difference is that in Stages IV and V the occurrence of the breach side-slope instability is mainly due to lateral erosion in the breach rather than vertical erosion. However as described above, in Stages I, II and III the flow shear erosion in vertical direction at the breach bottom is the main cause for the breach side-slope instability, consequently also for the breach enlargement.

## 4.8 Breach development in Stage IV

Stage IV starts when the dike body in the breach has been eroded down to the foundation of the dike or to the toe protection on the outer slope of the dike, if any. The erosion of the breach mainly takes place laterally in this stage (and also in the following Stage V, see Section 4.9). The extent of vertical erosion in these two stages relies primarily on the following geometrical and material characteristics of the dike:

- The resistance against further erosion of the dike foundation;

- The presence or not of a toe protection on the outer slope of the dike and its ability to protect the outer slope from further erosion;
- The presence or not of a relatively high foreland, and if so, its resistance against erosion, or the presence or not of an effective bottom protection on the foreland.

Depending on the above conditions, Visser (1998) distinguished three types of breach for Stages IV and V of the breach erosion process in sand-dikes. This distinguishing is also followed here for clay-dikes. If the vertical erosion at the breach inflow is prevented or strongly slowed down by either a solid dike foundation, a solid toe protection on the outer slope of the dike, a solid relatively high foreland, or an effective bottom protection on this foreland, then a Type A breach occurs (see Figures 4.16, 4.17 and 4.18). Solid means here with a relatively high resistance against erosion. A dike breaches as Type B when only a relatively high but erodible foreland is present (see Figure 4.19). All the other cases belong to Type C breaches (see Figure 4.20).

In Stage IV (and also in the subsequent Stage V), the breach side-slopes maintain the critical slope angle of  $\beta_l$  (see Figures 4.21 and 4.22). The dominating mechanisms of breach erosion are the flow shear erosion along the breach side-slopes and the resultant discrete soil mechanical breach side-slope instability.

The breach flow imposes shear stress on both the side-slopes and bottom of the breach, leading to steeper breach side-slopes due to the larger erosion rate at the lower parts than at the upper parts of the slopes. The slope angle therefore increases and exceeds the critical value of  $\beta_l$ , inducing mass failure from the over-steep side-slopes at a certain moment (see Figures 4.21 and 4.22). Later on the gradient of the side-slopes returns to  $\beta_l$  and a new cycle of breach boundary shear erosion and side-slope mass failure repeats. The over-steep portion of the breach side-slopes is observed in various experiments to often fail by overturning (around points A and B, as shown in Figures 4.21 and 4.22).

Figure 4.21 is a schematic illustration of the increase of the breach width in Stages IV and V for a Type A breach, in which  $E_{sl}$  is the rate of flow shear erosion at the toe of the breach side-slopes. The vertical erosion at the breach inflow is prevented or strongly slowed down by either a solid dike foundation, a solid toe protection on the outer slope of the dike, a solid and relatively high foreland, or an effective bottom protection on this foreland. In all these cases the erosion at the breach inflow can only take place in lateral direction, while vertical erosion to the breach bottom can be neglected. When the shear erosion at the toe of the side-slopes has developed to a certain degree, the side-slopes become too steep to remain stable and mass failure occurs.

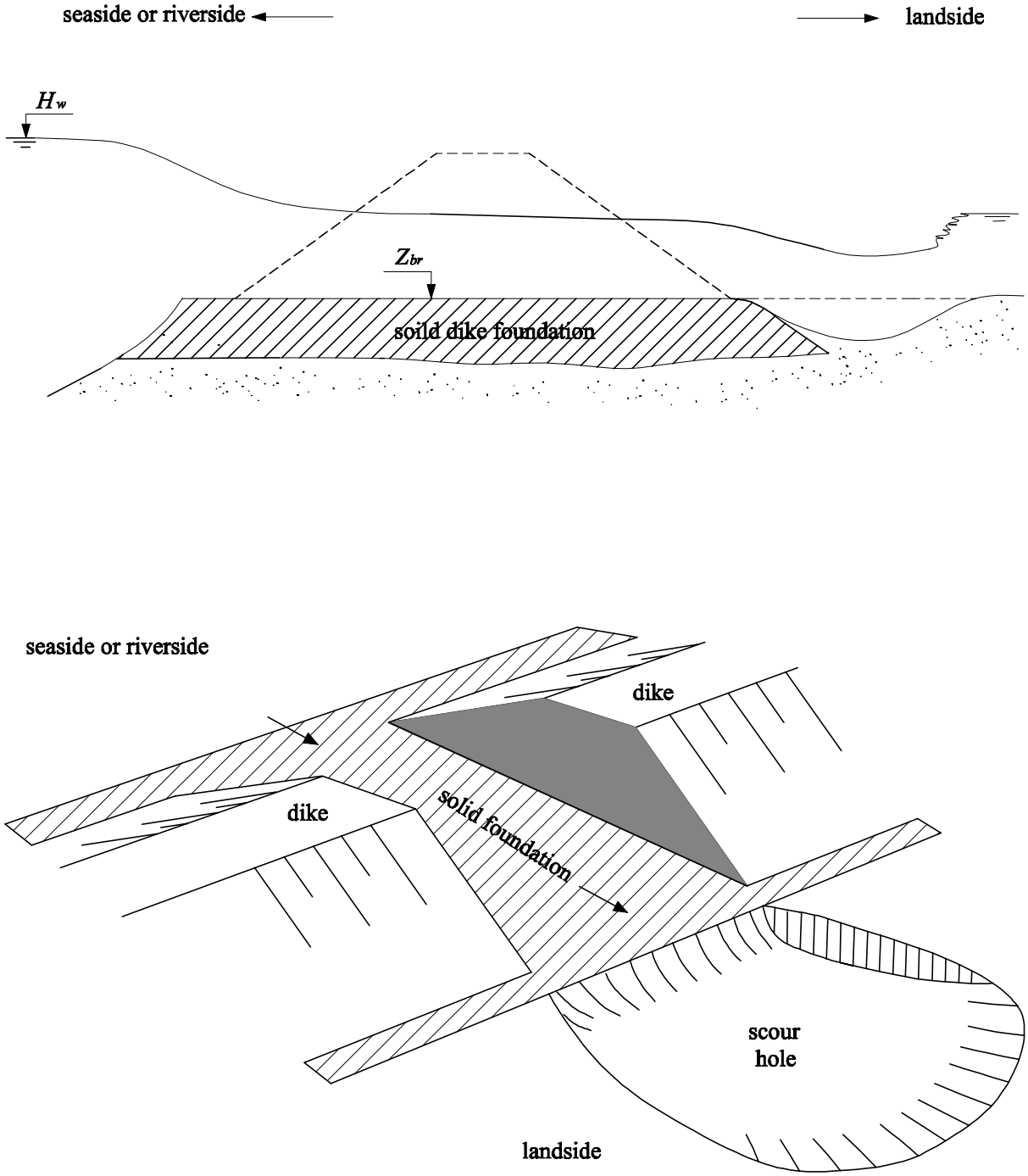


Figure 4.16 Vertical erosion at the breach inflow is obstructed by a solid dike foundation in Stage IV.

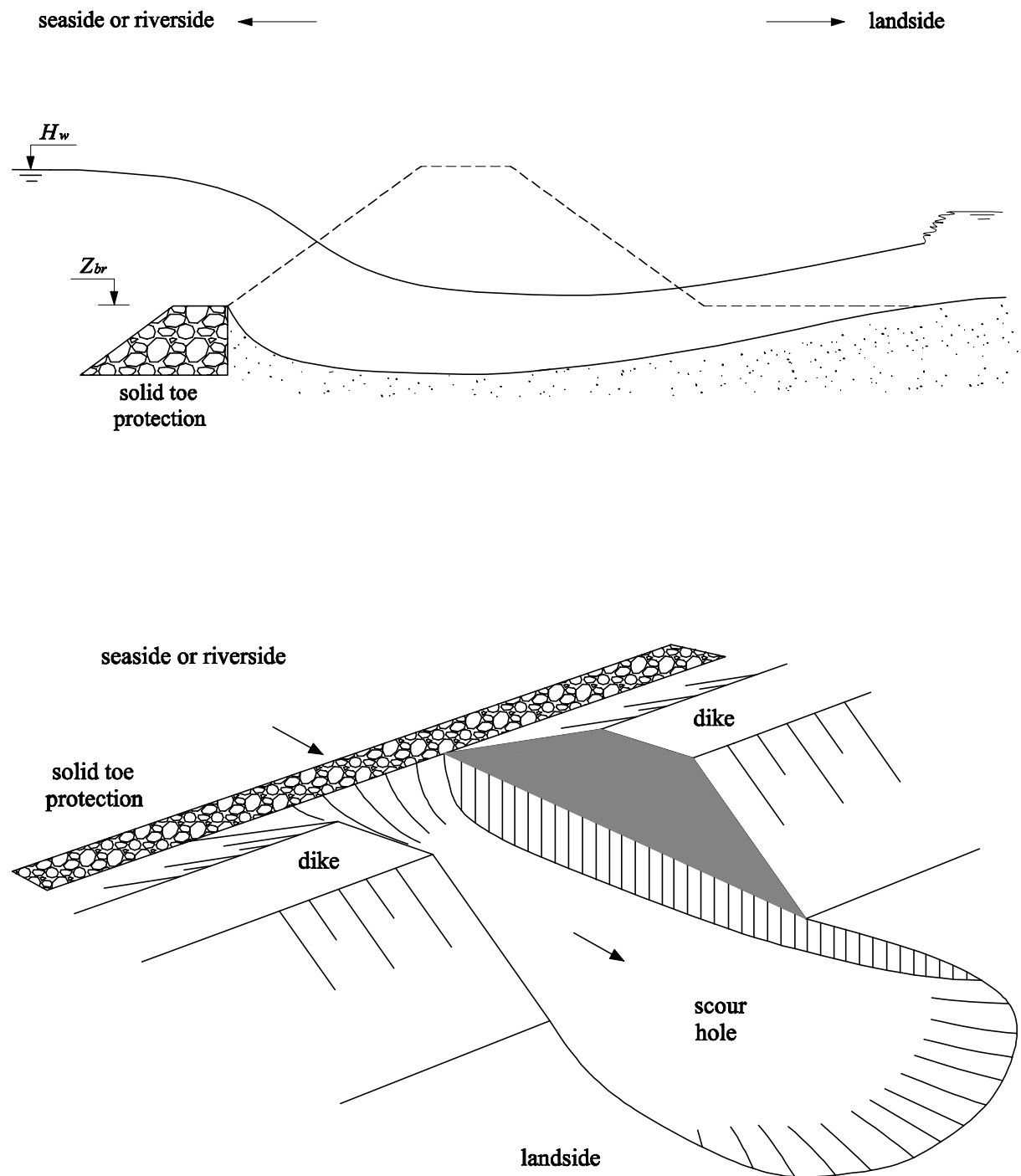


Figure 4.17 Vertical erosion at the breach inflow is obstructed by a solid toe protection on the outer slope of the dike in Stage IV.

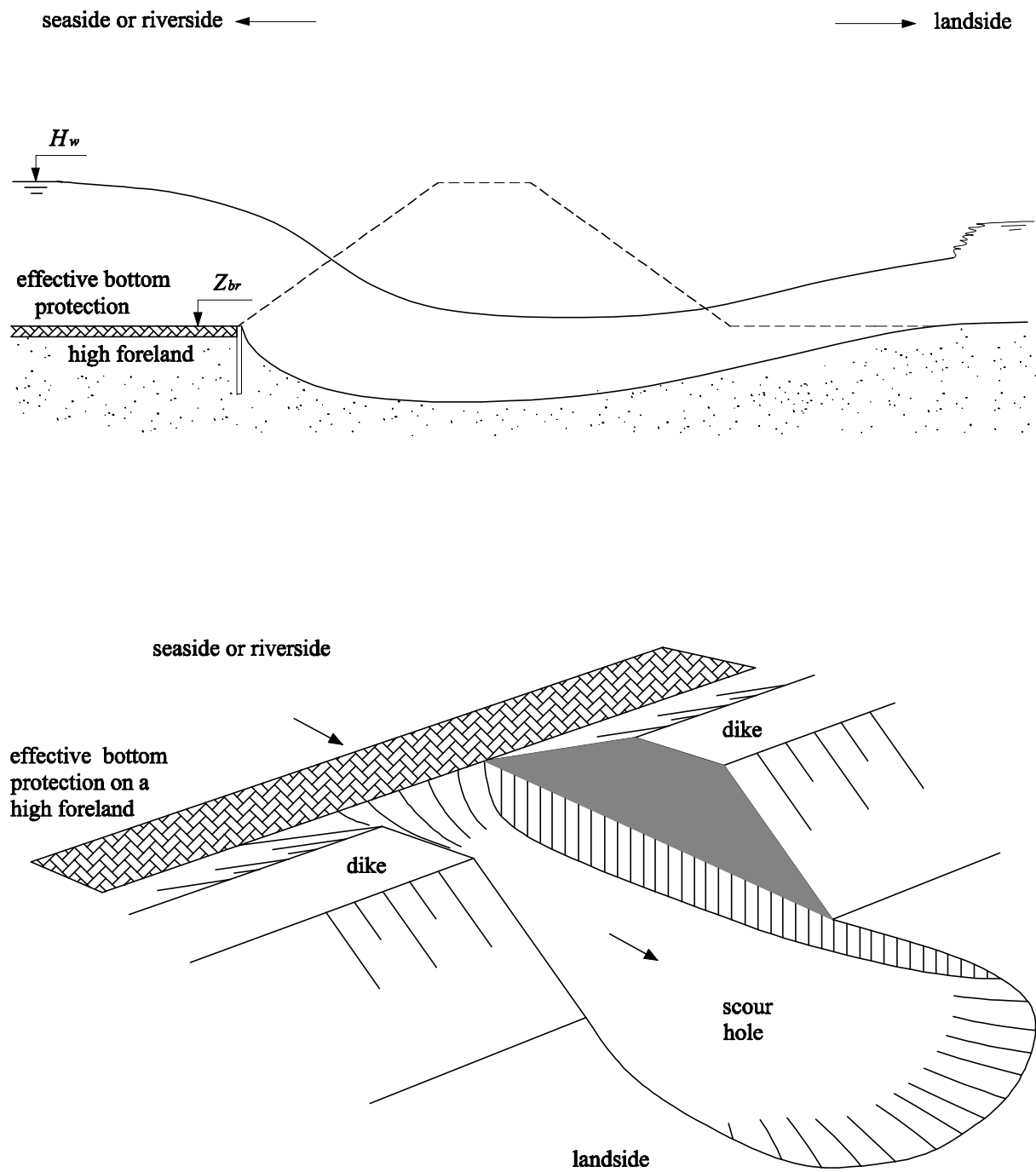


Figure 4.18 Vertical erosion at the breach inflow is obstructed by a solid relatively high foreland or by an effective bottom protection on that foreland.

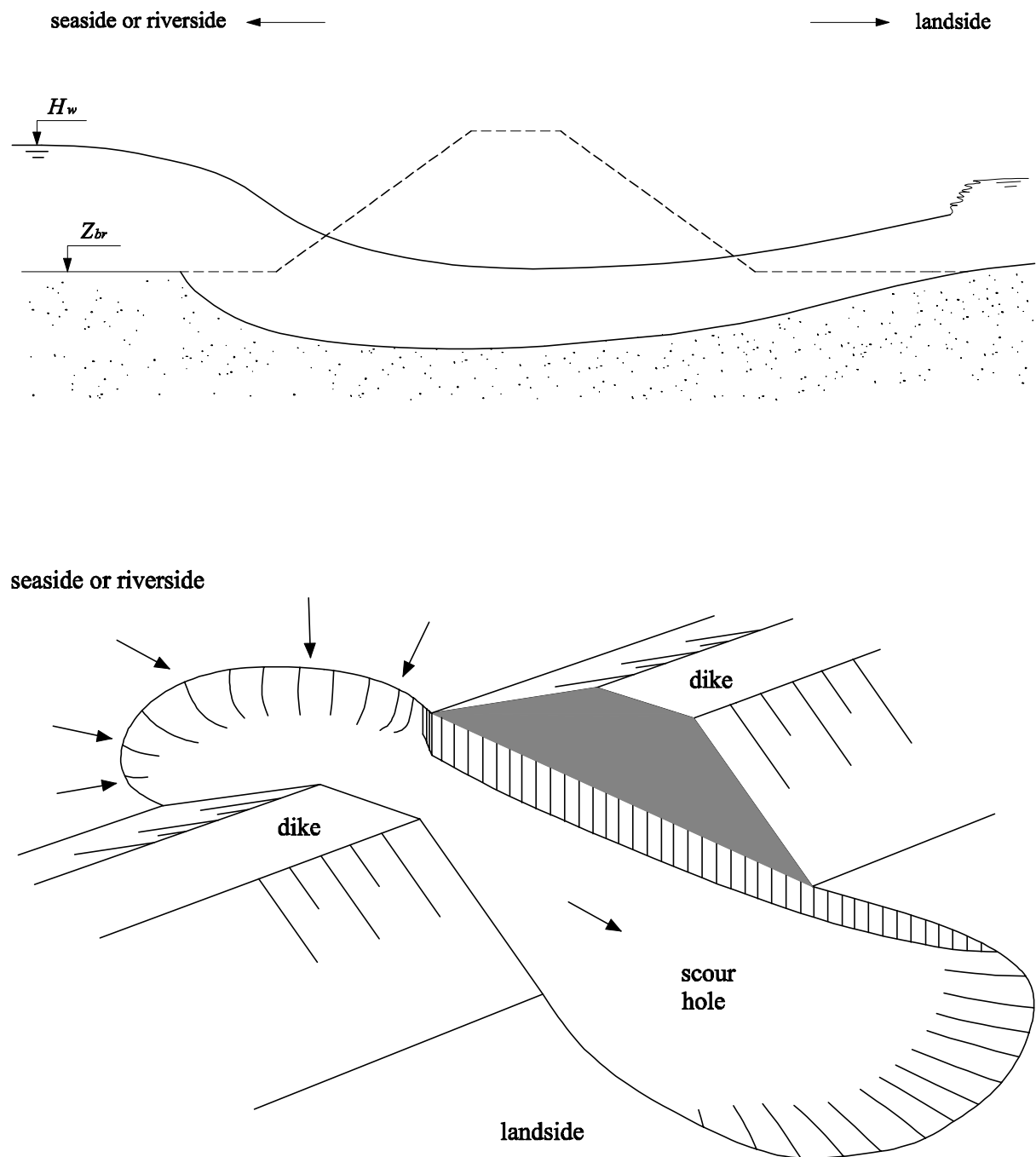


Figure 4.19 Vertical erosion in Stage IV with only a relatively high but erodible foreland presents.

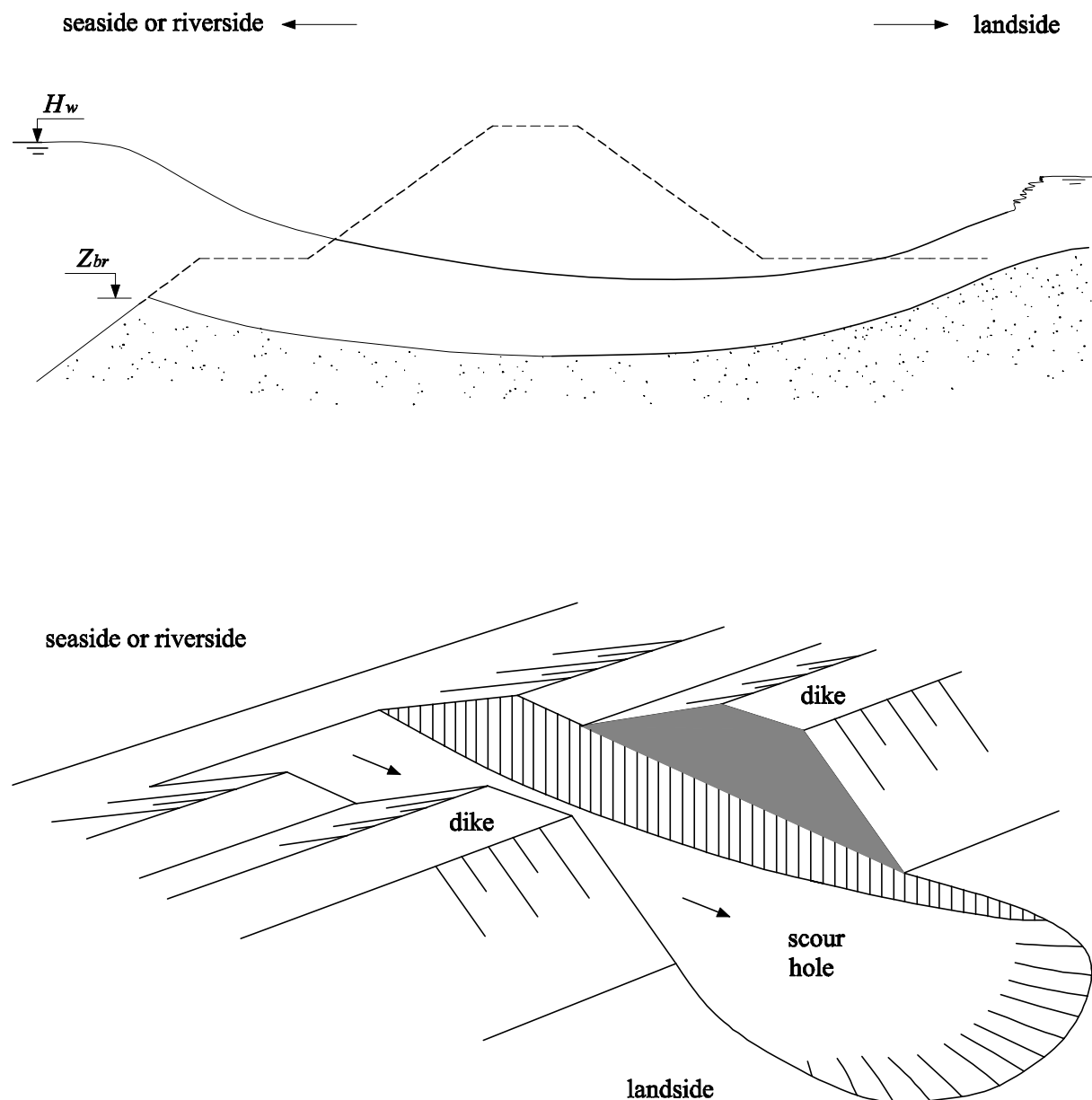


Figure 4.20 Vertical erosion in Stage IV in a Type C breach.

Figure 4.22 schematically shows the growth of the breach width in Stages IV and V when the dike foundation is erodible (i.e. Types B or C breach). Erosion in the breach takes place not only laterally (e.g.  $E_{sl}$  at the toe of the breach side-slopes), but also vertically ( $E_{bo}$  at the breach bottom). However, in real cases of dike failure, the final width of a dike breach generally has an order of magnitude of hundred meters, while its final depth most probably has an order of magnitude of ten meters. In other words, usually the final width of the breach is much larger than the final depth. Therefore, for a Type B or Type C breach, although the dike foundation is erodible, the erosion rate at the breach bottom (i.e.  $E_{bo}$  in Figure 4.22) is normally much smaller than at the toe of the side-slopes (i.e.  $E_{sl}$  in Figure 4.22) in most of Stages IV

and  $V$ . That is to say, the rate of growth of the breach width  $B_t$  depends mainly on  $E_{st}$  rather than on  $E_{bo}$  in the final two stages for Types B or C breaches.

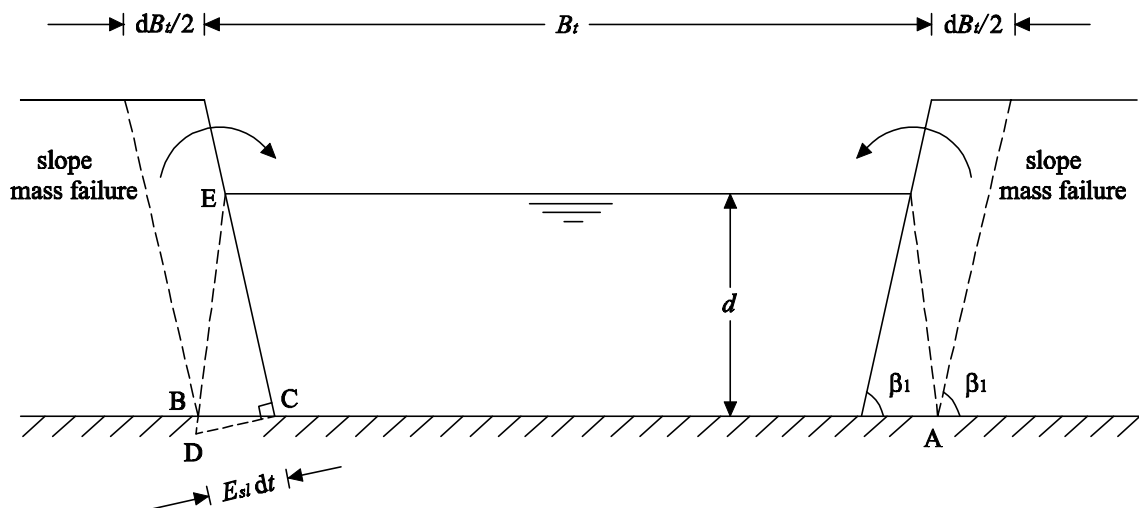


Figure 4.21 Breach width increase in Stages IV and V in a Type A breach.

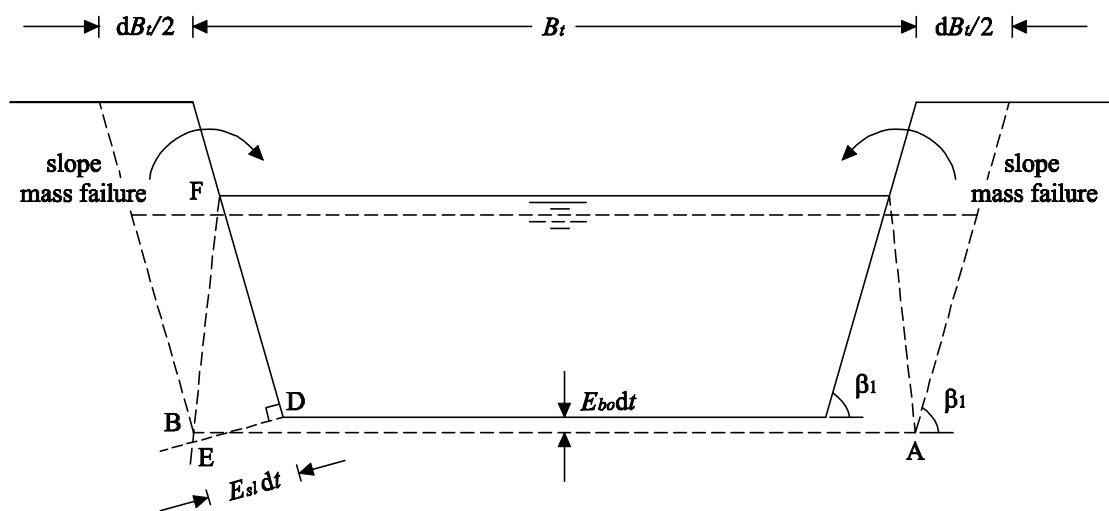


Figure 4.22 Breach width increase in Stages IV and V in Types B or C breaches.

It should be pointed out that in reality the breach side-slope mass failure occurs in a discrete manner. Accordingly the increase of the breach width in time in Stages IV and V is also in a discontinuous and stepwise pattern (see e.g. Figures 7.5, 7.6, 7.7 and 7.12, the measured breach width increase for the EC IMPACT Project experiments). However, in the model with  $dB_t/dt$  only determined by the rate of flow

shear erosion in the breach (see Chapter 5), the model-calculated breach width increase will be a relatively uniformly climbing smooth line (see Figures 7.6, 7.7 and 7.12, the calculated breach width increase for the EC IMPACT Project experiments).

During the process of dike breaching, along with the flow of water through the breach into the polder, the water level in the polder (i.e. the inner water level) rises continuously, especially after  $t = t_3$  when the dike is completely broken through. By the end of Stage IV at  $t = t_4$  the inner water level has risen to such a height that it begins to affect the inpouring pattern of the breach flow to the polder. The breach flow changes from free discharge to submerged discharge and from critical flow to subcritical flow due to the influence of the rising inner water level.

## 4.9 Breach development in Stage V

In Stage V, due to the growing obstructing effect from the rising inner water level, a gradual decrease of the breach flow velocity is induced; consequently the rate of breach erosion also decreases. The breach enlargement still occurs mainly laterally in this stage. Erosion in vertical direction in the breach is again primarily determined by the geometrical and material conditions of the dike. The main mechanisms of the breach erosion are the same as in Stage IV as shown in Figures 4.21 and 4.22: continuous breach flow shear erosion along the breach boundary and the resulting discrete side-slope mass failure.

By the end of Stage V at  $t = t_5$  the breach flow velocity is reduced to such a degree that it can no longer erode the dike body and dike foundation. Thus the breach reaches its final dimensions and the breach growth stops at  $t = t_5$ . Nevertheless, despite the small flow velocity, still there is water flowing through the breach into the polder after  $t = t_5$ . This flow does not cease until at  $t = t_6$  when either the inner and outer water levels (i.e. the water level of the river or sea) equal or the outer water level drops below the breach bottom.

## 4.10 Discussion

Similar to the division made by Visser (1998) for sand-dikes, the entire breach erosion process in clay-dikes can generally also be divided into five stages. However, slope mass failure plays a more important role in the breach erosion process in clay-dikes, compared with that in sand-dikes which is very likely dominated by flow shear erosion, especially in the first three stages. The soil cohesiveness in clay-dikes can strongly slow down the erosion rate, as was observed during the DUT laboratory experiments (see Chapter 6). To summarize, distinct from sand-dikes, the incomplete

understanding of the complicated cohesive soil features makes the breaching process in clay-dikes more intricate with more influential factors and more unknown aspects.

In case of a very huge polder, the rise of the inner water level can be very slow and the filling up of the polder may not be completed at all, because sometimes the breach can be closed with manpower at a certain moment and the breach growth stops accordingly (e.g. the breach closure near Jiujiang City in the 1998 big floods along the Yangtze River). Contrarily, in the case of a very small polder with very limited storage capacity, Visser (1998) noted that theoretically the submerging of the polder may occur in each of the Stages I, II and III, and in practice in such a case most probably takes place in Stage III due to the very small flow through the breach in the previous two stages. Under these circumstances Stages IV and V could therefore be ignored.

For the breach erosion process in both sand-dikes and clay-dikes, the first three stages (i.e. Stages I, II and III) have a relatively shorter duration than Stages IV and V do. The final breach dimensions are mostly developed in the last two stages. In addition, the rate of the breach flow in Stages I, II and III is also relatively small compared with that in Stages IV and V. Therefore it is natural that for the most significant final breach width and inundation speed of the polder, Stages IV and V are the most important two stages of the entire process of breach growth. However, this does not necessarily mean that the first three stages are insignificant. In case of a potential dike failure, to provide valuable information for the early warning and the emergency evacuation of people and properties under threat, accurate predictions of the breach formation and the breach flow discharge in the first three stages are vital. The duration of these three stages strongly affects the time people have for evacuation, thereby heavily impacting the magnitude of damage and losses caused by the dike failure. Furthermore, from the angle of gaining more insight into the physics of breach growth in dikes, Stages I, II and III are the most complicated and challenging stages and embody the main differences between clay-dikes and sand-dikes in the breach erosion mechanism.

# Chapter 5

## Mathematical model

### 5.1 Introduction

Based on the five-stage breach erosion process described in Chapter 4, a mathematical model for simulation of the breach growth in clay-dikes has been developed and is presented in this Chapter. The mathematical modeling of the breach development in Stages I, II and III is given in Sections 5.2 through 5.4, respectively. Section 5.5 deals with the process of breach enlargement in the dike crest in Stages I, II and III. The mathematical descriptions of further breach growth in Stages IV and V are presented in Sections 5.6 and 5.7, respectively. In Section 5.8 the input and output data of the model are outlined. Finally a discussion on the model is given in Section 5.9.

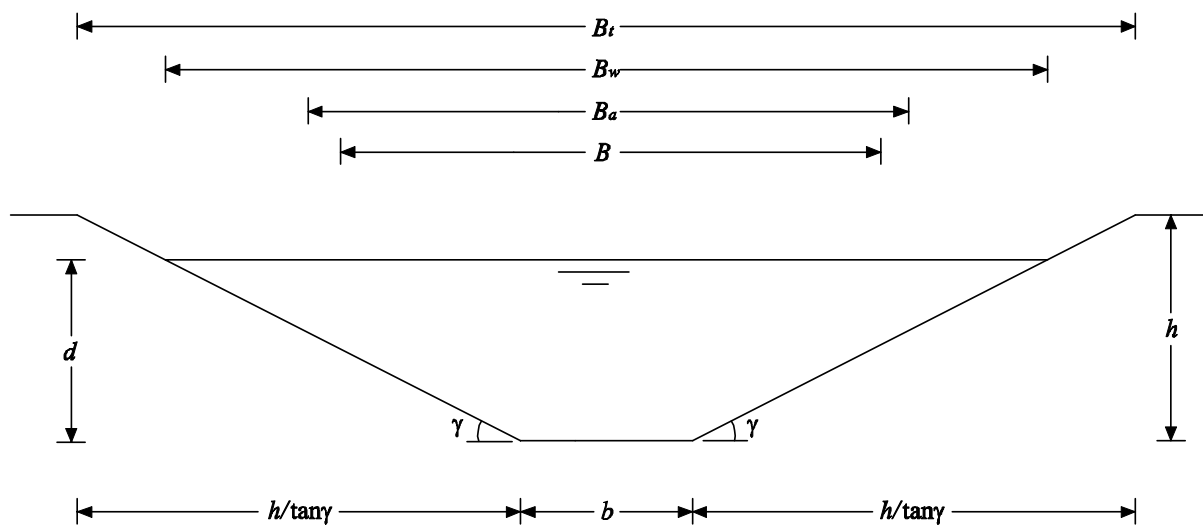


Figure 5.1 Cross-section of the initial breach in the dike crest (after Visser, 1998).

As stated in Chapter 4, it is the flow through an initial breach in the dike crest that starts the breach erosion process in the dike. The initial breach as shown in Figure 5.1, is assumed to have a trapezoidal cross-section with a side-slope angle  $\gamma$ ; a breach depth  $h$ , a water depth  $d$  in the breach, and a breach width  $b$  at the bottom (Visser, 1998). In Figure 5.1,  $B_t$  is the breach width at the dike crest,  $B_w$  is the breach width at the water surface,  $B_a$  is the averaged breach width over the breach depth  $h$ , and  $B$  is the averaged breach width over the water depth  $d$ . The equations for  $B_t$ ,  $B_w$ ,  $B_a$  and  $B$  are given respectively by:

$$B_t = b + 2h/\tan \gamma \quad (5.1)$$

$$B_w = b + 2d/\tan \gamma \quad (5.2)$$

$$B_a = b + h/\tan \gamma \quad (5.3)$$

$$B = b + d/\tan \gamma \quad (5.4)$$

The cross-section area  $A$  of the breach flow and the hydraulic radius  $R$  are read as

$$A = Bd \quad (5.5)$$

$$R = A/(b + 2d/\sin \gamma) \quad (5.6)$$

## 5.2 Breach development in Stage I

### 5.2.1 The breach flow

Stage I starts at  $t = t_0$  when flooding water of the river (or sea) flows through the initial breach in the dike crest and initiates erosion of the dike body. It is assumed that the breach acts as a broad-crested weir during the erosion process and therefore the discharge  $Q_{br}$  through the breach is calculated by:

$$Q_{br} = m \left( \frac{2}{3} \right)^{3/2} \sqrt{g} B (H_w - Z_{br})^{3/2} \quad (5.7)$$

in which  $m$  is the discharge coefficient ( $m \approx 1$ , see Visser, 1998),  $g$  is the gravity acceleration,  $H_w$  is the outer water level (water level of the river or sea), and  $Z_{br}$  is the height of the breach bottom (see Figure 5.2). Both  $H_w$  and  $Z_{br}$  are measured above one reference level  $Z = 0$ . Equation (5.7) applies not only to Stage I, but also to Stages II, III and IV.

Due to the large steepness of the inner slope of the dike, the flow over this slope is supercritical. The flow accelerates from  $x = 0$  ( $x$  is the coordinate along the inner

slope, see Figure 5.2, see also Chapter 4) at the crest to  $x = l_n$  where it reaches the normal flow velocity, if the slope is long enough to permit this (i.e.  $L > l_n$ , see Figure 5.2). Beyond  $x = l_n$  the breach flow remains uniform with its velocity and water depth being the normal values. The adaptation length  $l_n$  can be approximated with the following expression

$$l_n = \frac{2.5(Fr_n^2 - 1)d_n}{\tan \beta} \quad (5.8)$$

in which  $\beta$  is the inclination angle of the inner slope of the dike,  $d_n$  is the normal water depth on that slope and  $Fr_n$  is the Froude number at  $x = l_n$  (see Visser, 1998).  $Fr_n$  is given by

$$Fr_n^2 = \frac{U_n^2 (B_w)_n}{gd_n B_n \cos \beta} \quad (5.9)$$

in which  $U_n$  is the cross-sectional averaged normal flow velocity and the subscript '*n*' refers to the normal flow condition.

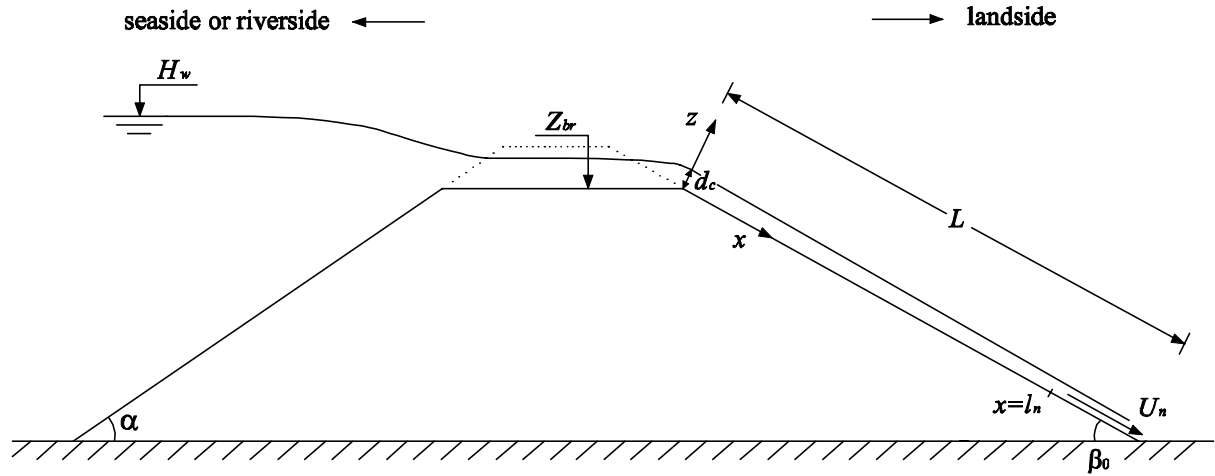


Figure 5.2 The breach flow on the inner slope of the dike in Stage I.

$U_n$  and  $d_n$  respectively are calculated as

$$U_n = C\sqrt{R_n \sin \beta} \quad \text{for } x \geq l_n \quad (5.10)$$

$$d_n = Q_{br} / (U_n B_n) \quad \text{for } x \geq l_n \quad (5.11)$$

in which  $C$  is the Chézy coefficient that can be calculated from the Manning Formula:

$$C = \frac{1}{n} R_n^{1/6} \quad (5.12)$$

in which  $n$  is Manning's roughness coefficient.

For the water depth  $d$  on the inner slope of the dike when  $0 \leq x < l_n$ , the following approximation was proposed by Visser (1998):

$$d \approx d_n + (d_c - d_n)e^{-5x/l_n} \quad \text{for } 0 \leq x < l_n \quad (5.13)$$

in which  $d_c$  is the critical water depth at  $x = 0$  on the inner slope. The equation for  $d_c$  is given by

$$d_c^3 = \frac{Q_{br}^2 (B_w)_c}{gB_c^3 \cdot \cos \beta} \quad (5.14)$$

in which the subscript 'c' refers to the critical flow condition.

### 5.2.2 Breach erosion in Stage I

As introduced in Section 4.4, in Stage I breach erosion occurs along the inner slope and, depending on the flow velocity, possibly also along the dike crest. Along the inner slope, two types of erosion might occur in Stage I, i.e. the breach flow shear erosion and the small-scale headcut erosion (see Chapter 4 and Zhu et al., 2005b). The random characteristics of these small-scale headcuts, including their dimensions, number, location and manner of appearance, however, bring large complexities and uncertainties to the breach erosion process in Stage I along the inner slope of the dike, hence make the mathematical modeling very difficult. Considering the relatively short duration of Stage I, in which only a relatively small flow rate occurs, and to avoid a very complicated model, the actual non-plane inner slope (with small-scale headcuts here and there on, see Figure 5.3) is simplified as a plane throughout Stage I. The possible small-scale headcut erosion is not treated in the present mathematical model.

For the flow erosion along the crest and inner slope of the dike in Stage I, the frequently used excess shear stress equation (Equation (3.18)) for the rate of cohesive soil erosion is applied:

$$E = M_e (\tau_b - \tau_c) \quad (3.18, 5.15)$$

The breach flow bed shear stress  $\tau_b$  in Equations (5.15) is calculated by

$$\tau_b = \frac{1}{C^2} \rho g U^2 \quad (5.16)$$

in which  $C$  is the Chézy coefficient,  $\rho$  is the water density and  $U$  is the cross-sectional averaged flow velocity.

If  $L \geq l_n$ ,  $\tau_b$  at  $x \geq l_n$  can also be calculated by

$$\tau_b = \rho g R \sin \beta \quad (5.17)$$

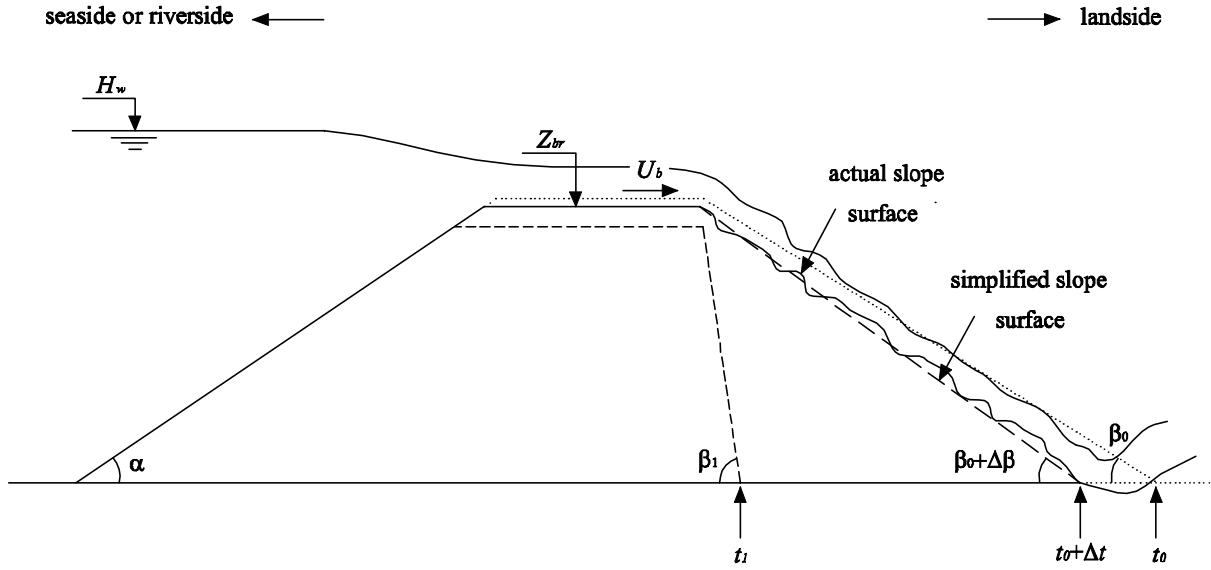


Figure 5.3 Simplification of the non-plane inner slope of the dike in Stage I.

### 5.2.3 Steepening of dike inner slope in Stage I

#### *No erosion occurring at dike crest*

In Stage I, provided that the breach flow velocity at the dike crest is not sufficiently large to erode soil material away from the dike, or the erosion rate at the dike crest is too small compared with that near the toe of the inner slope of the dike and can therefore be ignored, only the erosion occurring along the inner slope will be modeled.

As described in Chapter 4, when no erosion occurs at the dike crest in Stage I, the erosion along the inner slope is completely determined by the erosion close to the toe of the dike, i.e.  $x = x_E = l_n$  if  $l_n \leq L$ , or  $x = x_E = L$  if  $l_n > L$ . Due to the larger erosion rate at  $x = x_E$  than at the upper part of the inner slope, the slope becomes steeper and steeper in time and accordingly the slope angle increases from an initial value  $\beta_0$  at  $t = t_0$  to a critical value  $\beta_1$  at  $t = t_1$  (see Figure 5.4). Within one time step  $dt$  the increase of the slope angle  $d\beta$  is calculated as:

$$d\beta = \frac{E_1}{x_E} dt \quad (5.18)$$

in which  $E_1$  is the erosion rate at  $x = x_E$ ;  $x_E = l_n$  if  $l_n \leq L$ ,  $x_E = L$  if  $l_n > L$ .

Integration of Equation (5.18) between  $t_0$  and  $t_1$  gives

$$\beta_1 - \beta_0 = \int_{t_0}^{t_1} \frac{E_1}{x_E} dt \quad (5.19)$$

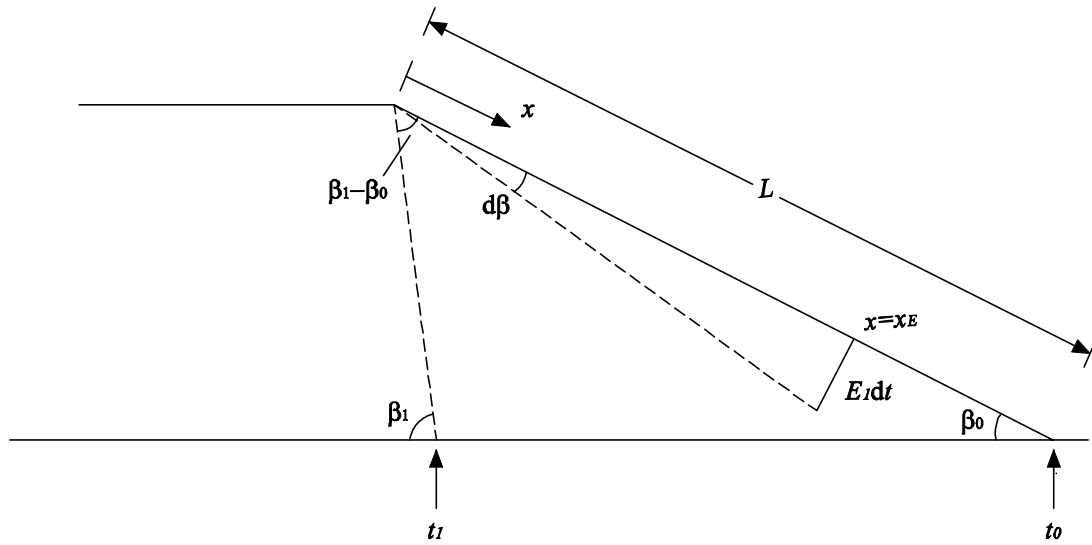


Figure 5.4 Steepening of dike inner slope in Stage I when no erosion occurs over dike crest.

### *Erosion occurring also at dike crest*

In case the breach flow velocity at the dike crest is sufficiently large and causes considerable erosion there in Stage I, the erosion occurring both at the crest and along the inner slope of the dike need to be taken into account in the model.

The flow shear erosion at the dike crest enlarges the breach cross-sectional area and lowers the height of the dike body in the breach by eroding away soil material from the breach boundary. The breach flow and the erosion rate increase in time accordingly. The lowering in time of the dike body in the breach is described by (see Figure 5.5)

$$dZ_{br} = -E_0 dt \quad (5.20)$$

in which  $E_0$  is the flow erosion rate at the dike crest, and the minus sign indicates that the height of the dike body is decreasing in time.

Along with the erosion occurring at the dike crest and along the inner slope, the width of the dike crest  $W$  (i.e. the length of the breach in the dike crest) also changes in time in Stage I (see Figure 5.5). This can be calculated as

$$dW = E_0 dt \left( \frac{1}{\tan \alpha} + \frac{1}{\tan \beta} \right) - (E_0 dt) \tan \beta \quad (5.21)$$

in which  $\alpha$  is the inclination angle of the outer slope of the dike.

The increase of the gradient of the inner slope of the dike within one time step  $dt$  is (see Figure 5.6):

$$d\beta = \frac{(E_1 - E_0/\cos\beta) dt}{x_E} \tag{5.22}$$

It is clear that Equation (5.18) is a special case of Equation (5.22) when the erosion rate at the dike crest becomes zero.

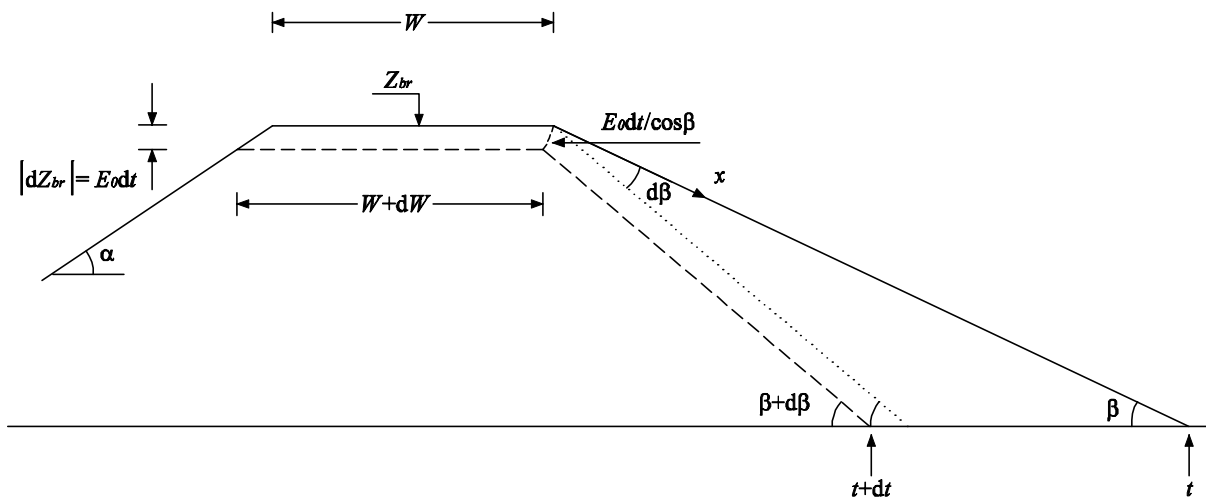


Figure 5.5 Lowering of the dike body in Stage I when erosion takes places at dike crest.

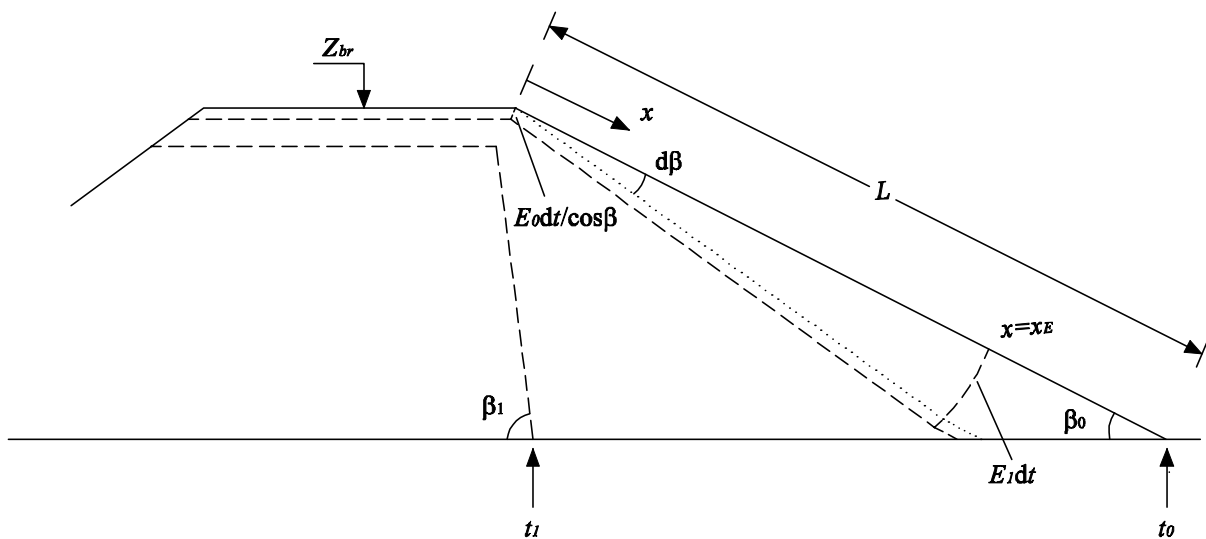


Figure 5.6 Steepening of dike inner slope in Stage I when erosion occurs also at dike crest.

The breach enlargement at the dike crest in Stage I (and the following Stages II and III) is described in Sections 4.7 and 5.5. Although the flow shear erosion deepens the breach in the dike crest, it is very likely that the breach width  $B_t$  remains unchanged in Stage I.

At  $t = t_i$  the gradient of the inner slope of the dike has reached the critical angle  $\beta_i$ , see Figures 5.4 and 5.6, and then Stage I ends.

Visser (1998) assumed  $\beta_i$  to be equal to the sand internal friction angle ( $\phi$ ) in his sand-dike breach model. For clay-dikes here, due to the considerable cohesion among cohesive soil particles,  $\beta_i$  is believed to be much larger than  $\phi$ . This was already observed in many experiments, e.g. the HERU large-scale embankment overtopping tests (see e.g. Hahn et al., 2000) and the Nordland field embankment breaching test in Norway (see Vaskinn et al., 2004).

$\beta_i$  is dependent on the soil properties and seems to increase with an increasing soil cohesion  $c$  and an increasing internal friction angle  $\phi$ . Unfortunately for the time being insufficient data is available to quantify the dependence of  $\beta_i$  on  $c$  and  $\phi$ . In the present model  $\beta_i$  is simply assumed to be in the range of  $80^\circ \sim 90^\circ$ .

## 5.3 Breach development in Stage II

### 5.3.1 Introduction

As described in Chapter 4, after reaching the critical slope angle  $\beta_i$  at  $t = t_i$ , the steepened inner slope of the dike acts as a headcut in the following Stages II and III due to its large steepness. Because of the high complexities involved in the erosion of multi-step headcuts, only the erosion at single-step headcuts during dike breaching with either erodible or non-erodible foundation is mathematically modeled in this section.

In general, four types of erosion may occur at a headcut in Stage II (and the successive Stage III), as shown in Figures 4.9 and 4.10. Considering the very steep slope of the headcut and the increasing breach flow during the process of breach growth, it is most likely that the breach flow flees away from the headcut at the headcut brink in most of Stages II and III. In addition, the flow erosion along the headcut slope and the fluidization of the slope surface due to the diffused falling water is discontinuous with also large uncertainties involved. Quantitative consideration of the erosion along the headcut slope surface in Stages II and III is therefore difficult and not included in the present model.

### 5.3.2 Trajectory of impinging jet of the breach flow

When the breach flow impinges on the dike foundation, the trajectory of the flow nappe can be interpreted by use of the principle of projectile (see Figure 5.7, see also Zhu et al., 2004a):

$$x'^2 = \frac{2U_b^2}{g} y' \quad (5.23)$$

in which  $x'$  and  $y'$  represent the horizontal and vertical positions of the trajectory, respectively, both originating from the middle of the approaching breach flow at the headcut brink;  $U_b$  is the approaching flow velocity at the headcut brink and is given by

$$U_b = \frac{Q_{br}}{Bd_b} \quad (5.24)$$

in which  $Q_{br}$  is still described by Equation (5.7);  $d_b$  is the water depth at the headcut brink and reads

$$d_b^3 = \frac{Q_{br}^2 B_w}{gB^3} \quad (5.25)$$

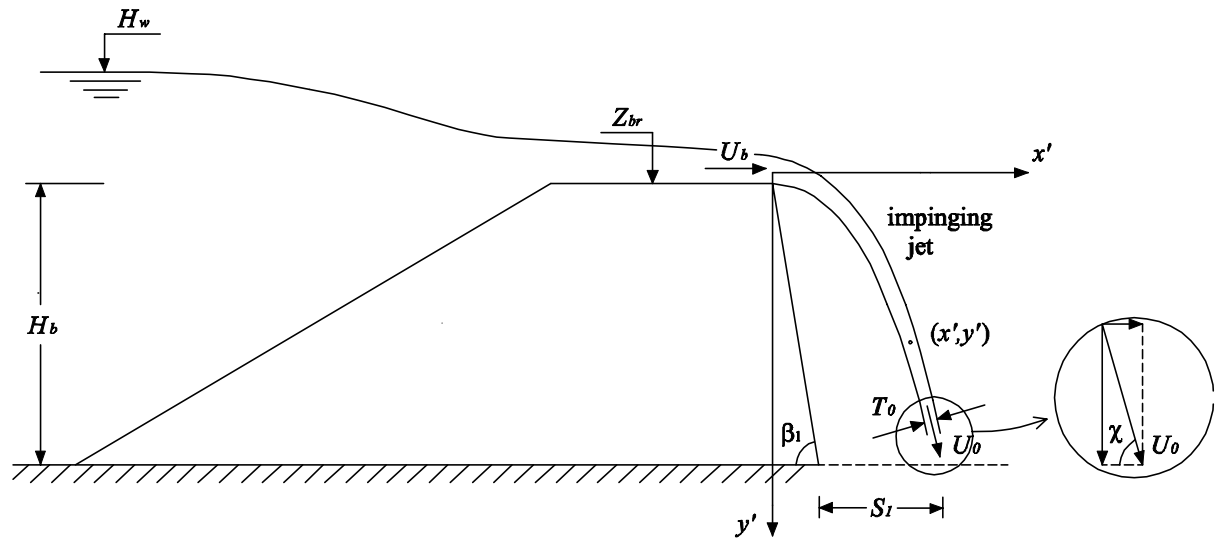


Figure 5.7 Trajectory of the impinging jet in Stage II.

At the jet action point on the dike foundation (or the entry point into the inner water), the equation for the jet velocity  $U_0$  is

$$U_0 = \sqrt{U_b^2 + 2g(H_b + d_b/2 - h_p)} \quad (5.26)$$

in which  $h_p$  is the inner water depth above the original dike foundation and  $H_b$  is the height of the headcut (or of the breach bottom) above the original dike foundation.

The thickness of the impinging jet at the action (entry) point, i.e.  $T_0$  in Figure 5.7, is then calculated as

$$T_0 = \frac{Q_{br}}{U_0 B} \quad (5.27)$$

The jet flow impinges on the dike foundation at an angle  $\chi$  which is given by

$$\tan \chi = \frac{\sqrt{2g(H_b + d_b/2 - h_p)}}{U_b} \quad (5.28)$$

The horizontal distance  $S_1$  between the toe of the headcut and the jet action point on the dike foundation is

$$S_1 = U_b \sqrt{2(H_b + d_b/2)/g} - H_b/\tan \beta_1 \quad (5.29)$$

### 5.3.3 Jet scour of dike foundation and headcut undermining

The plane jet produced by the free falling breach flow impinges on the downstream dike foundation (or the plunge pool) and imposes considerable erosive forces on both the dike foundation and the toe of the headcut. Depending on the erodibility of the dike foundation, two different methods can generally be used to calculate the scour (if any) of the dike foundation and the headcut undermining (see Zhu et al., 2005a and 2006b).

#### *Erodible dike foundation*

When the dike foundation is erodible, the impinging jet produces a scour hole in the foundation. This scour hole is gradually enlarged in time both vertically and horizontally, undermining the headcut from a certain moment on.

The analytical expression of Stein et al. (1993) is adopted in the model to calculate the development of the scour hole (Zhu et al., 2005a and 2006b). Figure 5.8 is an illustration of the jet scour downstream of a headcut with erodible foundation. The jet enters the plunge pool and diffuses throughout the surrounding water decreasing in velocity. The zone in which the jet centerline velocity remains constant at  $U_0$  defines the potential core, with a length of  $J_p$  from the jet entry point (Stein et al., 1993). Beyond  $J_p$ , the jet velocity decreases due to diffusion. In the region close to the bottom of the scour hole the jet is deflected, causing curving of the streamlines (Beltaos and Rajaratnam, 1973; Beltaos, 1976).

The maximum shear stress  $\tau_j$  acting on the bed in the impingement region is calculated by Stein et al. (1993) as follows:

$$\tau_j = C_f \rho U_0^2 \quad J \leq J_p \quad (5.30)$$

$$\tau_j = C_d^2 C_f \rho U_0^2 \frac{T_0}{J} \quad J > J_p \quad (5.31)$$

in which  $J$  is the distance from the jet entry point along the centerline,  $C_d$  is a diffusion constant.  $C_d \approx 2.28$  is suggested by Albertson et al. (1950) and 2.72 by Beltaos (1976). Stein et al. (1993) assumed  $C_d = 2.60$  in their development, and this value is followed in the present study.  $C_f$  is a friction coefficient and is determined from a Blasius flow assumption (see Stein et al., 1993):

$$C_f = (0.22/8) (q/\nu)^{-0.25} \quad (5.32)$$

in which  $q$  is the unit discharge,  $\nu$  is the kinematic viscosity and  $q/\nu$  is the Reynolds number.

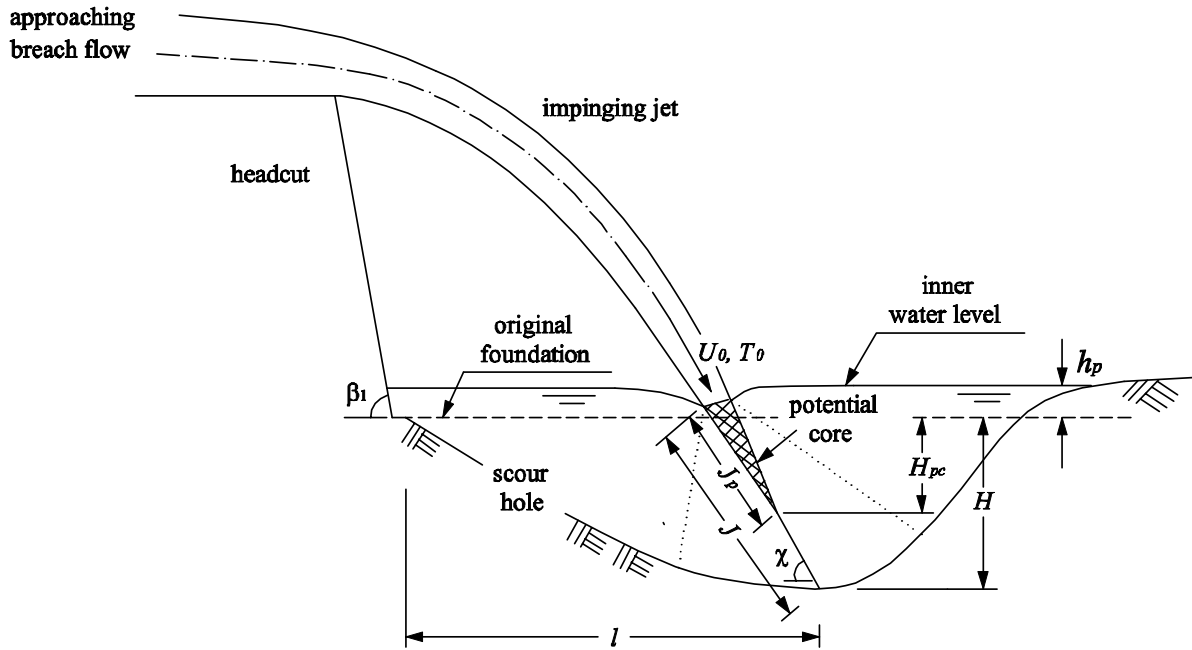


Figure 5.8 Illustration of jet scour downstream of a headcut with erodible foundation (modified after Stein et al., 1993).

The scour depth  $H$  in the dike foundation is found to have a relation with  $J$  and  $\chi$  as follows

$$H = J \sin \chi - h_p \quad (5.33)$$

The soil erosion rate  $E$  (length/time) at the point of maximum scour can be determined in a form similar to Equation (5.15) as follows:

$$E = \frac{dH}{dt} = M_{ef} (\tau_j - \tau_c)^\zeta \quad (5.34)$$

in which  $\zeta$  is an experimentally determined constant. Stein et al. (1993) derived that  $\zeta = 1.5$  for non-cohesive soil detachment and  $\zeta = 1.0$  for cohesive soil detachment.  $M_{ef}$  is a material dependent factor describing the erodibility of the erodible dike foundation.  $\tau_c$  is the critical shear stress for erosion of the foundation. Within the potential core, by combining Equations (5.30) and (5.34), the increase of the scour depth in time is given by

$$\frac{dH}{dt} = M_{ef} (C_f \rho U_0^2 - \tau_c)^\zeta \quad \text{for } H \leq H_{pc} \quad (5.35)$$

in which  $H_{pc}$  is the depth of the potential core and is expressed as

$$H_{pc} = C_d^2 T_0 \sin \chi - h_p \quad (5.36)$$

It can be indicated from Equation (5.35) that the scour depth increases linearly in time as long as the scour is within the potential core.

Beyond the potential core, the scour depth increase is described by a non-linear ordinary differential equation (Stein et al., 1993):

$$\frac{dH}{dt} = M_{ef} \left[ \frac{C_f \rho U_0^2 (H_{pc} + h_p)}{H + h_p} - \tau_c \right]^\zeta \quad \text{for } H > H_{pc} \quad (5.37)$$

### ***Non-erodible dike foundation***

In case of a non-erodible dike foundation, the breach flow falling jet impinges on the dike foundation and is deflected and bifurcated into two branches, of which one rushes towards the headcut and exerts considerable erosive forces on the toe of the headcut (see Figure 5.9). The hydraulic shear stress  $\tau_b$  near the toe of the headcut is calculated through the formula of Robinson (1992), see also Section 2.5 and Zhu et al. (2005a and 2006b):

$$\pi_1 = 0.025 \pi_2^{-1.295} \pi_3^{0.026} \pi_4^{0.221} \pi_5^{-1.062} \quad (5.38)$$

in which:

$$\pi_1 = \tau_b / (\rho g d_b) \quad (5.39)$$

$$\pi_2 = q^2 / (g d_b^3) \quad (5.40)$$

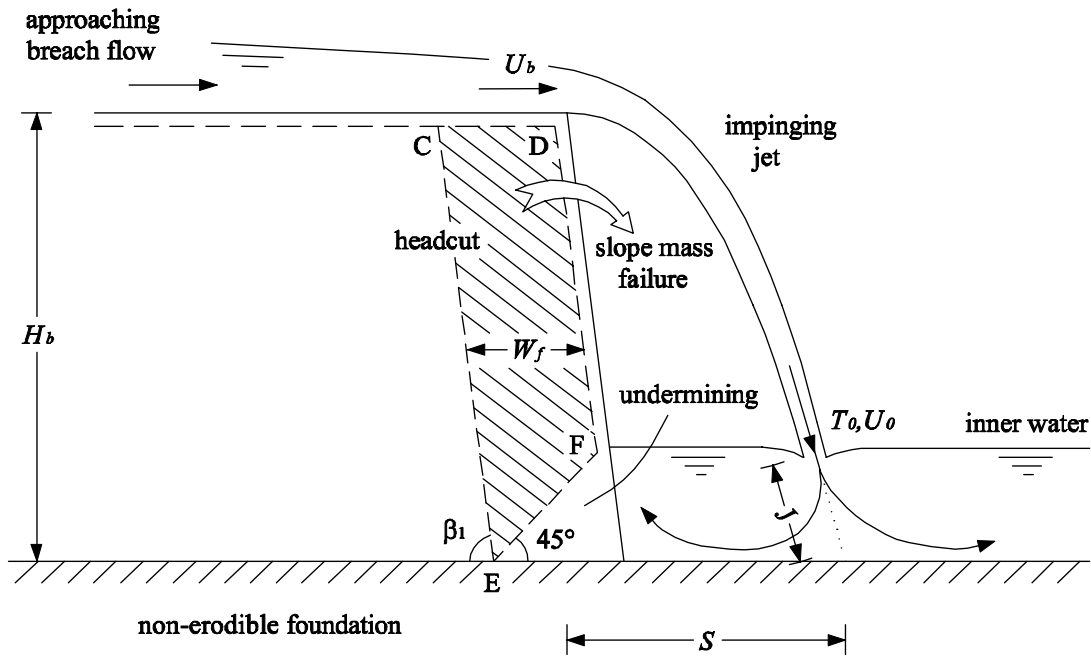


Figure 5.9 Sketch of jet impinging on a non-erodible dike foundation.

$$\pi_3 = H_b/d_b \quad (5.41)$$

$$\pi_4 = h_p/d_b \quad (5.42)$$

$$\pi_5 = X_p/d_b \quad (5.43)$$

in which  $\pi_1$ ,  $\pi_2$ ,  $\pi_3$ ,  $\pi_4$  and  $\pi_5$  are non-dimensional variables;  $X_p$  is given by

$$X_p = S - 0.154 \cdot J \cdot \cot(\chi) - T_o/2 \quad (5.44)$$

in which  $S$  is the horizontal distance between the headcut brink and the jet action point onto the dike foundation (m), see Figure 5.9.

The resulting erosion which undermines the headcut is then given by Equation (5.15).

For both erodible and non-erodible dike foundation, when the headcut undermining develops to a certain critical degree, the headcut loses stability and slope mass failure occurs under the action of gravity and seepage forces (Chapter 4, see also Zhu et al., 2005a and 2006a).

Based on observations of dike breaching in laboratory experiments (e.g. the DUT tests) and for the sake of simplicity, the upper surface of the headcut undermining EF is simplified as a plane with a slope angle  $45^\circ$  to the horizontal plane (see Figures 5.9 and 5.10). The upstream boundary of the scour hole is also assumed to be a plane with slope  $1/m_f$  (see Figure 5.10), in which  $m_f$  is a constant. Based on experiments on

headcut erosion (e.g. Stein et al., 1993 and Bennett et al., 2000a),  $m_f$  is often found in the range of 1.0~4.0, depending on the soil properties and flow conditions.

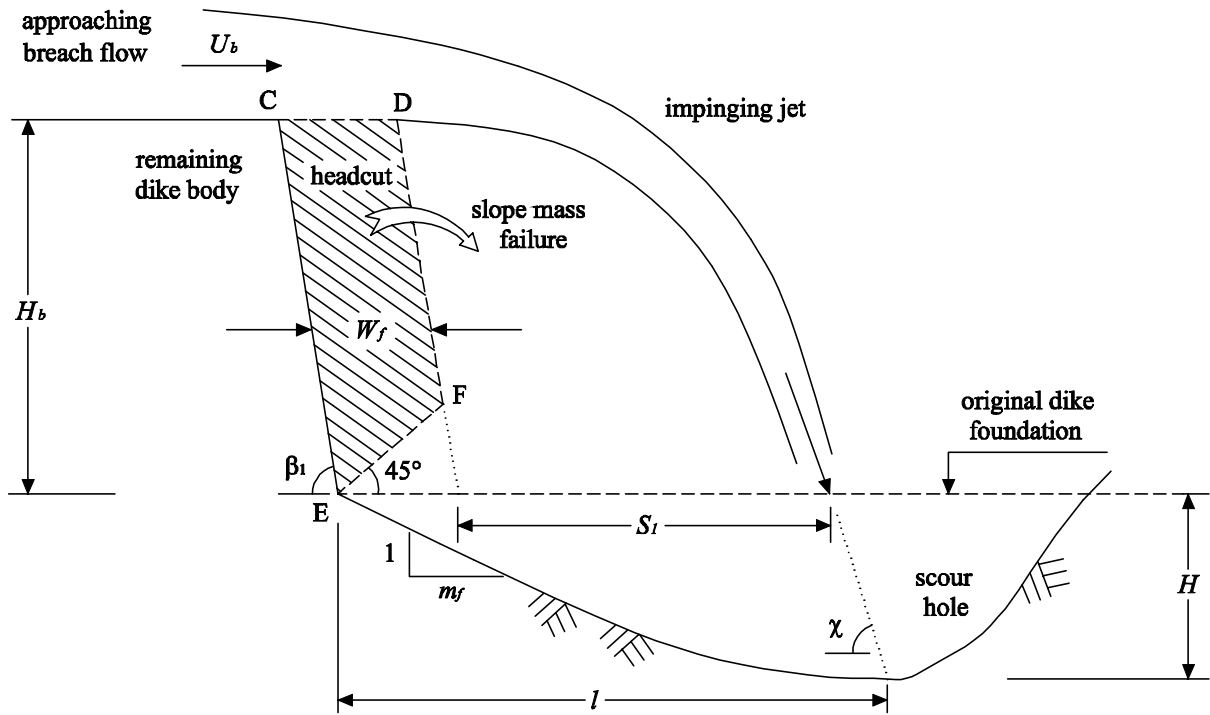


Figure 5.10 Sketch definition of scour hole dimensions.

### 5.3.4 Slope instability

The failure block CDFE from the headcut is assumed to fail by overturn around point E or line EE' (see Figure 5.11, and Figures 5.9 and 5.10). Figure 5.11 shows the various forces acting on the block. AB is the phreatic line, by which the block is divided into two parts, CDBA and ABFE, with weights of  $G_1$  and  $G_2$ , respectively. The influence of seepage on the headcut instability is embodied by  $P_3$ , which is the pore water pressure acting on the plane of AE.  $P_1$  and  $P_2$  are the weight and shear force of the breach flow acting on the block top, respectively;  $N$  is the soil interactional force between the failure block and the new headcut face; and  $F_{c,f}$  is the soil interactional force acting on the two lateral surfaces of the block. The forces imposed by the inner water are generally relatively small and therefore neglected here.

The equations for  $P_1$ ,  $P_2$  and  $P_3$  read, respectively

$$P_1 = \rho g d_b W_f b \quad (5.45)$$

$$P_2 = \tau_b W_f b \quad (5.46)$$

$$P_3 = \frac{1}{2} \rho g b (\overline{AE})^2 \quad (5.47)$$

in which  $\tau_b$  is the breach flow shear stress acting on the top of the failure block,  $W_f$  is the width of the block, and  $\overline{AE}$  is the length of the line AE.

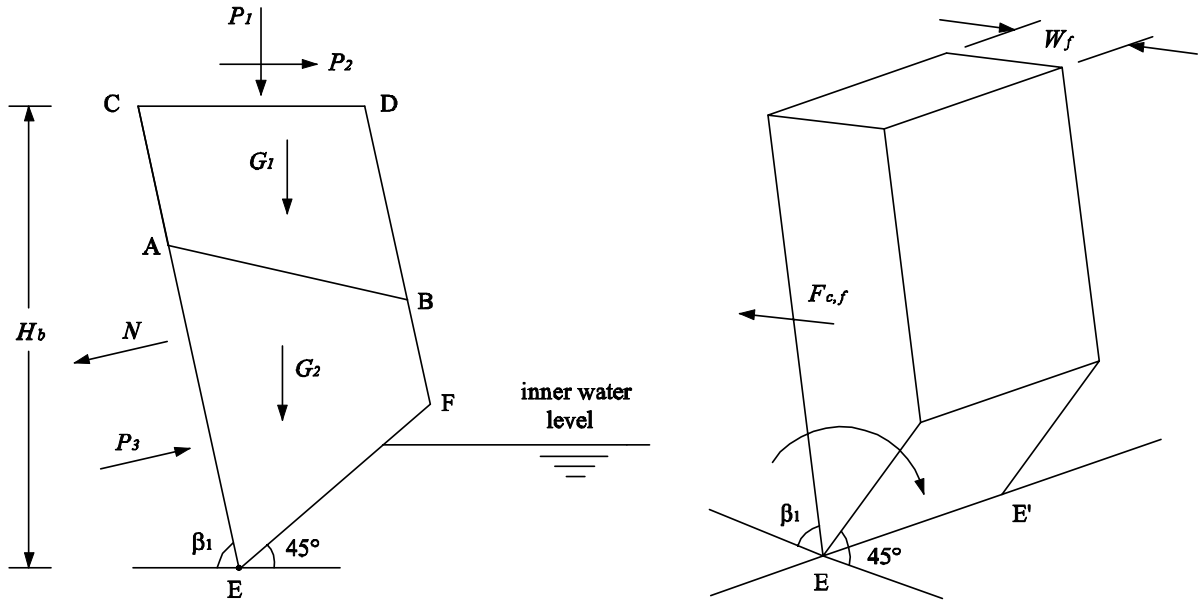


Figure 5.11 Sketch of forces acting on the block of slope mass failure in Stage II.

The soil interactional forces  $F_{c,f}$  and  $N$  are calculated as, respectively

$$F_{c,f} = A' \tau_s = \tau_s \left( \frac{H_b}{\sin \beta_1} - \frac{\sqrt{2} W_f}{4 \sin(135^\circ - \beta_1)} \right) W_f \sin \beta_1 \quad (5.48)$$

$$N = \frac{H_b}{\sin \beta_1} \cdot b \cdot \tau_t \quad (5.49)$$

in which  $A'$  is the area of the lateral surface of the failure block,  $\tau_s$  is the soil shear strength and  $\tau_t$  the soil tensile strength.

The block weights  $G_1$  and  $G_2$  are calculated as, respectively

$$G_1 = \rho_s g A_1 b \quad (5.50)$$

$$G_2 = \rho_{sat} g b (A' - A_1) \quad (5.51)$$

in which  $A_l$  is the area of the lateral surface of the block ACDB, and  $\rho_{sat}$  is the soil saturated density.

The driving forces of the headcut slope instability are  $P_1$ ,  $P_2$ ,  $P_3$ ,  $G_1$  and  $G_2$ , and the resisting forces include  $N$  and  $F_{c,f}$ . Among the various forces,  $P_1$ ,  $P_2$ ,  $P_3$ ,  $F_{c,f}$ ,  $G_1$  and  $G_2$  are functions of  $W_f$  (Zhu et al., 2005a and 2006a). In the critical status of failure occurrence, the moment of the driving forces equals that of the resisting forces, i.e.

$$f(W_f) = P_1 d_{P1} + P_2 d_{P2} + P_3 d_{P3} - 2F_{c,f} d_{c,f} + G_1 d_{G1} + G_2 d_{G2} - N d_N = 0 \quad (5.52)$$

in which  $d_{P1}$ ,  $d_{P2}$ ,  $d_{P3}$ ,  $d_{c,f}$ ,  $d_{G1}$ ,  $d_{G2}$  and  $d_N$  are the force arms to point E (or line EE') of  $P_1$ ,  $P_2$ ,  $P_3$ ,  $F_{c,f}$ ,  $G_1$ ,  $G_2$  and  $N$ , respectively.

After occurrence of the slope mass failure, the headcut retreats a distance  $W_f$ , and subsequently the jet relocates its entry point to the plunge pool and starts a new cycle of erosion in Stage II as shown in Figures 4.11 and 4.12 in Chapter 4. However, it is not necessary that  $W_f$  remains constant for different slope mass failures.

The height of the dike in the breach ( $H_b$ ) decreases in time in Stage II (and in the following Stage III) due to the flow shear erosion at the top of the headcut, which is described by Equation (5.15):

$$E = M_e(\tau_b - \tau_c) \quad (5.15)$$

The lowering of the dike height in one time step  $dt$  is then given by

$$dZ_{br} = -Edt \quad (5.53)$$

Accordingly, the width of the dike crest ( $W$ ) increases in time and is given by

$$dW = Edt \left( \frac{1}{\tan \alpha} + \frac{1}{\tan \beta_1} \right) \quad (5.54)$$

However, after each occurrence of the slope mass failure (at time  $t$ ),  $W$  is reduced by a width of  $W_f$  instantaneously:

$$W(t_+) = W(t_-) - W_f \quad (5.55)$$

Stage II ends at  $t = t_2$  when the headcut move backwards to the outer slope of the dike and the dike crest in the breach vanishes.

It should be mentioned here that a larger breach flow rate does not necessarily cause a quicker headcut retreat, because a larger flow rate leads to the jet scour fleeing further away from the headcut.

### 5.4 Breach development in Stage III

Stage III starts when the dike crest in the breach has vanished at  $t = t_2$  and the remaining dike body becomes triangular-shaped. Under the action of the breach flow, the thin tip of the dike body can hardly stand the water forces. It is washed (pushed) away very quickly down to a certain height (see Figure 5.12), resulting in a momentary breach enlargement and a flow rate increase.

The mechanism of this sudden pushing away is that of the driving forces acting on the failed triangle ABH by the breach flow exceeding the resisting forces acting on the failure plane AB (see Figure 5.12). However, the driving forces are composed of not only hydrostatic but also hydrodynamic water forces. Accurate calculation of the hydrodynamic water forces in such a case is not possible, therefore the height  $\Delta H$  of the pushed away dike tip cannot be accurately determined.

Similar to the mechanism of breach erosion in Stage II, the flow shear erosion at the breach bottom lowers the height of the dike in the breach and the discharge through the breach increases accordingly in Stage III. At the same time, the breach flow jet scour of the downstream dike foundation enlarges the scour hole (if any) and undermines the headcut bit by bit, leading to soil mechanical instability of the headcut at a certain moment, as shown in Figure 5.13 for dikes with erodible foundation. The unstable block CDFE is assumed to fail by overturn around point E (or line EE', see Figure 5.14).

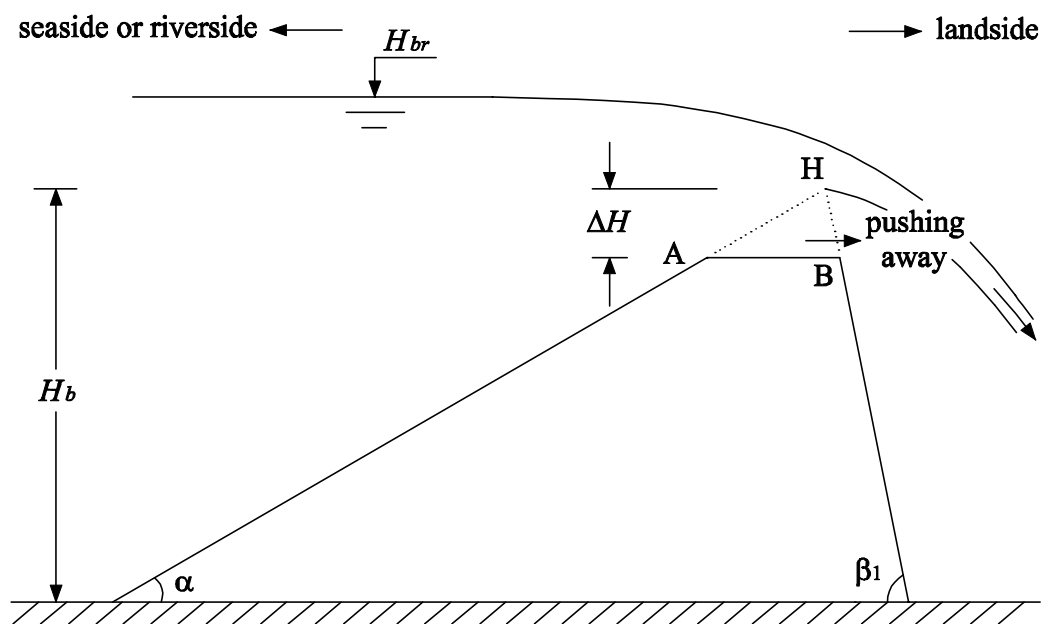


Figure 5.12 The quickly pushing away of the thin tip of the remaining dike body at  $t = t_2$ .

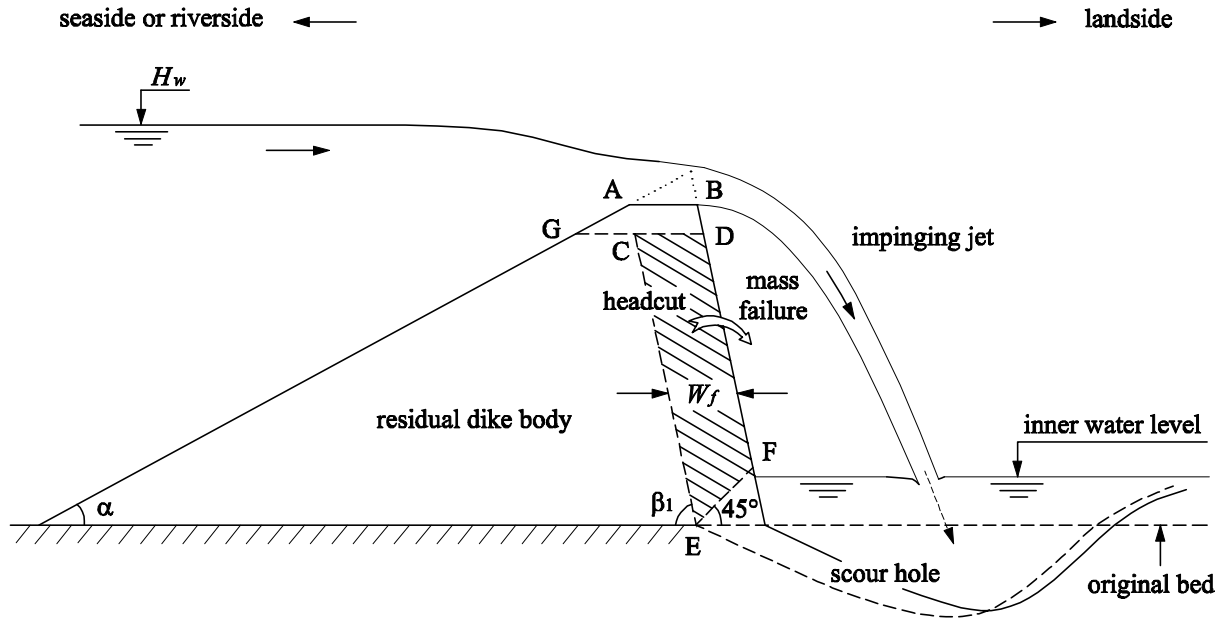


Figure 5.13 The breach erosion in Stage III when dike foundation is erodible.

Figure 5.14 shows the various forces acting on the failure block in Stage III. The forces are about the same as those shown in Figure 5.11 for Stage II, except that in Stage III the block is almost entirely below the phreatic line, the weight of the block is therefore calculated completely with  $\rho_{sat}$  and  $P_3$  acts on the whole plane of CE.

$P_1$ ,  $P_2$ ,  $F_{c,f}$  and  $N$  are given by Equations (5.45), (5.46), (5.48) and (5.49), respectively. The equations for  $P_3$  and  $G$  read, respectively

$$P_3 = \frac{1}{2} \rho g b \left( \frac{H_b}{\sin \beta_1} \right)^2 \quad (5.56)$$

$$G = \rho_{sat} g A' b \quad (5.57)$$

At the time of slope mass failure occurrence, the moment equilibrium equation for the block CDFE is written as

$$f(W_f) = P_1 d_{P1} + P_2 d_{P2} + P_3 d_{P3} - 2F_{c,f} d_{c,f} + G d_G - N d_N = 0 \quad (5.58)$$

in which  $d_G$  is the force arm of  $G$  to point E (or line EE').

Every time after the slope mass failure, the headcut retreats a distance of  $W_f$ , and subsequently the jet flow relocates its entry point to the plunge pool, starting a new cycle of breach erosion in Stage III. Stage III ends at  $t = t_3$  when the dike body in the breach is washed out down to the dike foundation or to the toe protection (if any) of the outer slope of the dike.

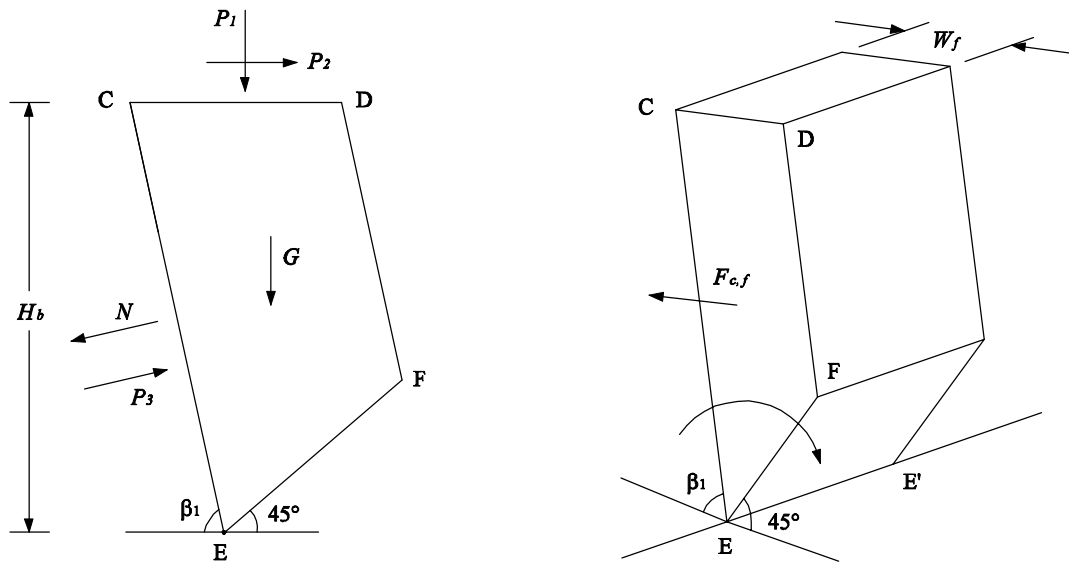


Figure 5.14 Schematic illustration of the forces acting on the failure block in Stage III.

## 5.5 Breach enlargement in the dike crest in Stages I, II and III

In Stages I, II and III of the process of breach growth, the initial breach in the dike crest is enlarged owing to erosion by flow, consequently the gradient of the breach side-slopes increases (see Figure 4.15 or Figure 5.15). The formula for the angle increase  $d\gamma$  in one time step  $dt$  is expressed as

$$\cot(d\gamma) = \tan \gamma + \frac{2h}{E_{bo} \cdot \sin 2\gamma \cdot dt} \quad (5.59)$$

in which  $E_{bo}$  is the rate of flow shear erosion in vertical direction at the breach bottom.  $E_{bo}$  is given by

$$E_{bo} = M_e(\tau_b - \tau_c) \quad (5.60)$$

Before the breach side-slopes reach  $\beta_1$  (see Figure 5.15a), the width of the breach at the dike top ( $B_t$ ) does not increase due to the erosion. In Figure 5.15b,  $\Delta Z_{br}'$  represents the depth required to erode down at the breach bottom to reach  $\beta_1$  along the whole breach side-slopes. It is given by

$$\Delta Z_{br}' = \frac{h \sin(\beta_1 - \gamma)}{\sin \gamma \cos \beta_1} \quad (5.61)$$

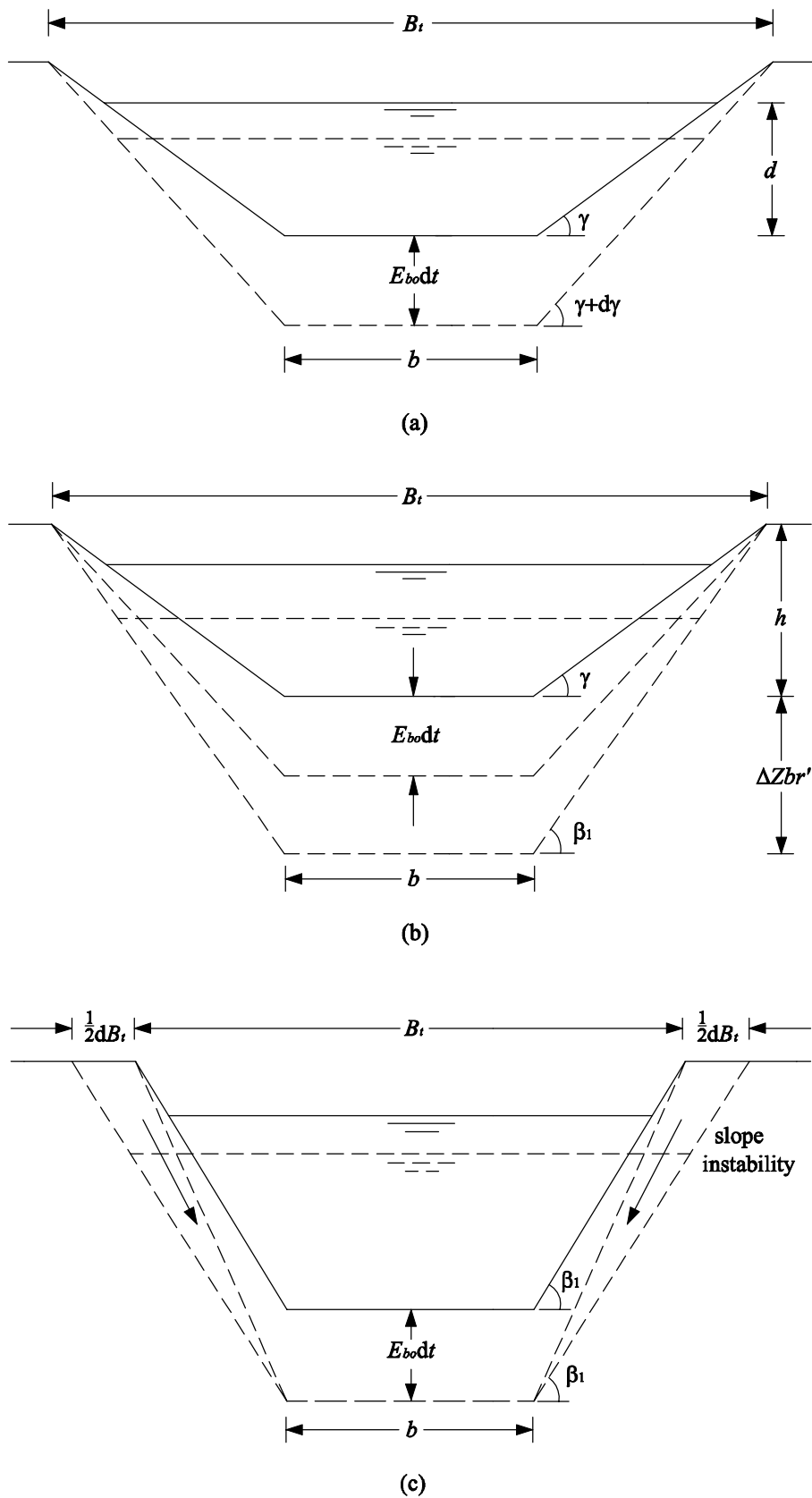


Figure 5.15 Breach Enlargement in the dike crest in Stages I, II and III: (a) steepening of breach side-slopes; (b) reaching of  $\beta_1$  by breach side-slopes; (c) breach enlargement after  $\beta_1$  is reached.

Any further erosion from then on at the breach bottom engenders over-steep breach side-slopes and induces increase of the breach width by means of slope instability (see Figure 5.15c). The occurrence of the instability of the breach side-slopes is assumed to be very quickly and the failed soil material is swept downstream away rapidly by the breach flow. No hindering effect has therefore been caused by the failure material on the successive breach erosion process. Hence, when all comes to all, the increase of the breach width is fully dependent on the rate of flow shear erosion at the breach bottom (i.e.  $E_{bo}$  in Figure 5.15), but has nothing to do with the time and frequency of the occurrence of the side-slope instability. In other words, it is not necessary to quantitatively investigate the criterion for the occurrence of the breach side-slope instability. The discrete breach width increase is then represented by a continuous curve in the mathematical model:

$$\frac{dB_t}{dt} = \frac{2E_{bo}}{\tan \beta_1} \quad (5.62)$$

## 5.6 Breach development in Stage IV

After the complete wash out of the dike body in the breach at  $t = t_3$ , depending on the geometrical and material conditions of the dike, three types of breach (Types A, B and C) have been distinguished for the continuation of breach growth in Stages IV and V, see Chapter 4 or Visser (1998).

### 5.6.1 Development of a Type A breach

In a Type A breach, the vertical erosion at the breach inflow is prevented or strongly slowed down by either a solid dike foundation, a solid toe protection on the outer slope of the dike, a solid and relatively high foreland, or an effective bottom protection on the foreland, see Figures 5.16, 5.17 and 5.18.

As described in Section 4.8, the dominating mechanisms of breach growth in Stages IV and V are the flow shear erosion along the breach boundaries and the resulting discrete breach side-slope mass failure. In a Type A breach, the rate of flow shear erosion at the breach inflow in vertical direction  $E_{bo} \approx 0$ , however, erosion along the breach side-slopes leads to over-steepness of the slopes (steeper than  $\beta_t$ ), inducing mass failure from the side-slopes (see Figure 5.19).

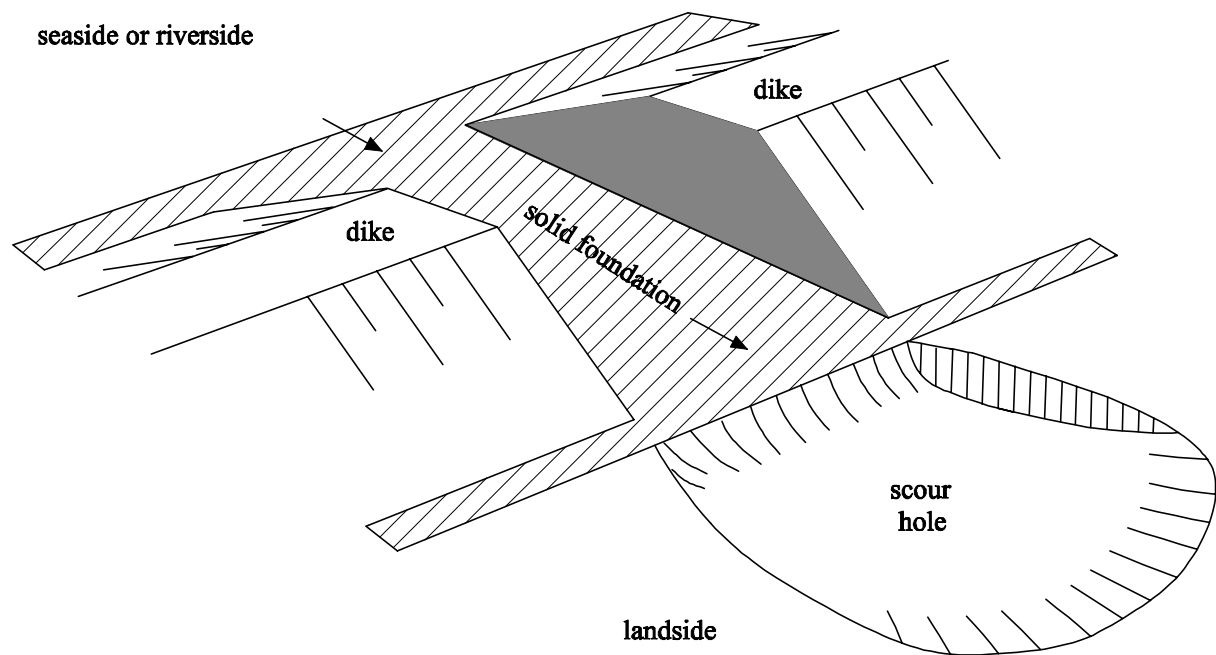


Figure 5.16 Vertical erosion is obstructed by a solid dike foundation in Stages IV and V.

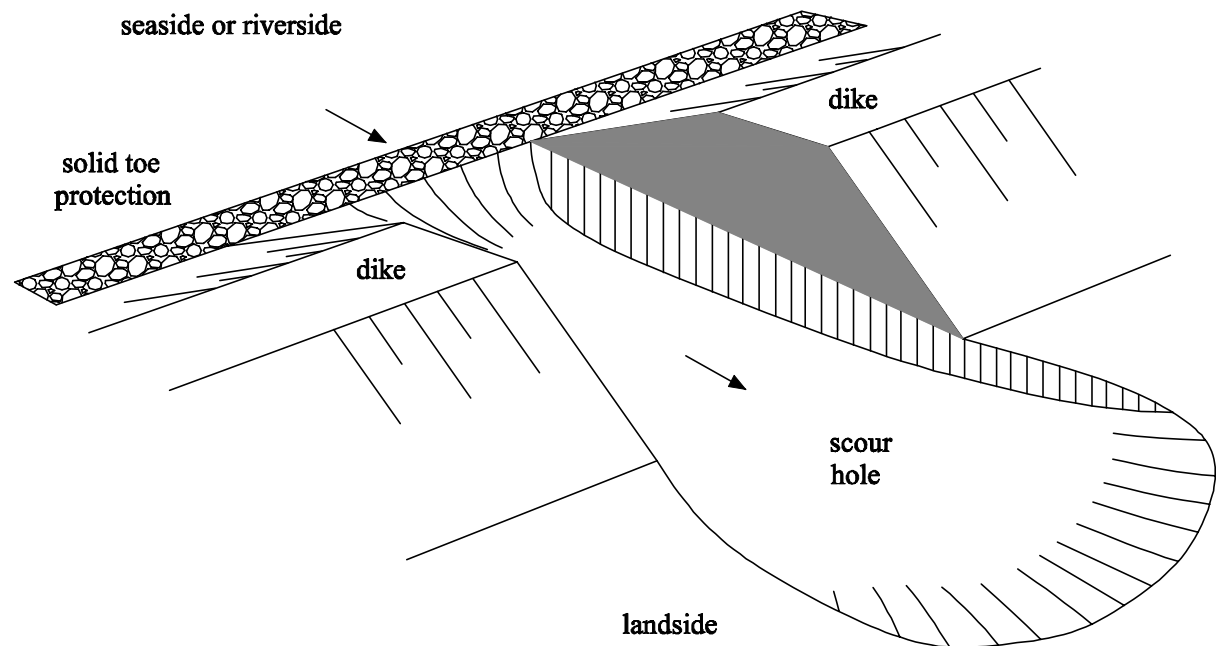


Figure 5.17 Vertical erosion at the breach inflow is obstructed by a solid toe protection on the outer slope of the dike in Stages IV and V.

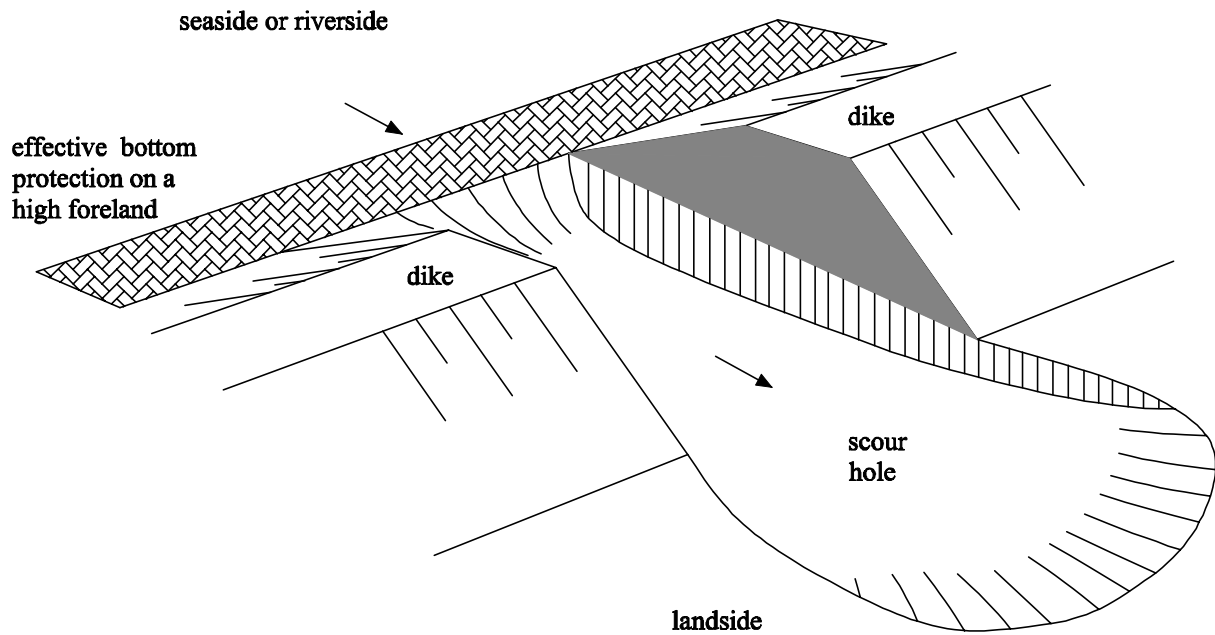


Figure 5.18 Vertical erosion at the breach inflow is obstructed by a solid and relatively high foreland or by an effective bottom protection on the foreland in Stages IV and V.

Provided that the occurrence of the mass failure from the breach side-slopes can be assumed to be instantaneous and the failed material is washed away very swiftly by the breach flow, then no delaying influence is brought on by the failed material on the following breach erosion process. Accordingly, the time and frequency of the occurrence of the breach side-slope instability do not affect the rate of breach widening. The growth in time of the breach width (i.e.  $dB_t/dt$ ) in Stages IV and V is therefore completely determined by the rate of the flow shear erosion in the breach (e.g.  $E_{sl}$  in Figure 5.19), no matter when the side-slope mass failure would occur and how large the failure block would be. Consequently, in this study only a qualitative analysis is performed for the side-slope instability (see Chapter 4). There is no need to quantitatively investigate the criterion for the occurrence of the breach side-slope instability.

The increase of the breach width ( $dB_t/dt$ ) in Stages IV and V in a Type A breach can be described in terms of the erosion rate  $E_{sl}$  as follows

$$\frac{dB_t}{dt} = \frac{2E_{sl} \cos \theta_1}{\sin(\beta_1 + \theta_1)} \quad (5.63)$$

in which  $\theta_1$  as shown in Figure 5.19 is given by

$$\tan \theta_1 = \frac{E_{sl} dt}{d/\sin \beta_1} \quad (5.64)$$

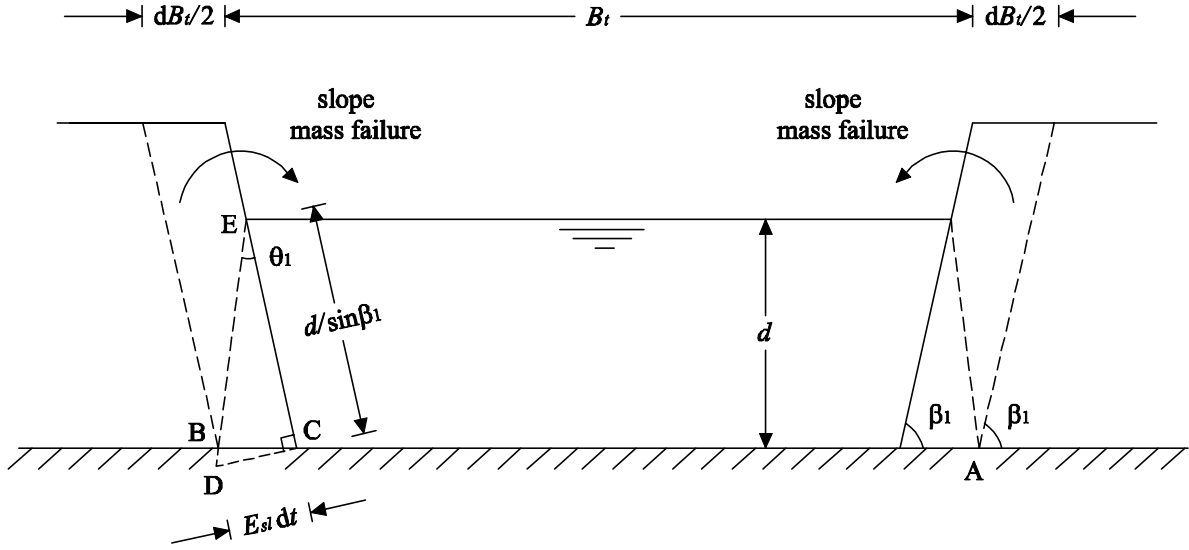


Figure 5.19 Breach width increase in Stages IV and V in a Type A breach.

Equation (5.63) can be rewritten as

$$\frac{dB_t}{dt} = \frac{2E_{sl}}{\sin \beta_1 + \cos \beta_1 \tan \theta_1} \quad (5.65)$$

Combining Equations (5.64) and (5.65) yields

$$\frac{dB_t}{dt} = \frac{2dE_{sl}}{\sin \beta_1 (d + E_{sl} dt \cdot \cos \beta_1)} \quad (5.66)$$

in which  $E_{sl}$  is the rate of flow shear erosion at the toe of the breach side-slopes perpendicular to the slope.  $E_{sl}$  is calculated by

$$E_{sl} = M_e (\tau_b - \tau_c) \quad (5.67)$$

If the time step  $dt$  is small enough, then  $E_{sl} dt \cdot \cos \beta_1 \ll d$ , and Equation (5.66) can be simplified as

$$\frac{dB_t}{dt} = \frac{2E_{sl}}{\sin \beta_1} \quad (5.68)$$

### 5.6.2 Development of a Type B breach

In a Type B breach, only a relatively high but erodible foreland is present outside of the dike. Accordingly, erosion occurs not only in lateral direction, but also to a certain degree in vertical direction in Stages IV and V. The backwards erosion to the foreland results in the formation of a curved spillway in the foreland where the breach inflow takes place (see Figure 5.20). The spillway controls the flow into the breach and has a length larger than  $b$ . Therefore, the discharge coefficient in the broad-

crested weir formula (Equation (5.69)) normally has a value of  $1 < m \leq \pi/2$  (yet, theoretically  $m$  may also be larger than  $\pi/2$  for an elliptical spillway) for a Type B breach in Stage IV:

$$Q_{br} = m \left( \frac{2}{3} \right)^{3/2} \sqrt{g} B (H_w - Z_{br})^{3/2} \quad \text{for } t_3 \leq t < t_4 \quad (5.69)$$

Generally, the final width of a prototype dike breach has an order of magnitude of a hundred meters, while its final depth most probably only has an order of magnitude of ten meters. That is, for a Type B (and also a Type C breach, see Section 5.6.3), although the dike foundation is erodible, the erosion rate at the breach bottom (i.e.  $E_{bo}$  in Figure 5.21) is normally much smaller than that at the toe of the side-slopes (i.e.  $E_{sl}$  in Figure 5.21) in most of Stages IV and V. In other words, the growth rate of the breach width  $B_t$  depends mainly on  $E_{sl}$  rather than on  $E_{bo}$  in the final two stages for Types B or C breaches.

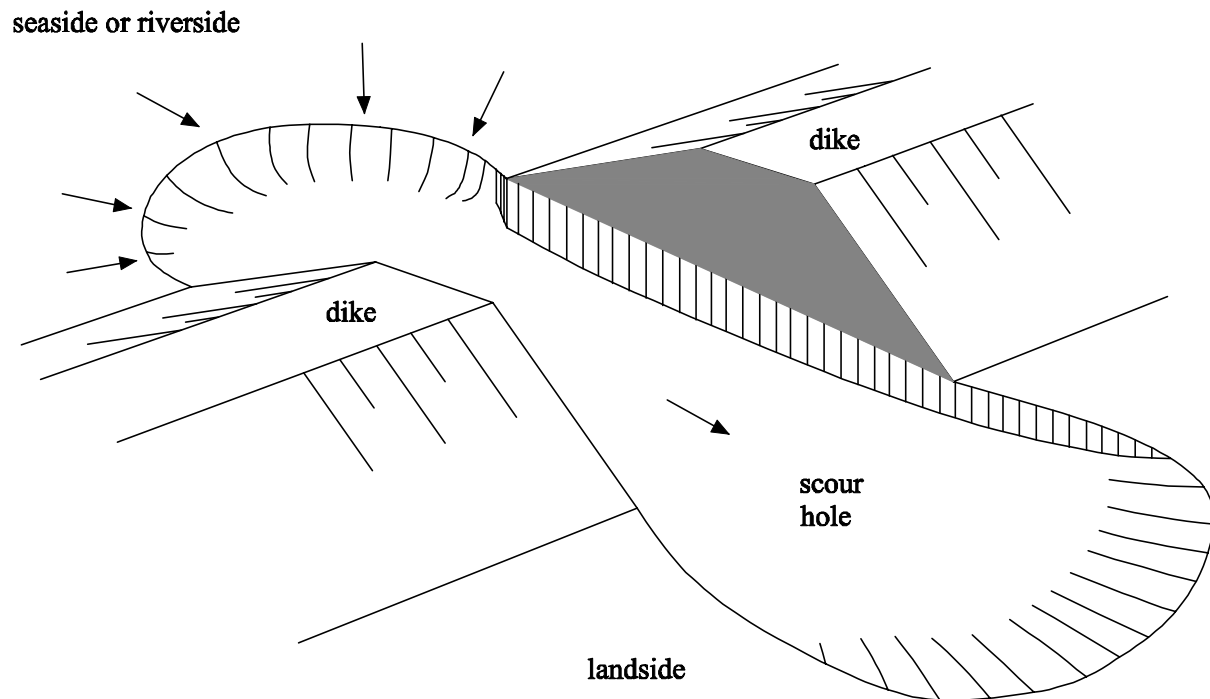


Figure 5.20 Breach erosion in Stages IV and V when only a relatively high and erodible foreland is present.

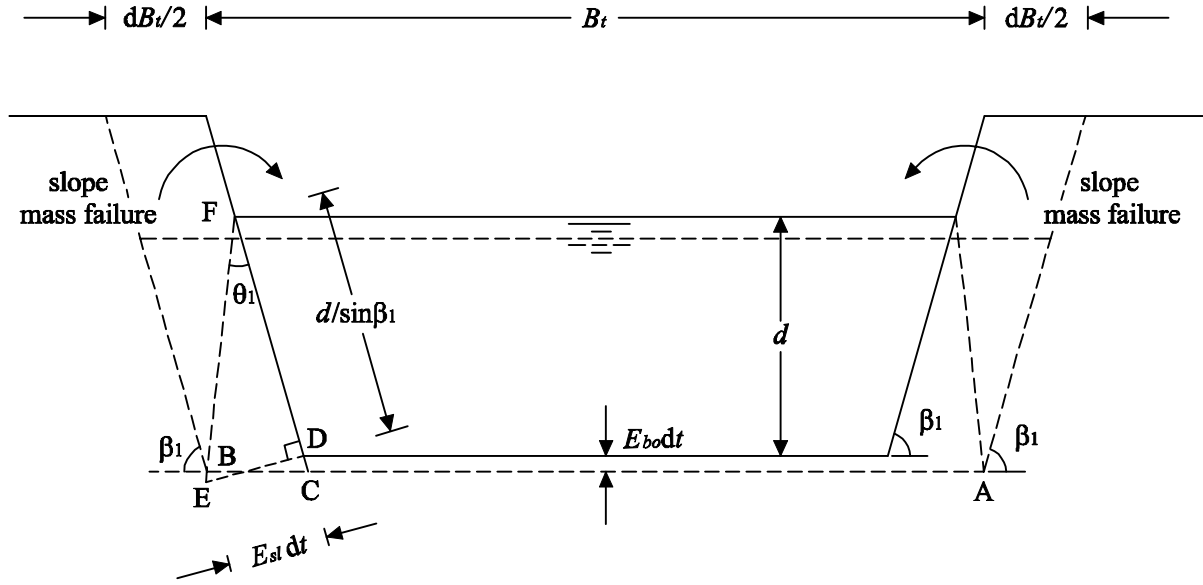


Figure 5.21 Breach width increase in a Type B breach in Stages IV and V.

Figure 5.21 is a schematic illustration of the breach width increase ( $dB_t/dt$ ) in a Type B breach in Stages IV and V. The critical slope angle  $\beta_1$  is related to  $dB_t$  as follows:

$$\frac{dB_t/2}{\sin\theta_1} = \frac{\overline{FC}}{\sin(\theta_1 + \beta_1)} \quad (5.70)$$

in which  $\overline{FC}$  and  $\theta_1$  are given by, respectively

$$\overline{FC} = (d + E_{bo}dt)/\sin\beta_1 \quad (5.71)$$

$$\sin\theta_1 = E_{sl}dt/\overline{EF} \quad (5.72)$$

in which

$$\overline{EF} = \sqrt{\left(d/\sin\beta_1\right)^2 + (E_{sl}dt)^2} \quad (5.73)$$

Substitution of Equations (5.71), (5.72) and (5.73) into (5.70) gives

$$\frac{dB_t}{dt} = \frac{2(d + E_{bo}dt)E_{sl}}{\sqrt{\left(d/\sin\beta_1\right)^2 + (E_{sl}dt)^2} \sin\beta_1 \sin(\beta_1 + \theta_1)} \quad (5.74)$$

Since  $E_{bo}$  is relatively small in most of Stage IV in a Type B breach,  $E_{bo}dt$  can be neglected in Equation (5.74) and the equation is then simplified as

$$\frac{dB_t}{dt} = \frac{2dE_{sl}}{\sqrt{\left(d/\sin\beta_1\right)^2 + (E_{sl}dt)^2} \sin\beta_1 \sin(\beta_1 + \theta_1)} \quad (5.75)$$

In addition, provided that the time step  $dt$  is small enough, thus  $E_{sl}dt \ll d/\sin\beta_1$  and  $\cos\theta_1 \approx 1$ , Equation (5.75) can be further simplified to be

$$\frac{dB_t}{dt} = \frac{2E_{sl}}{\sin\beta_1} \quad (5.76)$$

Equation (5.76) has the same shape as Equation (5.68) for a Type A Breach. It is clear that the rate of breach width increase depends on  $E_{sl}$  rather than  $E_{bo}$  for a Type B breach in Stage IV.

### 5.6.3 Development of a Type C breach

In Stages IV and V in a Type C breach, erosion takes place horizontally and, not hindered by either a solid dike foundation, a solid toe protection on the outer slope of the dike, a relatively high foreland, or an effective bottom protection on that foreland, also in vertical direction. However, the vertical erosion stops or strongly slows down at a certain time at a certain level, which could be a very erosion resistant deep layer in the dike foundation, dependent on the specific situation.

The increase of the breach width in time ( $dB_t/dt$ ) can also be described by Equation (5.74):

$$\frac{dB_t}{dt} = \frac{2(d + E_{bo}dt)E_{sl}}{\sqrt{\left(d/\sin\beta_1\right)^2 + (E_{sl}dt)^2} \sin\beta_1 \sin(\beta_1 + \theta_1)} \quad (5.74)$$

When the time step  $dt$  is chosen sufficiently small,  $E_{bo}dt$  and  $E_{sl}dt$  can be neglected and Equation (5.74) is then simplified as

$$\frac{dB_t}{dt} = \frac{2E_{sl}}{\sin\beta_1} \quad (5.76)$$

In a Type C breach, the height of the breach bottom  $Z_{br}$  at the breach inflow is not constant but decreases in time due to the vertical erosion (see Figure 5.22). The decrease of  $Z_{br}$  follows from

$$\frac{dZ_{br}}{dt} = E_{bo} \quad (5.77)$$

in which  $E_{bo}$  is the rate of flow shear erosion in vertical direction at the breach inflow. It is given by

$$E_{bo} = M_{ef}(\tau_b - \tau_c) \quad (5.78)$$

Due to the continuous water inflow through the breach, the inner water level in the polder keeps rising. At the end of Stage IV at  $t = t_4$ , the inner water level  $H_p$  has risen to such a level that

$$H_p - Z_{br} = \frac{2}{3}(H_w - Z_{br}) \quad (5.79)$$

From then on the inner water level starts to reduce the discharge through the breach, i.e. the breach flow is changed from free discharge to submerged discharge.

The increase of the inner water level in time in this study is simply calculated as

$$dH_p = \frac{Q_{br} dt}{A_p} \quad (5.80)$$

in which  $A_p$  is the area of the polder.

Recently some computer models have been developed for flood inundation simulation, e.g. Bates and De Roo (2000) and Hesselink et al. (2003). Coupling of the present dike breach model with one of these inundation models may give a better prediction of the inner water level variation during dike breaching.

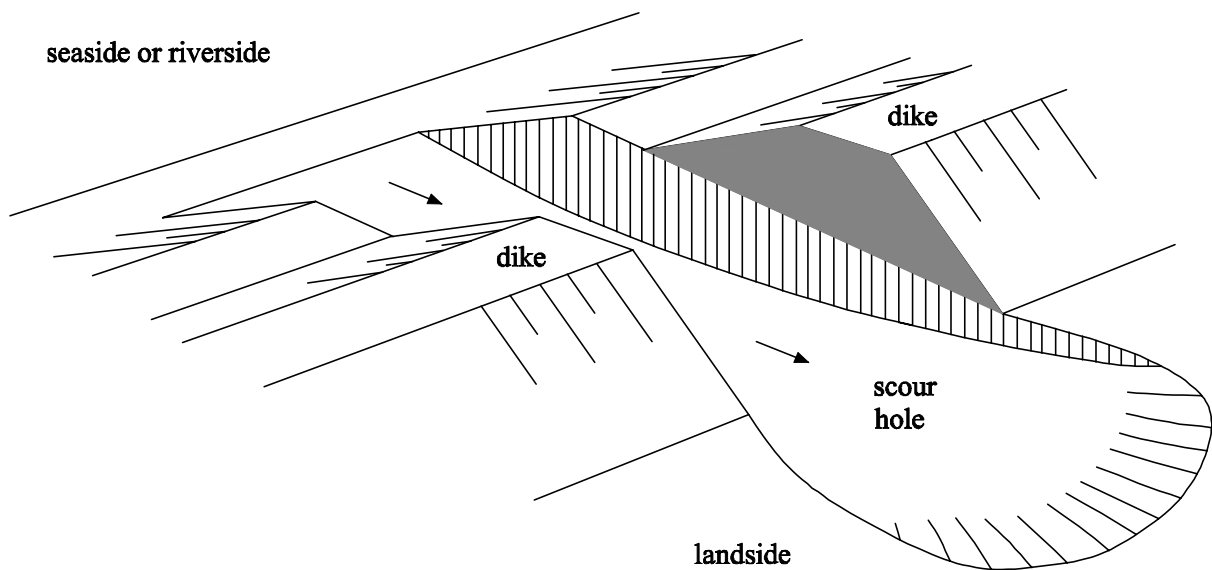


Figure 5.22 Vertical erosion in Stages IV and V in a Type C breach.

## 5.7 Breach development in Stage V

In Stage V, the breach erosion takes place in the same way as in Stage IV: mainly laterally with the extent of vertical erosion relying primarily on the geometrical and material features of the dike.

The breach flow is slowed down by the rising high inner water level and the flow rate in this stage is calculated as

$$Q_{br} = m\sqrt{2g}B(H_w - H_p)^{1/2}(H_p - Z_{br}) \quad \text{for } t_4 \leq t < t_5 \quad (5.81)$$

in which the discharge coefficient  $m \approx 1$  in Types A and C breaches and  $1 < m \leq \pi/2$  in Type B breaches.

The water depth in the breach in Stage V is roughly described by (see Visser, 1998)

$$d = H_p - Z_{br} \quad \text{for } t_4 \leq t < t_5 \quad (5.82)$$

The breach flow velocity is then given by

$$U = \frac{Q_{br}}{Bd} \quad (5.83)$$

The increase of  $B_t$  in Stage V is described by Equation (5.66) for Type A breaches, Equation (5.75) for Types B breaches and Equation (5.74) for Type C breaches. However, when the time step  $dt$  is chosen sufficiently small, the increase of the breach width for all the three types of breaches can be approximately described by Equation (5.68).

At the end of Stage V at  $t = t_5$ , the breach flow velocity is decreased by the rising inner water level to such a degree that it is no longer large enough to further erode the dike body and the dike foundation. Hence the breach growth process stops. In the model  $t = t_5$  is determined when the flow bed shear stress  $\tau_b$  is smaller than the critical shear stress for erosion of the dike body and dike foundation.

Yet, after  $t = t_5$  the flow through the breach does not cease until at  $t = t_6$  when either the inner and outer water levels equal (i.e.  $H_p = H_w$ ), or the outer water level drops below the breach bottom.

## 5.8 Input and output data

The input data for the present model consist of (1) data of the outside water level and water density, (2) data describing the geometry of the dike and the initial breach at  $t_0$ , (3) properties of the soils in the dike body and dike foundation, (4) data representing the polder and (5) other required data.

The input data for the outside water level and water density are:

- outside water level  $H_w(t)$  above a reference level  $Z = 0$ ;
- water density  $\rho$ .

The input data describing the geometry of the dike and the initial breach at  $t_0$  include:

- dike height  $H_d$  above  $Z = 0$ ;
- inclination angle  $\alpha$  of the outer dike slope and  $\beta_0$  of the inner dike slope;
- length  $W_0$  of the initial breach in the dike crest;
- inclination angle  $\gamma$  of the side-slopes of the initial breach;
- bottom level  $Z_{br}$  of the initial breach above  $Z = 0$ ;
- depth  $h$  of the initial breach;
- width  $b$  of the initial breach at its bottom.

The input data describing properties of the soils in the dike body and dike foundation are:

- Manning's roughness coefficient  $n$ ;
- soil cohesion  $c$ ;
- soil internal friction angle  $\phi$ ;
- critical slope angle  $\beta_1$  of the inner dike slope and the breach side-slopes;
- soil density  $\rho_s$ ;
- soil saturated density  $\rho_{sat}$ ;
- critical shear stress  $\tau_c$  for erosion of the soil;
- soil shear strength  $\tau_s$ ;
- soil tensile strength  $\tau_t$ ;
- erodibility factor  $M_e$  of the soil in the dike body;
- erodibility factor  $M_{ef}$  of the soil in the erodible dike foundation;
- thickness  $H_{max}$  of the erodible dike foundation.

The input data for the polder are:

- polder level  $Z_p$  above or below the reference level  $Z = 0$ ;
- water level  $H_p$  in the polder at  $t_0$  with respect to the reference level  $Z = 0$ ;
- polder area  $A_p$  as function of  $H_p$ .

Other input data include:

- discharge coefficient  $m$ ;
- slope  $m_f$  of the upstream boundary of the scour hole in Stages II and III;
- time step  $dt$ .

The output data of the present model contain the breach discharge  $Q_{br}(t)$ , the breach width  $B(t)$ , the inner water level  $H_p(t)$  above  $Z = 0$ , the bottom level  $Z_{br}(t)$  of the breach above  $Z = 0$ , the length  $W(t)$  of the breach in the dike crest, the volume  $V(t)$  of the diverted water through the breach and the transition times  $t_1, t_2, t_3, t_4, t_5$  and  $t_6$  with respect to  $t_0$ .

## 5.9 Discussion

Based on the five-stage breach erosion mechanism as described in Chapter 4, a mathematical model for the simulation of the breach growth process in clay-dikes has

been developed and presented in this chapter. Despite the many equations listed in the model, which seems complicated, considerable assumptions have been applied and some influential factors are still kept out of consideration. For instance, the influence of the dike surface protection layers on the breach erosion process, especially on the erosion initiation is not yet taken into account. Providing a vegetation cover is present on the dike surface, the erosion initiation can be slowed down dramatically or even prevented. Sprangers (1999) found that the vegetation cover can provide protection on the dike due to the following reasons: it protects the dike surface against impact from rainfall, which could happen frequently during flood season; it holds the dike soil particles in place; and it slows down the flow velocity on the dike surface.

Besides, during flood season, the dike generally stands high flood water level for a fairly long period before a potential dike failure occurs, during which the phreatic surface within the dike has risen considerably. The dike body below the phreatic surface is then saturated and softened, possessing decreased soil strength and erosion resistance. Unfortunately, the magnitude of the decrease of the soil erosion resistance is case-specific and difficult to be quantified. More research, especially more field investigations on this issue will surely benefit a better modeling of the breach growth in dikes.

As far as the headcut erosion in Stages II and III is considered, the erosion along the headcut slope surface is not yet well understood and therefore not modeled presently. However, this erosion does exist and can sometimes play a considerable role in the erosion process of clay-dike breaching, as observed in the DUT laboratory experiments, see Chapter 6.

Due to the high complexities and the numerous influential factors involved in and the unsatisfactory understanding of the breach erosion process in clay-dikes, the above-mentioned simplifications are necessary at least for the time being. Modeling of the breach growth process in dikes by means of step by step approach is regarded as an appropriate way.

More research, especially large-scale tests on the breach erosion of clay-dikes with specific aims are necessary to gain more insight into the physics of the breach growth in clay-dikes, and to develop a better mathematical model.



## Chapter 6

### Experiments for verification

#### 6.1 Introduction

As described before, our understanding of the dike breaching mechanism and our ability to predict the growth rate and final width of a breach is still limited. In order to gain more insight into the physics of the breach growth process in clay-dikes and to collect data for calibration and validation of the new mathematical model developed in Chapter 5, five laboratory experiments (including one preparatory experiment with pure sand) were performed at Delft University of Technology (DUT). These experiments are described in this chapter. The laboratory experiments conducted at HR Wallingford in the UK under the EC IMPACT Project have also been chosen to calibrate and validate the mathematical model and therefore a brief description of these tests is presented in this chapter as well.

In Section 6.2 the experimental set-up and the experimental results of the DUT laboratory experiments are described. Description of the EC IMPACT Project laboratory experiments is given in Section 6.3. Section 6.4 includes a discussion and a comparison between the DUT experiments and the EC IMPACT Project experiments.

#### 6.2 DUT laboratory experiments

##### 6.2.1 Introduction

The laboratory experiments were performed in two straight flumes in the Fluid Mechanics Laboratory of Delft University of Technology, from June to September of 2005 after a prolonged preparation. The tested dikes were constructed with two types of soil material, one is pure sand and the other is sand-silt-clay mixtures. The tests will be explained in further detail in Section 6.2.2.

## 6.2.2 Set-up of the laboratory experiments

### *Arrangement of the flumes*

Altogether two flumes were used jointly during the experiments, of which one is the testing flume with the tested dike constructed inside (see Flume 1 in Figures 6.1 and 6.2), the other served as a "storage basin" for water recirculation and as a sediment trap (see Flume 2 in Figures 6.1 and 6.2). Flume 1 has an effective length of 35.5 m, a width of 0.8 m and a depth of 0.85 m. This flume has sidewalls made of glass, which allow visual observations during the experiments. Flume 2, in addition to the sediment trap at one end and a water inlet at the other end, has an effective length of 27.0 m, a width of 2.0 m and a height of 0.4 m. The usable capacity for water storage during the experiments is about  $27.0 \times 2.0 \times 0.35 \approx 19.0 \text{ m}^3$ .

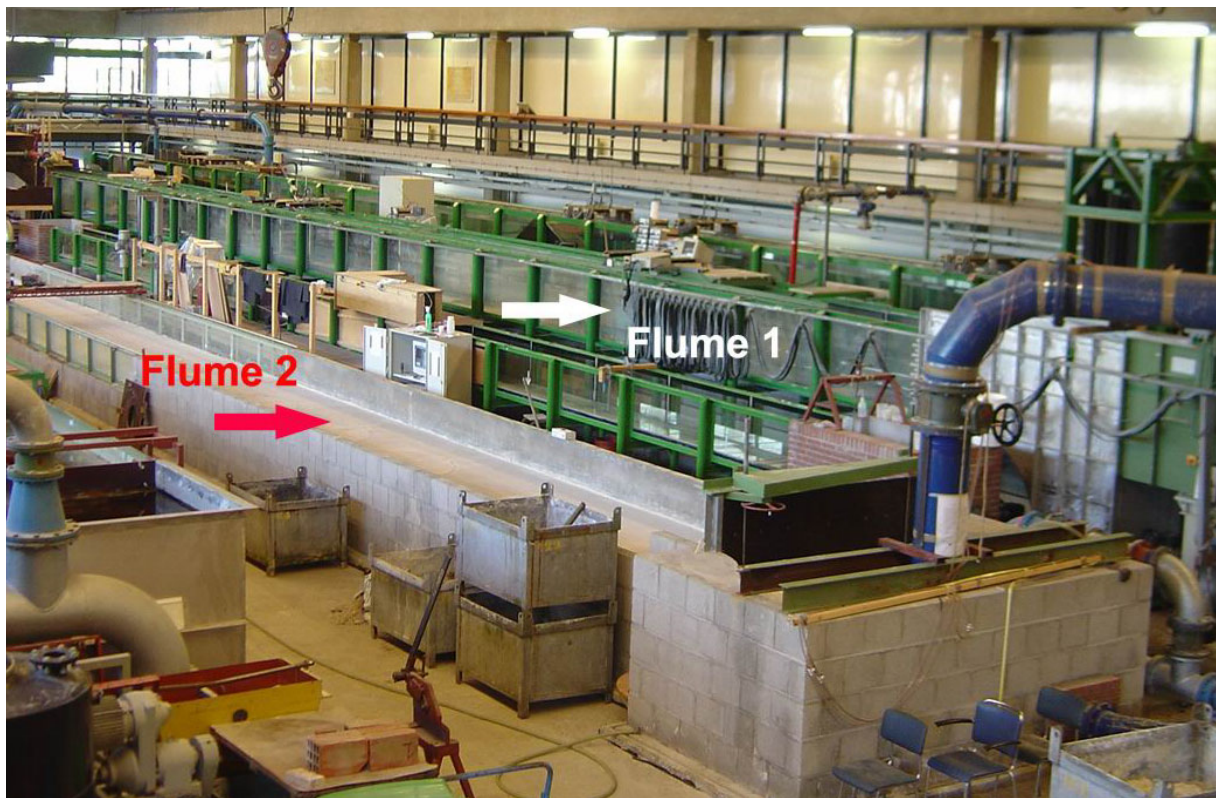


Figure 6.1 The experimental hall with the two flumes in the middle.

Figure 6.2 shows the layout of the two flumes during the tests. Due to the limited width of Flume 1, the tests focused on the first three stages of the five-step breach growth process (see Chapters 4 and 5), in which the breach develops mainly vertically with only ignorable widening. A vertical wooden wall was placed in the middle of the flume to narrow the length of the dike section to 40.0 cm. Another vertical wooden wall was constructed perpendicularly to the middle wall to separate the upstream

"river or sea" from the downstream "polder" in Flume 1. Positions of the dike, the middle wall and the separate wall in Flume 1 are shown in Figure 6.3.

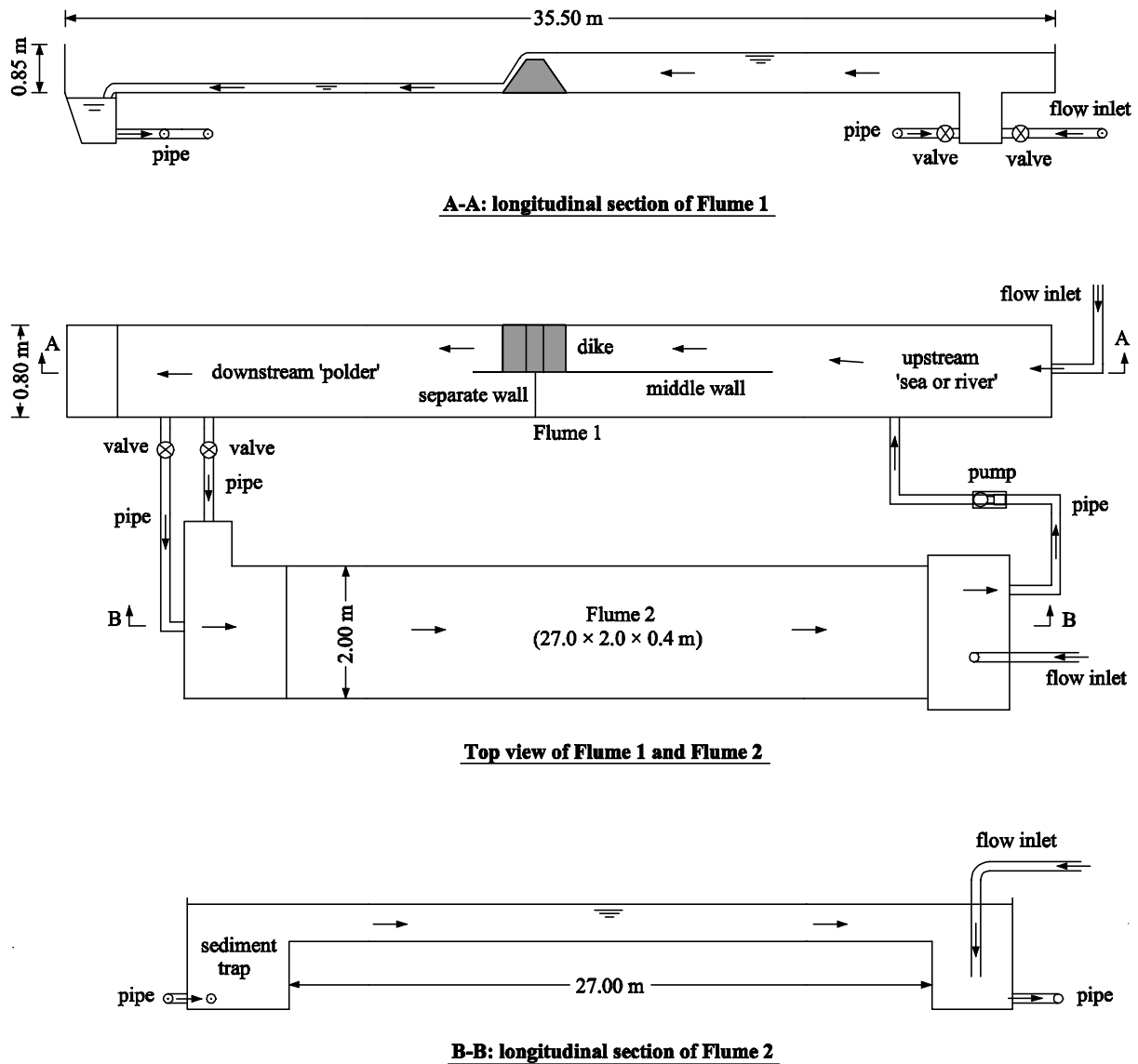


Figure 6.2 Sketch of the two flumes in the experiments.

### *Experimental program*

Altogether five tests were performed, one preparatory sand-dike test (test  $T_s$ ) and four formal tests with sand-silt-clay mixtures (tests  $T_1$ ,  $T_2$ ,  $T_3$  and  $T_4$ ). The objective of test  $T_s$  is mainly to serve as a starting point for the clay-dike tests, checking the influence of soil cohesiveness on the dike breach erosion process, to acquaint with measuring-instruments and to harmonize experimental operation.

Tests  $T_1$ ,  $T_2$ ,  $T_3$  and  $T_4$  differ in soil properties and hydraulic conditions. All the five tests have the same dike configuration and dimensions, as summarized in Table 6.1 and shown in Figures 6.3 and 6.4. The height of the dike was set as high as the flume permitted to allow observation of the dike breach erosion process as clear as possible under the given flume conditions.

Table 6.1 Dike dimensions and configurations of DUT laboratory experiments.

Parameter	Value
Dike height	75.0 cm
Dike crest length	40.0 cm
Dike crest width	60.0 cm
Dike inner slope	1:2.0
Dike outer slope	1:2.0
Thickness of soil foundation	0.0 cm

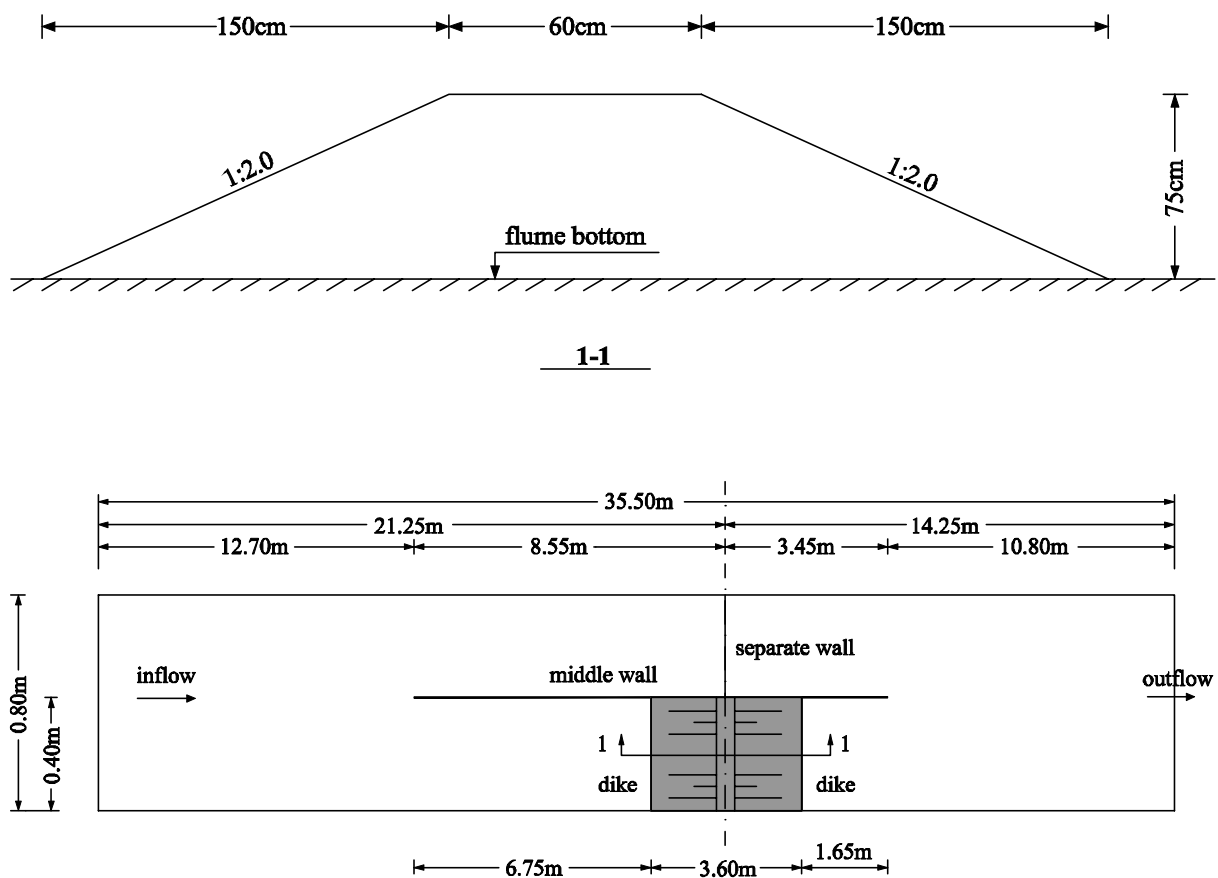


Figure 6.3 Cross-section of the dike (upper panel) and its position in Flume 1 (lower panel).

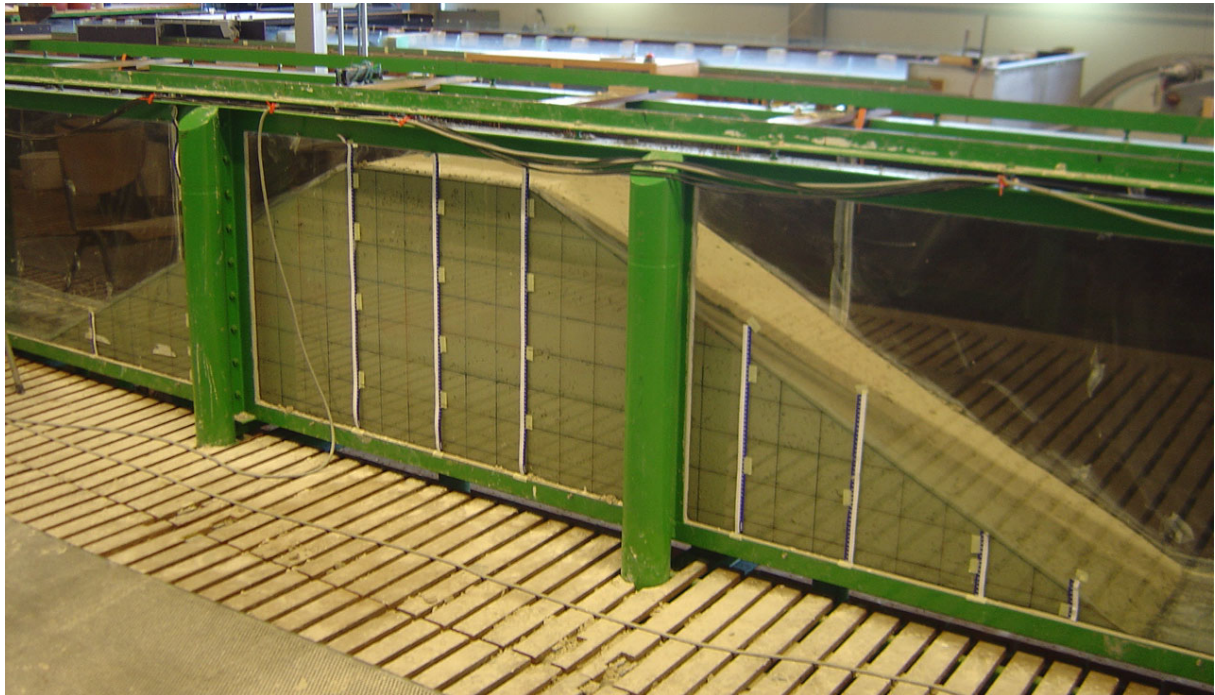


Figure 6.4 Photo of the dike after construction.

### *Soil material*

As described in Section 6.2.1, two types of soil were used for the dike construction, namely pure sand (for test  $T_s$ ) and sand-silt-clay mixtures (for tests  $T_1$ ,  $T_2$ ,  $T_3$  and  $T_4$ ). For test  $T_s$ , the sand used is the so-called Trip Popken Sand which is produced in the Netherlands and has a particle specific density  $G_s = 2.66$ ,  $D_{10} = 0.068$  mm,  $D_{50} = 0.091$  mm and  $D_{90} = 0.124$  mm.

The sand-silt-clay mixtures were prepared artificially by mixing four different soil products in a concrete mixer, including Trip Popken Sand, silt (Millisil M10 from Sibelco, Belgium), Polwhite E Kaolin from Imerys, England and Illite from Germany. The main features of Millisil M10, Polwhite E Kaolin and Illite are given in Appendix A. The soil mixtures used in tests  $T_1$ ,  $T_2$ ,  $T_3$  and  $T_4$  differ from each other in water content, soil density and in proportions of sand, silt and clay, as summarized in Table 6.2.

Since the capacity of the concrete mixer was relatively small, the production of sufficient soil mixture for each single clay-dike test needed more than ten mixer loads. Therefore it was important to look for a certain specific mixing procedure that is able to yield appropriate soil mixture, i.e. a well-mixed, moisture-uniform, reproducible and reasonable erosion-resistant cohesive soil mixture. Much attention was paid to this, including many trial-mixing tests that have been done before starting the formal mixing work.

Table 6.2 Summary of soil properties of DUT laboratory experiments.

Item		Soil material used for tests				
		T <sub>s</sub>	T <sub>1</sub>	T <sub>2</sub>	T <sub>3</sub>	T <sub>4</sub>
$G_s$		2.66	2.67	2.67	2.67	2.67
$\rho_s$ (kg/m <sup>3</sup> )		1650	1938	1936	1951	1948
$\omega$ (%)		20.1	17.6	16.7	16.7	15.4
$c_u$ (kPa)			22.10	24.63	26.42	26.75
$\omega_{opt}$ (%)			11.5			
$\rho_{dm}$ (kg/m <sup>3</sup> )			1940			
Void ratio		0.94	0.62	0.61	0.60	0.58
Degree of saturation (%)		57.1	75.8	73.2	74.7	70.7
Composition 1 (%)	Trip Popken Sand	100	45	50	50	50
	Millisil M10	0	35	35	35	35
	Polwhite E Kaolin	0	15	10	10	10
	Illite	0	5	5	5	5
Composition 2 (%)	Sand (> 50 $\mu\text{m}$ )	99.0	50.5	54.6	54.6	54.6
	Silt (> 2 $\mu\text{m}$ )	1.0	37.5	35.1	35.1	35.1
	Clay (< 2 $\mu\text{m}$ )	0.0	12.0	10.3	10.3	10.3
$D_{50}$ ( $\mu\text{m}$ )		91	53	63	63	63

A series of tests were carried out to measure the properties of the soil material used. Soil wet density ( $\rho_s$ ) and water content ( $\omega$ ) were determined for each compacted layer of the dike during dike construction. Soil particle size distribution was determined by sieve analysis and sedigraph analysis. The pycnometer was applied to measure the soil particle specific density ( $G_s$ ). Soil optimum water content ( $\omega_{opt}$ ) and maximum dry density ( $\rho_{dm}$ ) were determined by Proctor compaction tests for test T<sub>1</sub>. Soil unconfined compression tests were run by use of triaxial test apparatus to measure the undrained shear strength ( $c_u$ ) for each of the four clay-dike tests. Figure 6.5 shows the particle size distributions of the pure sand (for test T<sub>s</sub>) and the sand-silt-clay soil mixtures (for tests T<sub>1</sub>, T<sub>2</sub>, T<sub>3</sub> and T<sub>4</sub>). Table 6.2 presents the results of those soil property tests.

### ***Experimental procedure***

The dike was constructed in the flume by placing soil in horizontal loose lift layers about 0.10 m thick (except 0.20 m for test T<sub>s</sub>). A hand-operated compaction roller with a mass of 32.0 kg and 22.0 cm wide was specially manufactured to compact each loose layer. Special attention was paid to the compaction of soil against the two sidewalls. Before starting the dike construction, a soil fill test was performed to

establish a relationship between the number of passes ( $N_p$ ) of the roller and the achieved soil dry density ( $\rho_{dry}$ ). Except test  $T_1$  in which  $N_p = 4$ , for all the other tests, including test  $T_s$ ,  $N_p = 2$  was applied.

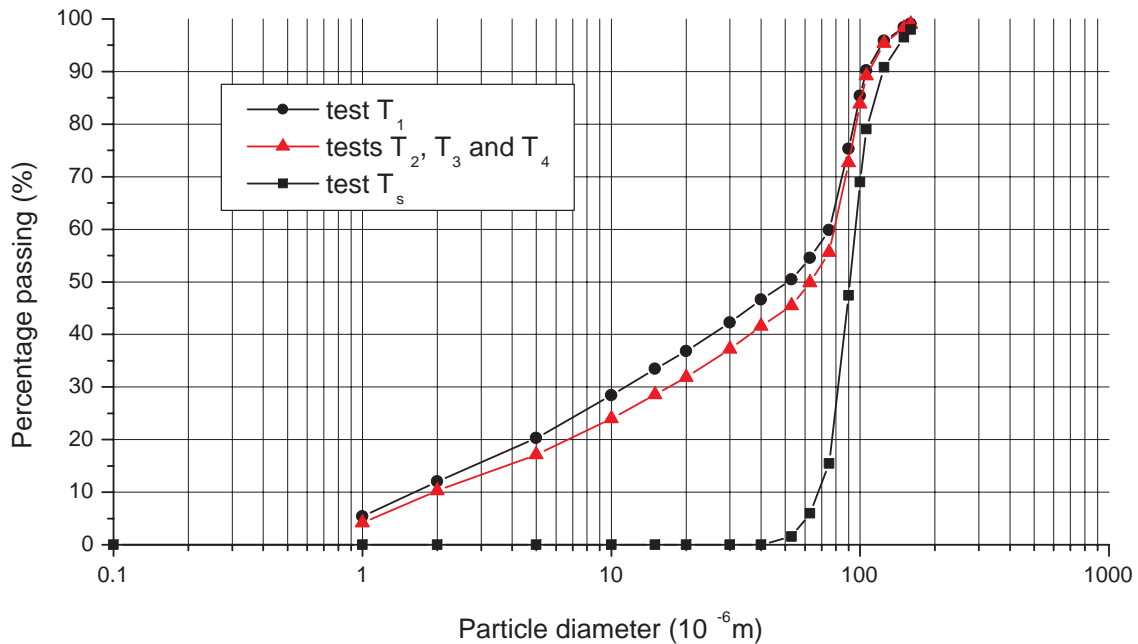


Figure 6.5 Soil particle size distribution of the soil material used.

During dike construction, at least one sample was taken from each layer to determine the compacted soil density. At least one other sample was taken from each layer to measure the water content as well. After the dike was built, careful trimming of the dike was done in accordance with the designed dike profile.

Water levels both upstream and downstream of the dike were measured with four wave height meters, see G14, G15, G16 and G17 in Figures 6.6 and 6.7. G15 was specially placed in a hole in the flume bottom, with the electrode of the wave height meter 5.0 cm below the bottom surface. This is because the water depth downstream of the dike was expected to be small during the testing period while the required immersion-depth of the electrode is at least 4.0 cm, preferably 7.0 cm. Flow velocities in flume axis and transverse directions were measured with three electromagnetic velocity sensors (EMSs, see E7, E10 and E11 in Figures 6.6 and 6.7). The process of breach growth was videotaped with two digital video cameras (see VC1 and VC2 in Figures 6.6 and 6.7) and photographed with two digital cameras (DC1 and DC2 in Figures 6.6 and 6.7) placed at one side of the flume, except DC2 above the flume at downstream side of the dike. To facilitate reading of the development of the dike

profile from the recorded pictures and videos, horizontal and vertical lines were drawn on the flume glass sidewall at mutual distances of 10 cm.

Before starting the test, water was first pumped into the "storage basin" Flume 2, and then the upstream section of Flume 1 was also filled through the water inlet. A suitable wood board and a suitable sandbag were cautiously placed on the dike crest to prevent water from overflowing the dike before the upstream water level had risen to a certain height (normally 5.0 cm above the dike crest). Whereafter the wood block and sandbag were taken away quickly to start the dike breaching process. From then on, water was recirculated by pipes and pump (see Figure 6.2).

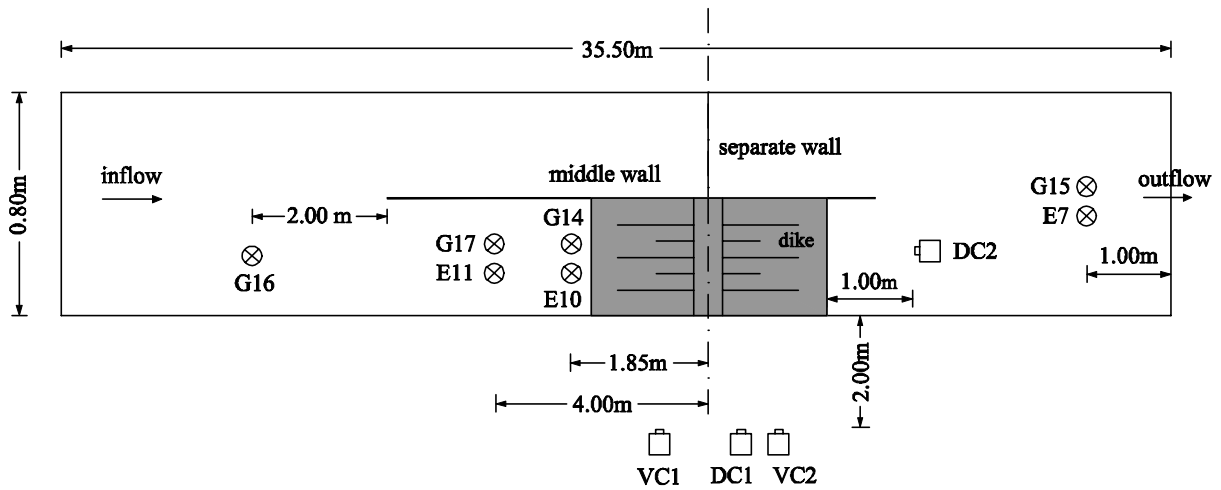


Figure 6.6 Top view of experimental apparatus in the flume (drawing not to scale).

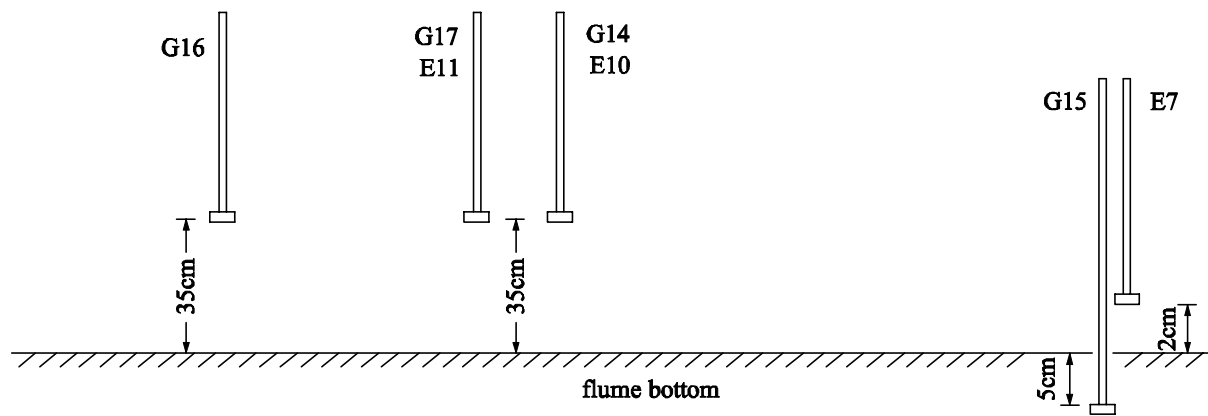


Figure 6.7 Vertical positions of experimental apparatus in the flume (drawing not to scale).

### 6.2.3 Experimental results

The results of the water level measurement at different measuring points (i.e. G14, G15, G16 and G17 in Figures 6.6 and 6.7) and the measured flow velocity of E7, E10 and E11 for all the five tests are shown in Figures A.4 through A.27 in Appendix A.

Evolution of the dike profile was determined from the videos and photographs. Figures 6.8 through 6.12 show this process for tests  $T_s$ ,  $T_1$ ,  $T_2$ ,  $T_3$  and  $T_4$ , respectively, providing a clear indication of the nature of the breach erosion. For tests  $T_s$  and  $T_4$ , places close to the toe of the dike occasionally could not be observed clearly from either the photographs or the videos due to the turbid water, which contained very high sediment concentration after the start of the test, see Figures 6.8 and 6.12.

For the tests with sand-silt-clay mixtures (i.e. tests  $T_1$ ,  $T_2$ ,  $T_3$  and  $T_4$ ), when the dike was overflowed, erosion usually occurred first at locations close to the toe of the dike (except for test  $T_4$ ), due to the acceleration of the breach flow along the downstream slope and the distinct change of gradient there, see Figures 6.9 through 6.11. Soon this erosion extended to the entire slope, with a larger erosion rate occurring at the lower part of the slope than at the upper part, consequently the slope became steeper in time. Besides the toe of the dike, the transition area between the dike crest and the downstream slope was the second place susceptible to earlier and faster erosion. By comparison, erosion at the dike crest was relatively slow, depending mainly on the erosion resistance of the soil material. Erosion at the dike crest lowered the height of the dike and increased the breach flow rate in time, which in its turn accelerated the dike breach erosion process.

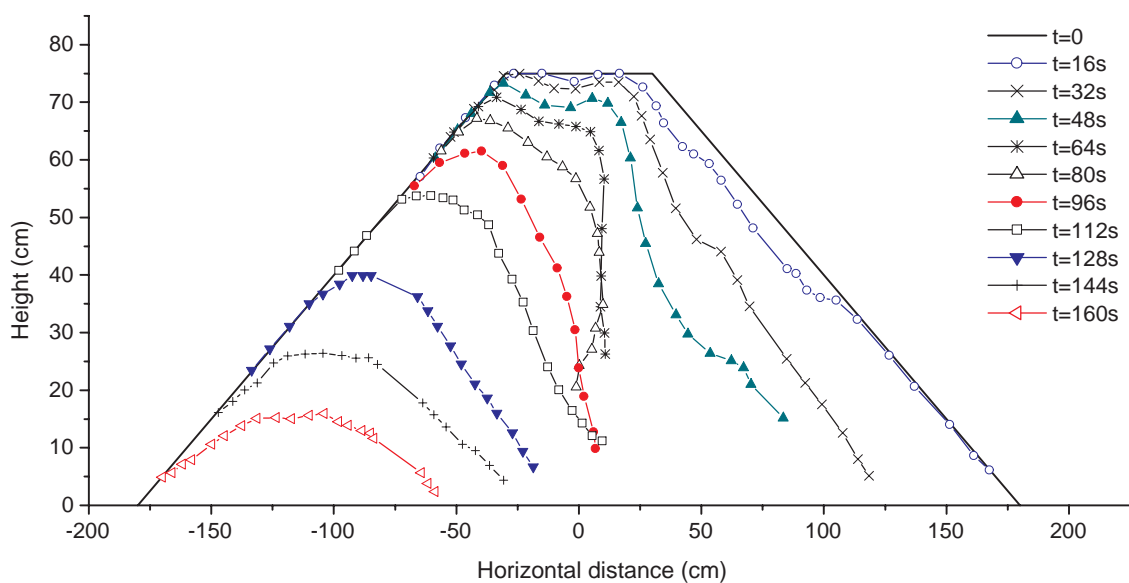
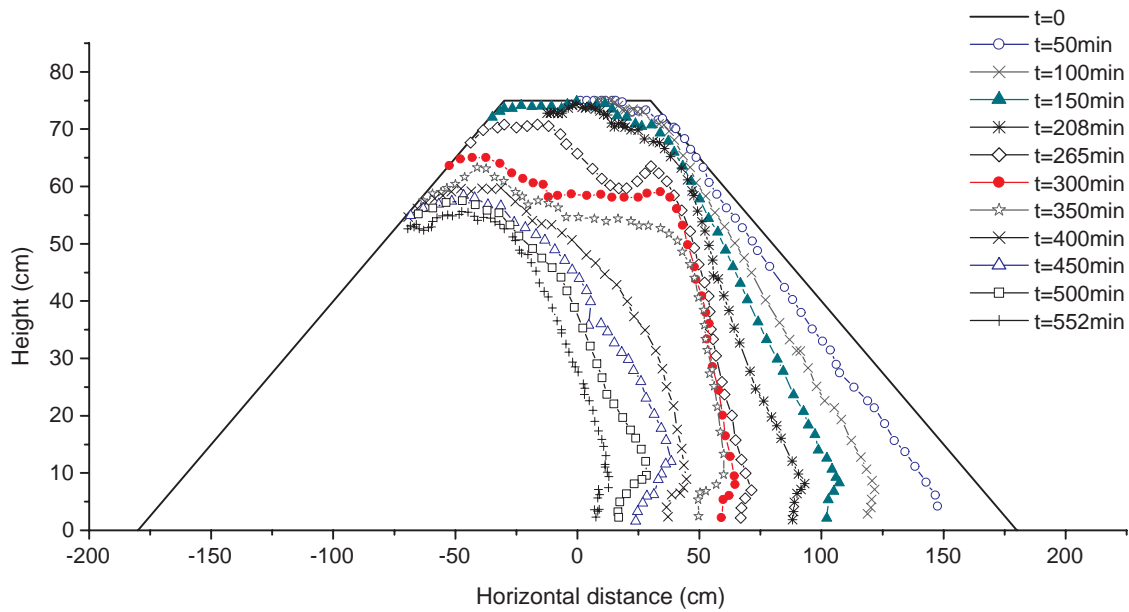
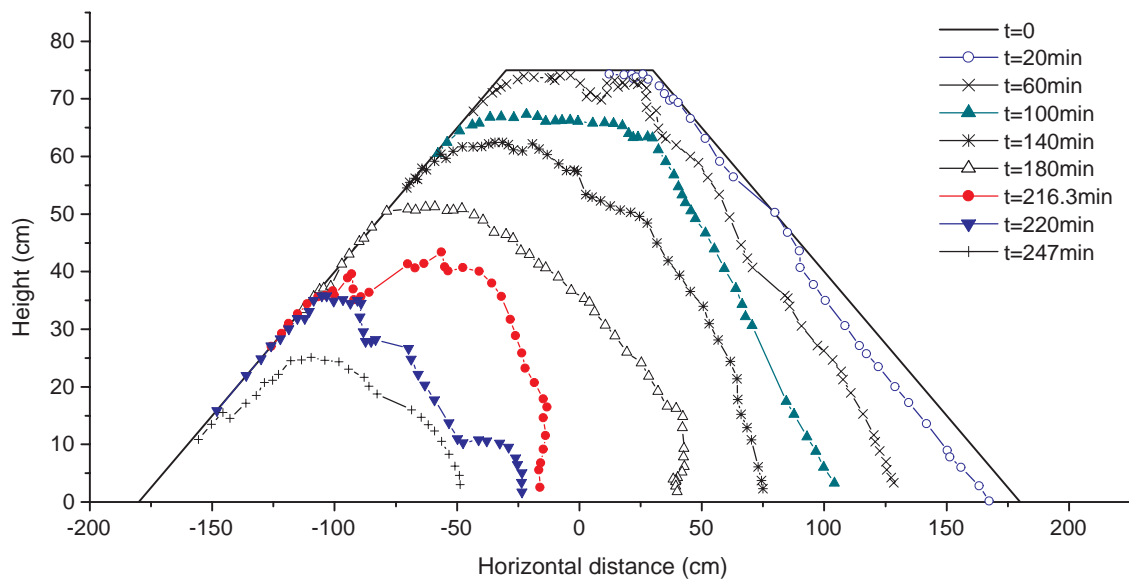
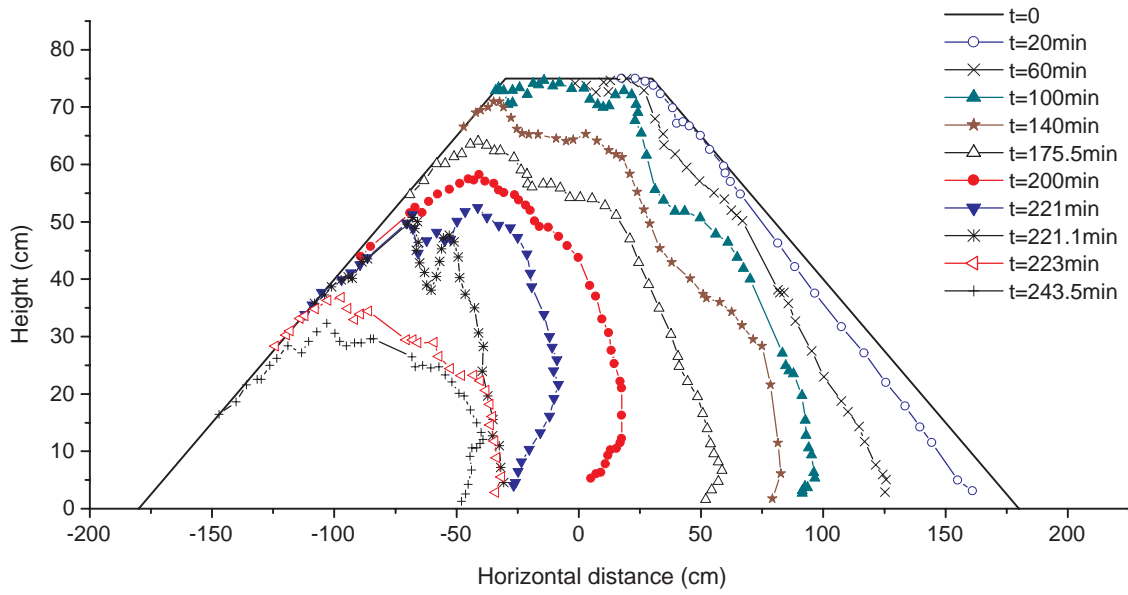
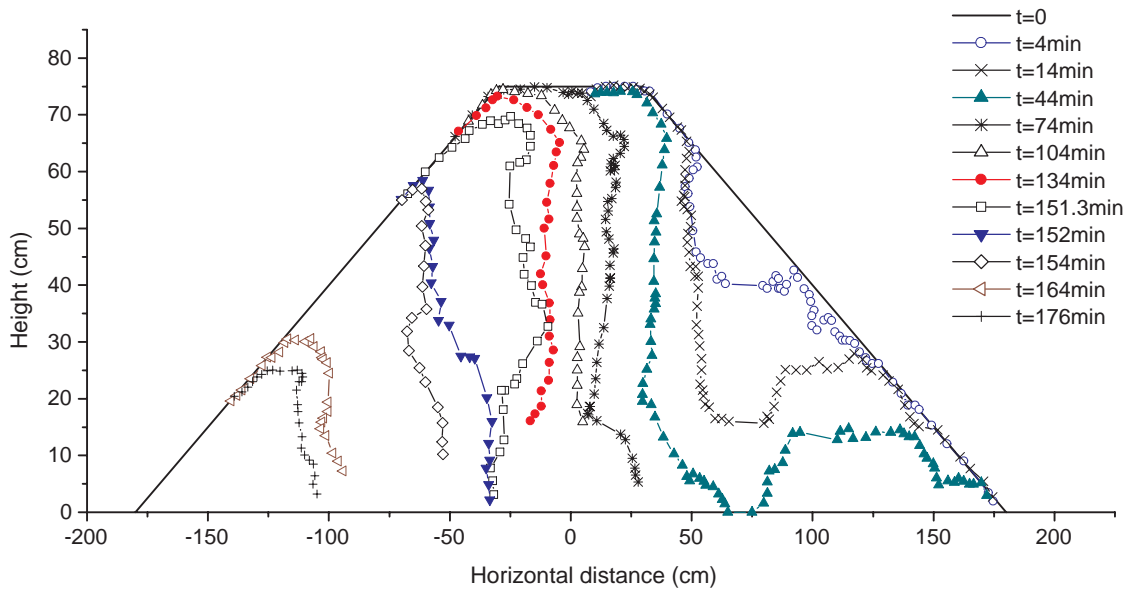


Figure 6.8 Dike profile development of test  $T_s$ .

Figure 6.9 Dike profile development of test  $T_1$ .Figure 6.10 Dike profile development of test  $T_2$ .

Figure 6.11 Dike profile development of test  $T_3$ .Figure 6.12 Dike profile development of test  $T_4$ .

The steepened downstream slope of the dike evolved gradually into a headcut. Then the breach flow was no longer attached to the headcut but impinged like a jet onto the downstream flume bottom, imposing considerable erosive forces on the toe of the slope (see Figure 6.13). Strong scour of the toe of the slope (i.e. headcut undermining) due to the jet impingement was observed in all of the four tests with sand-silt-clay soil mixtures. This undermining generally resulted in a reverse slope at the lower part of the headcut. It was observed that when the breach flow rate was very large, the action point of the jet flow on the flume bottom was relatively far away from the toe of the headcut. Under the circumstances of flat and non-erodible headcut foundation as in the present tests (i.e. the flat steel bottom of the flume), the portion of flow reflected towards the headcut was relatively small and therefore the headcut undermining actually was somewhat slower compared with a smaller flow rate situation. However, the erosion occurring at the top of the headcut was faster with a larger flow rate. In case of an erodible dike foundation, a scour hole would be expected to form in the foundation. It enlarged in time, both vertically and towards the headcut, undermining the headcut slope.

Fluidization and consequently failure of the headcut surface layer due to the diffused falling water was also observed during the tests. This effect speeded up the retreat of the headcut and consequently the overall rate of dike breaching. However, this process is very dynamic and irregular and therefore quantification of it is difficult.

During all of the four tests with cohesive soil mixtures (i.e. tests  $T_1$ ,  $T_2$ ,  $T_3$  and  $T_4$ ), soil mechanical slope mass failure occurred discretely from the steepened downstream slope of the dike (i.e. the headcut), however, not very frequently. Figures 6.14 through 6.17 show an example of the headcut slope mass failure observed during test  $T_4$  (when the pictures are printed black and white they may not be clear enough due to the very turbid water). When the slope mass failure occurred, the loss of soil from the headcut could be a very large chunk, followed by an instant increase of the breach flow. It was also noted that in many cases, the occurrence of the headcut slope mass failure was accompanied by appearance of crack(s) on the top of the headcut. This might indicate that consideration of the tensile stress in the soil is needed when dealing with clay-dike breach erosion, although in traditional soil mechanics theory soil tensile strength is often not taken into account.

For tests  $T_1$ ,  $T_2$ ,  $T_3$  and  $T_4$ , the transition between the dike crest and the downstream slope sometimes eroded into a rounded angle. Then the breach flow did not flee away from the downstream slope at the top, instead it rushed down along the slope and detached from the slope at a certain lower point and impinged towards the foundation with less strong scour potential.



Figure 6.13 Headcut and breach flow jet impingement (test T<sub>4</sub>).

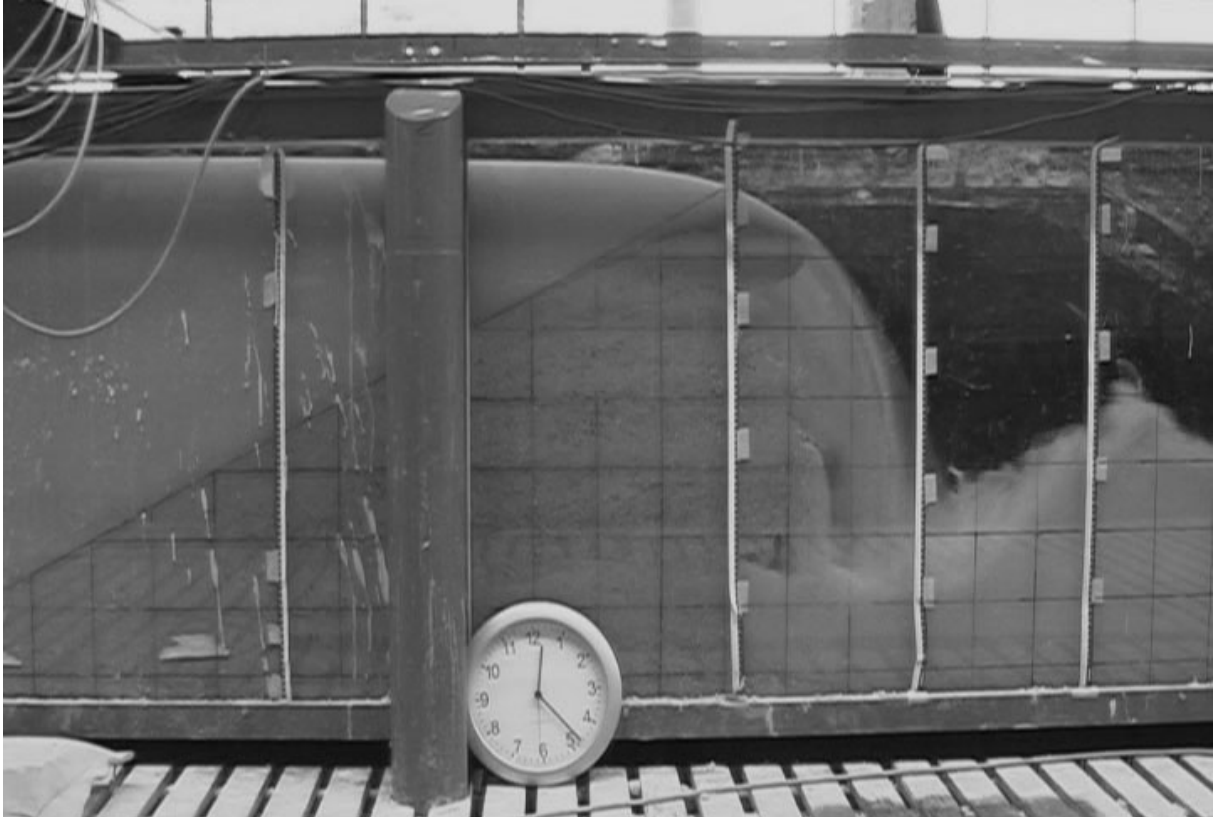


Figure 6.14 One minute before slope mass failure from the headcut (test T<sub>4</sub>).

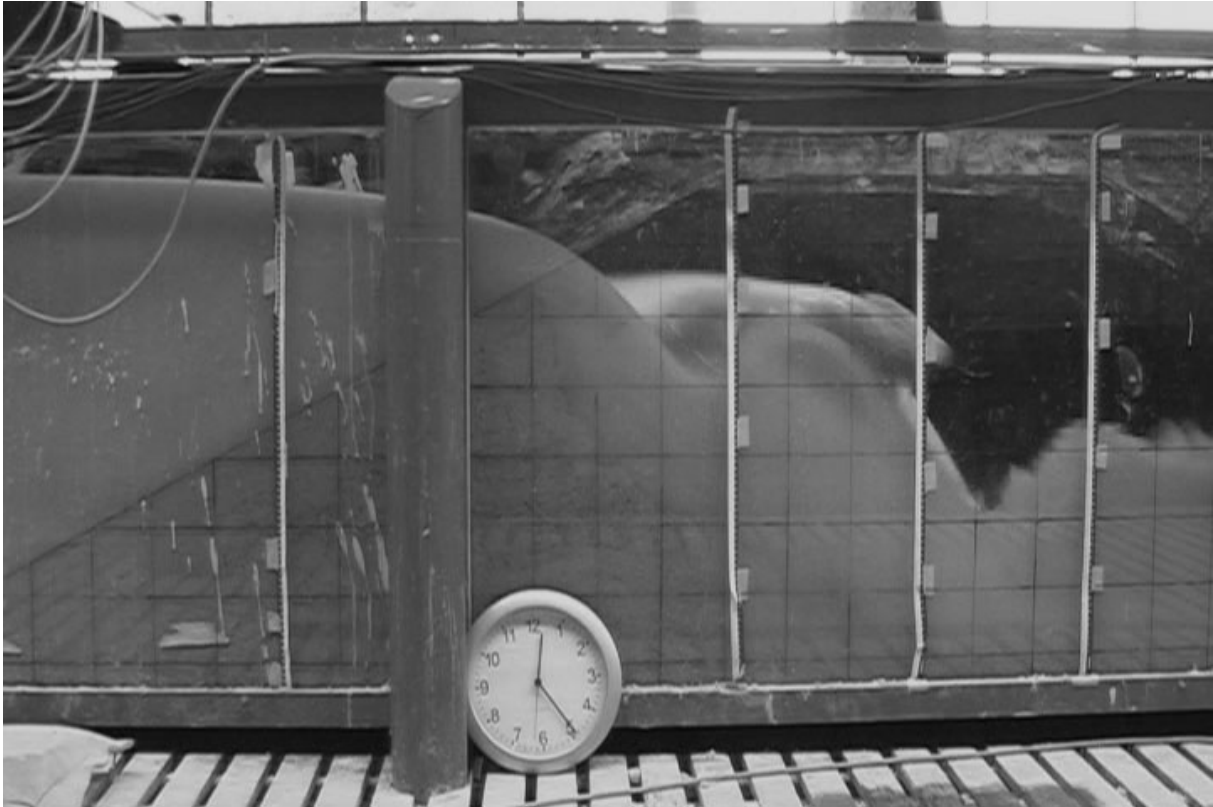


Figure 6.15 The moment of slope mass failure occurrence from the headcut (test  $T_4$ ).

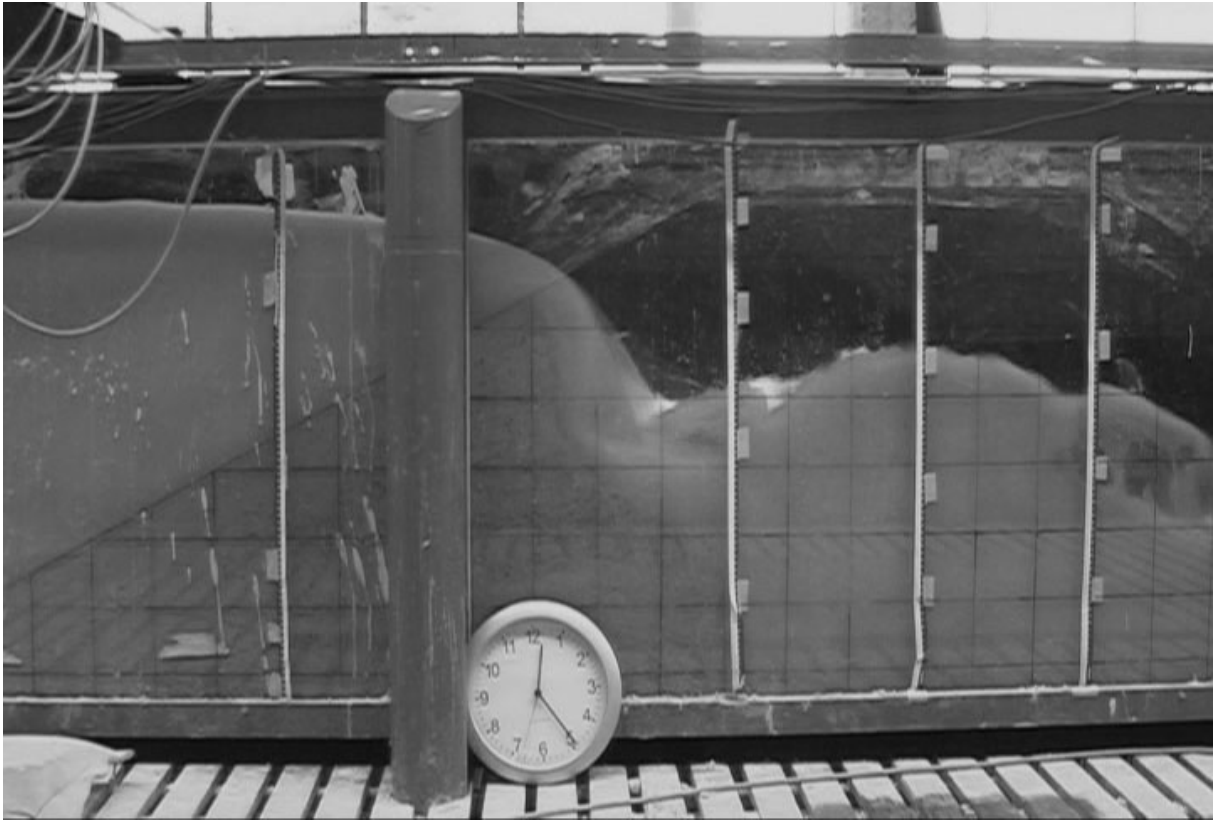


Figure 6.16 Just after the occurrence of slope mass failure from the headcut (test  $T_4$ ).

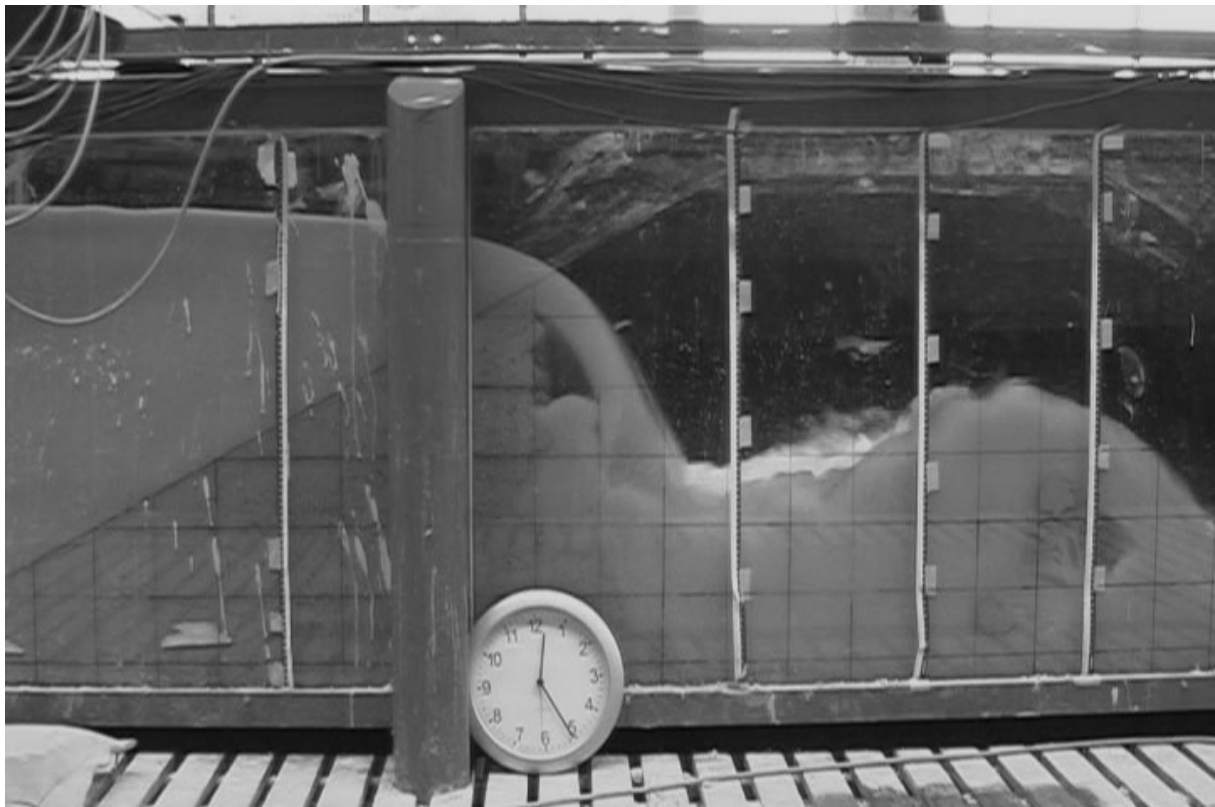


Figure 6.17 One minute after slope mass failure from the headcut (test  $T_4$ ).

For the sand-dike test  $T_s$ , erosion was first observed to occur at the upper half of the downstream slope of the dike, and then a bar was developed at the lower part of the slope (see Figure 6.8). The upper portion of the slope was steepened in time and a headcut was also formed, showing similar characteristics as the tests with sand-silt-clay mixtures. This was not expected. The mainstream of the breach flow also fled away from the headcut at the headcut brink, however, no large slope mass failure was observed from the headcut. The backward migration of the headcut was mainly due to the surface erosion from the slope. Later, when this erosion approached the upstream slope of the dike, the gradient of the headcut became gentler and remained more or less constant thereafter, indicating more or less uniform erosion along the slope.

Comparing the time scale of the test with pure sand (i.e. test  $T_s$ ) and the tests with sand-silt-clay soil mixtures (i.e. tests  $T_1$ ,  $T_2$ ,  $T_3$  and  $T_4$ ) shows that the influence of soil cohesiveness on the breach erosion process is very remarkable. Under the same dike profile and similar hydraulic conditions, the whole duration of test  $T_s$  lasted less than 3 minutes (as summarized in Table 6.3), which is very fast compared with the shortest clay-dike test  $T_4$ , which lasted almost 3 hours. This demonstrated that the cohesive portion in the sand-silt-clay soil mixtures strongly slowed down the erosion process. Among the four clay-dike tests performed, test  $T_1$  persisted about 9.2 hours however without being completely breached. Tests  $T_2$  and  $T_3$  both lasted about 4.1 hours. Among others (if any), the factors contributing to the very long breaching

duration of test  $T_1$  definitely include its higher (although not much) clay proportion and the larger compaction applied. For test  $T_4$ , unlike the other three tests with cohesive soil mixtures, the erosion initiated more or less in the middle of the downstream slope when it was overflowed, probably due to uneven compaction during the dike construction, resulting in the formation of a headcut much sooner than expected and considerable speeding up of the breach erosion process.

During the dike construction it was found that water content has an important influence on the performance of the sand-silt-clay soil mixtures. In general, when above the soil optimum water content, the higher the water content is, the harder it is to compact the soil to the desired soil density. In test  $T_1$  4 passes of the roller were applied to gain a soil density of  $1938 \text{ kg/m}^3$ , in contrast to test  $T_2$  with just 2 passes to achieve  $1936 \text{ kg/m}^3$  soil density, although there was only a minor difference (0.9%) in their water content (17.6% for test  $T_1$  and 16.7% for test  $T_2$ ). A larger water content also made the soil behave like a spring during the compaction, increasing the difficulties of compaction as experienced to a certain degree in test  $T_1$ . For unsaturated soil, an increase of the water content generally leads to a decrease in the soil strength (see e.g. Fredlund and Rahardjo, 1993). Nevertheless, in the present experiments this effect on the dike breach erosion process was overshadowed by the influences of the compaction effort and the uneven compaction (for test  $T_4$ ).

Table 6.3 Summary of time information for the five DUT laboratory experiments.

Test	Time started	Time ended	Test duration
$T_s$	10:00:00	10:02:43	2 min + 43 sec
$T_1^*$	10:28:40	16:24:45	5 h + 56 min + 5 s
	09:35:45	12:52:10	3 h + 16 min + 25 s
$T_2$	10:15:40	14:22:25	4 h + 6 min + 45 sec
$T_3$	10:02:53	14:07:23	4 h + 4 min + 30 sec
$T_4$	09:51:30	12:49:26	2 h + 57 min + 56 sec

\* Test  $T_1$  was first performed on 9 August from 10:28:40 to 16:24:45 with only partial breaching, then the test continued on 10 August, started from 09:35:45 and stopped at 12:52:10 with still about 55 cm high dike body left (see the dike profile development shown in Figure 6.9). For tests  $T_2$ ,  $T_3$  and  $T_4$ , tests proceeded until only a very small residual dike body was left.

### 6.3 EC IMPACT Project laboratory experiments

In 2003 a series of laboratory experiments were undertaken at HR Wallingford in the UK under the EC IMPACT Project to improve understanding of the breach erosion process in embankments (Mohamed et al., 2004). Among these experiments, tests no.

10 through no. 16 (here named tests  $T_{10}$  through  $T_{16}$ ) were done with cohesive soil with  $D_{50} = 0.005$  mm,  $D_{10} = 0.001$  mm and  $D_{90} = 0.018$  mm. Figure 6.18 shows the soil particle size distribution of these tests. It can be seen from the figure that the soil is approximately composed of 24% clay, 75% silt and 1% sand. Some soil tests were performed to characterize the soil properties, and the results of these tests are summarized in Table 6.4. The soil cohesion and angle of friction were obtained by undertaking the drained shear box tests.

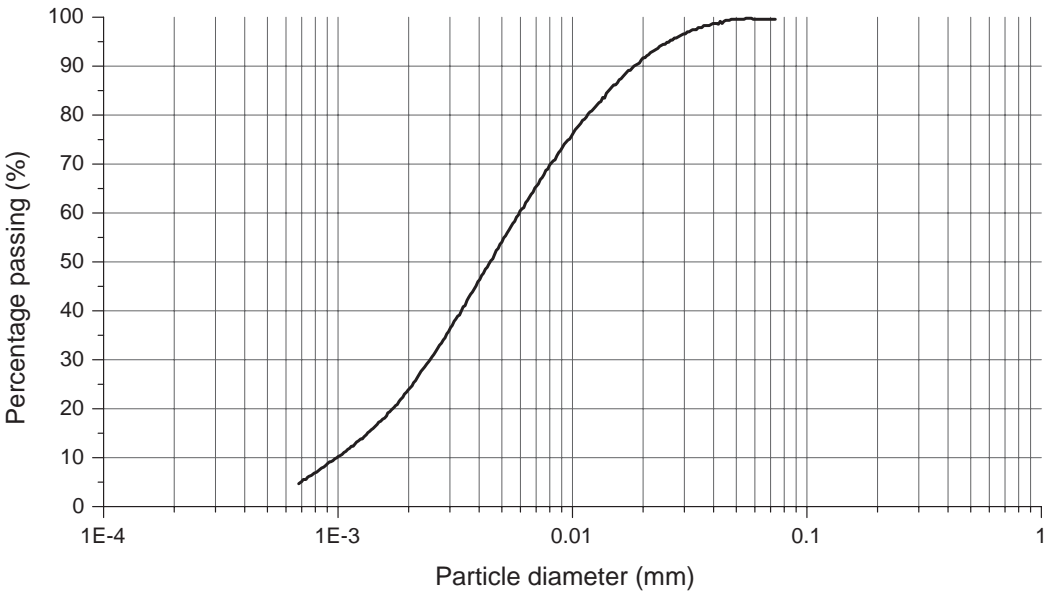


Figure 6.18 Soil particle size distribution of the EC IMPACT Project experiments (tests  $T_{10}$  through  $T_{16}$ ).

Table 6.4 Summary of results of the soil property tests for the IMPACT Project tests.

	Sample		
	Test $T_{10}$	Test $T_{11}$	Test $T_{12}$
Plastic limit (%)	31	32	---
Liquid limit (%)	66	55	---
Specific gravity (-)	2.58	2.58	2.58
Friction angle ( $^{\circ}$ )	22.5	22.5	22.5
Cohesion (kPa)	31	31	31
Water content (%)	25	25	25
Void ratio	1.22	1.22	1.38

The tests were conducted in a large basin with a length of approximately 50.0 m and a width of about 10.0 m. A number of pumps were equipped allowing over 1.0 m<sup>3</sup>/s discharge to be pumped through the facility (see IMPACT, 2005). A large volume of storage upstream of the test section allowed for continued flow as breach formation through an embankment occurred. An automated control system was developed to control operation of the pumps so as to maintain a steady upstream water level for a period as long as possible. A large pit at the lower end of the facility acted as a sediment trap before the water was released into a re-circulating sump system.

All the tested embankments have a height of 0.6 m, a crest width of 0.2 m and a crest length of 4.0 m (see Figure 6.19). The embankment's upstream slope is 1:2, and the downstream slope varies from 1:1 to 1:3. The initial breach in the embankment crest has a depth of 0.05 m, a width of 0.54 m and two side-slopes of 1:2 (see Figure 6.20). The following data were collected during the tests (IMPACT, 2005):

- inflow into the flume;
- water levels upstream and downstream of the embankment;
- approach velocity (upstream of the embankment);
- pore water pressure in the embankment;
- photos and videos for monitoring breach development.

The measured upstream water level and the breach outflow discharge are given in Figures A.28 through A.34 in Appendix A. Figure 6.21 shows a top view photo taken during test T<sub>12</sub>, in which failure (by overturning) of the breach side-slopes can be observed. Mohamed et al. (2004) described that during the tests headcutting was observed on the embankment's downstream face. The headcut migrated upstream and then eroded downward. For more details on the EC IMPACT Project tests, a reference is made to IMPACT (2005).

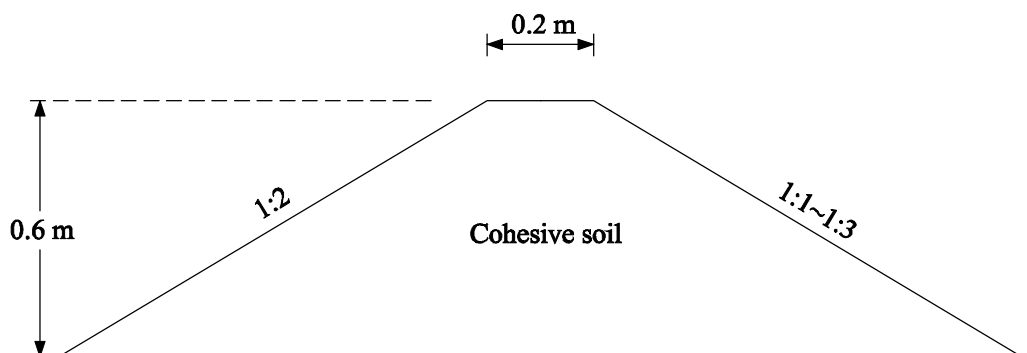


Figure 6.19 Cross-section of the tested embankments.

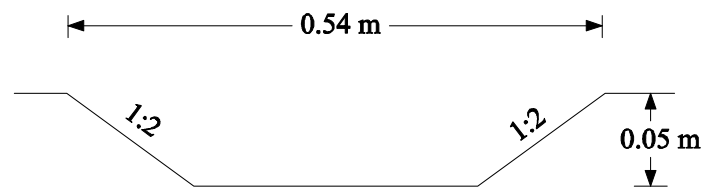


Figure 6.20 The initial breach in the embankment crest.

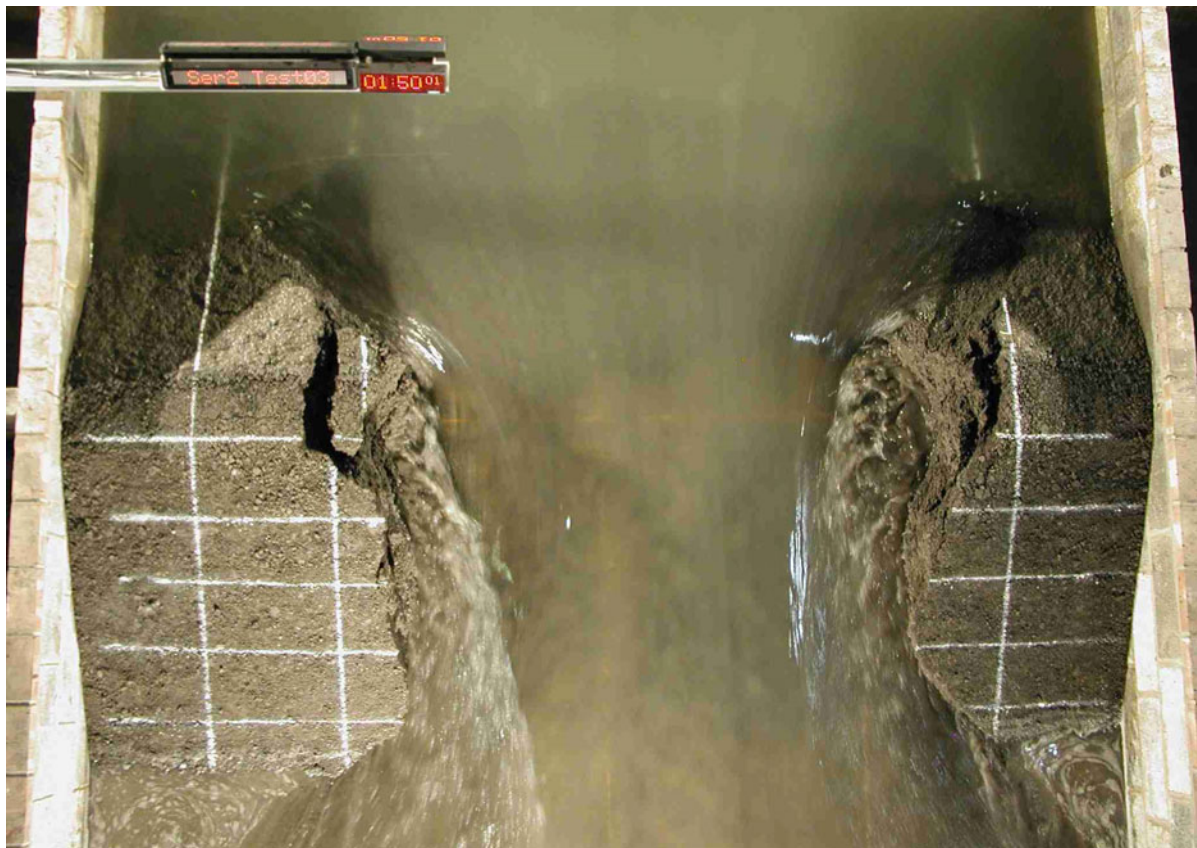


Figure 6.21 Top view photo of breach erosion taken during test  $T_{12}$  of the EC IMPACT Project laboratory experiments.

## 6.4 Discussion

The DUT laboratory experiments have confirmed the breach erosion mechanism of clay-dikes of the first three stages (as described in Chapter 4). Both the DUT laboratory experiments and the EC IMPACT Project laboratory experiments are very useful for understanding the physics of breach growth in clay-dikes and the calibration and validation of mathematical models.

Table 6.5 gives a comparison between the DUT laboratory experiments and the EC IMPACT Project laboratory experiments (with only tests  $T_{10}$  and  $T_{12}$  as examples). In addition to the big difference in dike dimensions, it is notable that although the EC IMPACT Project tests possessed considerable higher clay content, the dikes were breached within much shorter durations. The explanation for this could rely mainly on two points. Firstly, the DUT laboratory experiments had a much larger soil dry density and a much smaller void ratio, which indicate that more compaction efforts were applied during the dike construction. A decrease in compaction efforts reduces the soil erosion resistance and accelerates the breach erosion process, and vice versa (see also Chapter 3). Secondly, the erosion resistance of a cohesive soil mixture is not only determined by the clay proportion, but is to a large degree also dependent on the type of the clay minerals, e.g. kaolinite, illite or montmorillonite. This is because different clay minerals hold very dissimilar properties, including, among others, the soil strength, compressibility, permeability and plasticity (see Chapter 3). Therefore, as far as experiments on the breach erosion of clay-dikes are concerned, it is necessary to make clear what type of clay minerals is involved.

Since the breach growth in clay-dikes is such a complicated process and is susceptible to so many factors, it is still necessary to continue the research with more experiments (especially large-scale experiments) and with more pertinence, even after the performance of these two series of tests.

Table 6.5 Comparison between the IMPACT Project experiments and the DUT experiments.

		IMPACT tests		DUT tests			
		T <sub>10</sub>	T <sub>12</sub>	T <sub>1</sub>	T <sub>2</sub>	T <sub>3</sub>	T <sub>4</sub>
Shape and dimension of dike	Height (cm)	60	60	75	75	75	75
	Crest length (m)	4.0	4.0	0.4	0.4	0.4	0.4
	Crest width (cm)	20	20	60	60	60	60
	Upstream slope	1:2	1:2	1:2	1:2	1:2	1:2
	Downstream slope	1:2	1:2	1:2	1:2	1:2	1:2
	Foundation	not erodible	not erodible	not erodible	not erodible	not erodible	not erodible
Properties of soil	Void ratio	1.22	1.38	0.62	0.61	0.60	0.58
	Water content (%)	25.0	25.0	17.6	16.7	16.7	15.4
	Degree of saturation (%)	52.9	46.7	75.8	73.2	74.7	70.7
	Soil bulk density (kg/m <sup>3</sup> )	1451	1350	1938	1936	1951	1948
	Soil dry density (kg/m <sup>3</sup> )	1161	1083	1648	1659	1672	1688
	Undrained shear strength (kPa)	-	-	22.1	24.6	26.4	26.8
	Cohesion (kPa)	31.0	31.0	-	-	-	-
	Internal friction angle (°)	22.5	22.5	-	-	-	-
	D <sub>50</sub> (µm)	5	5	53	63	63	63
Composition of soil (%)	Clay (<2 µm)	24.0	24.0	12.0	10.3	10.3	10.3
	Silt (> 2 µm)	75.0	75.0	37.5	35.1	35.1	35.1
	Sand (> 50 µm)	1.0	1.0	50.6	54.6	54.6	54.6
Test duration <sup>1</sup>		about 2.92 hrs	about 0.93 hrs	9.20 hrs	4.12 hrs	4.07 hrs	2.97 hrs

<sup>1</sup> For tests T<sub>10</sub> and T<sub>12</sub>, the test duration is estimated from the measured breach outflow rate. For tests T<sub>2</sub>, T<sub>3</sub> and T<sub>4</sub>, the test stopped when only a very small dike body was left; however, for test T<sub>1</sub>, the test was stopped after more than 9 hours of erosion with still a considerable dike body remaining (see Figure 6.9).



## Chapter 7

### Model calibration and validation

#### 7.1 Introduction

In this chapter the newly developed breach growth model (as outlined in Chapter 5) is calibrated (see Section 7.2) and validated (see Section 7.3) with the experimental data from both the DUT laboratory experiments (i.e. tests  $T_1$ ,  $T_2$ ,  $T_3$  and  $T_4$ ) and the EC IMPACT Project laboratory experiments (i.e. tests  $T_{10}$  and  $T_{12}$ ). To investigate the sensitivity of the model to the soil erodibility coefficient  $M_e$ , a model comparison with test  $T_{11}$  of the EC IMPACT Project laboratory experiments is conducted (see Section 7.4).

The breaching of dikes is not a rare phenomenon in the world; however, data from these failures are scarce. In the summer of 1998, due to extremely heavy rainfall, an extraordinarily huge basin wide flood occurred along the Yangtze River in China (see Chapter 1). The flood overtopped the dike crest at numerous locations in the river basin and breached the dikes of many larger and smaller polders. Among others the Lizhou Polder was flooded (for reasons of confidentiality, the real name of the polder has been modified here). Fortunately some data of this dike failure have been collected, providing a possibility to confront the mathematical model with this prototype case. The results of this confrontation are given in Section 7.5. In Section 7.6 a discussion on the model calculation is presented.

#### 7.2 Model calibration with tests $T_1$ , $T_2$ , $T_{10}$ and $T_{12}$

##### 7.2.1 Model calibration with tests $T_1$ and $T_2$

The experiments performed in the laboratory of Delft University of Technology focused on the first three stages of the five-step breach erosion process (see Chapters

4 and 5). Among the four tests with sand-silt-clay mixtures (i.e.  $T_1$ ,  $T_2$ ,  $T_3$  and  $T_4$ ), tests  $T_1$  and  $T_2$  are applied to calibrate the material dependent factor  $M_e$  in the model. Tests  $T_3$  and  $T_4$  are then utilized for the model validation (see Section 7.3). The input data for the model prediction for tests  $T_1$  and  $T_2$  are summarized in Tables 7.1 and 7.2, respectively.

In the model, the critical shear stress for erosion ( $\tau_c$ ) of the soil material is an important parameter, especially for the early stage of the dike breach erosion process. However, determination of this value requires additional measurements with difficulties in, e.g. selecting a criterion to define the initiation of erosion (see Chapter 3). In view of the very small erosion rate at the dike crest in a considerably long period after starting of the tests, in the present study  $\tau_c$  is determined according to the calculated breach flow bed shear stress ( $\tau_b$ ) at the dike crest for the time shortly after  $t = t_0$ , with  $\tau_c$  assuming slightly smaller than  $\tau_b$ .

Manning's roughness coefficient ( $n$ ) follows the recommended value for the tests of  $T_{10}$  and  $T_{12}$  (see Section 7.2.2). A critical slope angle (i.e.  $\beta_i$ ) of  $80^\circ$  is adopted for all the calculations in this study. The input dike height is set at  $H_d = 0.85$  m (instead of 0.75 m) just to accommodate an "imaginary" initial breach with a depth of  $h = 0.1$  m, which is just deep enough to hold the initial water depth over the dike crest.

Table 7.1 Input data for test  $T_1$ .

Item		Value	Item		Value
Shapes and dimensions of the dike and initial breach	$H_d$ (m)	0.85	Properties of the dike material	$n$ (-)	0.025
	$Z_{br}$ (m)	0.75		$\phi$ ( $^\circ$ )	-
	$\gamma$ ( $^\circ$ )	90.0		$c$ (N/m <sup>2</sup> )	-
	$b$ (m)	0.4		$\tau_c$ (N/m <sup>2</sup> )	6.8
	$h$ (m)	0.1		$\tau_t$ (N/m <sup>2</sup> )	6300
	$\beta_0$ ( $^\circ$ )	26.5		$\tau_s$ (N/m <sup>2</sup> )	22100
	$\beta_i$ ( $^\circ$ )	80.0		$M_e$ (s-m <sup>2</sup> /kg)	1.0E-6
	$W_0$ (m)	0.6		$\rho_s$ (kg/m <sup>3</sup> )	1938
	$\alpha$ ( $^\circ$ )	26.5		$\rho_{sat}$ (kg/m <sup>3</sup> )	2031
Others	$m$ (-)	1.0	Polder	$Z_p$ (m)	0.0
	$\rho$ (kg/m <sup>3</sup> )	1000.0		$H_p$ (m)	0.05
	$t_0$ (s)	0.0	Properties of the dike foundation	non-erodible	-
	$dt$ (s)	1.0			

Table 7.2 Input data for test T<sub>2</sub>.

Item		Value	Item		Value
Shapes and dimensions of the dike and initial breach	$H_d$ (m)	0.85	Properties of the dike material	$n$ (-)	0.025
	$Z_{br}$ (m)	0.75		$\phi$ (°)	-
	$\gamma$ (°)	90.0		$c$ (N/m <sup>2</sup> )	-
	$b$ (m)	0.4		$\tau_c$ (N/m <sup>2</sup> )	5.0
	$h$ (m)	0.1		$\tau_t$ (N/m <sup>2</sup> )	7000
	$\beta_o$ (°)	26.5		$\tau_s$ (N/m <sup>2</sup> )	24630
	$\beta_t$ (°)	80.0		$M_e$ (s·m <sup>2</sup> /kg)	2.7E-6
	$W_o$ (m)	0.6		$\rho_s$ (kg/m <sup>3</sup> )	1936
	$\alpha$ (°)	26.5		$\rho_{sat}$ (kg/m <sup>3</sup> )	2038
Others	$m$ (-)	1.0	Polder	$Z_p$ (m)	0.0
	$\rho$ (kg/m <sup>3</sup> )	1000.0		$H_p$ (m)	0.05
	$t_o$ (s)	0.0	Properties of the dike foundation	non-erodible	-
	$dt$ (s)	1.0			

Since the flow at the downstream side of the dike in Flume 1 is very dynamic with a small water depth and a large flow velocity (see Appendix A), the results of measurements from the instruments of G15 and E7 at the downstream end of the flume are fluctuating strongly and are therefore not suitable for estimation of the "measured" breach flow rate. The "measured" breach flow rate is thus deduced from the water level measurement of G17 and the flow velocity measurement of E11 (see Figures 6.6 and 6.7), by combining the volume change of the water stored between the measuring point and the breach. A certain error could be induced by assuming a uniformly distributed flow velocity over the flume width; however, the calculated thickness of the boundary sublayer due to flume sidewalls (e.g. through equation 3.146 on page 122 in Simons and Sentürk, 1992) is of the order of magnitude of 1 mm.

The soil tensile strength is a property that is difficult to quantify. Comparing with the many experimental data on the soil shear strength, those on the soil tensile strength are much scarcer. In geotechnical engineering it is common to assume a zero value for the soil tensile strength (see e.g. Huang, 1983; Amer, 1991; Krishnayya et al., 1974). Yet, some investigators have tried to find a relationship between the soil tensile strength ( $\tau_t$ ) and the compressive strength ( $\sigma_u$ ). Results of drained tension and compression tests on "intact" blue London Clay (see Bishop and Garga, 1969) yielded values of  $\sigma_u/\tau_t$  of 5.6 and 7.0. Narain and Rawat (1970) performed diametral compression tests and unconfined compression tests on six different compacted soils and found that the ratio of  $\sigma_u/\tau_t$  at optimum water content varies from 6 to 12. Amer (1991) conducted unconfined and confined compression tests, and stress concentration tension tests on three different soil types: CL (clay of low plasticity), CH (clay of high plasticity) and ML (silt of low plasticity). The ratio of  $\sigma_u/\tau_t$  was found to vary in a

relatively wide range for the CL soil (from 3.4 to 15.0). The ratio of cohesion ( $c$ ) to the tensile strength for the CH soil falls in the scope of 0.7 to 1.4, and for the CL soil in the scope of 0.9 to 3.5. In the present calculation a ratio of 7.0 for  $\sigma_u/\tau_t$  for tests T<sub>1</sub>, T<sub>2</sub>, T<sub>3</sub> and T<sub>4</sub>, a ratio of 1.1 for  $c/\tau_t$  for tests T<sub>10</sub>, T<sub>11</sub> and T<sub>12</sub> (CH soil), and 2.2 for  $c/\tau_t$  for the prototype dike failure (CL soil) is used to estimate the soil tensile strength.

As described in Appendix A, the flow velocity measurement of E11 failed during test T<sub>4</sub> and during test T<sub>1</sub> on 9 August 2005 due to instrument failure. Accordingly the "measured" breach flow rate cannot be calculated for these two cases.

Figures 7.1 and 7.2 present the model prediction results vs. experimental measurements of the breach flow for tests T<sub>1</sub> and T<sub>2</sub>, respectively, and Figures 7.3 and 7.4 the evolution of the dike height for these two tests, respectively. The agreement between the results of model prediction and experimental data is good. Furthermore, Table 7.3 gives a comparison between the model predictions and the measurements on the peak breach flow rate and the averaged lowering rate of the dike height.

For test T<sub>2</sub> (and tests T<sub>3</sub> and T<sub>4</sub> as well, see Section 7.3), heavy slope mass failure occurred when the headcut migrated backwards to the upstream slope of the dike, leading to a rapid fall of the dike height and an instant increase of the breach flow, see Figures 7.2 and 7.4, and Figures 7.9 through 7.11 in Section 7.3. In all these three tests the limit of the pump capacity (about 100 l/s) was reached at that time, hence the upstream water level soon dropped sharply, consequently the breach flow rate also. However, during the model calculation no slope mass failure was reproduced at the corresponding moment, which makes the fall of the calculated breach flow rate much more notable.

Table 7.3 Comparisons of measured and predicted peak breach flow rate and averaged lowering rate of dike height for tests T<sub>1</sub> and T<sub>2</sub>.

Test	Peak breach flow rate			Averaged lowering rate of dike height		
	measured (l/s)	predicted (l/s)	error (%)	measured (cm/hr)	predicted (cm/hr)	error (%)
T <sub>1</sub> (10 August 2005)	67.8	54.3	-19.9	2.22	1.91	-14.0
T <sub>2</sub>	117.0	123.2	5.3	12.12	11.04	-8.9

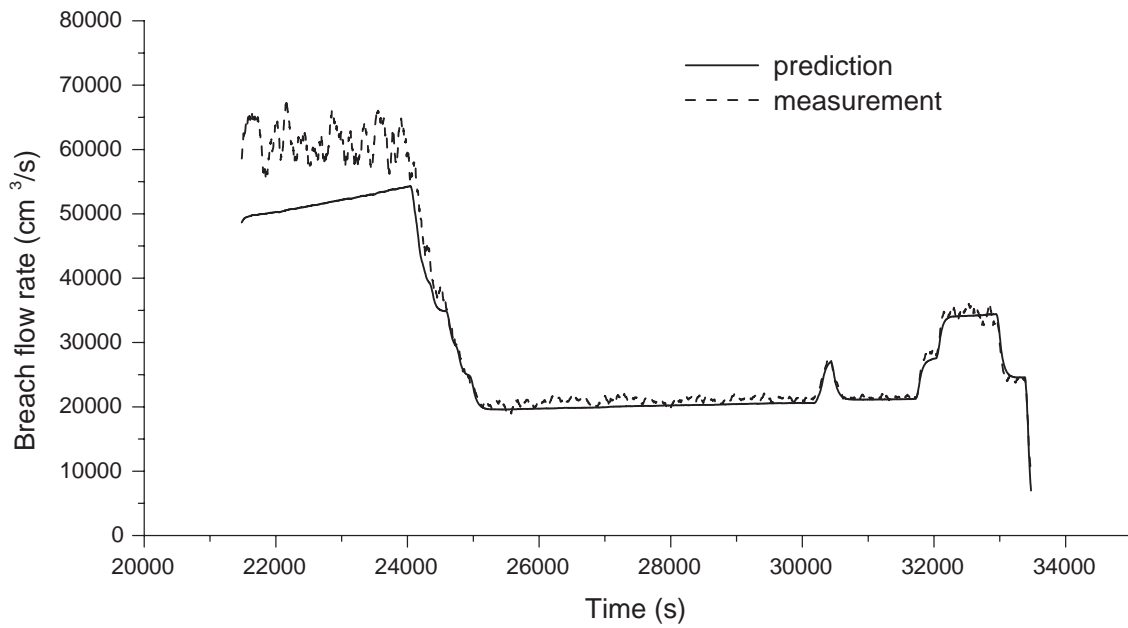


Figure 7.1 Comparison of predicted and measured breach flow rate for test T<sub>1</sub> (for 10 August 2005).

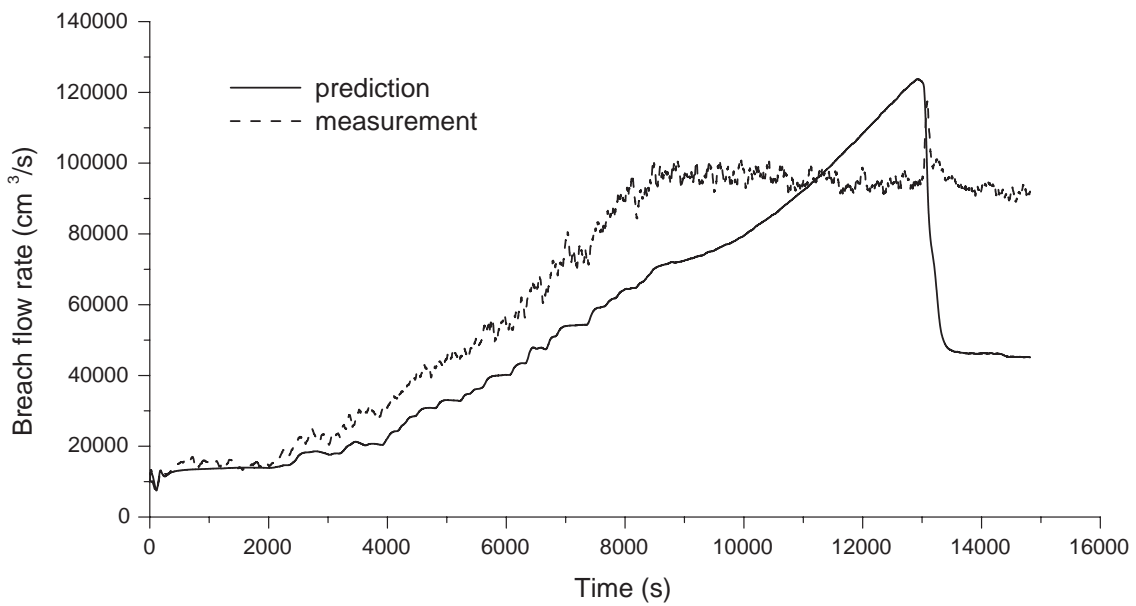


Figure 7.2 Comparison of predicted and measured breach flow rate for test T<sub>2</sub>.

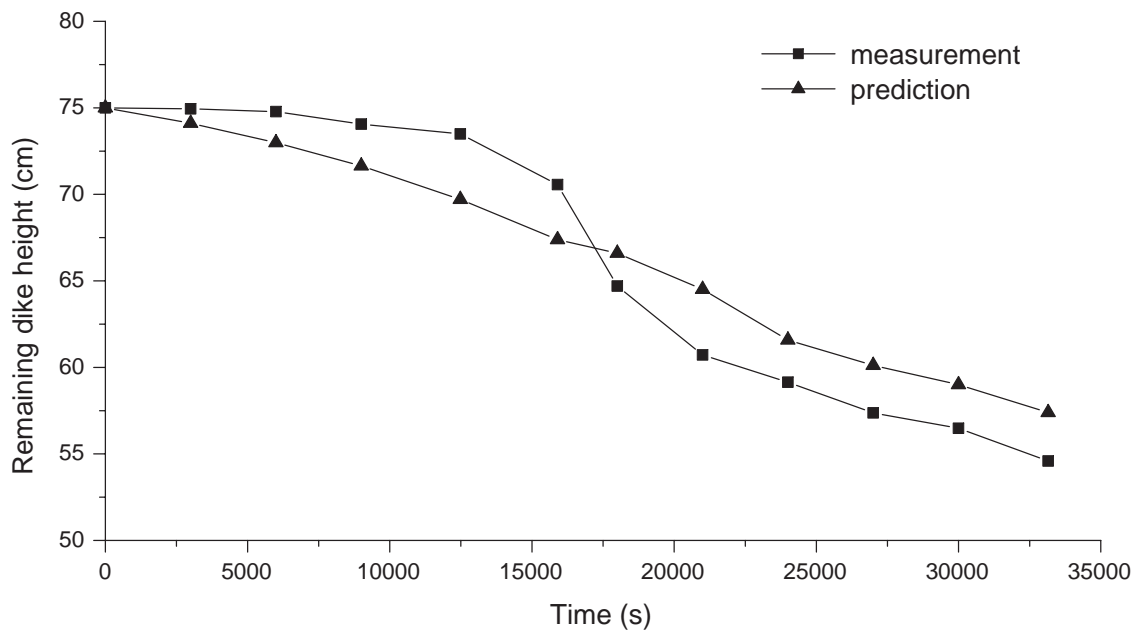


Figure 7.3 Comparison of predicted and measured dike height evolution for test  $T_1$ .

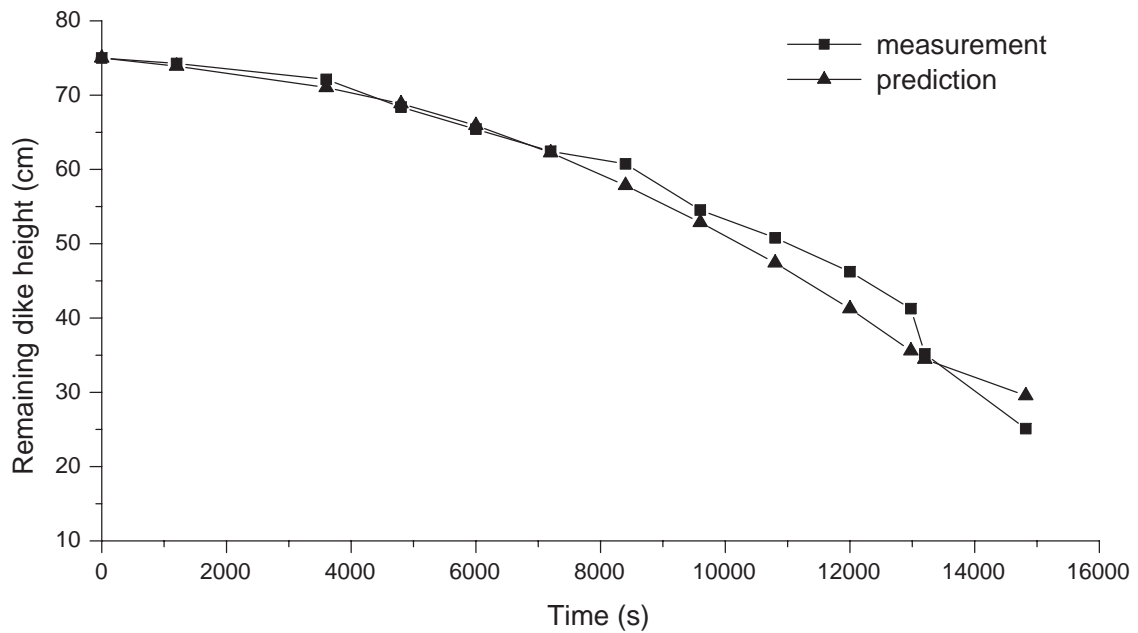


Figure 7.4 Comparison of predicted and measured dike height evolution for test  $T_2$ .

### 7.2.2 Model calibration with tests T<sub>10</sub> and T<sub>12</sub>

During the EC IMPACT Project laboratory experiments the starting point of breach erosion  $t_0$  was not sharply specified, making the comparison between different tests very difficult. For instance, it is claimed that the laboratory dikes in tests T<sub>10</sub> and T<sub>16</sub> were built with the same cohesive soil and that their embankment profiles are almost the same except the downstream slope of test T<sub>16</sub> being gentler (1:3) than that of test T<sub>10</sub> (1:2). However, from the experimental data it is found that under even lower upstream water level, test T<sub>16</sub> has a much faster breach width growth and a larger breach outflow discharge than test T<sub>10</sub> (see Figure 7.5, and Figures A.28 and A.34 in Appendix A).

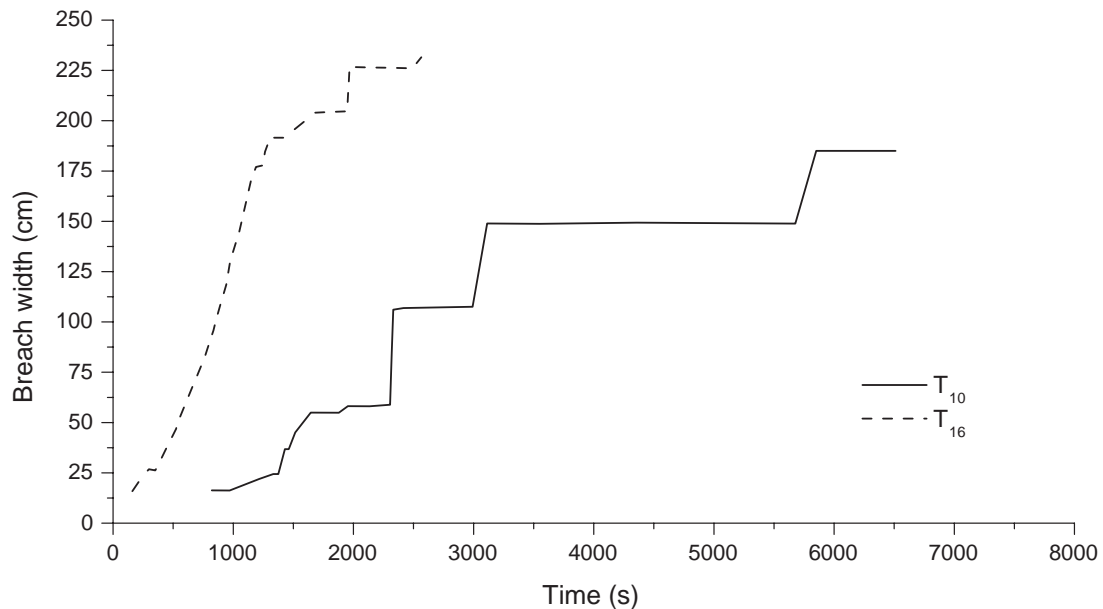


Figure 7.5 Comparison of breach width increase between tests T<sub>10</sub> and T<sub>16</sub>.

In the present study only tests T<sub>10</sub>, T<sub>11</sub> and T<sub>12</sub> are selected for the model calculation, in which tests T<sub>10</sub> and T<sub>12</sub> are employed to calibrate the material dependent factor  $M_e$  in the model. The soil material used in the three tests is the same except test T<sub>12</sub> in which only half the compaction effort was applied. Since test T<sub>11</sub> was aimed at a reproduction of test T<sub>10</sub>, it is not applicable for either model calibration or validation here. Instead, a calculation with test T<sub>11</sub> to check the sensitivity of the model to the erosion coefficient  $M_e$  is performed, see Section 7.4.

The input data for tests T<sub>10</sub> and T<sub>12</sub> are summarized in Tables 7.4 and 7.5, respectively. In the provided experimental data, a value of 0.025 was recommended for Manning's roughness coefficient ( $n$ ). Since no information has been gained on the soil erosion resistance, the critical shear stress for erosion ( $\tau_c$ ) is determined by

reference to Kamphuis et al. (1983, see their Table 1), in which  $\tau_c$  was measured for a series of cohesive soil with different proportions of clay, silt and sand. This is a rough estimation for  $\tau_c$ , however, since  $\tau_c$  is much smaller than the flow induced bed shear stress  $\tau_b$ , the error generated is not significant.

The calibration results of tests T<sub>10</sub> and T<sub>12</sub> indicate that a smaller value of  $M_e$  is required for Stages IV and V than for the first three stages. The diminishing ratio is 1/2.7 for these two calibrated tests ( $M_e = 2.0\text{E-}5$  s-m<sup>2</sup>/kg for T<sub>10</sub> and 7.2E-5 s-m<sup>2</sup>/kg for T<sub>12</sub> for Stages I, II and III, and  $M_e = 7.4\text{E-}6$  s-m<sup>2</sup>/kg for T<sub>10</sub> and 2.7E-5 s-m<sup>2</sup>/kg for T<sub>12</sub> for Stages IV and V). This ratio is followed in the model confrontation with the prototype dike failure in Section 7.5. The flow regime changes dramatically from the first three stages to the last two stages during the breach erosion process of clay-dikes, e.g. the Froude number varies from values of order 8 at the toe of the dike in the first three stages to 1 in Stage IV and practically 0 at the end of Stage V, see also Visser's (1998) model for sand-dikes. Therefore, adopting two values of  $M_e$  (instead of one) in the present model, one for the first three stages, one for Stages IV and V, is necessary.

Figures 7.6 and 7.7 show the comparisons between the measured and predicted breach flow rate and breach width increase of tests T<sub>10</sub> and T<sub>12</sub>, respectively. It can be seen from the figures that the agreement between the model predictions and the experimental data is good. Table 7.6 compares the results of model prediction with the measurements of the peak breach flow rate and the final breach width for the two tests.

Table 7.4 Input data for test T<sub>10</sub>.

Item		Value	Item		Value
Shapes and dimensions of the dike and initial breach	$H_d$ (m)	0.6	Properties of the dike material	$n$ (-)	0.025
	$Z_{br}$ (m)	0.55		$\phi$ (°)	22.5
	$\gamma$ (°)	26.5		$c$ (N/m <sup>2</sup> )	31000
	$b$ (m)	0.34		$\tau_c$ (N/m <sup>2</sup> )	2.0
	$h$ (m)	0.05		$\tau_t$ (N/m <sup>2</sup> )	28200
	$\beta_o$ (°)	26.5		$\tau_s$ (N/m <sup>2</sup> )	31900
	$\beta_i$ (°)	80.0		$M_e$ (s-m <sup>2</sup> /kg)	2.0E-5
	$W_o$ (m)	0.4		$\rho_s$ (kg/m <sup>3</sup> )	1451
	$\alpha$ (°)	26.5		$\rho_{sat}$ (kg/m <sup>3</sup> )	1711
Others	$m$ (-)	1.0	Polder	$Z_p$ (m)	0.0
	$\rho$ (kg/m <sup>3</sup> )	1000.0		$H_p$ (m)	0.02
	$t_o$ (s)	0.0	Properties of the dike foundation	non-erodible	-
	$dt$ (s)	2.0			

Table 7.5 Input data for test T<sub>12</sub>.

Item		Value	Item		Value
Shapes and dimensions of the dike and initial breach	$H_d$ (m)	0.6	Properties of the dike material	$n$ (-)	0.025
	$Z_{br}$ (m)	0.55		$\phi$ (°)	22.5
	$\gamma$ (°)	26.5		$c$ (N/m <sup>2</sup> )	31000
	$b$ (m)	0.34		$\tau_c$ (N/m <sup>2</sup> )	1.5
	$h$ (m)	0.05		$\tau_t$ (N/m <sup>2</sup> )	28200
	$\beta_o$ (°)	26.5		$\tau_s$ (N/m <sup>2</sup> )	31800
	$\beta_l$ (°)	80.0		$M_e$ (s-m <sup>2</sup> /kg)	7.2E-5
	$W_o$ (m)	0.4		$\rho_s$ (kg/m <sup>3</sup> )	1354
	$\alpha$ (°)	26.5		$\rho_{sat}$ (kg/m <sup>3</sup> )	1664
Others	$m$ (-)	1.0	Polder	$Z_p$ (m)	0.0
	$\rho$ (kg/m <sup>3</sup> )	1000.0		$H_p$ (m)	0.02
	$t_o$ (s)	0.0	Properties of the dike foundation	non-erodible	-
	$dt$ (s)	2.0			

Table 7.6 Comparisons of measured and predicted peak breach flow rate and final breach width for tests T<sub>10</sub> and T<sub>12</sub>.

Test	Peak breach flow rate			Final breach width		
	measured (m <sup>3</sup> /s)	predicted (m <sup>3</sup> /s)	error (%)	measured (cm)	predicted (cm)	error (%)
T <sub>10</sub>	0.332	0.316	-4.8	185.1	183.6	-0.8
T <sub>12</sub>	0.541	0.540	-0.2	254.9	216.0	-15.3

The initial breach width  $B_t = 0.54$  m for the three EC IMPACT Project laboratory tests (i.e. T<sub>10</sub>, T<sub>11</sub> and T<sub>12</sub>) has been obtained from the provided data (see Figures 7.6 and 7.7, and Figure 7.12 in Section 7.4). As for the breach width growth, the measurements shown in these figures indicate that a few number of massive mass failures occurred discretely from the breach side-slopes, which increased the breach width in a stepwise pattern in time with large steps. However, in the model, as described in Chapter 5, where the occurrence of mass failure from the breach side-slopes is assumed to be instantaneous and the failure soil is assumed to be washed away quickly from the field, the time and frequency of the occurrence of the side-slope mass failure will have no influence on the holistic rate of breach widening in Stages IV and V. The breach width increase is therefore only determined by the erosion rate at the toe of the breach side-slopes. This means that the model prediction tends to replace the actual stepwise increase of the breach width in time

with a more uniformly-climbing smooth line, see Figures 7.6 and 7.7, and Figure 7.12 in Section 7.4.

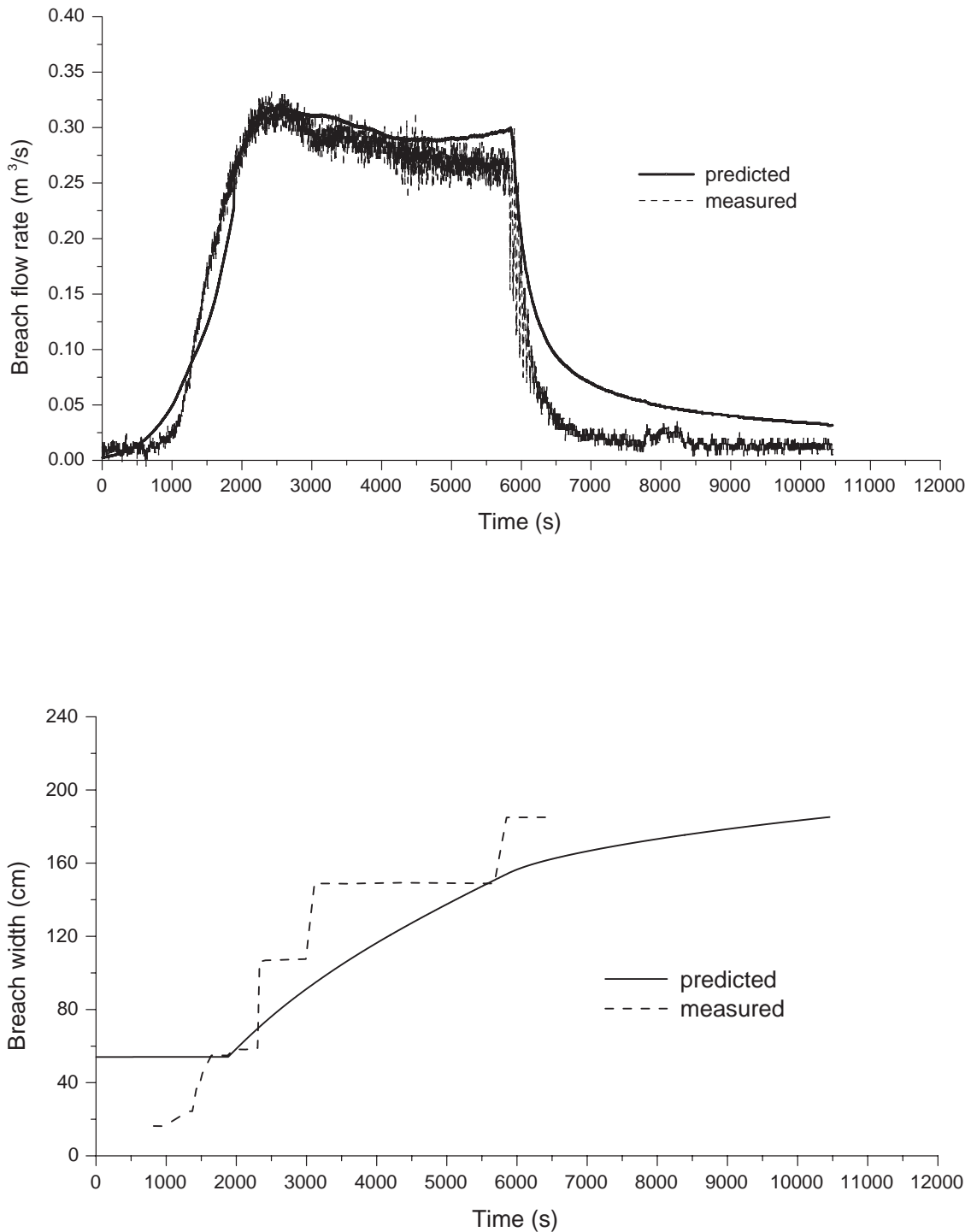


Figure 7.6 Comparisons of predicted and measured breach flow rate (upper panel) and breach width increase (lower panel) for test T<sub>10</sub>.

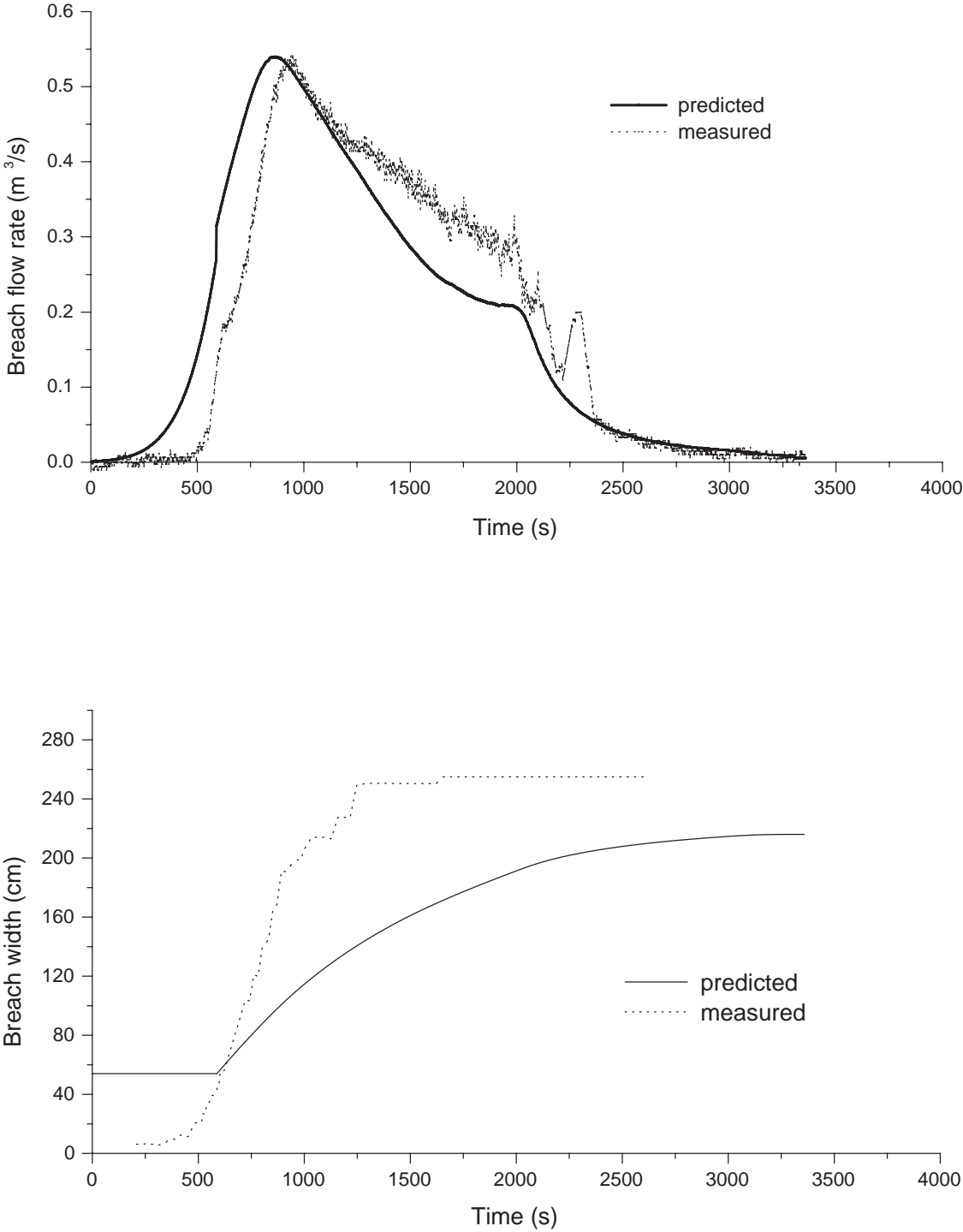


Figure 7.7 Comparisons of predicted and measured breach flow rate (upper panel) and breach width increase (lower panel) for test T<sub>12</sub>.

### 7.2.3 Establishment of a relationship between $M_e$ and soil properties

As described in Chapter 3, not much quantitative information can be found in the literature on the soil erodibility coefficient  $M_e$ . In addition, most of the reported values of  $M_e$  are for soft cohesive sediment or mud. The formula proposed by Winterwerp and Van Kesteren (2004) is also for mud and was only validated against data of experiments on mud.

Therefore, in this section, an effort is made to establish a relationship between  $M_e$  and the available soil properties as listed in Table 6.5 for the shear erosion of cohesive soil during dike breaching based on the calibration results of  $M_e$  for tests T<sub>1</sub>, T<sub>2</sub>, T<sub>10</sub> and T<sub>12</sub>.

$M_e$  should increase with a larger particle diameter (i.e. less cohesive), and decrease with an increasing soil cohesion and soil dry density (which is a combination of soil bulk density and water content and is commonly used to assess the compaction quality of soil fills). A detailed examination of the calibrated  $M_e$  and the available soil properties yields the following relationship

$$M_e = \frac{K [(s-1) g D_{50}]^{0.5}}{c (s-1)^{3.0}} \quad (7.1)$$

in which  $K$  is a non-dimensional coefficient,  $K = 0.642$ , see Figure 7.8,  $s = \rho_{dry}/\rho$  is the soil relative density,  $D_{50}$  is the median particle diameter in m and  $c$  is the soil cohesion in N/m<sup>2</sup>.

Figure 7.8 gives a graphical representation of Equation (7.1). It should be mentioned clearly that the values for the soil cohesion of tests T<sub>1</sub> and T<sub>2</sub> adopted here are the undrained shear strengths obtained through unconfined compression test (see Chapter 6), however, the values for the cohesion of tests T<sub>10</sub> and T<sub>12</sub> resulted from drained direct shear test (see Chapter 6). The reason that the DUT laboratory experiments did not follow the same method as the EC IMPACT Project laboratory experiments to measure the soil shear strength is, in the opinion of the author, that the clay-dikes were most likely under undrained (instead of drained) condition during the breaching processes which lasted only a couple of hours.

Further, the power of 3.0 in the denominator of Equation (7.1) is just a data fitted result lacking a clear physical meaning. There are presumably more of the numerous soil erodibility-influential factors (see Chapter 3) that should be included in the relationship for  $M_e$ . However, due to the limited data available, a simple formula is inevitable and probably also the most appropriate one. Further research in the future with more reliable experimental as well as prototype data is required to improve this expression.

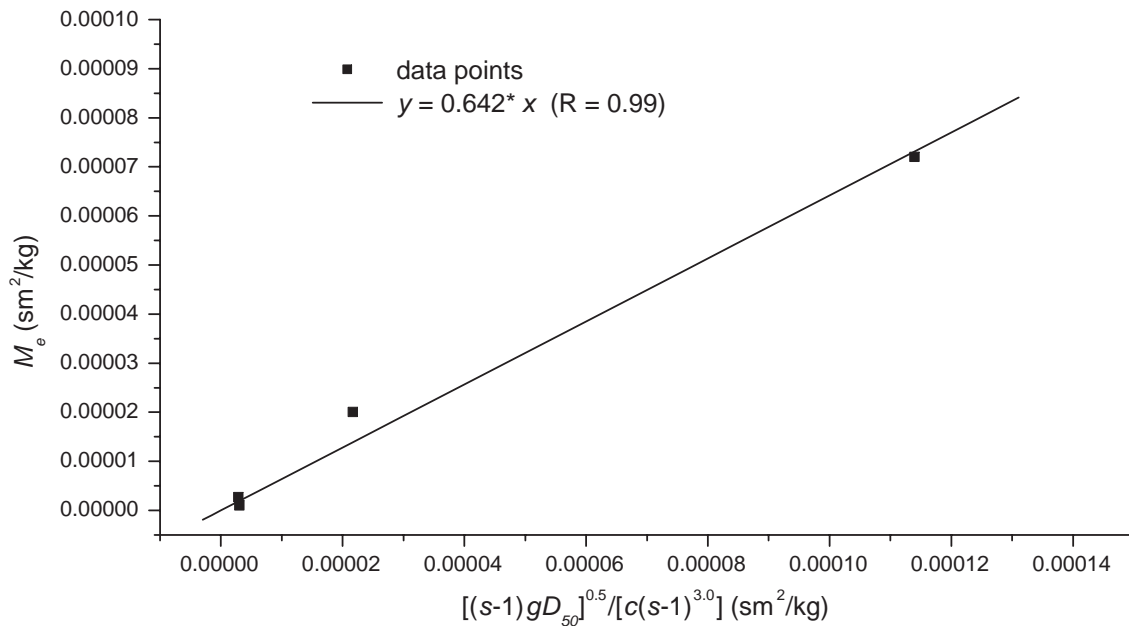


Figure 7.8 The calibrated  $M_e$  and Equation (7.1).

### 7.3 Model validation with tests T<sub>3</sub> and T<sub>4</sub>

Tests T<sub>3</sub> and T<sub>4</sub> are applied for validation of the model. The value of  $M_e$  for these two tests are determined by substituting the soil properties of the two tests (as listed in Table 6.5) into Equation (7.1). The input data for tests T<sub>3</sub> and T<sub>4</sub> are summarized in Tables 7.7 and 7.8, respectively.

Figures 7.9 through 7.11 show the model predictions vs. the measurements. For test T<sub>3</sub>, the model predicted breach flow is generally in the same tendency as the measurements, however, smaller for  $t > 7000$  s, indicating a slower predicted erosion rate than the measured one. Before that the agreement is rather good. Actually, during test T<sub>3</sub>, quite some (relatively small) mass erosion occurred over the dike crest after about 2 hours of testing (see e.g. Figure 6.11), which increased the breach flow accordingly. Then when the headcut migrated backwards to the upstream slope of the dike, massive slope mass failures occurred and led to a rapid fall of the dike height and an instant increase of the breach flow (see Figures 7.9 and 7.10, and Figures A.20, A.22 and A.23 in Appendix A). As stated earlier in Section 7.2, the limit of the pump capacity (about 100 l/s) was reached at that time during the experiment, as a result the upstream water level soon dropped rapidly, consequently also the breach flow (see the sharp-angled up and down of the measured flow rate in Figure 7.9). Unfortunately no slope mass failures were reproduced at the corresponding time in

the model prediction. Then the upstream water level soon became lower than the predicted remaining dike body and the calculation stops.

Table 7.7 Input data for test T<sub>3</sub>.

Item		Value	Item		Value
Shapes and dimensions of the dike and initial breach	$H_d$ (m)	0.85	Properties of the dike material	$n$ (-)	0.025
	$Z_{br}$ (m)	0.75		$\phi$ (°)	-
	$\gamma$ (°)	90.0		$c$ (N/m <sup>2</sup> )	-
	$b$ (m)	0.4		$\tau_c$ (N/m <sup>2</sup> )	5.0
	$h$ (m)	0.1		$\tau_t$ (N/m <sup>2</sup> )	7500
	$\beta_0$ (°)	26.5		$\tau_s$ (N/m <sup>2</sup> )	26420
	$\beta_t$ (°)	80.0		$M_e$ (s-m <sup>2</sup> /kg)	1.64E-6
	$W_0$ (m)	0.6		$\rho_s$ (kg/m <sup>3</sup> )	1951
	$\alpha$ (°)	26.5		$\rho_{sat}$ (kg/m <sup>3</sup> )	2046
Others	$m$ (-)	1.0	Polder	$Z_p$ (m)	0.0
	$\rho$ (kg/m <sup>3</sup> )	1000.0		$H_p$ (m)	0.05
	$t_0$ (s)	0.0	Properties of the dike foundation	non-erodible	-
	$dt$ (s)	1.0			

Table 7.8 Input data for test T<sub>4</sub>.

Item		Value	Item		Value
Shapes and dimensions of the dike and initial breach	$H_d$ (m)	0.85	Properties of the dike material	$n$ (-)	0.025
	$Z_{br}$ (m)	0.75		$\phi$ (°)	-
	$\gamma$ (°)	90.0		$c$ (N/m <sup>2</sup> )	-
	$b$ (m)	0.4		$\tau_c$ (N/m <sup>2</sup> )	5.6
	$h$ (m)	0.1		$\tau_t$ (N/m <sup>2</sup> )	7600
	$\beta_0$ (°)	26.5		$\tau_s$ (N/m <sup>2</sup> )	26750
	$\beta_t$ (°)	80.0		$M_e$ (s-m <sup>2</sup> /kg)	1.52E-6
	$W_0$ (m)	0.6		$\rho_s$ (kg/m <sup>3</sup> )	1948
	$\alpha$ (°)	26.5		$\rho_{sat}$ (kg/m <sup>3</sup> )	2056
Others	$m$ (-)	1.0	Polder	$Z_p$ (m)	0.0
	$\rho$ (kg/m <sup>3</sup> )	1000.0		$H_p$ (m)	0.05
	$t_0$ (s)	0.0	Properties of the dike foundation	non-erodible	-
	$dt$ (s)	1.0			

As described in Appendix A, due to failure of the flow velocity instrument of E11 during test T<sub>4</sub>, no "measured" breach flow hydrograph can be determined for this test. Therefore, only the dike height evolution has been compared between the model prediction and the measurement as shown in Figure 7.11. For test T<sub>4</sub>, as introduced in Chapter 6, the headcut was formed much earlier than expected because the erosion was initiated at the middle of the downstream slope of the dike. The erosion process therefore went considerably faster than it should go. At about  $t = 150$  min the headcut already retreated to the upstream slope of the dike, soon followed by some massive slope mass failures (see Figure 6.12). This explains the distinct difference between the model prediction for the dike height evolution and the observed one after about  $t = 9000$  s as shown in Figure 7.11. Before that the agreement between the predicted and measured dike height evolution is good.

It will be shown in the following Section 7.4 that the model is very sensitive to the soil erodibility coefficient  $M_e$ . Due to the limitation of available data to develop the relationship between  $M_e$  and the soil characteristics (i.e. Equation (7.1)), the accuracy of  $M_e$  resulting from Equation (7.1) could be not very high. This on one hand illustrates the importance to improve the relationship with more reliable experimental as well as prototype data in the future, on the other hand, may also partially explain the gap between the model predictions and the measurements as shown in Figures 7.9 through 7.11 for tests T<sub>3</sub> and T<sub>4</sub>.

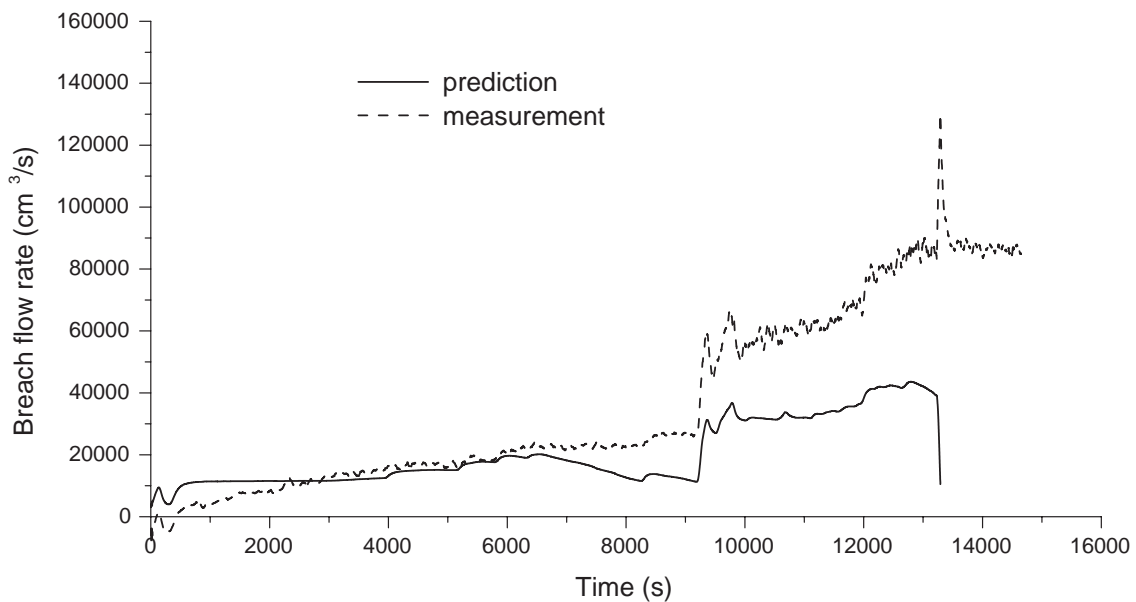


Figure 7.9 Comparison of predicted and measured breach flow rate for test T<sub>3</sub>.

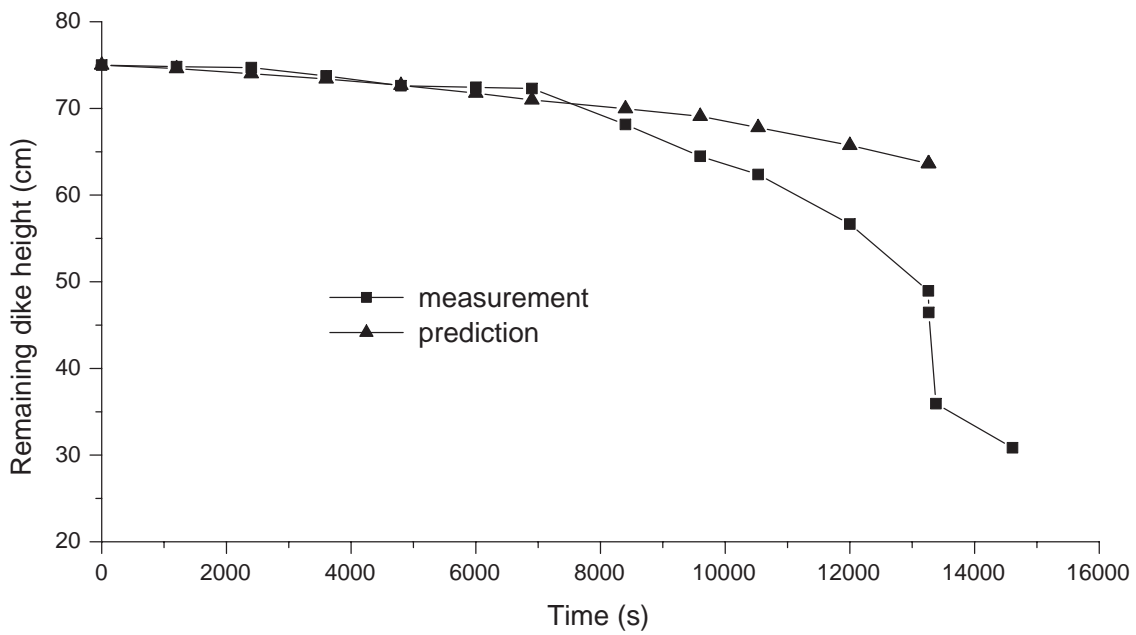


Figure 7.10 Comparison of predicted and measured dike height evolution for test  $T_3$ .

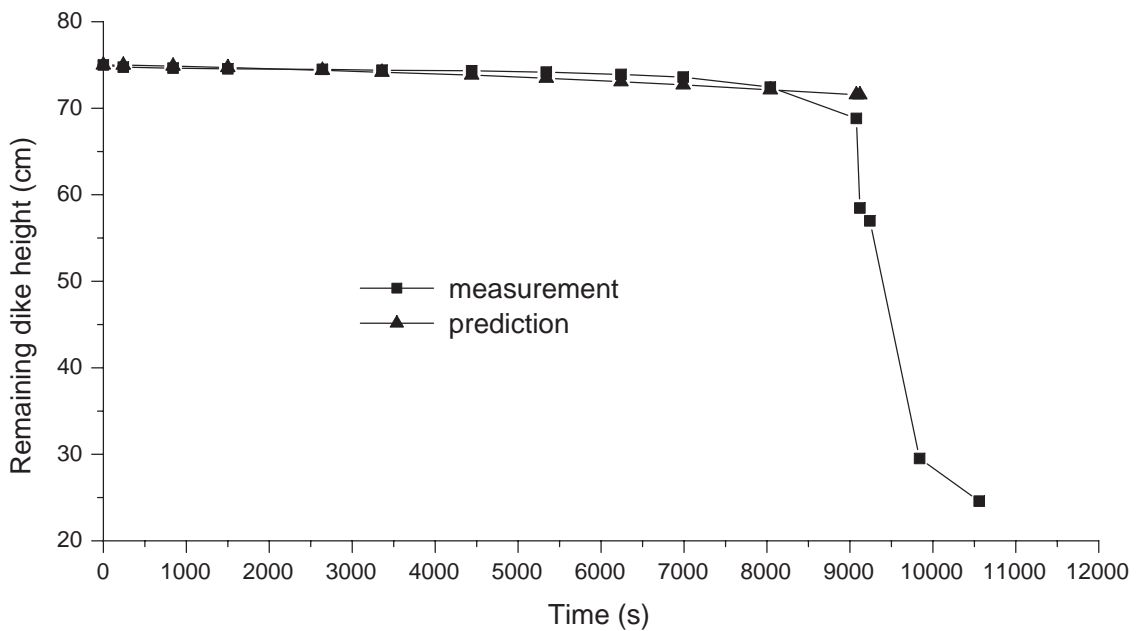


Figure 7.11 Comparison of predicted and measured dike height evolution for test  $T_4$ .

## 7.4 Sensitivity of the model to $M_e$

As described in Section 7.2.2, test T<sub>11</sub> was aimed at a reproduction of test T<sub>10</sub> to assess the test repeatability. It is therefore excluded from both the model calibration and validation. However, the sensitivity of the model to the soil erodibility coefficient  $M_e$  is investigated through calculation with test T<sub>11</sub> in this section. Three different values of  $M_e$  (namely, 1.8E-5 s-m<sup>2</sup>/kg, 2.0E-5 s-m<sup>2</sup>/kg and 2.2E-5 s-m<sup>2</sup>/kg, in which 2.0E-5 s-m<sup>2</sup>/kg is the calibrated  $M_e$  for test T<sub>10</sub>) have been chosen for the model calculation for test T<sub>11</sub>, see the input data summarized in Table 7.9.

Computed results are shown in Figure 7.12. It can be seen from the figure that the dependence of the model on  $M_e$  is significant. When  $M_e$  decreases from 2.0E-5 to 1.8E-5 s-m<sup>2</sup>/kg (i.e. 10% decrease), the predicted peak breach flow rate decreases by 16.6% (from 299.1 l/s to 249.6 l/s), the predicted final breach width decreases by 9.5% (from 1.68 m to 1.52 m), see Table 7.10 for a summary. When  $M_e$  increases from 2.0E-5 to 2.2E-5 s-m<sup>2</sup>/kg (i.e. 10% increase), the model predicted peak breach flow rate increases by 17.3% (from 299.1 l/s to 350.8 l/s), the model predicted final breach width increases by 11.3% (from 1.68 m to 1.87 m). Generally, the model predicted breach flow rate is more sensitive to variation of  $M_e$  than the final breach width.

In addition, the model predicted time of reaching the peak breach flow also varies when  $M_e$  changes (see Figure 7.12).

Table 7.9 Input data for test T<sub>11</sub>.

Item		Value	Item		Value
Shapes and dimensions of the dike and initial breach	$H_d$ (m)	0.6	Properties of the dike material	$n$ (-)	0.025
	$Z_{br}$ (m)	0.55		$\phi$ (°)	22.5
	$\gamma$ (°)	26.5		$c$ (N/m <sup>2</sup> )	31000
	$b$ (m)	0.34		$\tau_c$ (N/m <sup>2</sup> )	2.0
	$h$ (m)	0.05		$\tau_t$ (N/m <sup>2</sup> )	28200
	$\beta_0$ (°)	26.5		$\tau_s$ (N/m <sup>2</sup> )	31900
	$\beta_i$ (°)	80.0		$M_e$ (s-m <sup>2</sup> /kg)	1.8E-5/ 2.0E-5/ 2.2E-5
	$W_0$ (m)	0.4		$\rho_s$ (kg/m <sup>3</sup> )	1451
Others	$\alpha$ (°)	26.5	$\rho_{sat}$ (kg/m <sup>3</sup> )	1711	
	$m$ (-)	1.0	Polder	$Z_p$ (m)	0.0
	$\rho$ (kg/m <sup>3</sup> )	1000.0		$H_p$ (m)	0.02
	$t_0$ (s)	0.0	Properties of the dike foundation	non-erodible	-
$dt$ (s)	2.0				

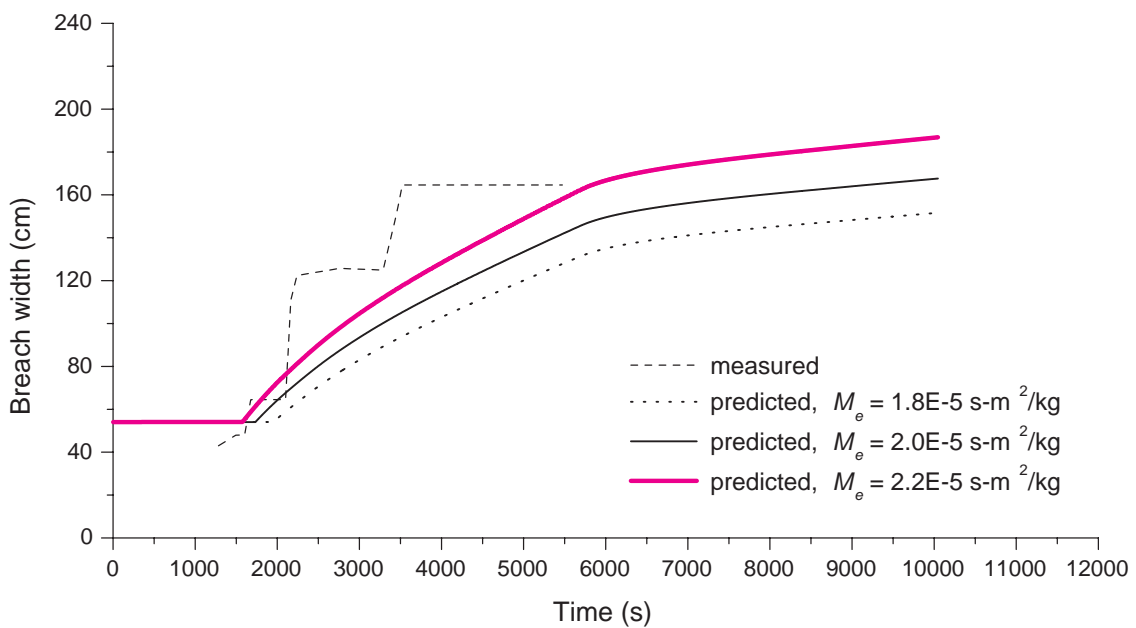
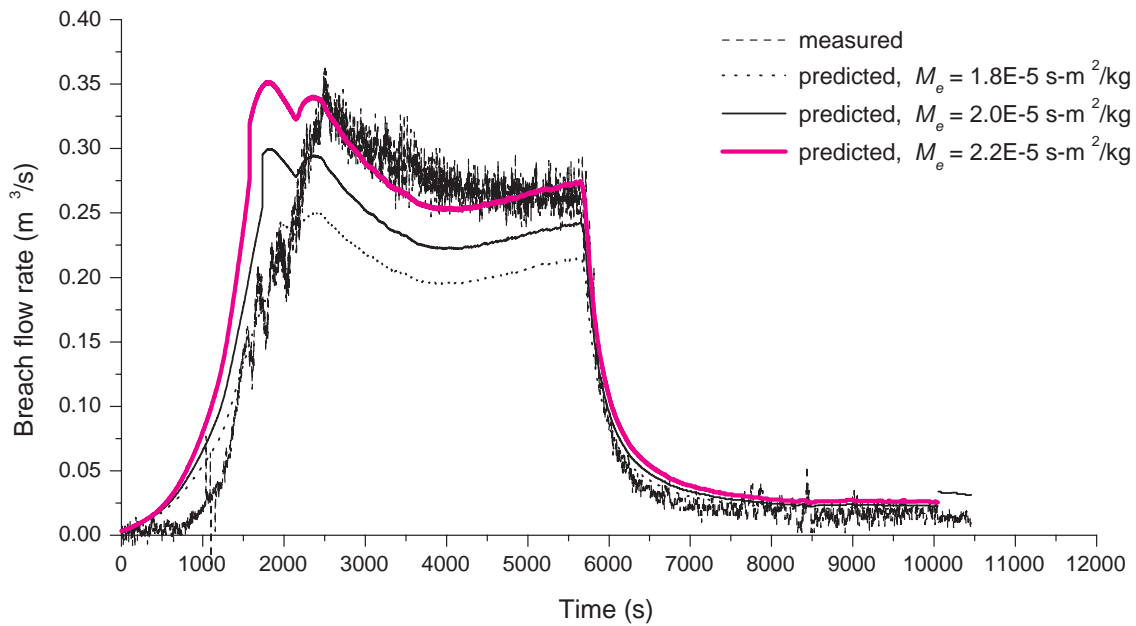


Figure 7.12 Sensitivity of the model predicted breach flow (upper panel) and the model predicted breach width increase (lower panel) to the soil erodibility coefficient  $M_e$  for test T<sub>11</sub>.

Table 7.10 Sensitivity of the model predicted peak breach flow and final breach width to variations of  $M_e$ .

No.	$M_e$ (s-m <sup>2</sup> /kg)	Change in $M_e$ (= $\frac{A_{2,3}-A_1}{A_1}$ )	Peak breach flow $Q_{brm}$ (l/s)	Change in $Q_{brm}$ (= $\frac{C_{2,3}-C_1}{C_1}$ )	Final breach width $B_{tm}$ (m)	Change in $B_{tm}$ (= $\frac{E_{2,3}-E_1}{E_1}$ )
	A	B	C	D	E	F
1	2.0E-5	-	299.1	-	1.68	-
2	1.8E-5	-10%	249.6	-16.5%	1.52	-9.5%
3	2.2E-5	10%	350.8	17.3%	1.87	11.3%

## 7.5 Model applied to a prototype dike failure

### 7.5.1 Description of polder and 1998 floods

Lizhou Polder is a flood storage polder in the drainage basin of the Yangtze River. It is completely surrounded by rivers and has a total area of 70.0 km<sup>2</sup>. The polder is subdivided by a secondary dike into two sub-polders: Li Polder (24.0 km<sup>2</sup>) and Zhou Polder (46.0 km<sup>2</sup>). The topography in Lizhou Polder is rather flat with an ordinarily low ground elevation RL + 30.9 m and a highest ground elevation RL + 33.8 m (RL = reference level; the levels of water, dike crest and others mentioned later in this section are all based on this reference level unless stated otherwise). Outside of the polder dike, a foreland of silty clay is present with reed and crops on most of it.

The earliest construction of the polder dike started in the early 20th century. Later the dike was repaired and strengthened intermittently for many times. However, due to lack of reasonable design and financing, hidden dangers such as incomplete dike foundation stripping and inadequate soil compaction are unavoidable. The quality of the dike is therefore questionable at some locations.

The crest level of the polder dike varies from 39.7 m to 40.7 m. The crest width is 6.0 to 8.0 m and the inner and outer slopes are 1:2.0 to 1:3.0. The dike body was mainly built with silty clay. The formation of the dike foundation from the top down is: (1) silty clay with thin interspersed fine sand layers, 5.0 to 12.0 m thick (② in Figure 7.13); (2) clay layer 1, 1.0 to 3.0 m thick (③ in Figure 7.13); (3) clay layer 2, 3.0 to 6.0 m thick (④ in Figure 7.13); and (4) sandy gravel, thicker than 2.0 m (⑤ in Figure 7.13). The physical and mechanical indices of the various soils are listed in Table 7.11.

In the morning of 24 July 1998, the water level in the river surrounding Lizhou Polder rose very quickly because of heavy rains. Although a 0.5 to 0.8 m high sub-dike was built urgently on top of the original dike, this sub-dike was broken through and washed away due to the very strong rainstorm at about 08:05 hr of 24 July at the eastern part of Li Polder. Consequently the dike of Li Polder was overtopped and

the breaching process began. Figure 7.14 shows the water level of the river outside of Lizhou Polder from 08:00 hr of 20 July to 05:00 hr of 29 July.

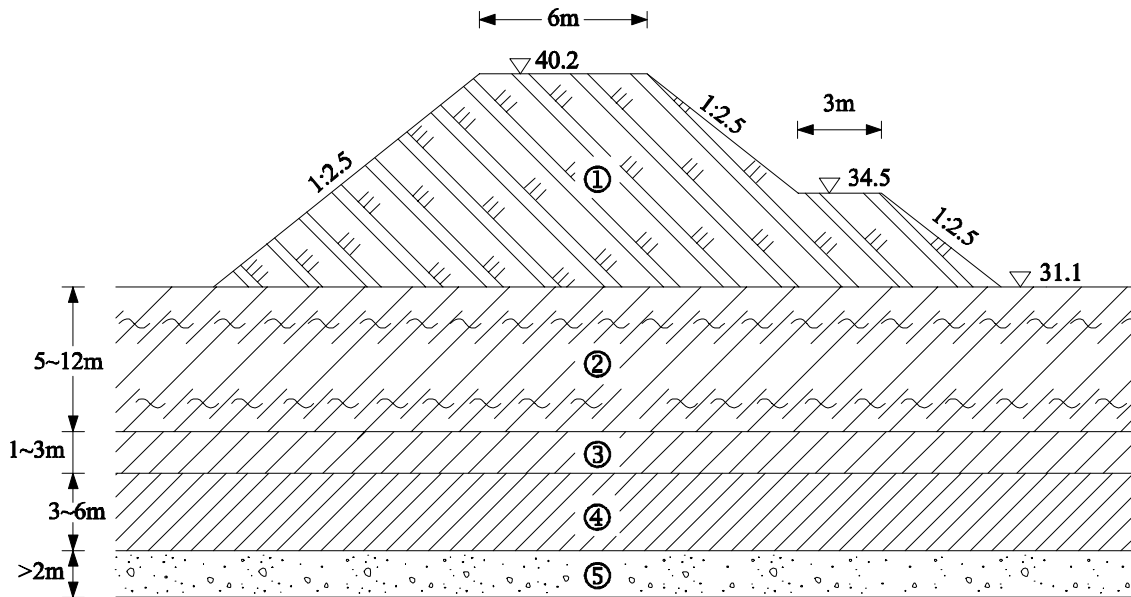


Figure 7.13 Cross-section of the dike body and dike foundation at the breach location: ①-silty clay; ②-silty clay with thin interspersed fine sand layers; ③-clay layer 1; ④-clay layer 2; ⑤-sandy gravel.

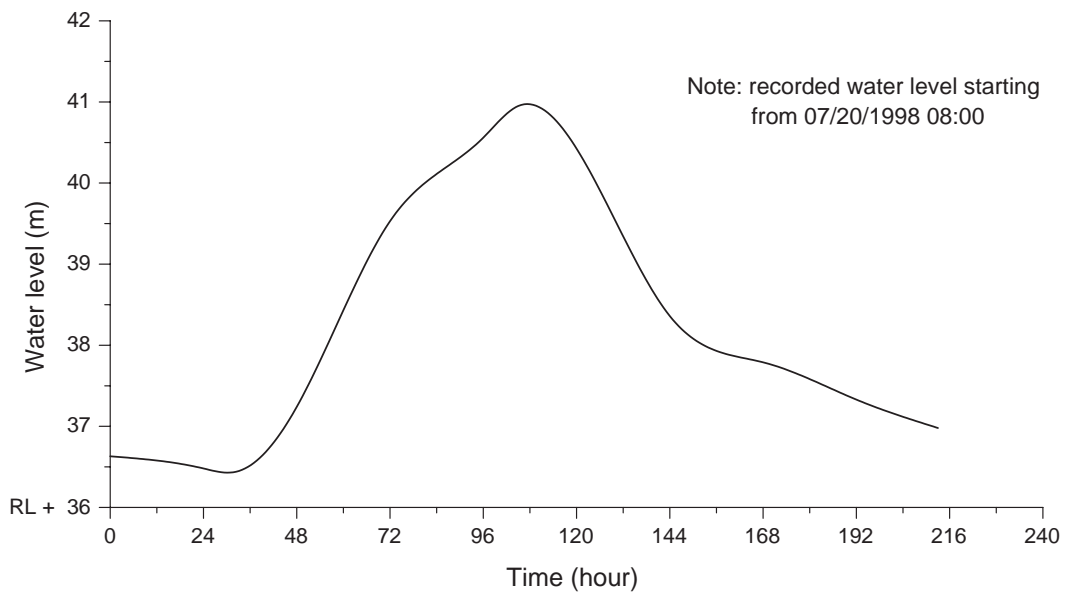


Figure 7.14 Water level of the river surrounding Lizhou Polder from 08:00 hr of 20 July to 05:00 of 29 July.

Table 7.11 Recommended values for the soil physical and mechanical indices.

Physical and mechanical indices	Dike body		Dike foundation		
	Silty clay	Silty clay with thin interspersed fine sand layers	Clay layer 1	Clay layer 2	Sandy gravel
Natural water content (%)	29~32	36.4	29.1	26.5	-
Natural Wet density (kg/m <sup>3</sup> )	1850	1840	1900	1960	-
Specific density	2.76	2.74	2.73	2.74	2.8
Internal friction angle (°)	13	6	10	-	25
Cohesion (kP <sub>a</sub> )	11	8	18	-	0
Critical velocity of incipient motion (m/s)	0.35 ~ 0.4	0.3 ~ 0.35	-	-	-

The breach in the dike of Li Polder developed rapidly and Li Polder was flooded shortly. The breach water marched towards the secondary dike separating Li Polder and Zhou Polder and overtopped the secondary dike at around 00:00 hr of 25 July, despite the emergent construction of a 1.0 m high sub-dike on the secondary dike a few hours before. At 02:15 hr of 25 July the secondary dike was breached and the whole Lizhou Polder was then inundated.

The final width of the breach in the protecting dike of Li Polder was 390 m, according to the post-flood investigation. The averaged inundation depth in Lizhou Polder was 7.5 m, and the total volume of diverted floodwater is estimated at about  $5.2 \times 10^8 \text{ m}^3$ .

### 7.5.2 Model prediction

The input data for the model prediction for Lizhou Polder dike breach are summarized in Table 7.12. An initial breach with a depth of 0.1m, a width at the bottom of 2.0 m and side-slopes of 1:5 is assumed in the crest of the dike. A value of 0.03 is taken for Manning's roughness coefficient according to the list of  $n$  values for channels of various kinds recommended by Chow (1959, Table 5-6 on page 112). The critical shear stress for erosion ( $\tau_c$ ) is estimated through the critical velocity of incipient motion listed in Table 7.11.  $M_e$  and  $M_{ef}$  are resulted from Equation (7.1) with  $D_{50}$  estimated according to the Chinese Code for Design of Levee Project ( $D_{50} = 35 \mu\text{m}$  for the dike body material and  $D_{50} = 40 \mu\text{m}$  for the dike foundation material).

Figure 7.15 shows the model results for the breach width increase in time. The predicted final breach width is 274 m, which is about 40% smaller than the post-flood investigated result of 390 m. Figure 7.16 shows the model results for the breach outflow discharge and the volume of diverted floodwater through the breach during the breach erosion process. The resulted  $5.6 \times 10^8 \text{ m}^3$  of diverted floodwater volume is very close to the investigation-based estimation of  $5.2 \times 10^8 \text{ m}^3$ .

Table 7.12 Summary of input data for Lizhou Polder dike breach.

Item		Value	Item		Value
Shapes and dimensions of the dike and initial breach	$H_d$ (m)	40.2	Properties of dike material	$n$ (-)	0.03
	$Z_{br}$ (m)	40.1		$\phi$ ( $^\circ$ )	13.0
	$\gamma$ ( $^\circ$ )	11.5		$c$ (N/m <sup>2</sup> )	11000
	$b$ (m)	2.0		$\tau_c$ (N/m <sup>2</sup> )	1.5
	$h$ (m)	0.1		$\tau_t$ (N/m <sup>2</sup> )	5000
	$\beta_o$ ( $^\circ$ )	19.5		$\tau_s$ (N/m <sup>2</sup> )	20700
	$\beta_l$ ( $^\circ$ )	80.0		$M_e$ (s-m <sup>2</sup> /kg)	9.6E-6
	$W_o$ (m)	6.53		$\rho_s$ (kg/m <sup>3</sup> )	1850
	$\alpha$ ( $^\circ$ )	21.8		$\rho_{sat}$ (kg/m <sup>3</sup> )	1900
Others	$m$ (-) <sup>1</sup>	1.0/1.3	Properties of dike foundation	$\tau_c$ (N/m <sup>2</sup> )	1.1
	$\rho$ (kg/m <sup>3</sup> )	1000.0		$M_{ef}$ (s-m <sup>2</sup> /kg)	2.2E-5
	$m_f$ (-)	2.0		$H_{max1}^2$ (m)	9.0
	$t_o$ (s)	0.0	Polder	$Z_p$ (m)	31.1
	$dt$ (s)	10.0		$H_p(t=0)$ (m)	30.9

<sup>1</sup>  $m = 1.0$  for Stages I through III;  $m = 1.3$  for Stages IV and V for this Type B breach.

<sup>2</sup>  $H_{max1}$  represents the thickness of the first layer composing the dike foundation. Model calculation indicates that the scour is restricted to the first layer of the dike foundation.

## 7.6 Discussion

Calibration of the model with tests T<sub>1</sub>, T<sub>2</sub>, T<sub>10</sub> and T<sub>12</sub> shows a good agreement between the model predictions and the experimental data. Based on the calibrated soil erodibility coefficient  $M_e$  for these four tests, a relationship has been established between  $M_e$  and the available soil properties. With this relationship, validation of the model against the data of tests T<sub>3</sub> and T<sub>4</sub> yields reasonable agreement between the model predictions and the measurements. The model has been confronted with a prototype dike failure in 1998 in China. The observed final breach width and the estimated diverted floodwater volume have been well reproduced.

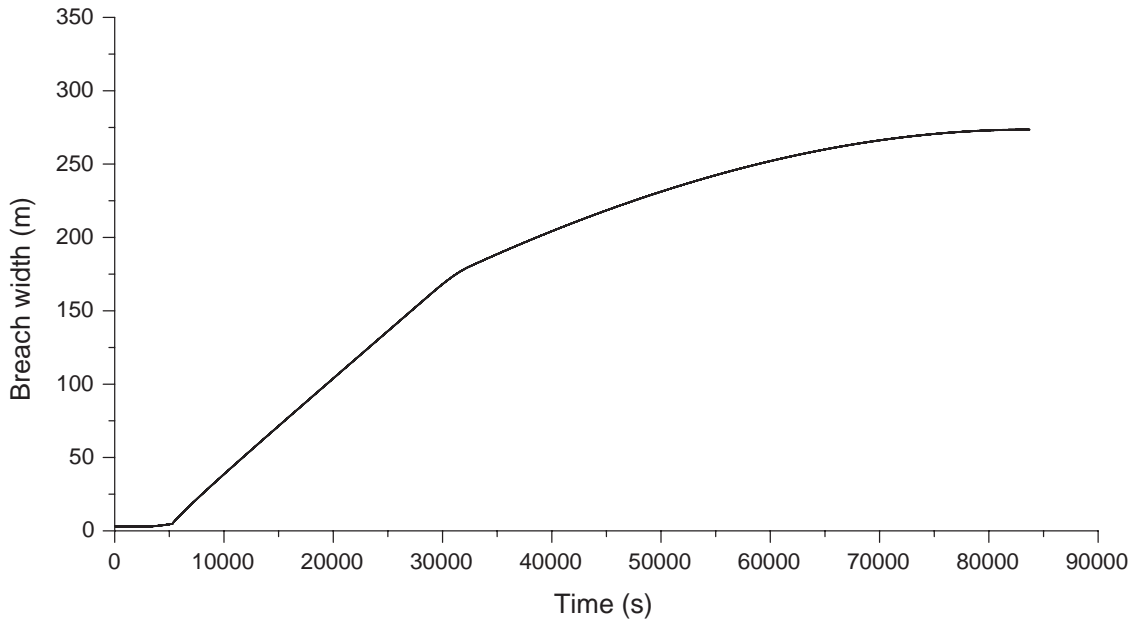


Figure 7.15 Model predicted breach width increase in time.

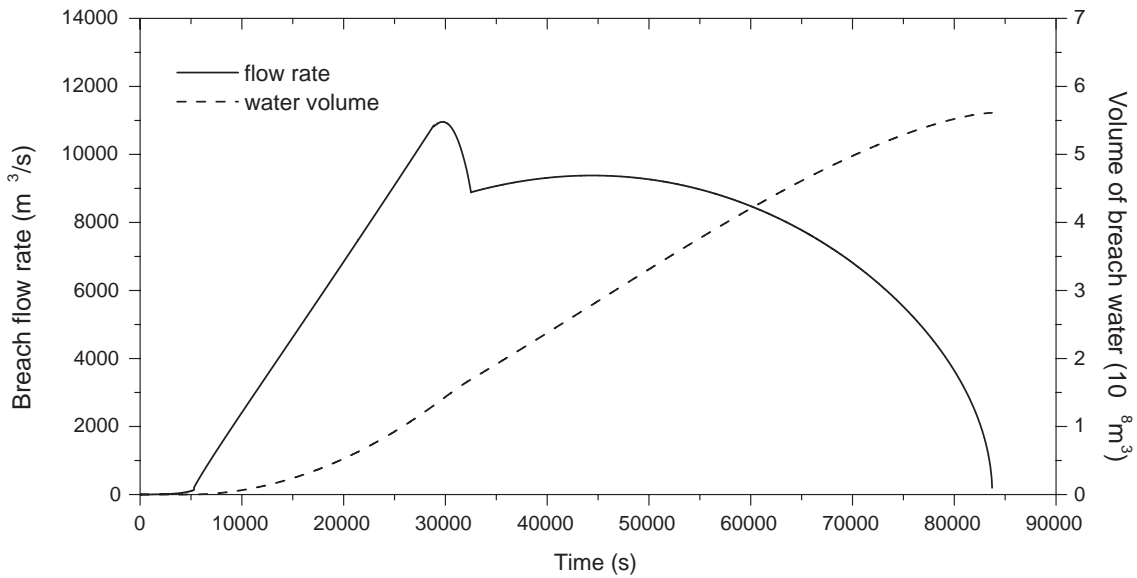


Figure 7.16 Model predicted breach outflow hydrograph and the volume of diverted floodwater.

Yet, for Stages II and III in the five-stage breach erosion process, it seems difficult to simulate the slope mass failure of the headcut in terms of the occurrence time and frequency, as summarized from the results of the model calculations for the DUT laboratory experiments and the EC IMPACT Project laboratory experiments. This is probably partly due to the assumption of a regular shape for the failure block of the headcut slope mass failure. Most importantly, no consideration has been taken into account (yet) of either the possible tensile crack(s) that appearing on the headcut crest or the water pressure (both dynamic and static) from the upstream flowing water acting on the upstream side of the failure block when the headcut migrates to the upstream slope of the dike.

Due to the limitation of the available data for establishing the relationship between  $M_e$  and the soil properties, the accuracy of the relationship could not be very high. More reliable data, from both laboratory and/or field experiments as well as prototype dike failures are strongly needed to further improve this relationship, which is very important for the applicability of the model.

## Chapter 8

### Conclusions and recommendations

#### 8.1 Introduction

In this thesis the physics of the breach erosion process in clay-dikes (i.e. dikes constructed with cohesive soil) has been investigated, based on which a mathematical model has been developed for this process. The model simulates the growth of a relatively small initial breach in the top of the dike and the development of the flow rate through the breach. Flow shear erosion, impinging jet scour, headcut slope mass failure and breach side-slope instability have been included in the model. Due to the large complexities involved, the present study aims only at homogeneous clay-dikes. In addition, possible effects of protection layers (e.g. vegetation cover and revetments) on the surface of the dike are not included, except those of a toe protection on the outer slope. Effects of waves are also not taken into account.

The model has been calibrated with the data of four laboratory experiments on clay-dike breaching and validated against the data of two other experiments. Finally, the model has been applied to a prototype dike failure in China in 1998.

The main conclusions of this thesis are summarized in the following section. At the end of this chapter in Section 8.3, recommendations for future research are given.

#### 8.2 Conclusions

The following conclusions are drawn from this study:

- In the process of breach development in clay-dikes, generally five stages can be distinguished, similar to that of sand-dikes (see Visser, 1998). However, as distinct from sand-dikes, headcut erosion can play a significant role in the breaching of clay-dikes. In Stage I, erosion occurs along the inner slope and, depending on the

flow velocity, possibly also along the dike crest, resulting in a decrease of the width and the height of the dike in the breach. Then in Stages II and III, the dike body in the breach is further eroded through a combination of (1) flow shear erosion, (2) fluidization of the surface of the slope, (3) impinging jet scour of the dike foundation and (4) discrete headcut slope mass failure, until at the end of Stage III the dike body in the breach has been washed away completely. In the following Stages IV and V, the breach grows further mainly laterally due to principally flow shear erosion along the side-slopes of the breach and the resulting discrete side-slope instability. The breach growth in vertical direction in these two stages relies mainly on the erodibility of the dike foundation, the presence and, if any, strength of a toe protection on the outer slope of the dike, and the presence and, if any, erodibility of a relatively high foreland. Three types of breach (Types A, B and C, see Chapters 4 and 5, see also Visser, 1998) have been distinguished for the further growth of the breach in Stages IV and V based on these conditions. The flow through the breach is decelerated by the rising inner water in the polder in Stage V, consequently also the breach enlargement. This flow ultimately stops when either the inner and outer water levels equal or the outer water level drops below the breach bottom.

- Headcut erosion plays a very important role in the process of breach growth in clay-dikes. The DUT laboratory experiments on clay-dike breaching have clearly shown this. In the process of breach growth, soil mechanical slope mass failure occurs discretely from the steepened downstream slope (i.e. headcut) of the dike in Stages II and III, however, not very frequently. Yet, when this headcut slope mass failure occurs, the loss of soil from the headcut could be a very large chunk, followed by an instant increase of the breach flow. Appearance of crack(s) is found to accompany the occurrence of headcut slope mass failure in many cases. Therefore for the erosion at a headcut, to sum up, two general mechanisms are involved: hydraulic erosion (including flow shear erosion, jet scour and fluidization, etc.) and soil mechanical slope mass failure.
- The DUT laboratory experiments on clay-dike breaching have also shown that erosion usually first occurs at locations close to the toe of the dike when the dike is overflowed. Soon this erosion extends to the entire slope, with a larger erosion rate occurring at the lower part of the slope than at the upper part, inducing a steepening of the slope in time. Besides the toe of the dike, the transition area between the dike crest and the downstream slope is the second place susceptible to earlier and faster erosion. Erosion at the dike crest is relatively slow.
- It can be concluded from the comparison between the four DUT laboratory experiments on dike breaching with cohesive soil mixtures and the one with pure sand that soil cohesiveness affects remarkably the breach erosion process. The cohesive portion in the soil mixtures strongly slowed down the speed of breach growth in the dike.

- Comparison between the DUT laboratory experiments and the EC IMPACT Project laboratory experiments on clay-dike breaching indicates that soil compaction (namely, soil dry density) is a very important factor affecting the rate of breach erosion (or the resistance of the soil against erosion). It even overshadowed the influence of the proportion of clay in the soil material on the breach erosion rate within the studied experiments.
- For the modeling of breach growth in dikes (and in earth dams), the key problem is the description of the rate of erosion of the dike by the flow. This conclusion applies to sand-dikes and, with greater force to dikes built with cohesive soil.
- The model has first been calibrated with the data of two DUT laboratory experiments and two EC IMPACT Project laboratory experiments on breach growth in clay-dikes. The model predictions are in good agreement with the experimental data. Based on the calibrated soil erodibility coefficient  $M_e$  for these four experiments, a relationship has been established between  $M_e$  and the available soil properties. With this relationship, the validation of the model against the other two DUT laboratory experiments yields reasonable agreement between the model predictions and the measurements. Finally, the model has been confronted with a prototype dike failure in China in 1998. The predicted final breach width of 274 m is about 40% smaller than the observed 390 m. The predicted  $5.6 \times 10^8 \text{ m}^3$  of diverted floodwater volume is very close to the investigation-based estimation of  $5.2 \times 10^8 \text{ m}^3$ .

### 8.3 Recommendations

The following recommendations are given for further research:

- Breach growth in clay-dikes is a very complicated process with unsatisfactory understanding so far. Therefore, in the present model some influential factors have been left out of consideration, e.g. effects of the dike surface protection layers, effects of waves and effects of composite structure of the dike. When the dike has a composite structure, different parts of the dike possess different characteristics. Simulation of breach growth in such a case is more complicated and the interactions between different parts of the dike should be taken into account. The influence of waves is especially important for the failure of sea dikes, but other dikes can also be attacked by relatively high waves. Waves will increase the erosion rate in the breaching process, in particular in Stages I, II and III. Dike surface protection layers affect considerably the breach growth, particularly the initiation of breach erosion and the breaching process in Stage I. More researches, including both desktop work and experiments, especially large-scale or full-scale experiments with specific interest on these aspects are recommended. Data from

these experiments are also important for the calibration and validation of the mathematical models.

- As concluded earlier in Chapter 2 and in this chapter, the description of the rate of flow erosion of the dike is a key issue for the simulation of breach growth in clay-dikes. Unfortunately, erosion of cohesive soil is a complicated process, and the state-of-the-art of the mathematical modeling of it is still not advanced. The expression developed in this study for calculation of the soil erodibility coefficient  $M_e$  is based on the calibration results of four laboratory experiments and the available (relatively limited) soil properties, which are not considered sufficient to guarantee high accuracy and reliability of the relationship. Improvement of the expression with more experimental as well as prototype data of good quality is recommended for future research.
- Headcut erosion has been discovered to play an important role in the breach growth in clay-dikes. However, difficulties are encountered in predicting the time and frequency of occurrence of headcut slope mass failure during clay-dike breaching. As a matter of fact, little information exists as yet on the headcut erosion process, especially on the headcut migration dynamics. Mathematical modeling of headcut erosion is only in an initial phase and far from mature. Improvement in these fields will surely benefit not only the research on headcut erosion itself, but also the mathematical modeling of breach growth in clay-dikes.
- It is recommended that the scale effect in experiments on clay-dike breaching and headcut erosion should be clearly recognized and more attention should be paid to it. For instance, in most of the laboratory (small-scale) experiments the properties of the cohesive soil (e.g. cohesion and strength) is not really (seriously) scaled, however, the hydraulic conditions are. Further, the (relatively) small height of the dike or headcut permitted in laboratory experiments affect substantially the slope stability conditions and consequently also the shape (i.e. single-step or multi-step) and migration of the headcut.
- Despite numerous prototype dike breaches occurring every year worldwide, data on these failures has been found to be limited, incomplete and of poor quality. However, reliable prototype data is of great significance for the calibration and validation of the breach erosion models. Of course when dike failure occurs, evacuation of people and property under threat is of the highest priority, but this can only partly explain the status quo of the available prototype data. Social cognition on the risk of dike failure is insufficient. The significance of the dike breach erosion simulation and of the prototype data collection and preservation has not been adequately acknowledged and emphasized. Practically, the risk of dike failure always exists and does not vanish with people's good wishes and the higher design standard applied for dikes. It is worthwhile to improve people's knowledge in these fields and, very importantly, it is recommended to set up special national organizations particularly being responsible for the data collection

and preservation in case of prototype dike failures. In addition, the rapidly developing satellite imagery technology provides a potential handy approach for the data collection of dike failures (e.g. shape and final width of the breach) in the future. For instance, the newly developed Google Earth already covers the whole world with medium resolution imagery (additional high resolution imagery for USA, Canada and Western Europe) and terrain data. Unfortunately, for the time being the images in Google Earth are photographs taken by satellites and aircraft not in real time, but sometime in the last three years instead. Further, specifying the date of the imagery for a specific position is also not yet possible.

- The final objective of mathematical modeling of breach growth in dikes is most likely to use the model for practical problems like dike safety assessment, or to implement the model into a decision-making support system for flood management and prevention. To be more specific, e.g. given a certain section of a prototype dike and given a certain forecasted flood, the following questions need to be answered by the model. Could a failure of the dike occur under this flood? If so, when and where? How fast would the breach develop and how large could the flow rate through the breach be? To answer these questions, on the one hand, the breach erosion models developed so far need further improvement; on the other hand, clear and accurate information on the dike itself needs to be known, e.g. dike structure, soil properties of the dike and foundation, caves, cracks or other weak points inside the dike. This information is not completely available for most of the prototype dikes in the world. An extensive field investigation of the dikes with attention on these aspects is worthwhile.



## References

- Alberle, J., Nikora, V. and Walters, R., 2004. Effects of bed material properties on cohesive sediment erosion. *Marine Geology*, 207, 83-93.
- Albertson, M.L., Dai, Y.B., Johnson, R.A. and Rouse, H., 1950. Diffusion of submerged jets. *Transactions of the ASCE*, 115, 639-697.
- Alonso, C.V., Bennett, S.J. and Stein, O.R., 2002. Predicting head cut erosion and migration in concentrated flows typical of upland areas. *Water Resources Research*, 38(12), 1303, doi: 10.1029/2001WR001173.
- Amer, K., 1991. *The tensile strength of soils and its importance*. PhD thesis, Arizona State University, USA.
- Amos, C.L., Daborn, G.R., Christian, H.A., Atkinson, A. and Robertson, A., 1992. In situ erosion measurements on fine-grained sediments from the Bay of Fundy. *Marine Geology*, 108, 175-196.
- Andrews, D.P., Coleman, S.E., Webby, M.G. and Melville, B.W., 1999. Noncohesive embankment failure due to overtopping flow. *Proc. 28<sup>th</sup> IAHR Congress*, Graz, Austria, 1999, (CD-ROM).
- Ariathurai, R. and Arulanandan, K., 1978. Erosion rates of cohesive soils. *Journal of Hydraulic Division*, 104(2), 279-283.
- Arulanandan, K., 1975. Fundamental aspects of erosion of cohesive soils. *Journal of Hydraulic Division*, 101(5), 635-639.
- Bates, P.D. and De Roo, A.P.J., 2000. A simple raster-based model for flood inundation simulation. *Journal of Hydrology*, 236, 54-77.
- Bechteler, W. and Broich, K., 1991. Effects in dam-break modeling. *Proc. 24<sup>th</sup> IAHR Congress*, Madrid, Spain, 1991, A189-A200.
- Beltaos, S., 1976. Oblique impingement of plane turbulent jets. *Journal of Hydraulic Division*, 102(9), 1177-1192.
- Beltaos, S. and Rajaratnam, N., 1973. Plane turbulent impinging jets. *Journal of Hydraulic Research*, 11(1), 29-59.
- Bennett, S.J., Alonso, C.V., Prasad, S.N. and Römken, M.J.M. 2000a. Experiments on headcut growth and migration in concentrated flows typical of upland areas. *Water Resources Research*, 36(7), 1911-1922.

- Bennett, S.J. and Casall, J., 2001. Effect of initial step height on headcut development in upland concentrated flows. *Water Resources Research*, 37(5), 1475-1484.
- Bennett, S.J., Robinson, K.M., Simon, A. and Hanson, G.J., 2000b. Stable knickpoints formed in cohesive sediment. *Proc. 2000 Joint Conf. Water Resources Engineering and Water Resources Planning and Management*, Minneapolis, USA, (CD-ROM).
- Berry, P.L. and Reid D., 1987. *An introduction to soil mechanics*. McGraw-Hill, London, UK.
- Bishop, A.W. and Garga, V.K., 1969. Drained tension tests on London Clay. *Geotechnique*, 19(2), 309-313.
- Brown, C.A and Graham, W.J., 1988. Assessing the threat to life from dam failure. *Water Resources Bulletin*, 24(6), 1303-1309.
- Brown, R.J. and Rogers, D.C., 1981. *BRDAM users manual*. Water and Power Resources Services, U.S. Department of the Interior, Denver, Colorado, USA.
- Busnelli, M.M., 2001. *Numerical simulation of free surface flows with steep gradients*. PhD thesis, Delft University of Technology, the Netherlands.
- Chapalain, G., Sheng, Y.P. and Temperville, A.T., 1994. About the specification of erosion flux for soft stratified cohesive sediments. *Mathematical Geology*, 26(6), 651-676.
- Chen, Y.H. and Anderson, B.A., 1987. *Development of a methodology for estimating embankment damage due to flood overtopping*. Report No. FHWA/RD-86/126, Federal Highway Administration, US Department of Transportation.
- Chien, N., 1990. Fluvial processes in the lower Yellow River after levee breaching at Tongwaxiang in 1855. *International Journal of Sediment Research*, 5(2), 1-14.
- Chien, N. and Wan, Z.H., 1999. *Mechanics of sediment transport*. ASCE Press, Reston, Virginia, USA.
- Chow, V.T., 1959. *Open-channel hydraulics*. McGraw-Hill, Auckland, New Zealand.
- Coleman, S.E., Andrews, D.P. and Webby, M.G., 2002. Overtopping breaching of noncohesive homogeneous embankments. *Journal of Hydraulic Engineering*, 128(9), 829-838.
- Craig, R.F., 1997. (6<sup>th</sup> ed.) *Soil mechanics*. Chapman & Hall, London, UK.
- Cristofano, E.A., 1965. *Method of computing erosion rate for failure of earthfill dams*. Bureau of Reclamation, Denver, Colorado, USA.
- CUR/TAW, 1990. *Probabilistic design of flood defences*. Rep. 141, Technical Advisory Committee on Water Defences, Center for Civil Engineering Research and Codes, Gouda, the Netherlands.
- CUR/TAW, 1991. *Guide for the design of river dikes*. Rep. 142, Technical Advisory Committee on Water Defences, Center for Civil Engineering Research and Codes, Gouda, the Netherlands.

- De Loeff, H., Steetzel, H.J. and Kraak, A.W., 1997. Breach growth: experiments and modeling. *Proc. 25<sup>th</sup> Int. Conf. Coastal Engineering*, Orlando, USA, 1996, 2746-2755.
- De Ploey, J., 1989. A model for headcut retreat in rills and gullies. *CATENA Supplement*, 14, 81-86.
- De Vroeg, J.H., Kruse, G.A.M. and Van Gent, M.R.A., 2002. *Erosion due to overtopping and overflow*. Technical report, Project identification: DC030202/H3803, Delft Cluster, Delft, the Netherlands.
- Dodge, R.A., 1988. *Overtopping flow on low embankment dams – summary report of model tests*. REC-ERC-88-3, U.S. Bureau of Reclamation, Denver, USA.
- Eikenberry, F.W., Arthur, H.G., Bogner, N.F., Lacy, F.P., Schuster, R.L. and Willis, H.B., 1977. *Failure of Teton Dam: a report on findings*. USGPO, Washington, USA.
- Fread, D.L., 1988a. *The NWS DAMBRK model: theoretical and background/user documentation*. National Weather Service (NWS) Report, NOAA, Silver Spring, Maryland, USA.
- Fread, D.L., 1988b. *BREACH: an erosion model for earthen dam failures*. National Weather Service (NWS) Report, NOAA, Silver Spring, Maryland, USA.
- Fredlund, D.G. and Rahardjo, H., 1993. *Soil mechanics for unsaturated soils*. John Wiley & Sons, New York, USA.
- Fujita, Y. and Tamura, T., 1987. Enlargement of breaches in flood levees on alluvial plains. *Journal of Natural Disaster Science*, 9(1), 37-60.
- Giuseppetti, G. and Molinaro, P., 1989. A mathematical model of the erosion of an embankment dam by overtopping. *Proc. Int. Symp. Analytical Evaluation of Dam Related Safety Problems*, Copenhagen, Denmark, 1989, 329-341.
- Grimshaw, R.W., 1971. *The chemistry and physics of clays and allied ceramic materials*. Benn, London, UK.
- Grissinger, E.H., 1966. Resistance of selected clay systems by water. *Water resources research*, 2(1), 131-138.
- Hahn, W., Hanson, G.J. and Cook, K.R., 2000. Breach morphology observations of embankment overtopping tests. *Proc. 2000 Joint Conf. Water Resources Engineering and Water Resources Planning and Management*, Minneapolis, USA, (CD-ROM).
- Hanson, G.J., 1992. Erosion resistance of compacted soils. *Transportation Research Record*, 1369, 26-30.
- Hanson, G.J., 1993. Effects of consolidation on soil erodibility. ASAE paper 932091, St. Joseph, Michigan, ASAE.
- Hanson, G.J., 1996. Investigating soil strength and stress-strain indices to characterize erodibility. *Transactions of the ASAE*, 39(3), 883-890.
- Hanson, G.J., Robinson, K.M. and Cook, K.R., 2001. Prediction of headcut migration using a deterministic approach. *Transactions of the ASAE*, 44(3), 525-531.

- Hanson, G.J., Temple, D.M. and Cook, K.R., 1999. Dam overtopping resistance and breach processes research. *Proc. 1999 Annual Conf. Association of State Dam Safety Officials*, St. Louis, Missouri, USA, (CD-ROM).
- Havnø, K., Van Kalken, T. and Olesen, K., 1989. A modeling package for dam break simulation. *Proc. Int. Symp. Analytical Evaluation of Dam Related Safety Problems*, Copenhagen, Denmark, 1989, 387-397.
- Hayter, E.J., Bergs, M.A., Gu, R., McCutcheon, S.C., Smith, S.J. and Whiteley, H.J., 1995. *HSCTM-2D, a finite element model for depth-averaged hydrodynamics, sediment and contaminant transport*. Technical report, U.S. Environment Protection Agency, Athens, Georgia, USA.
- Hesselink, A.W., Stelling, G.S., Kwadijk, J.C.J. and Middelkoop, H., 2003. Inundation of a Dutch river polder, sensitivity analysis of a physically based inundation model using historic data. *Water Resources Research*, 39(9), 1234, doi:10.1029/2002WR001334.
- Höeg K., Lövoll, A. and Vaskinn K.A., 2004. Stability and breaching of embankment dams: field tests on 6 m high dams. *International Journal on Hydropower and Dams*, 11(1), 88-92.
- Houwing, E.J., 1999. Determination of critical erosion threshold of cohesive sediments on intertidal mudflats along the Dutch Wadden Sea coast. *Estuarine, Coastal and Shelf Science*, 49, 545-555.
- Huang Wenxi, 1983. *Engineering properties of soil*. Water Resources & Hydropower Press, Beijing, China. (in Chinese).
- Huisman, P., Cramer, W., van Ee, G., Hooghart, J.C., Salz, H. and Zuidema, F.C., 1998. *Water in the Netherlands*. Netherlands Hydrological Society, Delft, the Netherlands.
- IMPACT, 2005. *IMPACT-investigation of extreme flood processes and uncertainty*, Final Technical Report, HR Wallingford, UK.
- Johansen, C., Larsen, T. and Petersen, O., 1997. Experiments on erosion of mud from the Danish Wadden Sea. In: Burt, N., Parker, R. and Watts, J. (Eds), *Proc. 4<sup>th</sup> Nearshore and Estuarine Cohesive Sediment Transport Conf.*, John Wiley & Sons, New York, USA, 305-314.
- Kamphuis, J.W., 1990. Influence of sand or gravel on the erosion of cohesive sediment. *Journal of Hydraulic Research*, 28(1), 43-53.
- Kamphuis, J.W. and Hall, K.R., 1983. Cohesive material erosion by unidirectional current. *Journal of Hydraulic Engineering*, 109(1), 49-61.
- Kelly, W.E. and Gularte, R.C., 1981. Erosion resistance of cohesive soils. *Journal of Hydraulic Division*, 107(10), 1211-1224.
- Kraak, A.W., Bakker, W.T., Van de Graaff, J., Steetzel, H.J. and Visser, P.J., 1995. Breach-growth research programme and its place in damage assessment for a polder. *Proc. 24<sup>th</sup> Int. Conf. Coastal Engineering*, Kobe, Japan, 1994, 2197-2206.

- Kranck, K., 1986. Settling behavior of cohesive sediment, In: Mehta, A.J. (Ed.), *Lecture notes on coastal and estuarine studies, Vol 14, Estuarine cohesive sediment dynamics*, Springer-Verlag, Berlin, 151-169.
- Krishnayya, A.V.G., Eisenstein, Z. and Morgenstern, N.R., 1974. Behavior of compacted soil in tension. *Journal of the Soil Mechanics and Foundations Division*, 100(9), 1051-1061.
- Lambe, T.W. and Whitman R.V., 1969. *Soil mechanics*. John Wiley and Sons, New York, USA.
- Liang, L., Ni, J.R., Borthwick, A.G.L. and Rogers, B.D., 2002. Simulation of dike-break processes in the Yellow River. *Science in China, Series E-Technological Sciences*, 45(6), 606-619. (in Chinese).
- Loukola, E. and Huokuna, M., 1998. A numerical erosion model for embankment dams failure and its use for risk assessment. *Proc. CADAM (EU Concerted Action on Dam Break Modelling) Munich meeting*, Munich, Germany, 1998.
- Mathewson, C.C., Cato, K. D. and May, J.H., 1998. *Geotechnical aspects of rock erosion in emergency spillway channels*. Technical Report REMR-GT-3, U.S. Army Corps of Engineers, Waterways Experiment Station, Vicksburg, Mississippi, USA.
- Meadowcroft, I.C, Morris, M.W., Allsop, N.W.H. and McConnell, K., 1996. *Tollesbury managed set back experiment: breach design and construction, and embankment failure experiment*. HR Wallingford Report TR 5, Wallingford, UK.
- Mehta, A.J., 1986. Characterization of cohesive sediment properties and transport processes in estuaries, In: Mehta, A.J. (Ed.), *Lecture notes on coastal and estuarine studies, Vol 14, Estuarine cohesive sediment dynamics*, Springer-Verlag, Berlin, 290-325.
- Mehta, A.J. and Partheniades, E., 1983. Resuspension of deposited cohesive sediment beds. *Proc. 18<sup>th</sup> Int. Conf. Coastal Engineering*, Capetown, South Africa, 1982, 1569-1588.
- Mei, C.C., Fan, S.J. and Jin, K.R., 1997. Resuspension and transport of fine sediments by waves. *Journal of Geophysical Research*, 102(C7), 15807-15821.
- Mirstkhoulova TS. E., 1991. Scouring by flowing water of cohesive and non-cohesive beds, *Journal of Hydraulic Research*, 29(3), 343-354.
- Mitchener, H. and Torfs, H., 1996. Erosion of mud/sand mixtures. *Coastal Engineering*, 29, 1-25.
- Mohamed, M.A.A., Morris, M., Hanson, G.J. and Lakhali, K., 2004. Breach formation: laboratory and numerical modeling of breach formation. *Proc. Dam Safety 2004*, ASDSO Phoenix, Arizona, USA, (CD-ROM).
- Mohamed, M.A.A., Samuels, P.G. and Morris, M.W., 2002. Improving the accuracy of prediction of breach formation through embankment dams and flood embankments. In: Bousmar & Zech (Eds), *River Flow 2002*, Swets & Zeitlinger, Lisse, the Netherlands, 663-673.
- Morgan, R.P.C., 1995. (2<sup>nd</sup> ed.) *Soil erosion and conservation*. Longman, Essex, UK.

- Murthy, V.N.S., 2003. *Geotechnical engineering: principles and practices of soil mechanics and foundation engineering*. Marcel Dekker, New York, USA.
- MWR, 1999. *The 1998 Big floods in China*. Ministry of Water Resources of China. Water Resources & Hydropower Press, Beijing, China. (in Chinese).
- MWR/CWRC, 2002. *The 1998 storm flood in the Yangtze River*. Ministry of Water Resources of China, Changjiang Water Resources Commission. Water Resources & Hydropower Press, Beijing, China. (in Chinese).
- Nagakawa, H. and Tsujimoto, T., 1980. Sand bed instability due to bed load motion. *Journal of Hydraulic Division*, 106(12), 2029-2051.
- Narain, J. and Rawat, P.C., 1970. Tensile strength of compacted soils. *Journal of the Soil Mechanics and Foundation Division*, 96(SM6), 2185-2190.
- Okagbue, C.O., 1989. An analysis of erosional processes along a river bank in the Niger Delta and its implications on control measures. *Proc. 23<sup>rd</sup> IAHR Congress*, Ottawa, Canada, 1989, 215-224.
- OSFCDRH/NIHWR, 1997. *Flood and drought disasters in China*. The Office of State Flood Control and Drought Relief Headquarters, Nanjing Institute of Hydrology & Water Resources. Water Resources & Hydropower Press, Beijing, China. (in Chinese).
- Otsubo, K. and Muraoka, K., 1988. Critical shear stress of cohesive bottom sediments. *Journal of Hydraulic Engineering*, 114(10), 1241-1256.
- Pan Jiazheng, 2000. *Merits of dams*. Tsinghua University Press, Beijing, China. (in Chinese).
- Pan Shuibo and Loukola, E., 1993. *Chinese-Finnish cooperative research work on dam break hydrodynamics*. National Board of Waters and the Environment, Helsinki, Finland.
- Paquier, A., Nogues, P. and Herledan, R., 1998. Model of piping in order to compute dam-break wave. *Proc. CADAM (EU Concerted Action on Dam Break Modelling) Munich meeting*, Munich, Germany, 1998.
- Parchure, T.M. and Mehta, J.A., 1985. Erosion of soft cohesive sediment deposits. *Journal of Hydraulic Engineering*, 111(10), 1308-1326.
- Partheniades, E., 1965. Erosion and deposition of cohesive soils. *Journal of Hydraulic division*, 91(1), 105-138.
- Partheniades, E., 1986. A fundamental framework for cohesive sediment dynamics, In: Mehta, A.J. (Ed.), *Lecture notes on coastal and estuarine studies, Vol 14, Estuarine cohesive sediment dynamics*, Springer-Verlag, Berlin, 219-250.
- Peviani, M.A., 1999. Simulation of earth-dams breaking processes by means of a morphological numerical model. *Proc. CADAM (EU Concerted Action on Dam Break Modelling) Zaragoza meeting*, Zaragoza, Spain, 381-397.
- Ponce, V.M. and Tsivoglou, A.J., 1981. Modeling gradual dam breaches. *Journal of hydraulic division*, 107(7), 829-838.

- Powledge, G.R. and Dodge, R.A., 1985. Overtopping of small dams – an alternative for dam safety. In: Waldrop, W.R. (Ed.), *Hydraulics and Hydrology in the Small Computer Age: Proceedings of Specialty Conference*, New York, ASCE, 1071-1076.
- Powledge, G.R., Ralston, D.C., Miller, P., Chen, Y.H., Clopper, P.E., and Temple, D.M., 1989. Mechanics of overflow erosion on embankments. II: hydraulic and design considerations. *Journal of Hydraulic Engineering*, 115(8), 1056-1075.
- Qian Jiahuan and Yin Zongze, 1995. (2<sup>nd</sup> ed.) *Principle and calculation of geotechnical engineering*. Water Resources & Hydropower Press, Beijing, China. (in Chinese).
- Ralston, D.C., 1987. Mechanics of embankment erosion during overflow. *Proc. 1987 ASCE National Conf. Hydraulic Engineering*, Williamsburg, Virginia, USA, 1987, 733-738.
- Robinson, K.M., 1992. Predicting stress and pressure at an overfall. *Transactions of the ASAE*, 35(2), 561-569.
- Robinson, K. M., 1996. *Gully erosion and headcut advance*. PhD thesis, Oklahoma State University, Stillwater, Oklahoma, USA.
- Robinson, K.M., Cook, K.R. and Hanson, G.J., 2000. Velocity field measurements at an overfall. *Transactions of the ASAE*, 43(3), 665-670.
- Robinson, K.M. and Hanson, G.J., 1994. A deterministic headcut advance model. *Transactions of the ASAE*, 37(5), 1437-1443.
- Rozov, A.L., 2003. Modeling of washout of dams. *Journal of Hydraulic Research*, 41(6), 565-577.
- Sandford, L.P. and Maa, J.P.Y., 2001. A unified erosion formulation for fine sediments. *Marine Geology*, 179, 9-23.
- Schaaff, E., Grenz, C., Pinazo, C. and Lansard, B., 2006. Field and laboratory measurements of sediment erodibility: a comparison. *Journal of Sea Research*, 55, 30-42.
- Shaikh, A., Ruff, J.F. and Abt, S.R., 1988. Erosion rate of compacted namontmorillonite soils. *Journal of geotechnical Engineering*, 114(3), 296-305.
- Sheng, Y.P., 1986. Modeling bottom boundary layer and cohesive sediment dynamics in estuarine and coastal waters, In: Mehta, A.J. (Ed.), *Lecture notes on coastal and estuarine studies, Vol 14, Estuarine cohesive sediment dynamics*, Springer-Verlag, Berlin, 360-400.
- Shroff, A.V. and Shah, D.L., 2003. *Soil mechanics and geotechnical engineering*. Belkema, Rotterdam, the Netherlands.
- Simon, A. and Collison, A.J.C., 2001. Pore-water pressure effects on the detachment of cohesive streambeds: seepage forces and matric suction. *Earth Surface Processes and Landforms*, 26, 1421-1442.
- Simons, D.B. and Sentürk, F., 1992. *Sediment transport technology*. Water Resources Publications, Littleton, Colorado, USA.
- Singh, V.P., 1996. *Dam breach modeling technology*. Kluwer, Dordrecht, the Netherlands.

- Singh, V.P. and Scarlatos, P.D., 1988. Analysis of gradual earth-dam failure. *Journal of Hydraulic Engineering*, 114(1), 21-42.
- Sprangers, J.T.C.M., 1999. *Vegetation dynamics and erosion resistance of sea dyke grassland*. PhD thesis, Wageningen University, the Netherlands.
- Steezel, H.J. and De Vroeg, J.H., 1998. *Extension and validation of the BREACH-model*. Technical report A094R1r2, Alkyon/Delft Hydraulics for Rijkswaterstaat/DWW, Delft, the Netherlands.
- Steezel, H.J. and Visser, P.J., 1992. *Bresgroei, deel II: 2DV-ontwikkeling initiële bres; band A: verslag modelonderzoek Scheldegoot (Breach growth, part II: 2DV-development initial breach; report experiments in Schelde Flume)*. Rep. H1242-IIA, Delft Hydraulics and Delft University of Technology, Delft, the Netherlands.
- Steezel, H.J. and Visser, P.J., 1993. Profile development of dunes due to overflow. *Proc. 23<sup>rd</sup> Int. Conf. Coastal Engineering*, Venice, Italy, 1992, 2669-2679.
- Stein, O.R. and Julien, P.Y., 1993. Criterion delineating the mode of headcut migration. *Journal of Hydraulic Engineering*, 119(1), 37-50.
- Stein, O.R., Julien, P.Y. and Alonso, C.V., 1993. Mechanics of jet scour downstream of a headcut. *Journal of Hydraulic Research*, 31(6), 723-737.
- Stein, O.R. and LaTray, D. A. 2002. Experiments and modeling of head cut migration in stratified soils. *Water Resources Research*, 38(12), 1284, doi: 10.1029/2001WR001166.
- Teisson, C., Ockenden, M., Le Hir, P., Kranenburg, C. and Hamm, L., 1993. Cohesive sediment transport processes. *Coastal Engineering*, 21, 129-162.
- Temple, D.M., 1992. Estimating flood damage to vegetated deep soil spillways. *Applied Engineering in Agriculture*, 8(2), 237-242.
- Temple, D.M. and Hanson, G.J., 1994. Headcut development in vegetated earth spillways. *Applied Engineering in Agriculture*, 10(5), 677-682.
- Temple, D.M. and Hanson, G.J., 1998. Overtopping of grassed embankments. *Proc. 1998 Annual Conf. Association of State Dam Safety Officials*. Las Vegas, Nevada, USA, (CD-ROM).
- Temple, D.M. and Moore, J.S., 1997. Headcut advance prediction for earth spillways. *Transactions of the ASAE*, 40(3), 557-562.
- Thorn, M.F.C. and Parsons, J.G., 1980. Erosion of cohesive sediments in estuaries: an engineering guide. *Proc. 3<sup>rd</sup> Int. Symp. Dredging Technology*, Bordeaux, France, 349-358.
- Tingsanchali, T. and Chinnarasri, C., 2001. Numerical modeling of dam failure due to flow overtopping. *Hydrological Sciences Journal*, 46(1), 113-130.
- Tolhurst, T.J., Black, K.S., Paterson, D.M., Mitchener, H.J., Termaat, G.R. and Shayler, S.A., 2000. A comparison and measurement standardisation of four in situ devices for determining the erosion shear stress of intertidal sediments. *Continental Shelf Research*, 20, 1397-1418.
- Torfs, H., 1997. Erosion of mixed cohesive/non-cohesive sediments in uniform flow. In: Burt, N., Parker, R. and Watts, J. (Eds), *Proc. 4<sup>th</sup> Nearshore and Estuarine*

- Cohesive Sediment Transport Conf.*, John Wiley & Sons, New York, USA, 245-252.
- Van de Ven, G. P., 1993. *Man-made lowlands, history of water management and land reclamation in the Netherlands*. Uitgeverij Matrijs, Utrecht, the Netherlands.
- Van Olphen, H., 1977. *An introduction to clay colloid chemistry for clay technologists, geologists, and soil scientists*. Wiley, New York, USA.
- Van Rijn, L.C., 1984. Sediment pick-up functions. *Journal of Hydraulic Engineering*, 110(10), 1494-1502.
- Van Rijn, L.C., 1993. *Principles of sediment transport in rivers, estuaries, coastal seas*. Aqua Publications, Amsterdam, the Netherlands.
- Vaskinn, K.A., Løvoll, A., Höeg, K., Morris, M., Hanson, G. and Hassan, M., 2004. Physical modelling of breach formation: large scale field tests. *Proc. Dam Safety 2004*, ASDSO Phonex, Arizona, USA, (CD-Rom).
- Visser, P.J., 1998. *Breach growth in sand-dikes*. PhD thesis, Delft University of Technology, Delft, the Netherlands.
- Visser, P.J., Kraak, A.W., Bakker, W.T., Smit, M.J., Snip, D.W., Steetzel, H.J. and Van de Graaff, J., 1996. A large-scale experiment on breaching in sand-dikes. *Proc. Coastal Dynamics'95*, Gdansk, Poland, 583-594.
- Visser, P.J., Vrijling, J.K. and Verhagen, H.J., 1991. A field experiment on breach growth in sand-dikes. *Proc. 22<sup>nd</sup> Int. Conf. Coastal Engineering*, Delft, the Netherlands, 1990, 2087-2100.
- Vrijling, J.K., 2001. Probabilistic design of water defense systems in the Netherlands. *Reliability Engineering and System Safety*, 74, 337-344.
- Wahl, T.L., 1998. Prediction of embankment dam breach parameters: a literature review and needs assessment. DSO-98-004, Dam Safety Research Report, U.S. Bureau of Reclamation.
- Wahl, T.L., 2004. Uncertainty of predictions of embankment dam breach parameters. *Journal of Hydraulic Engineering*, 130(5), 389-397.
- Wang, Z.G. and Bowles, D.S., 2005a. Three-dimensional non-cohesive earthen dam breach model. Part 1: theory and methodology. *Advances in Water Resources*. (in press).
- Wang, Z.G. and Bowles, D.S., 2005b. Three-dimensional non-cohesive earthen dam breach model. Part 2: validation and applications. *Advances in Water Resources*. (in press).
- Wetmore, J.N. and Fread, D.L., 1991. *The NWS simplified dam-break flood forecasting model*. National Weather Service Report, NOAA, Silver Spring, Maryland, USA.
- Whitehouse, R., Soulsby, R., Roberts, W. and Mitchener, H., 2000. *Dynamics of estuarine muds*. Thomas Telford, London, UK.
- Winterwerp, J.C. and Van Kesteren, W.G.M., 2004. *Introduction to the physics of cohesive sediment in the marine environment*. Elsevier, Amsterdam, the Netherlands.

- Wu, W.M., Wang, S.S.Y., Jia, Y.F. and Robinson, K.M., 1999. Numerical simulation of two-dimensional headcut migration. *Proc. ASCE Int. Water Resources Engineering Conf.*, Seattle, USA, 1999, (CD-ROM).
- Wurbs, R.A., 1987. Dam-breach flood wave models. *Journal of Hydraulic Engineering*, 113(1), 29-46.
- Xie Renzhi, 1993. *Hydraulics of dam break*. Shandong Science & Technology Press, Jinan, China. (in Chinese).
- Yalin, M.S., 1977. *Mechanics of sediment transport*. Pergamon Press, Oxford, England.
- Zhu, Y., Visser, P.J. and Vrijling, J.K., 2004a. A model for prediction of headcut migration. In: Hu, C. Tan, Y. & Liu, C. (Eds.), *Proc. 9<sup>th</sup> Int. Symp. River Sedimentation*, Tsinghua University Press, Beijing, China, 2146-2152.
- Zhu, Y., Visser, P.J. and Vrijling, J.K., 2004b. Review on embankment dam breach modeling. In: Wieland, M., Ren, Q. and Tan, J.S.Y. (Eds), *New Developments in Dam Engineering*, Taylor & Francis Group, London, UK, 1189-1196.
- Zhu, Y., Visser, P.J. and Vrijling, J.K., 2005a. A model for headcut erosion during embankment breaching. In: Parker & Garcia (Eds), *River, Coastal and Estuarine Morphodynamics: RCEM 2005*, Taylor & Francis Group, London, UK, 1183-1190.
- Zhu, Y., Visser, P. J. and Vrijling, J.K., 2005b. Breach erosion in clay-dikes. *Proc. 31<sup>st</sup> IAHR Congress*, Seoul, Korea, 2005, 3808-3817.
- Zhu, Y., Visser, P. J. and Vrijling, J.K., 2006a. Soil headcut erosion: process and mathematical modeling. *To appear in Proc. 8<sup>th</sup> Int. Conf. Cohesive Sediment Transport*, Saga, Japan, 2005.
- Zhu, Y., Visser, P. J. and Vrijling, J.K., 2006b. A model for breach erosion in clay-dikes. *To appear in Proc. 5<sup>th</sup> Int. Conf. Coastal Dynamics*, Barcelona, Spain, 2005.
- Zhu, Y., Visser, P.J. and Vrijling, J.K., 2006c. Preliminary results of embankment breaching tests. *To appear in Proc. 7<sup>th</sup> Int. Conf. Hydroscience and Engineering*, Philadelphia, USA, 2006.
- Zreik, D.A., Krishnappan, B.G., Germaine, J.T., Madsen, O.S. and Ladd, C.C., 1998. Erosional and mechanical strength of deposited cohesive sediments. *Journal of Hydraulic Engineering*, 124(11), 1076-1085.

# Appendix A

## Data of laboratory experiments

### A.1 Introduction

In this appendix some data of the DUT laboratory experiments as well as the EC IMPACT Project laboratory experiments are given. These data include

- The DUT experiments: main characteristics of Millisil M10, Polwhite E Kaolin and Illite (Section A.2).
- The DUT experiments: results of water level and flow velocity measurements (Section A.3).
- The EC IMPACT Project experiments: measured water level and outflow discharge (Section A.4).

### A.2 Main characteristics of Millisil M10, Polwhite E Kaolin and Illite

The silt Millisil M10 and the clays Polwhite E Kaolin and Illite are the other three soil products utilized for the preparation of the sand-silt-clay soil mixtures in the DUT laboratory experiments, in addition to Trip Popken Sand as mentioned in Chapter 6. Table A.1 summarizes the main characteristics of Millisil M10 and Polwhite E Kaolin mainly obtained from the supplier. Figure A.1 shows the particle size distribution of Millisil M10, Polwhite E Kaolin and Illite, respectively. The mineralogical composition of Polwhite E Kaolin and Illite were analysed by X-ray diffraction measurement, and the results are shown in Figures A.2 and A.3. It is found that Polwhite E Kaolin is composed of almost pure kaolinite, however, Illite approximately half kaolinite and half illite.

Table A.1 Summary of main characteristics of Millisil M10 and Polwhite E Kaolin.

		Millisil M10	Polwhite E Kaolin
Specific density		2.68	2.70
pH		7	5.0
Specific surface (m <sup>2</sup> /g)		0.5	8
Oil absorption (g/100g)		17.5	33
Chemical analysis (XRF, %)	SiO <sub>2</sub>	99.5	50.0
	Al <sub>2</sub> O <sub>3</sub>	0.20	35.0
	Fe <sub>2</sub> O <sub>3</sub>	0.03	

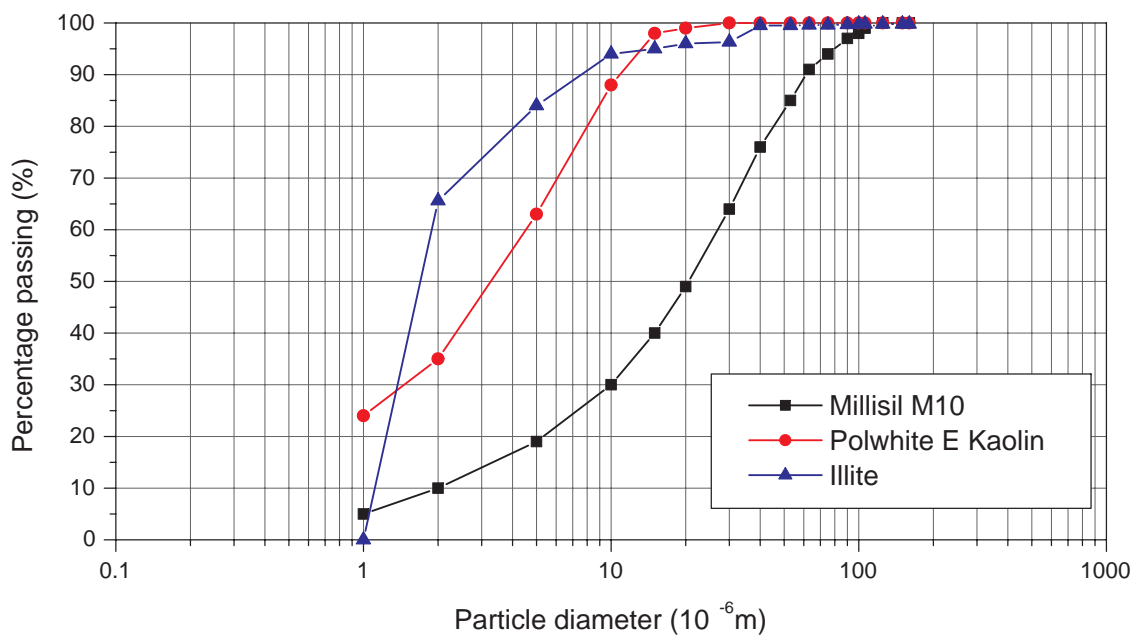


Figure A.1 Particle size distributions of Millisil M10, Polwhite E Kaolin and Illite.

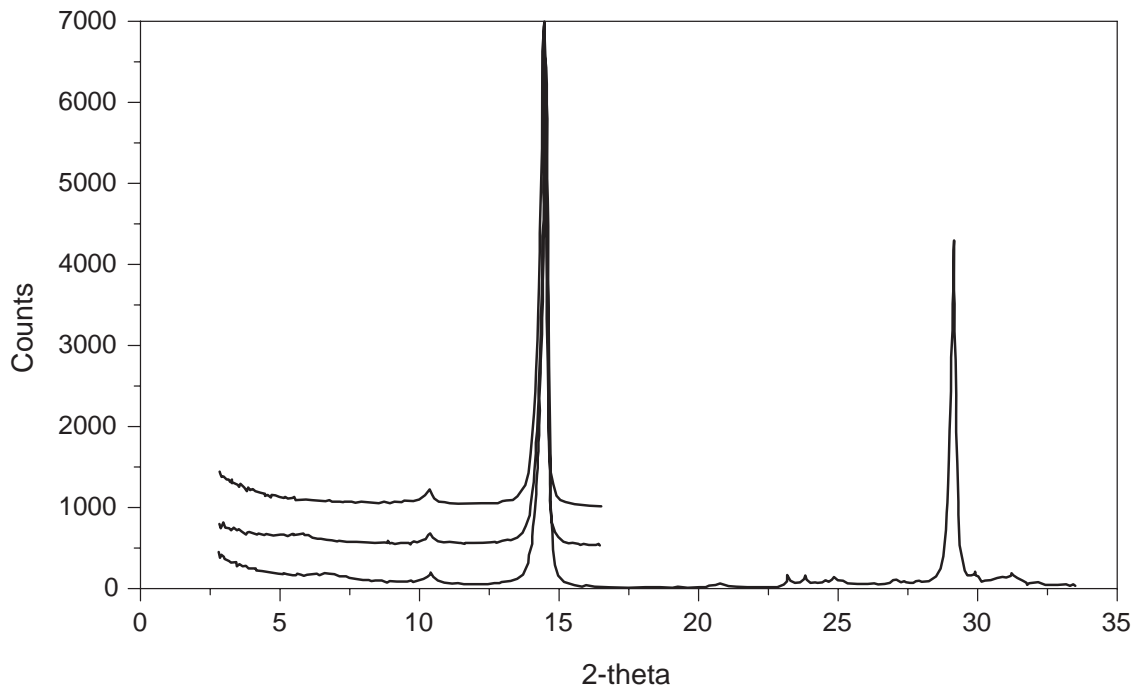


Figure A.2 Mineralogical analysis of Polwhite E Kaolin.

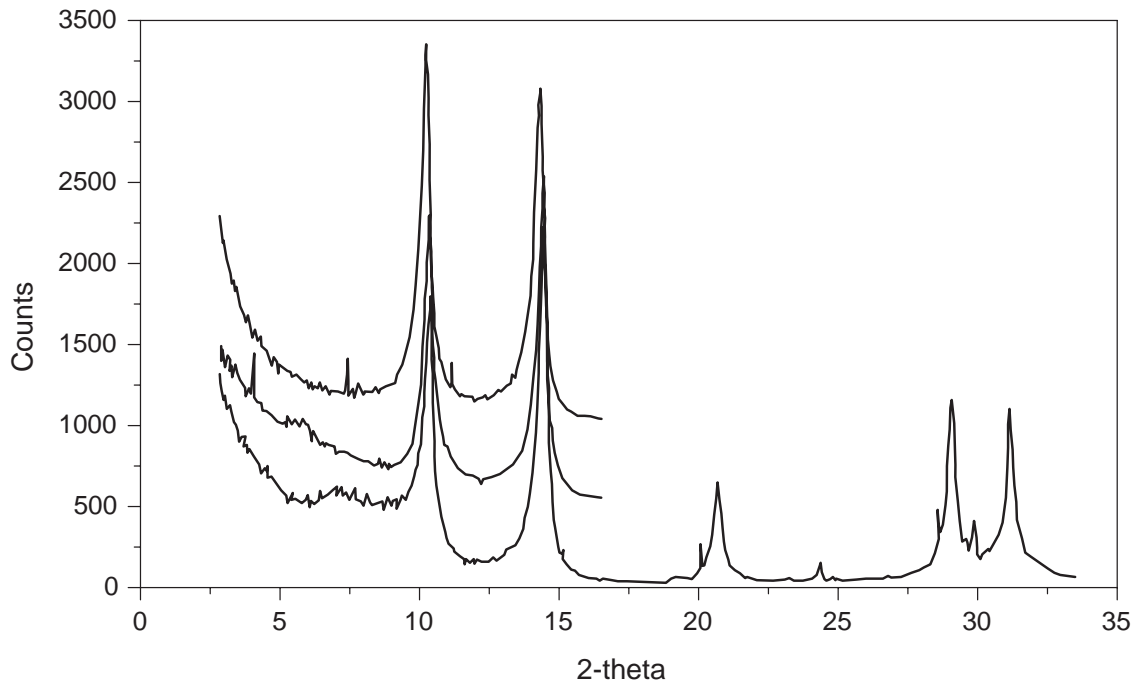


Figure A.3 Mineralogical analysis of Illite.

### A.3 Results of water level and flow velocity measurements, the DUT tests

For the measurements of both the water level and the flow velocity during the DUT laboratory experiments, data were recorded every 0.02 second (i.e. 50 data per second). Figure A.4 presents the original measurement results of the water level of G17 and the flow velocity of E11 for test  $T_2$ , in which a large vibration can be observed in the flow velocity measurements. However, for these clay-dike tests that last several hours, the erosion is believed not to be mainly controlled by the instantaneous value but by the mean value of the flow velocity. Therefore, Figures A.5 through A.7 present the one-second-averaged measurement results for test  $T_s$ , and Figures A.8 through A.27 present the one-minute-averaged measurement results for tests  $T_1$ ,  $T_2$ ,  $T_3$  and  $T_4$ . The symbol  $u_x$  in the figures indicates the flow velocity measured in the flume axis direction, and  $u_y$  in the transverse direction.

The flow is very dynamic at the downstream end of the testing flume (i.e. Flume 1, see Figures 6.1 and 6.2), where the water level is generally very small and the flow velocity is very large, making the measurements (G15 for the water level and E7 the flow velocity, see Figures 6.6 and 6.7) difficult as reflected in Figures A.9, A.13, A.17, A.21 and A.25. Furthermore, due to some disturbance (probably coming from the pump), measurements of  $u_x$  at E10 for test  $T_1$  on 9 August 2005 from 1400 s to 3000 s and for test  $T_3$  from 8000 s to 10600 s show some strong turbulence, see Figures A.8 and A.20. In addition, the flow velocity measuring equipment E11 failed during test  $T_4$  and during test  $T_1$  on 9 August 2005.

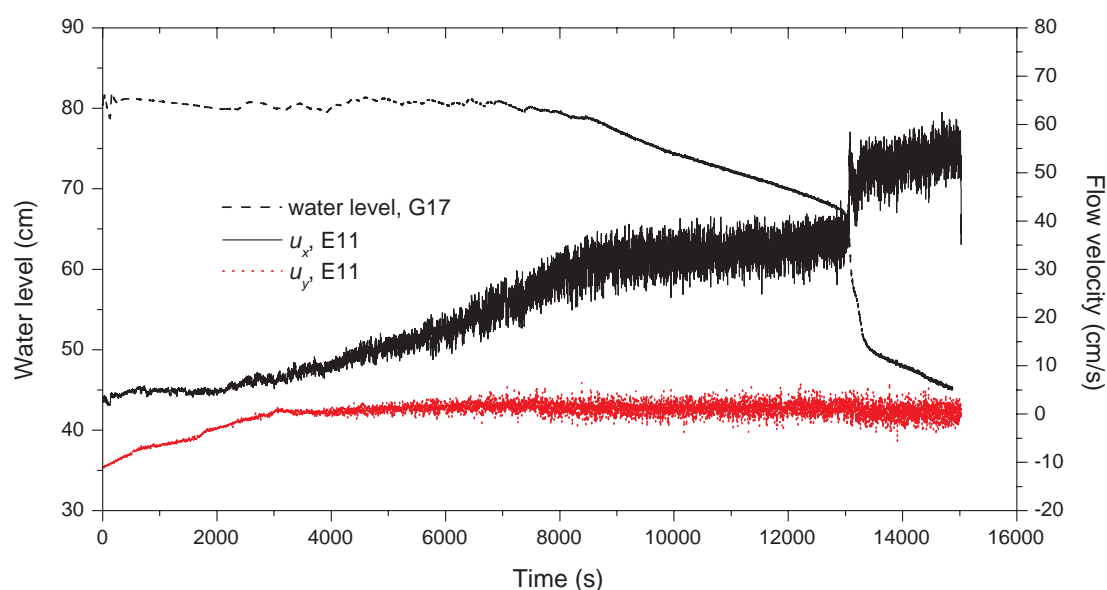


Figure A.4 Original measurement results of water level of G17 and flow velocity of E11 for test  $T_2$  (50 recorded data per second).

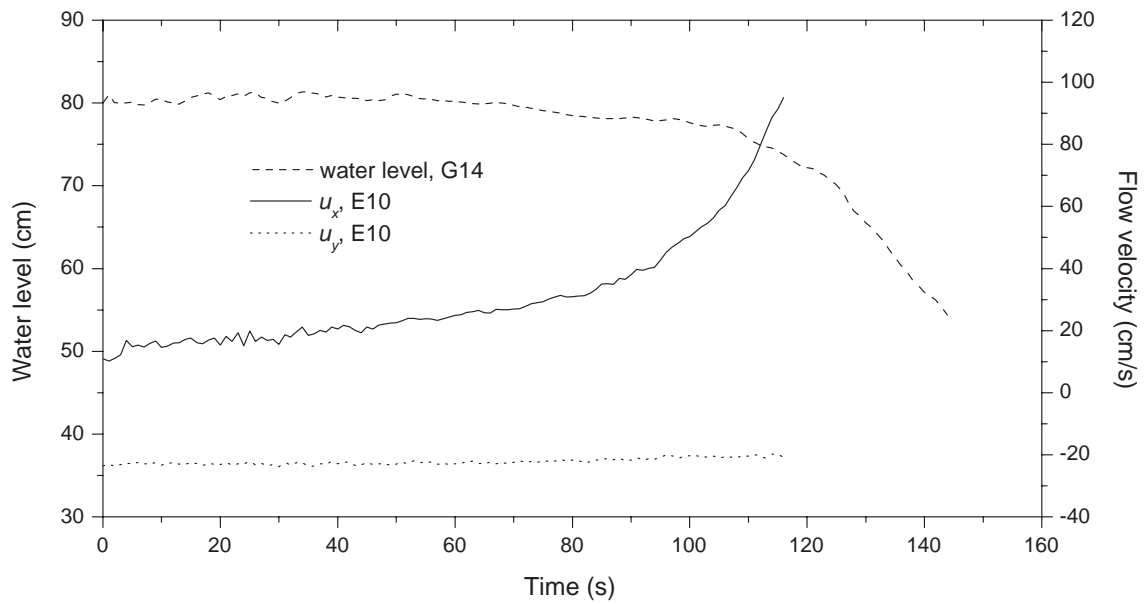


Figure A.5 Results of water level measurement of G14 and flow velocity measurement of E10 for test  $T_s$ .

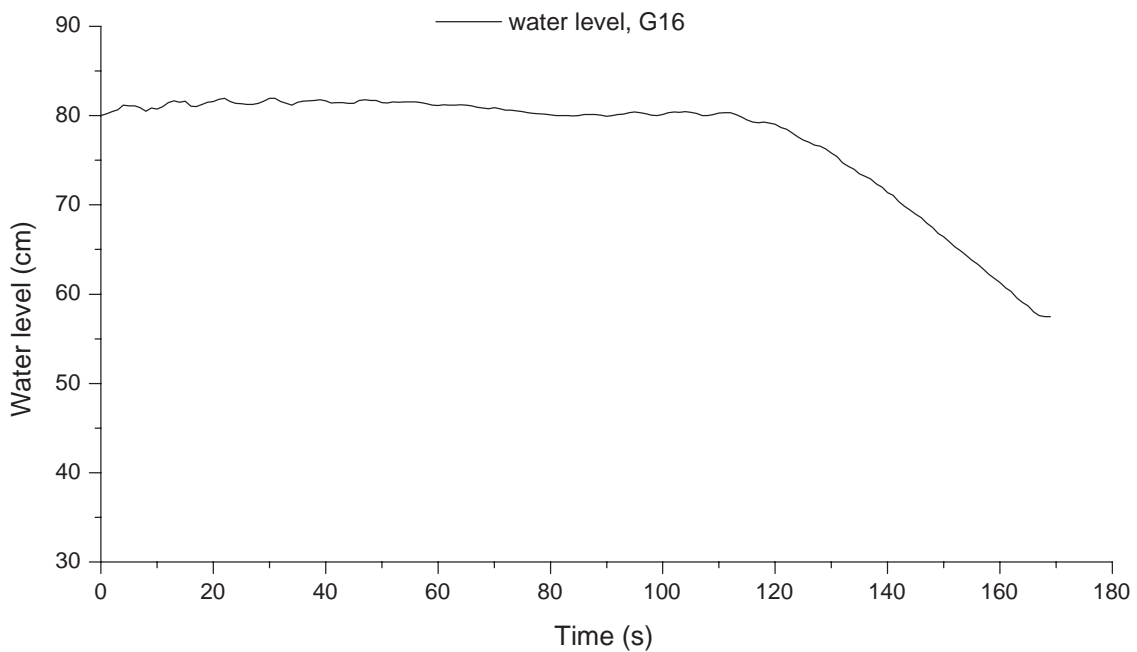


Figure A.6 Results of water level measurement of G16 for test  $T_s$ .

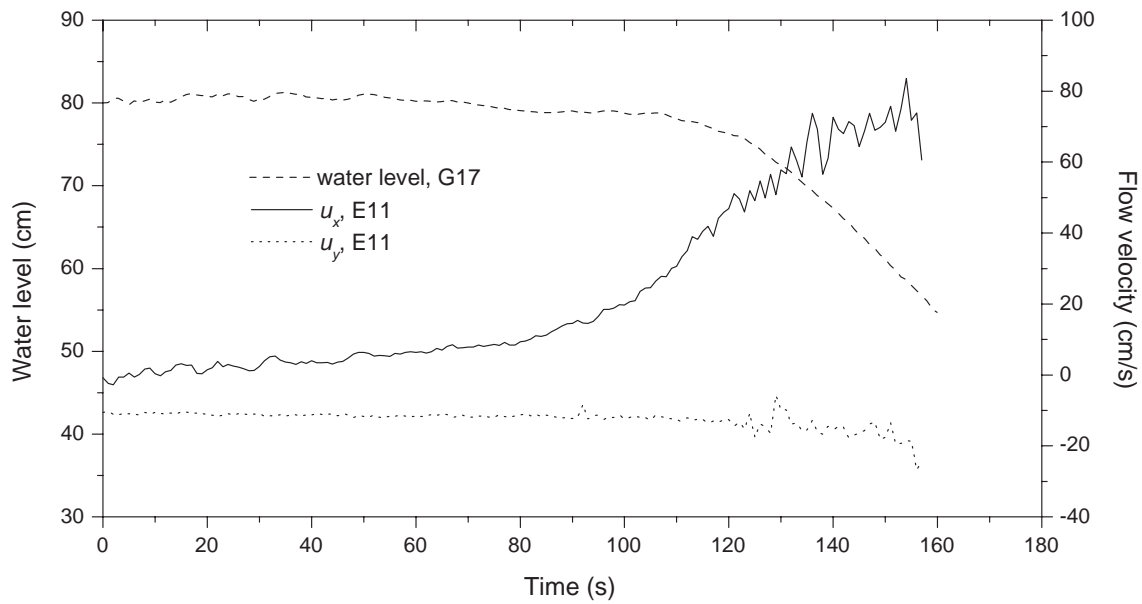


Figure A.7 Results of water level measurement of G17 and flow velocity measurement of E11 for test  $T_s$ .

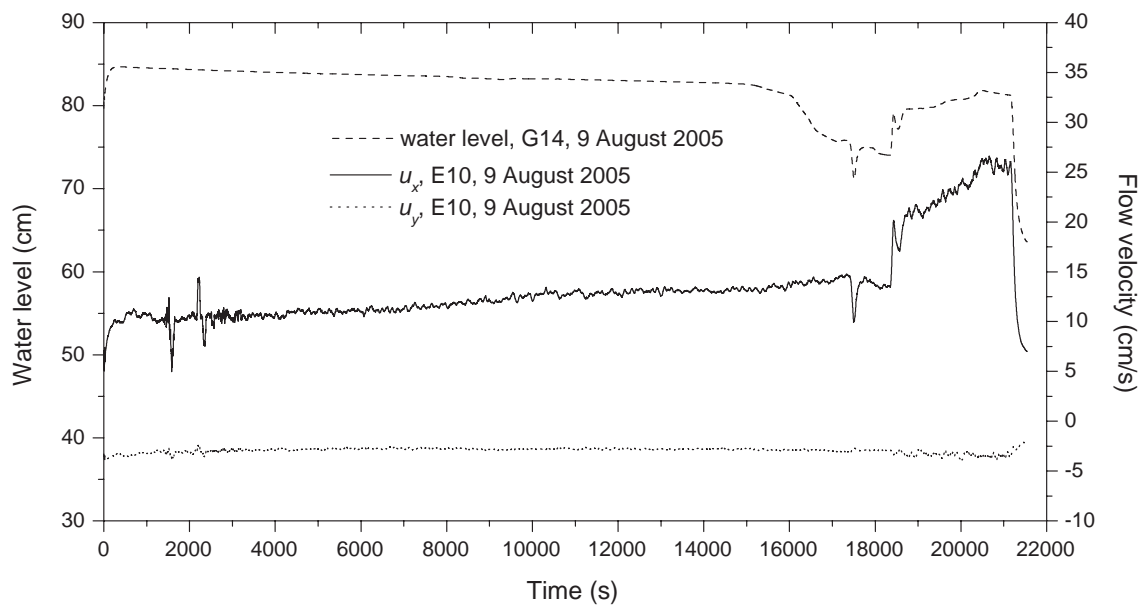


Figure A.8 Results of water level measurement of G14 and flow velocity measurement of E10 for test  $T_1$  on 9 August 2005.

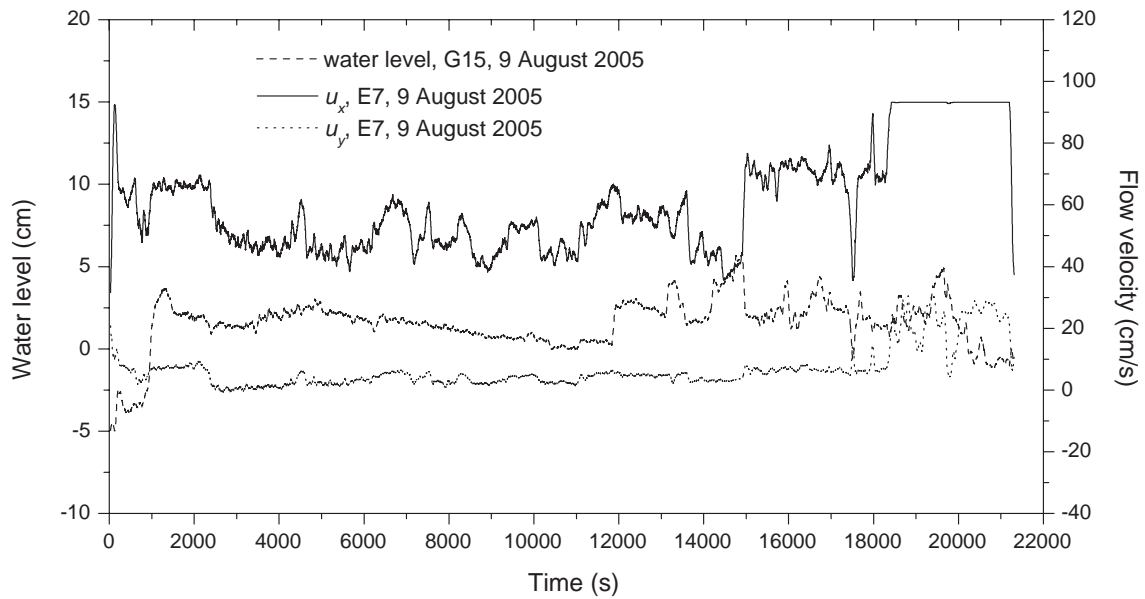


Figure A.9 Results of water level measurement of G15 and flow velocity measurement of E7 for test  $T_1$  on 9 August 2005.

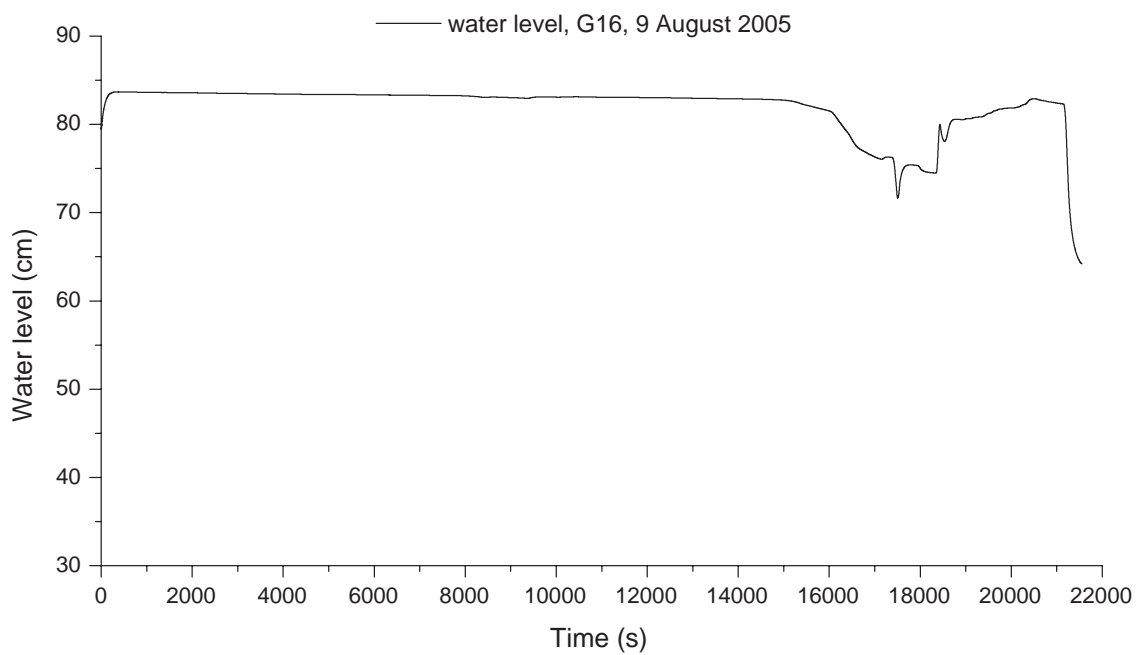


Figure A.10 Results of water level measurement of G16 for test  $T_1$  on 9 August 2005.

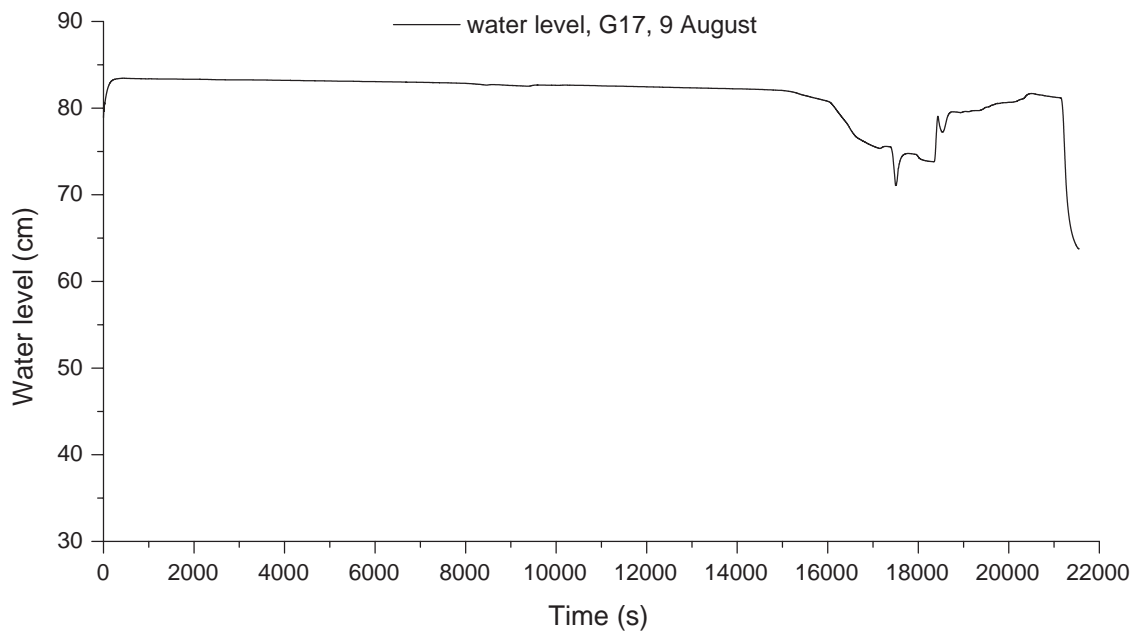


Figure A.11 Results of water level measurement of G17 for test T<sub>1</sub> on 9 August 2005.

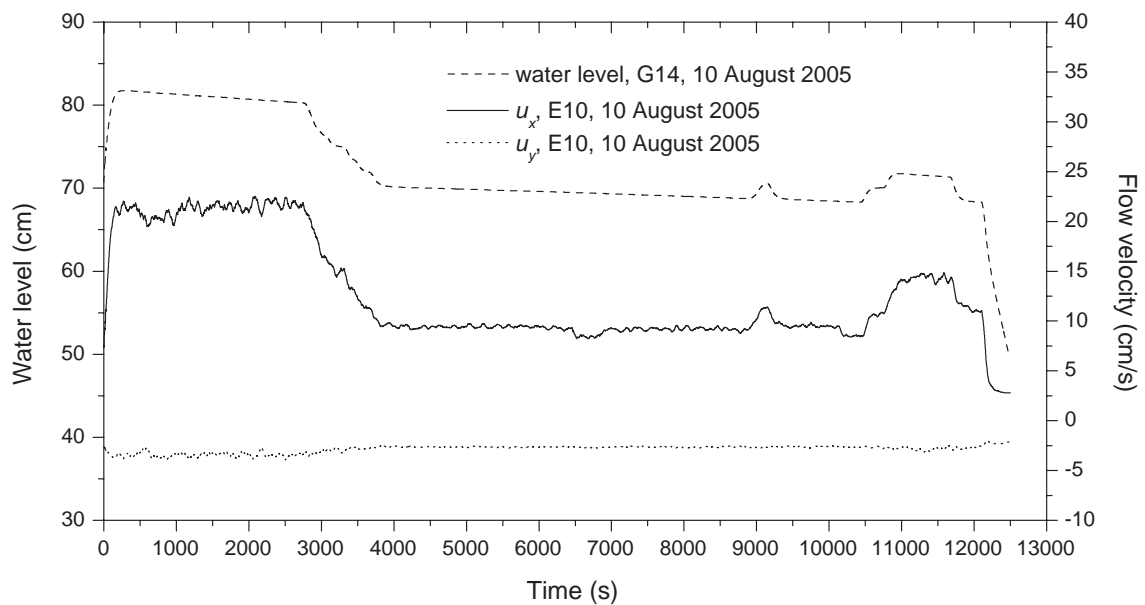


Figure A.12 Results of water level measurement of G14 and flow velocity measurement of E10 for test T<sub>1</sub> on 10 August 2005.

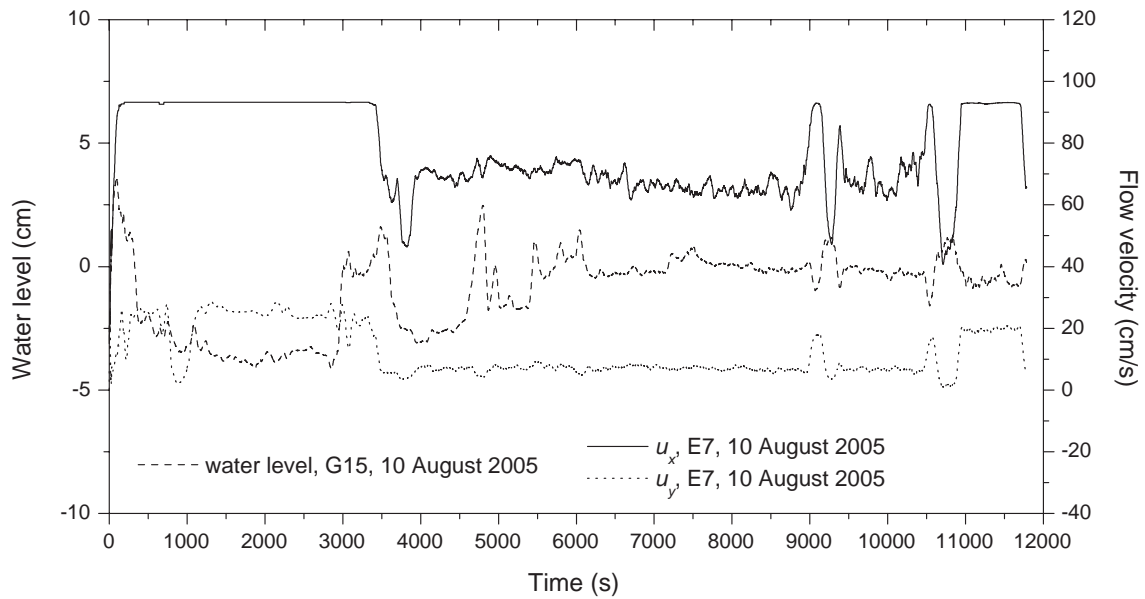


Figure A.13 Results of water level measurement of G15 and flow velocity measurement of E7 for test  $T_1$  on 10 August 2005.

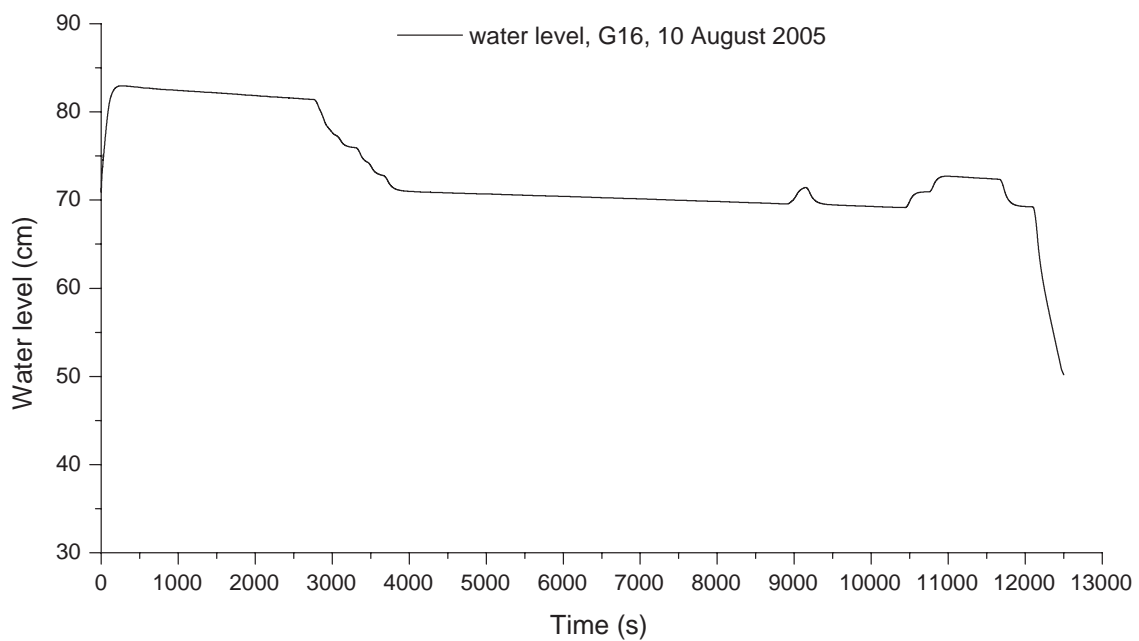


Figure A.14 Results of water level measurement of G16 for test  $T_1$  on 10 August 2005.

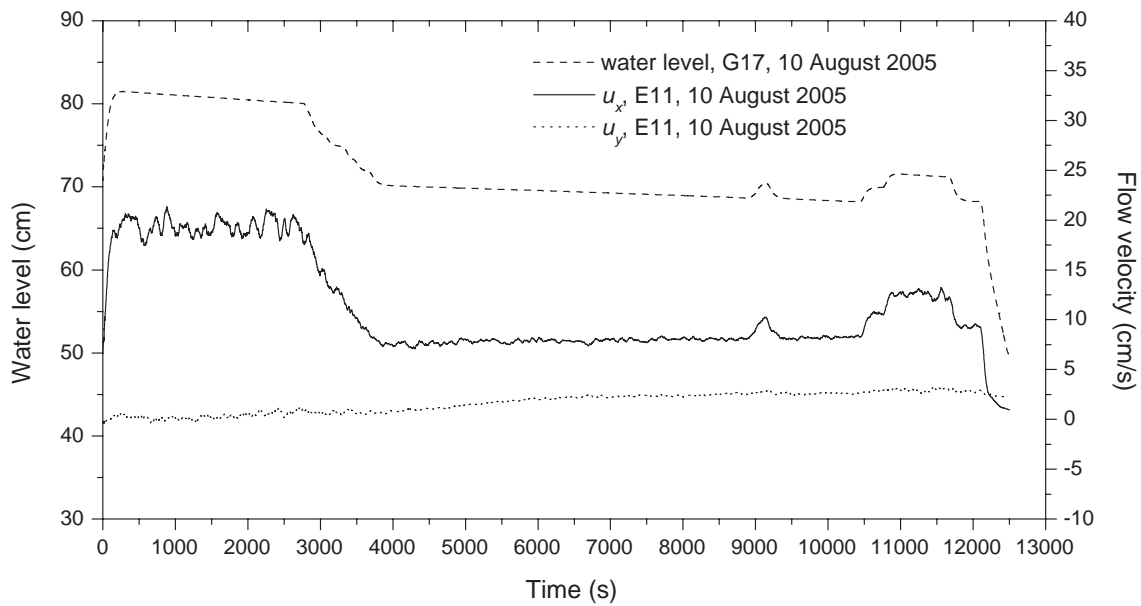


Figure A.15 Results of water level measurement of G17 and flow velocity measurement of E11 for test  $T_1$  on 10 August 2005.

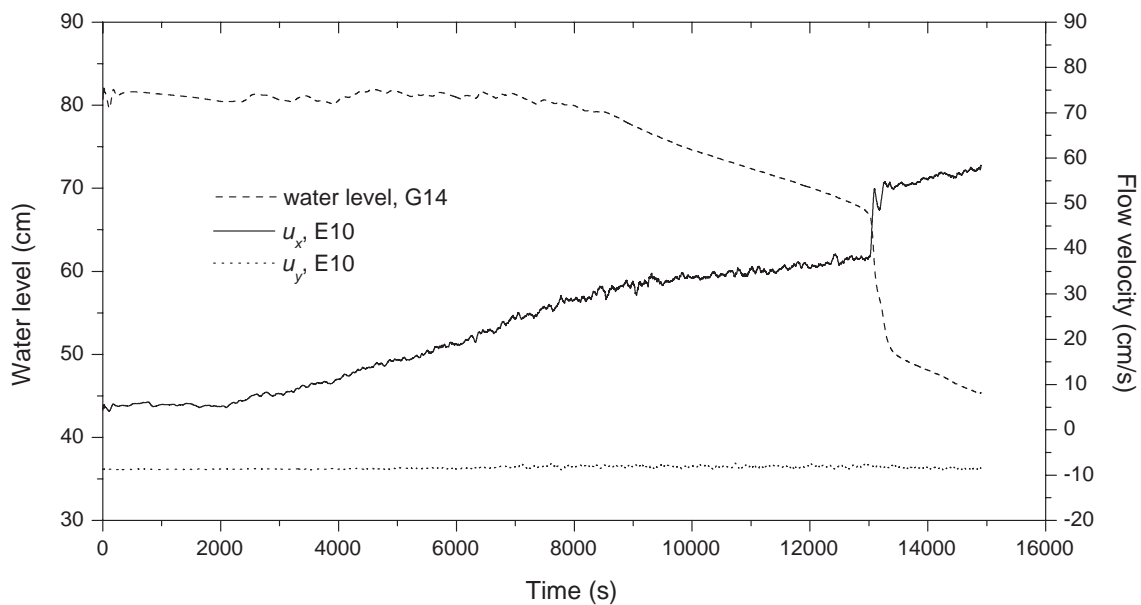


Figure A.16 Results of water level measurement of G14 and flow velocity measurement of E10 for test  $T_2$ .

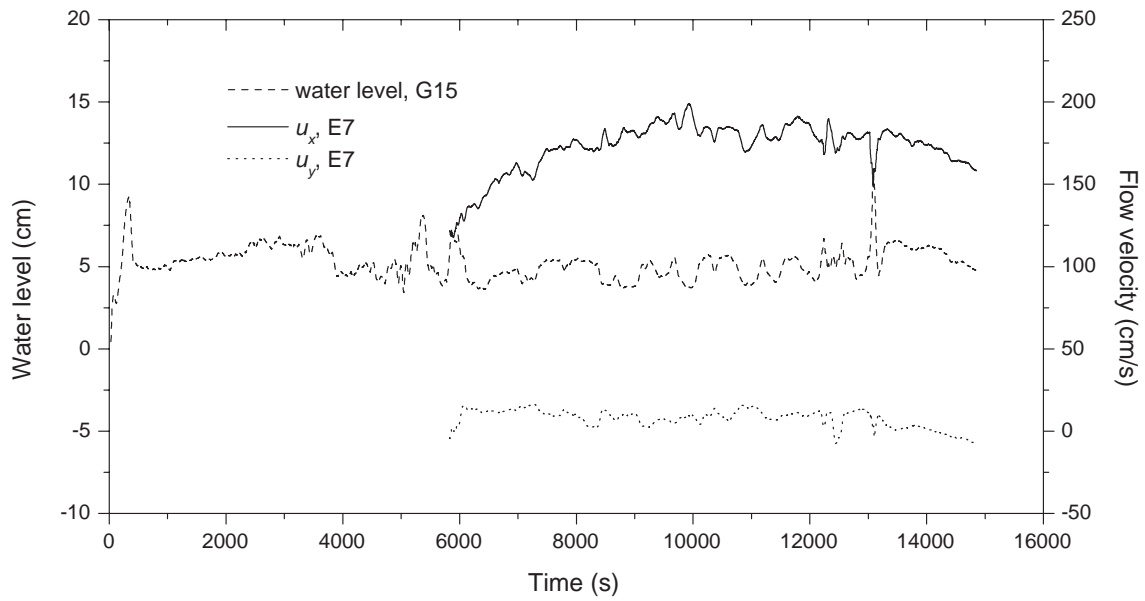


Figure A.17 Results of water level measurement of G15 and flow velocity measurement of E7 for test  $T_2$ .

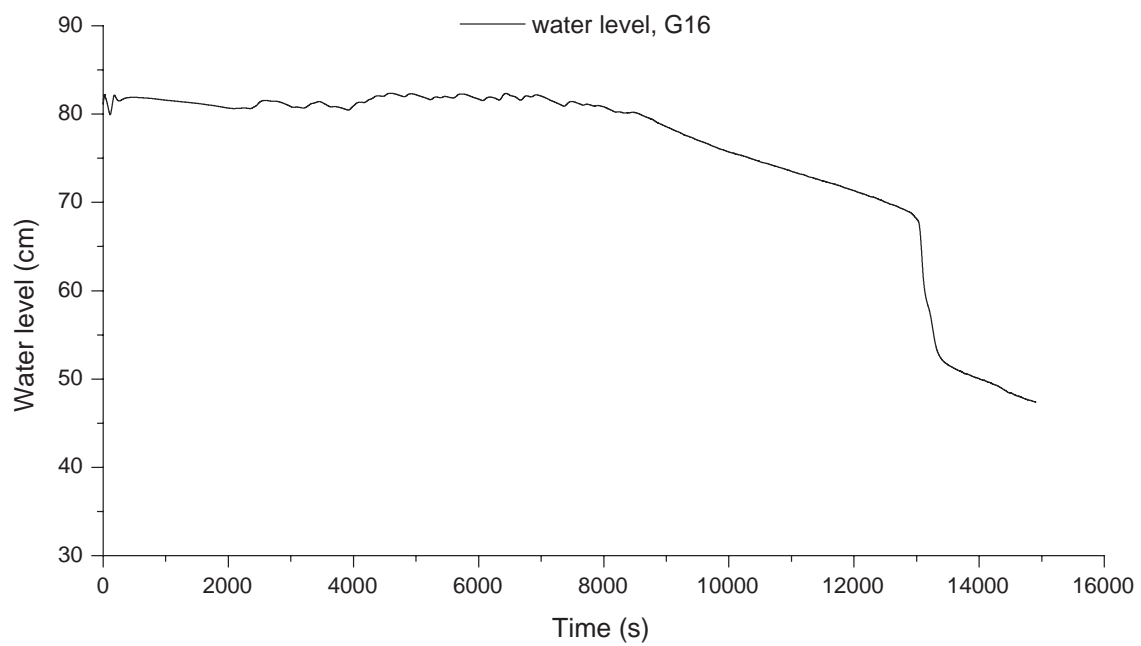


Figure A.18 Results of water level measurement of G16 for test  $T_2$ .

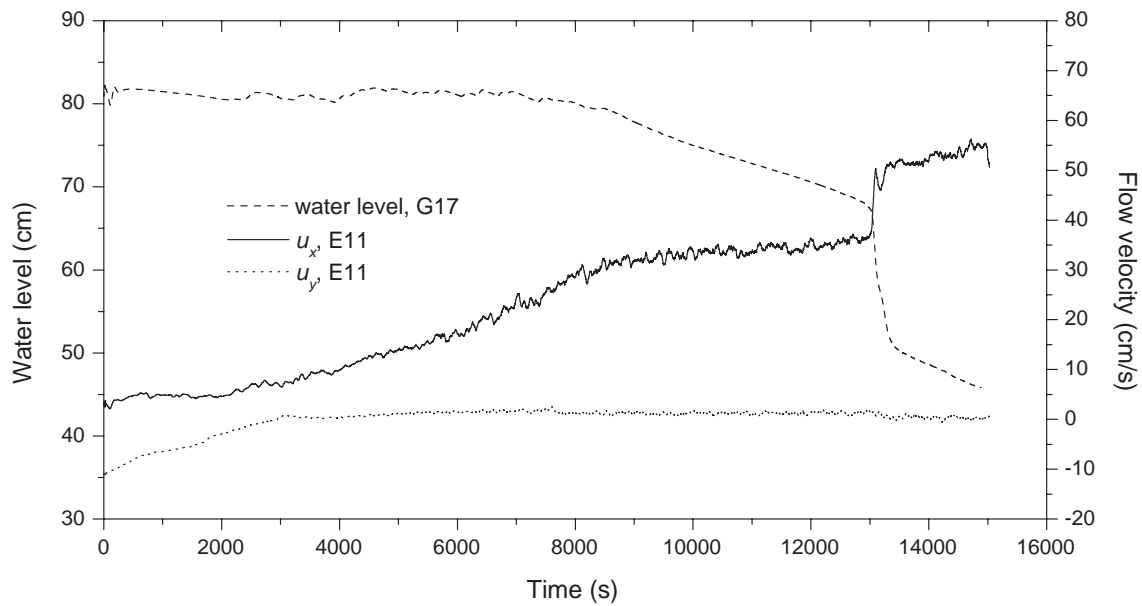


Figure A.19 Results of water level measurement of G17 and flow velocity measurement of E11 for test  $T_2$ .

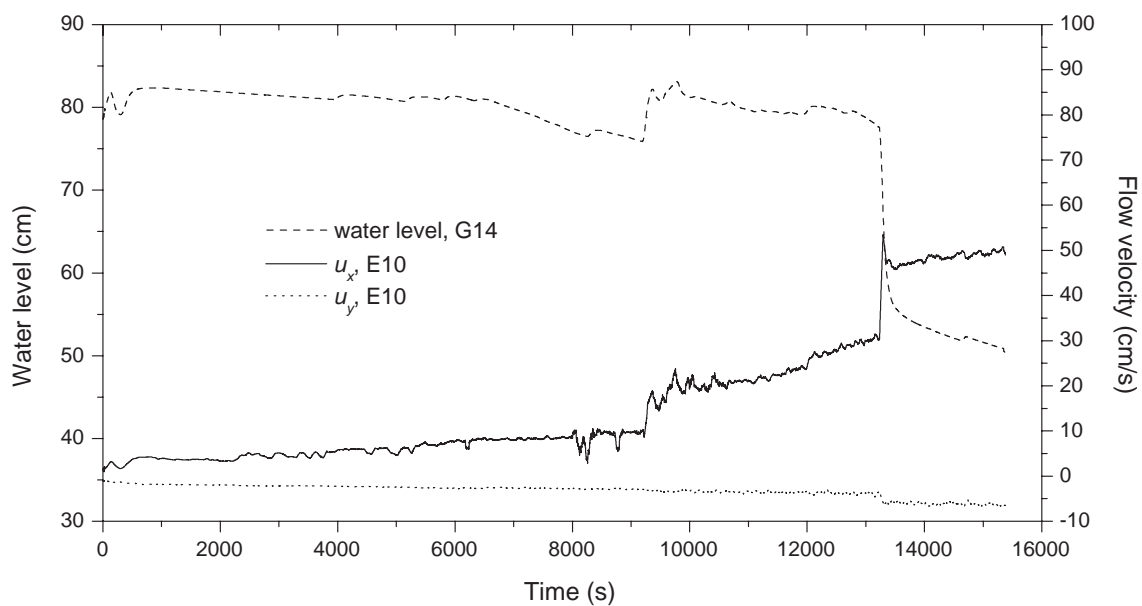


Figure A.20 Results of water level measurement of G14 and flow velocity measurement of E10 for test  $T_3$ .

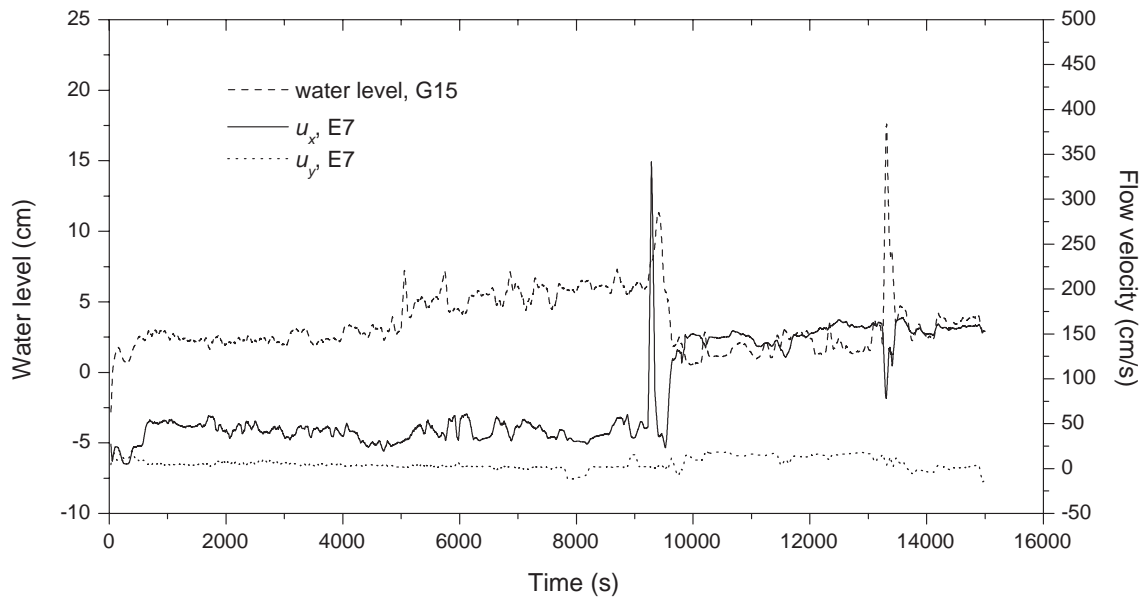


Figure A.21 Results of water level measurement of G15 and flow velocity measurement of E7 for test T3.

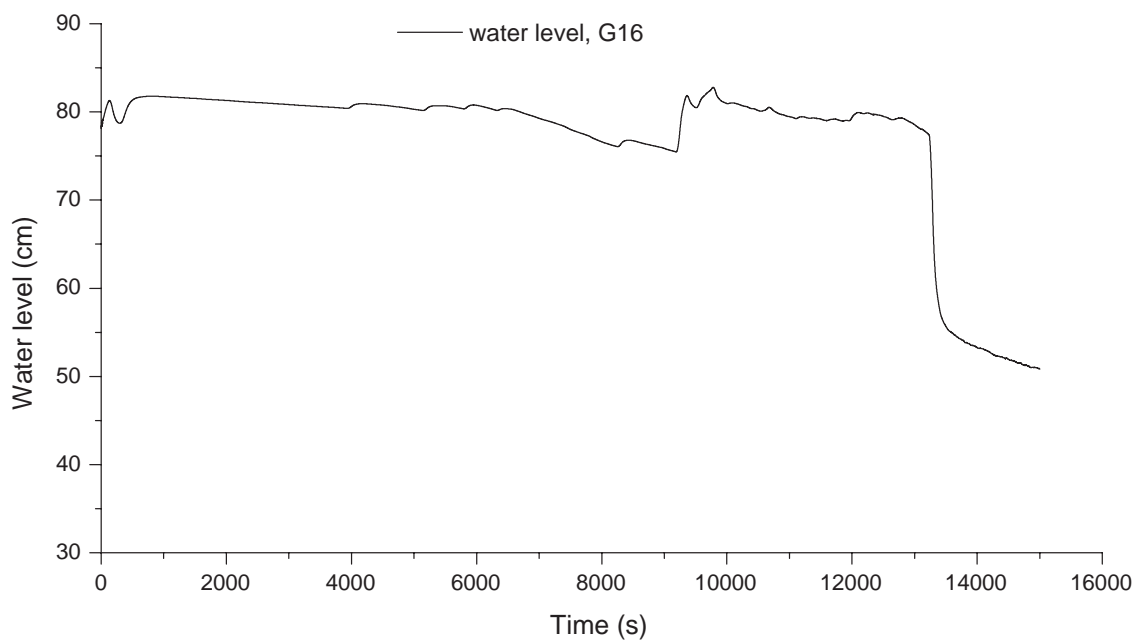


Figure A.22 Results of water level measurement of G16 for test T3.

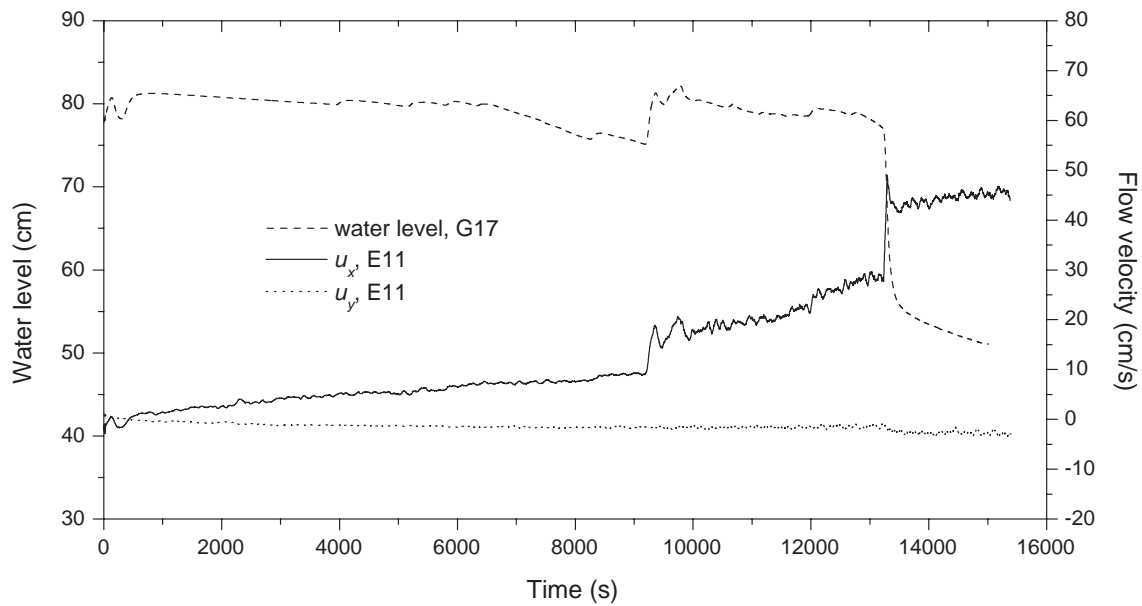


Figure A.23 Results of water level measurement of G17 and flow velocity measurement of E11 for test  $T_3$ .

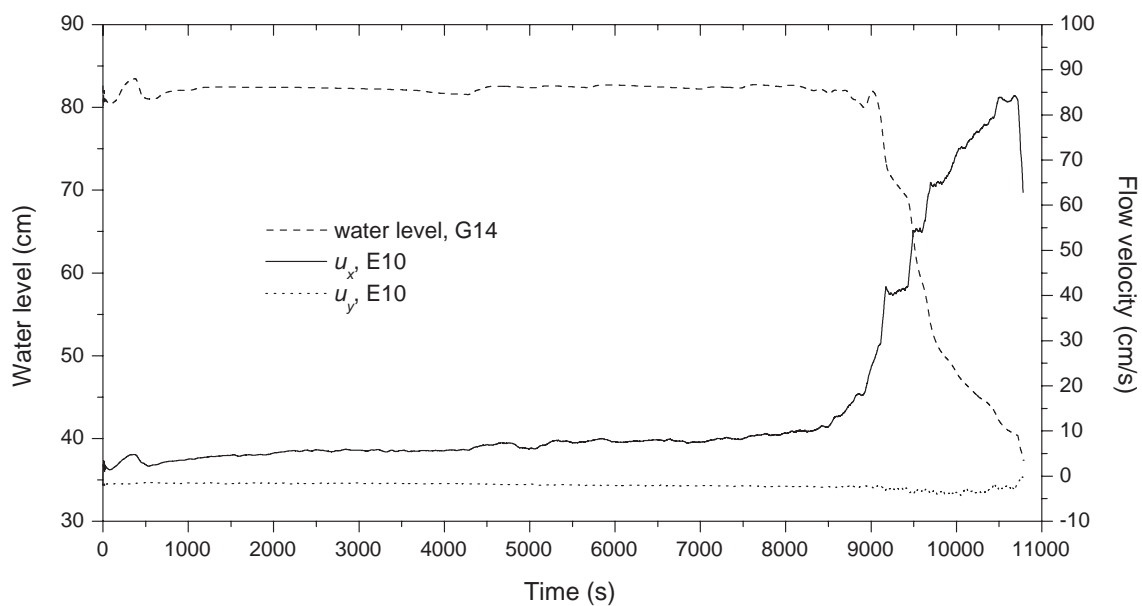


Figure A.24 Results of water level measurement of G14 and flow velocity measurement of E10 for test  $T_4$ .

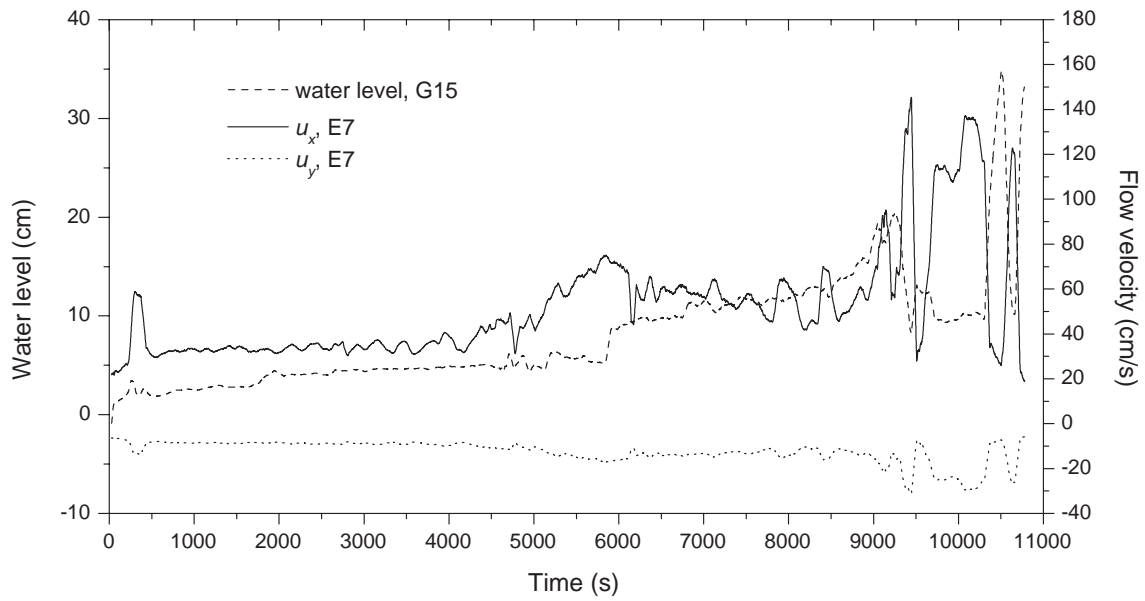


Figure A.25 Results of water level measurement of G15 and flow velocity measurement of E7 for test  $T_4$ .

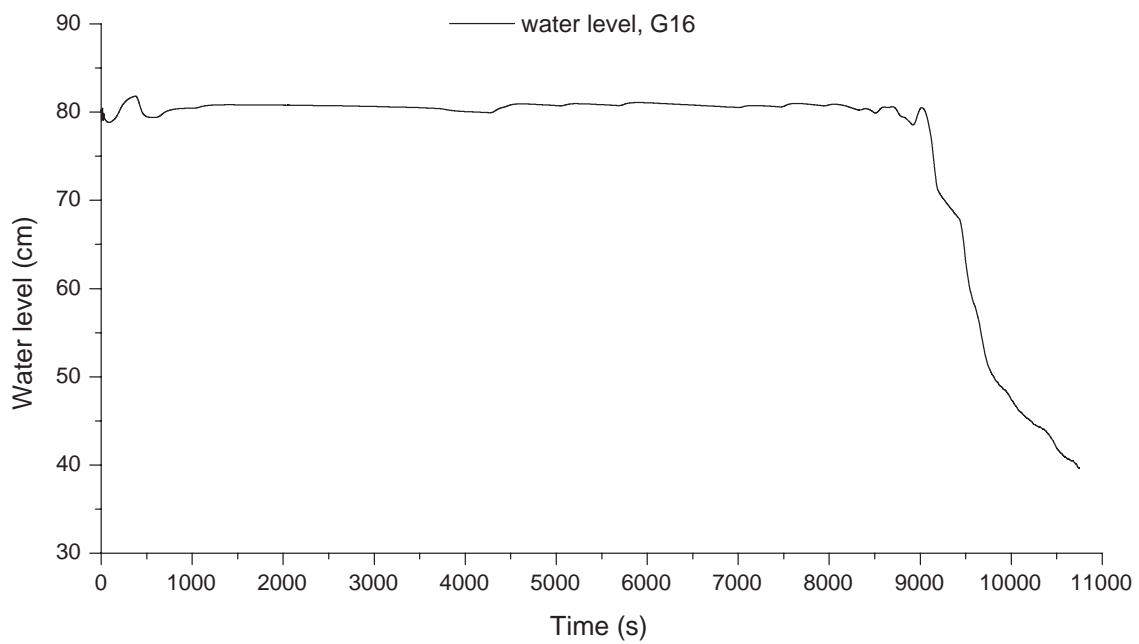


Figure A.26 Results of water level measurement of G16 for test  $T_4$ .

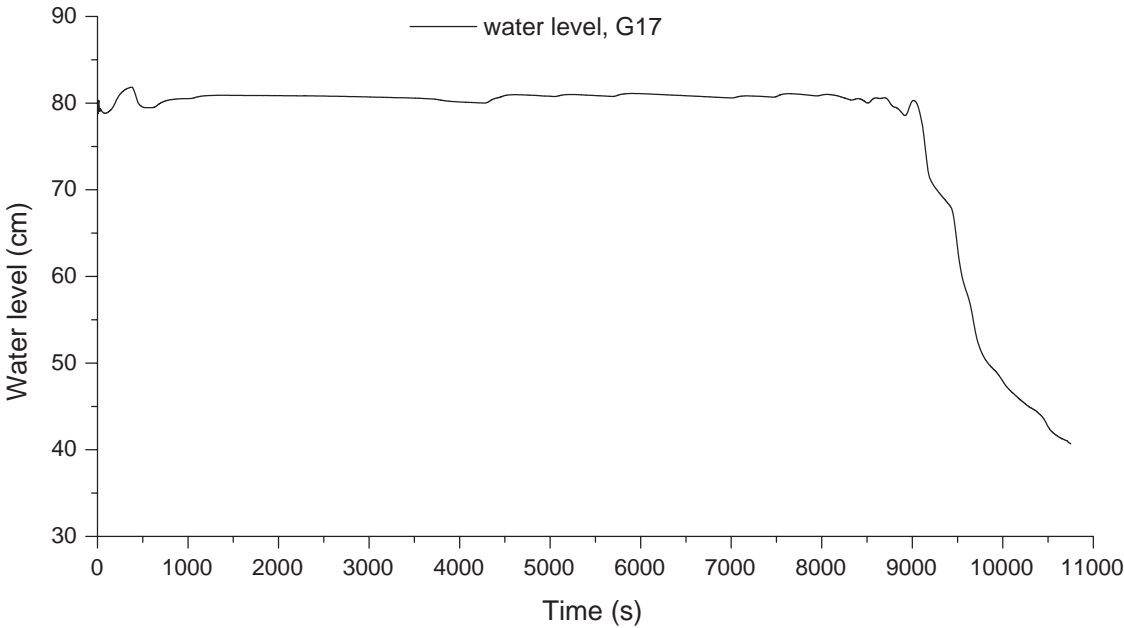


Figure A.27 Results of water level measurement of G17 for test T<sub>4</sub>.

## A.4 Measured water level and breach flow rate, the IMPACT Project tests

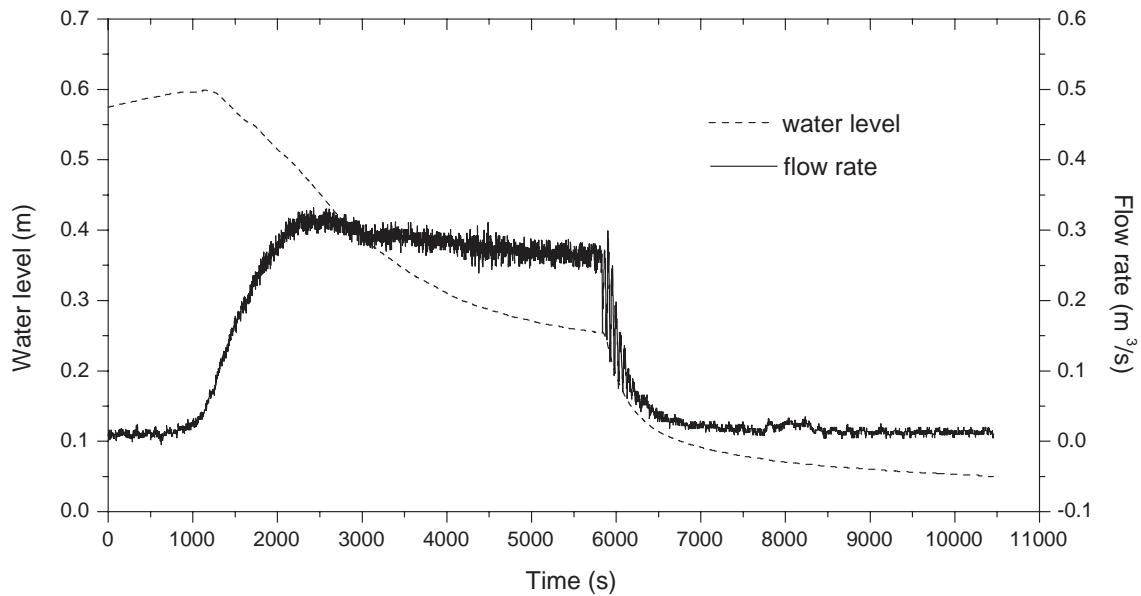


Figure A.28 Water level and breach flow rate of test T<sub>10</sub>.

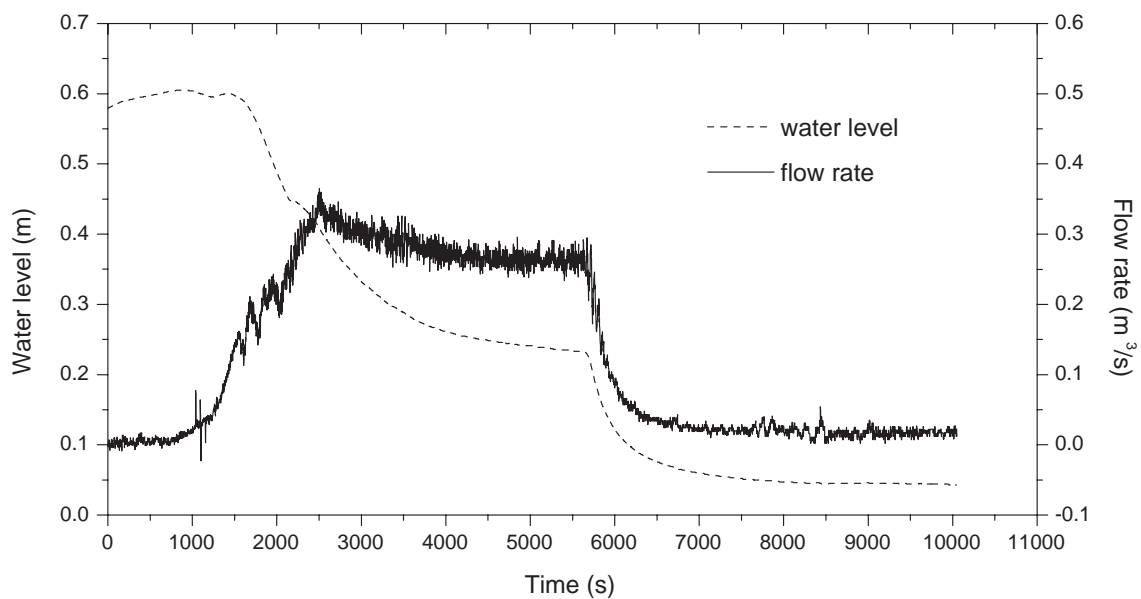
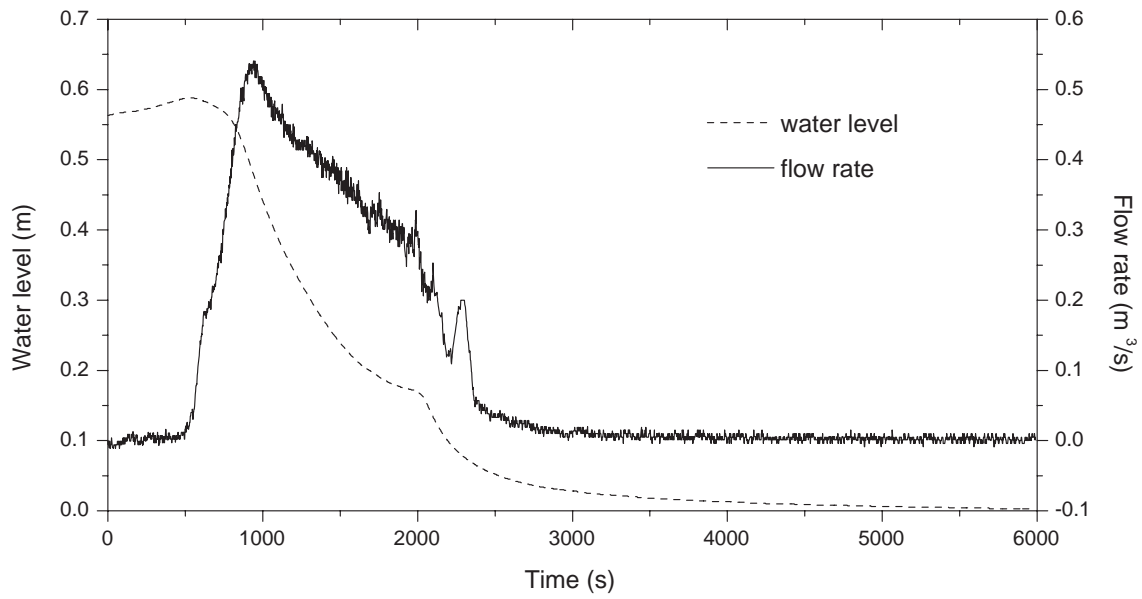
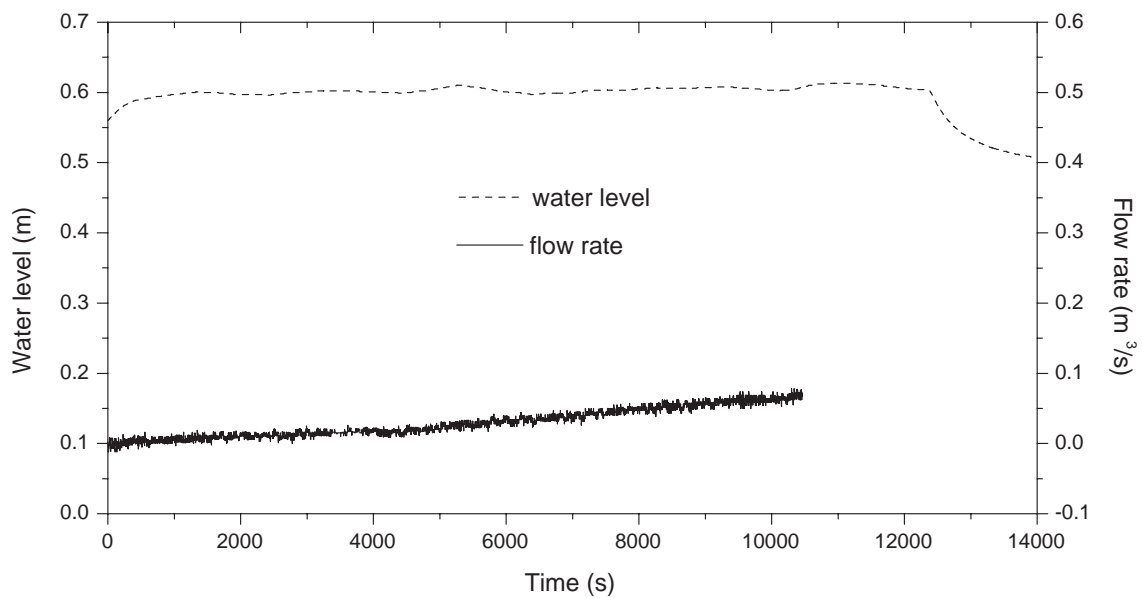
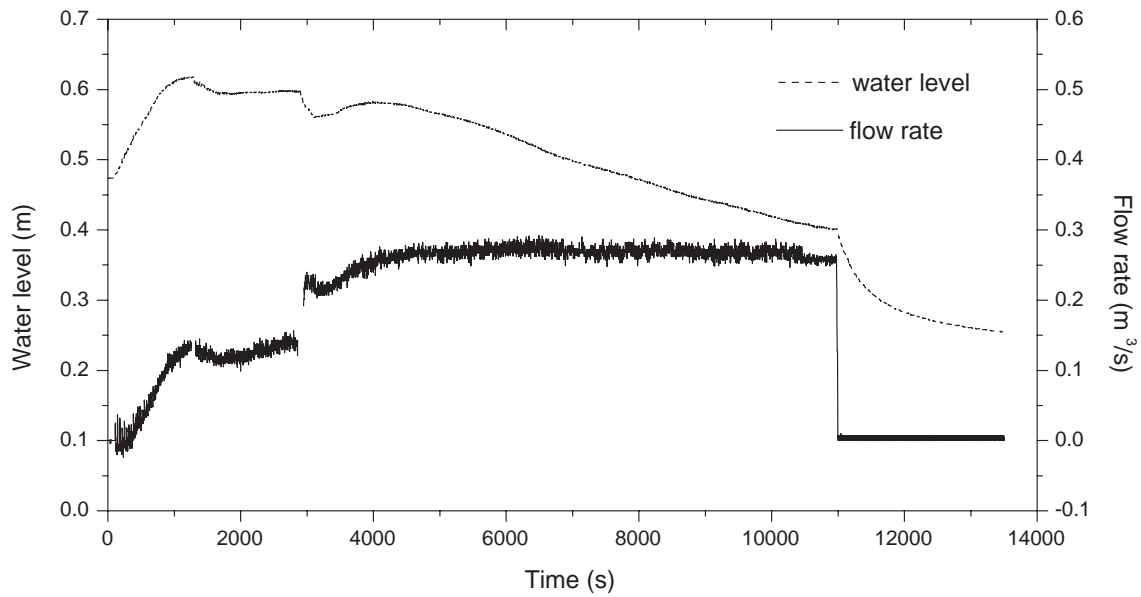
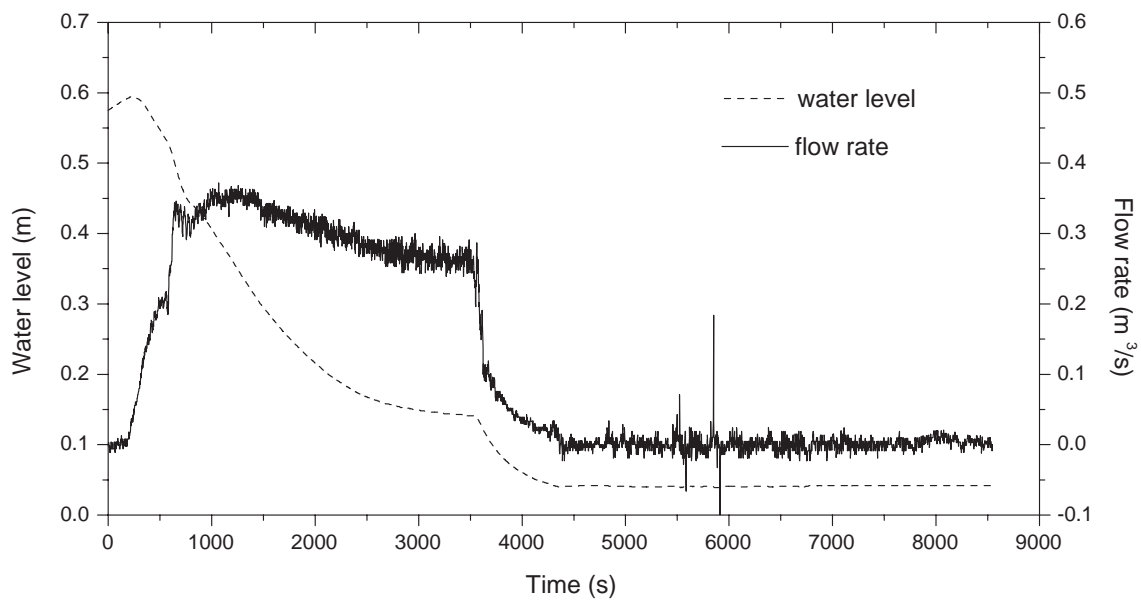


Figure A.29 Water level and breach flow rate of test T<sub>11</sub>.

Figure A.30 Water level and breach flow rate of test T<sub>12</sub>.Figure A.31 Water level and breach flow rate of test T<sub>13</sub>.

Figure A.32 Water level and breach flow rate of test T<sub>14</sub>.Figure A.33 Water level and breach flow rate of test T<sub>15</sub>.

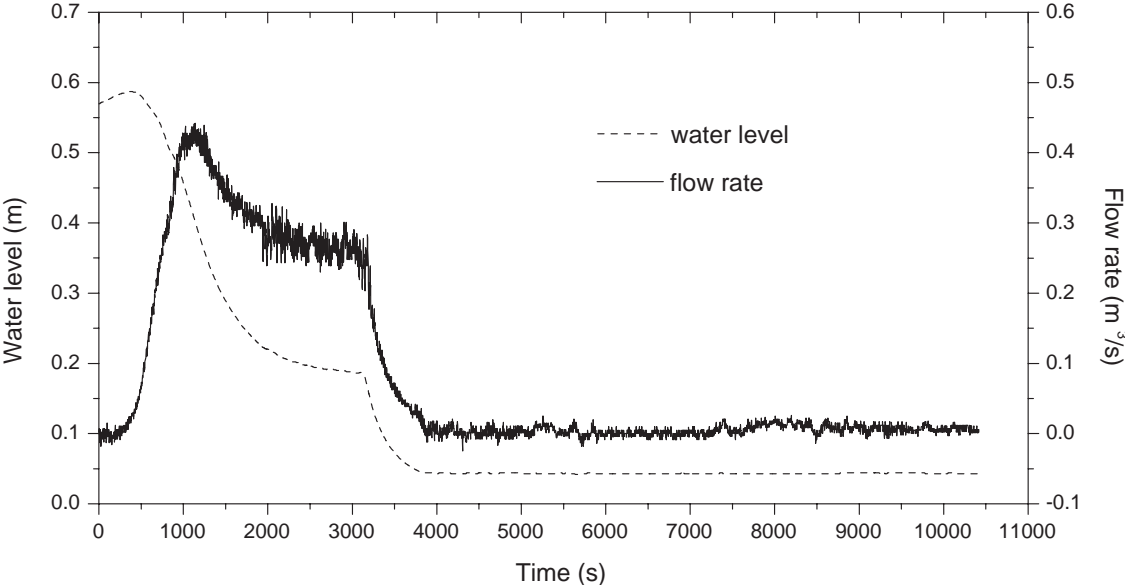


Figure A.34 Water level and breach flow rate of test T<sub>16</sub>.

## Appendix B

### Height limitation of a headcut

#### B.1 Introduction

This appendix gives basic and approximate information on the soil mechanical height limitation of a (vertical) headcut through three different methods:

- Circular surface analysis (Section B.2).
- Planar surface analysis (Section B.3).
- Lateral earth pressure analysis (Section B.4).

For the sake of simplicity, a simple case which has a slope angle  $\beta_1 = 90^\circ$  (i.e. vertical), horizontal beds both upstream and downstream of the slope, an internal friction angle  $\phi = 0^\circ$  and has no seepage or other external forces, is adopted here for the illustration, see Figures B.1 through B.3.

#### B.2 Circular surface analysis

As shown in Figure B.1, the potential failure surface is assumed to be a circular arc (centre O, radius  $r$  and length  $L_a$ ). The forces acting on the potential failure mass are the weight of the soil ( $G_m$ ), the resisting force due to the shear strength along the failure surface ( $\tau_s L_a$ ), and the normal force on the failure surface ( $N_m$ ). Equating moments about O gives

$$G_m d_{G_m} = \frac{\tau_s L_a r}{F} \quad (\text{B.1})$$

in which  $d_{G_m}$  is the force arm of  $G_m$  to O,  $\tau_s = c + \sigma \tan \phi$ , and  $F$  is the factor of safety. To keep the slope stable,  $F \geq 1.0$ .

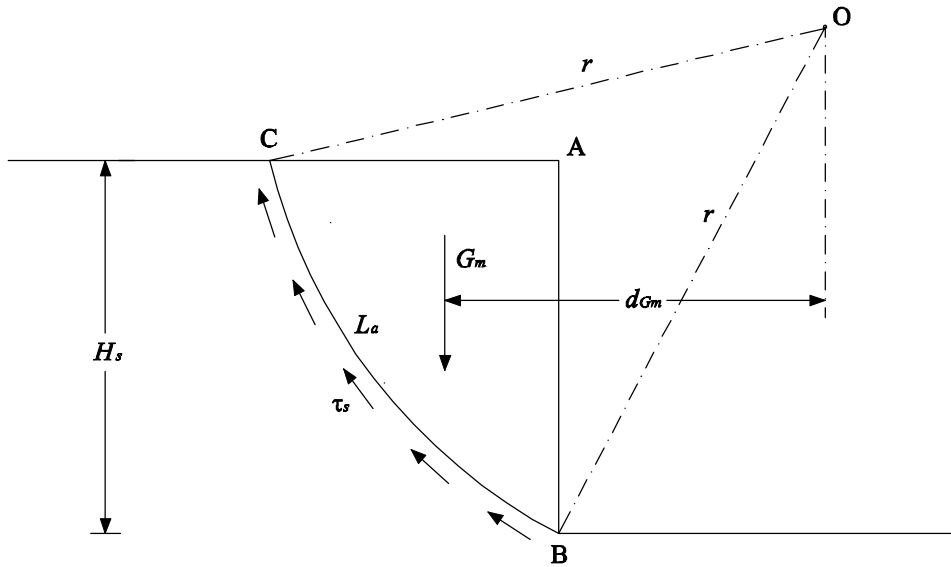


Figure B.1 Circular surface analysis of the slope stability of a vertical headcut.

For saturated soil under undrained conditions,  $\phi = 0^\circ$ , therefore Equation (B.1) is simplified as

$$G_m d_{Gm} = \frac{c_u L_a r}{F} \quad (\text{B.2})$$

in which  $c_u$  is the undrained soil shear strength.

Taylor (1937, see Craig, 1997) published stability coefficients for the analysis of homogeneous slopes in terms of total stress. The stability coefficient ( $N_s$ ) that gives a minimum  $F$  for a slope of height  $H_s$  is

$$N_s = \frac{c_u}{F \rho_s g H_s} \quad (\text{B.3})$$

When the slope is vertical (i.e.  $\beta_1 = 90^\circ$ ),  $N_s = 0.26$  (Taylor, 1937, see Craig, 1997). Since  $F \geq 1$ , Equation (B.3) gives the maximum height of the vertical headcut

$$H_{s \max} = \frac{3.85 c_u}{\rho_s g} \quad (\text{B.4})$$

### B.3 Planar surface analysis

Figure B.2 assumes the potential slope instability along a planar surface at an angle  $\alpha_1$  with the vertical direction. The weight of the sliding wedge is

$$G_m = \frac{1}{2} \rho_s g H_s^2 \tan \alpha_1 \quad (\text{B.5})$$

Following from the condition of equilibrium in the direction of sliding we have

$$T = G_m \cos \alpha_1 = \frac{1}{2} \rho_s g H_s^2 \sin \alpha_1 \quad (\text{B.6})$$

Because the length of the sliding surface is  $H_s / \cos \alpha_1$  it follows that

$$T = \frac{cH_s}{\cos \alpha_1} + G_m \sin \alpha_1 \tan \phi \quad (\text{B.7})$$

Combination of Equations (B.6) and (B.7) gives

$$H_s = \frac{4c}{\rho_s g} \frac{1}{(1 - \tan \alpha_1 \tan \phi) \sin 2\alpha_1} \quad (\text{B.8})$$

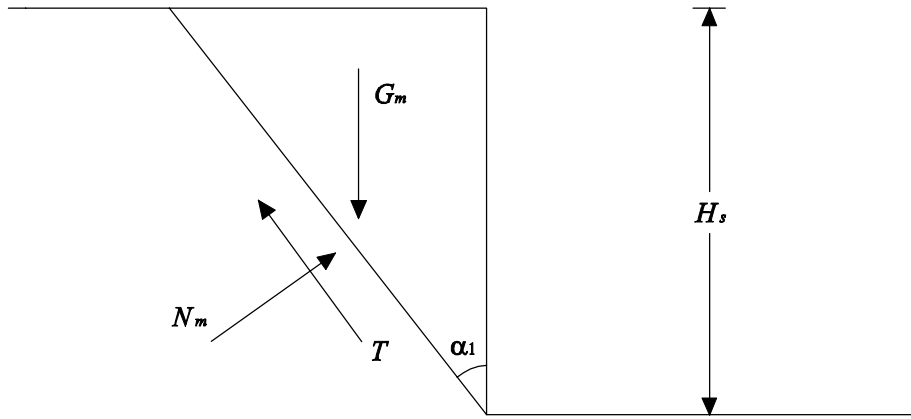


Figure B.2 Planar surface analysis of the slope stability of a vertical headcut.

To get the maximum value of  $H_s$ ,  $f(\alpha_1) = (1 - \tan \alpha_1 \tan \phi) \sin 2\alpha_1$  should be minimal, i.e.  $\frac{\partial f}{\partial \alpha_1} = 0$ , at which  $\alpha_1 = \frac{1}{2}(90^\circ - \phi)$ , therefore

$$H_{s \max} = \frac{4c}{\rho_s g} \frac{1 + \sin \phi}{\cos \phi} \quad (\text{B.9})$$

Again, when  $\phi = 0^\circ$ , the above equation is simplified as

$$H_{s \max} = \frac{4c_u}{\rho_s g} \quad (\text{B.10})$$

### B.4 Lateral earth pressure analysis

As shown in Figure B.3, for a vertical headcut with a height of  $H_s$ , the vertical stress ( $\sigma_v$ ) acting on a soil element at the toe of the headcut is

$$\sigma_v = \rho_s g H_s \quad (\text{B.11})$$

At the maximum possible headcut height  $H_{s\max}$ , the horizontal stress ( $\sigma_H$ ) acting on the soil element can be expressed as

$$\sigma_H = \sigma_v \frac{1 - \sin \phi}{1 + \sin \phi} - 2c \frac{1 - \sin \phi}{\cos \phi} = 0 \quad (\text{B.12})$$

Transformation of the above equation gives

$$H_{s\max} = \frac{2c}{\rho_s g} \frac{1 + \sin \phi}{\cos \phi} \quad (\text{B.13})$$

This  $H_{s\max}$  is also the maximum possible depth of a tension crack (Lambe and Whiteman, 1969).

Again, when  $\phi = 0^\circ$ ,  $H_{s\max}$  reads

$$H_{s\max} = \frac{2c_u}{\rho_s g} \quad (\text{B.14})$$

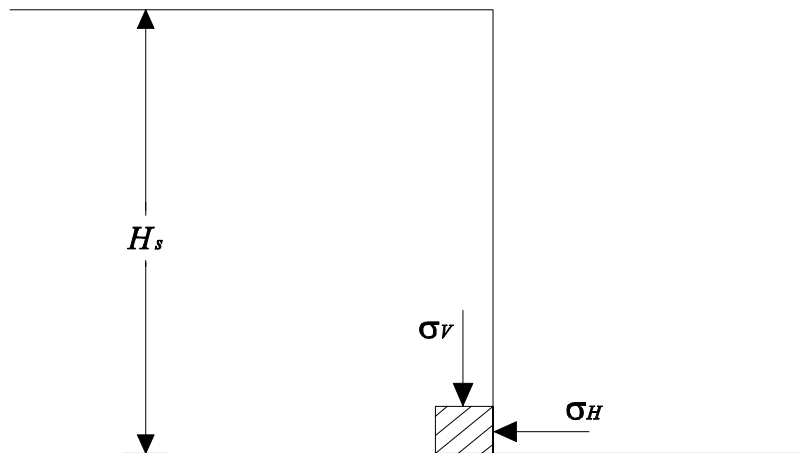


Figure B.3 Lateral earth pressure analysis of the slope stability of a vertical headcut.

## B.5 Examples

In this section, using the three methods described above, examples of the determination of the soil mechanical height limitation for a headcut with various values of  $c_u$  are given (see Table B.1). It is assumed that the headcut slope is vertical ( $\beta_l = 90^\circ$ ), the beds both upstream and downstream of the headcut are horizontal, there are no influences from seepage or other external forces,  $\phi = 0^\circ$ , and the soil density is assumed to be  $1900 \text{ kg/m}^3$ . The results of the calculation are summarized in Table B.1. Among the three methods, the lateral earth pressure analysis gives the smallest  $H_{\text{smax}}$ , which is smaller than 4.0 m for all the values of  $c_u$  studied.

Table B.1 Results of calculation for  $H_{\text{smax}}$  (m).

	$c_u$ (kPa)				
	10	20	25	30	35
CSA*	2.07	4.14	5.18	6.21	7.25
PSA*	2.15	4.30	5.37	6.45	7.52
LEPA*	1.07	2.15	2.68	3.22	3.76

\*CSA: circular surface analysis; PSA: planar surface analysis; LEPA: lateral earth pressure analysis.



## List of main symbols

### Roman letters

Symbol	Description	SI-unit
$A$	cross-sectional breach flow area	[m <sup>2</sup> ]
$A'$	area of lateral surface of headcut failure block	[m <sup>2</sup> ]
$A_p$	polder area	[m <sup>2</sup> ]
$b$	breach width at its bottom	[m]
$B$	depth-averaged (over water depth $d$ ) breach width	[m]
$B_a$	depth-averaged (over breach depth $h$ ) breach width	[m]
$B_t$	breach width at dike crest	[m]
$B_w$	breach width at water surface	[m]
$c$	cohesion of soil	[N/m <sup>2</sup> ]
$c_s$	sediment concentration	[-]
$c_u$	undrained shear strength of soil	[N/m <sup>2</sup> ]
$c_v$	consolidation coefficient of sediment	[m <sup>2</sup> /s]
$C$	Chézy coefficient	[m <sup>1/2</sup> /s]
$C_d$	diffusion constant of jet	[-]
$C_f$	friction coefficient	[-]
$d$	water depth in the breach	[m]
$d_b$	water depth at headcut brink in Stages II and III	[m]
$d_c$	critical flow depth at $x = 0$ on dike inner slope	[m]
$d_n$	normal flow depth	[m]
$d_{c,f}$	force arm of $F_{c,f}$	[m]
$d_G$	force arm of $G$	[m]
$d_{G1}$	force arm of $G_1$	[m]
$d_{G2}$	force arm of $G_2$	[m]
$d_N$	force arm of $N$	[m]
$d_{P1}$	force arm of $P_1$	[m]
$d_{P2}$	force arm of $P_2$	[m]

$d_{P_3}$	force arm of $P_3$	[m]
$dt$	time step	[s]
$D_i$	particle diameter such that $i$ % of sediment volume has a diameter smaller than $D_i$	[m]
$D_{50}$	median particle diameter	[m]
$E$	rate of erosion	[m/s]
$E_0$	rate of erosion at the dike crest	[m/s]
$E_1$	rate of erosion at $x = x_E$ on dike inner slope	[m/s]
$E_{bo}$	rate of erosion at breach bottom	[m/s]
$E_{st}$	rate of erosion at toe of breach side-slopes	[m/s]
$F_{c,f}$	soil interactional force acting on lateral surfaces of headcut failure block	[N]
$Fr_n$	Froude number at $x = l_n$ on dike inner slope	[-]
$g$	acceleration of gravity	[m/s <sup>2</sup> ]
$G$	weight of headcut failure block	[N]
$G_1$	weight of one part of headcut failure block	[N]
$G_2$	weight of the other part of headcut failure block	[N]
$G_s$	particle specific density	[-]
$h$	depth of breach	[m]
$h_p$	inner water depth above original dike foundation	[m]
$H$	scour depth in dike foundation	[m]
$H_b$	height of breach bottom above dike foundation	[m]
$H_d$	height of dike above $Z = 0$	[m]
$H_p$	water level in polder above $Z = 0$ (inner water level)	[m]
$H_{pc}$	depth of potential core of impinging jet	[m]
$H_w$	water level against dike above $Z = 0$ (outside water level)	[m]
$J$	jet centerline length from entry point	[m]
$J_p$	length of jet potential core along jet centerline	[m]
$K$	non-dimensional coefficient in Equation (7.1)	[-]
$l$	horizontal distance between the maximum scour point and the upstream end of the scour hole	[m]
$l_n$	adaptation length of flow	[m]
$L$	length of dike inner slope	[m]
$m$	discharge coefficient	[-]
$m_f$	slope of scour hole upstream boundary	[-]
$M_e$	material dependent factor describing the erodibility of soil	[s·m <sup>2</sup> /kg]
$M_{ef}$	material dependent factor describing the erodibility of erodible dike foundation	[s·m <sup>2</sup> /kg] <sup>1</sup>
$n$	Manning's roughness coefficient	[-]

$N$	soil interactional force between headcut failure block and new headcut surface	[N]
$N_p$	number of passes of roller during dike construction	[-]
$P_1$	water weight acting on top of headcut failure block	[N]
$P_2$	flow shear force acting on top of headcut failure block	[N]
$P_3$	seepage force acting on the headcut failure block	[N]
$q$	unit flow discharge	[(m <sup>3</sup> /s)/m]
$Q_{br}$	breach flow discharge	[m <sup>3</sup> /s]
$R$	hydraulic radius of breach	[m]
$s_1$	$= \rho_s / \rho$	[-]
$s$	$= \rho_{dry} / \rho$ , relative density	[-]
$S_1$	horizontal distance from toe of headcut to jet action point on dike foundation	[m]
$S$	horizontal distance between jet action point on dike foundation and headcut brink	[m]
$t$	time	[s]
$T_0$	thickness of jet flow at action point on foundation or entry point into inner water	[m]
$U$	cross-sectional averaged flow velocity	[m/s]
$U_0$	jet velocity at action point on foundation or entry point into inner water	[m/s]
$U_b$	flow velocity over the breach bottom (for Stage II the flow velocity at the headcut brink)	[m/s]
$U_c$	critical flow velocity	[m/s]
$U_n$	normal flow velocity	[m/s]
$V$	volume of diverted water through the breach	[m <sup>3</sup> ]
$W$	length of breach in crest of dike	[m]
$W_0$	length of initial breach in crest of dike	[m]
$W_f$	width of failure headcut block	[m]
$x$	coordinate along dike inner slope in Stage I ( $x = 0$ at the top of the slope)	[m]
$x_E$	distance from top of inner slope where the erosion rate on this slope reaches a maximum	[m]
$x'$	horizontal coordinate describing position of jet trajectory	[m]
$y'$	vertical coordinate describing position of jet trajectory	[m]
$Z$	vertical coordinate, $Z = 0$ is reference level	[m]
$Z_{br}$	height of breach bottom above reference level $Z = 0$	[m]
$\Delta Z_{br}'$	depth required to erode down at the breach bottom for reaching $\beta_i$ along the entire breach side-slopes	[m]
$Z_p$	polder level above reference level $Z = 0$	[m]

## Greek letters

Symbol	Description	SI-unit
$\alpha$	inclination angle of dike outer slope	[°]
$\beta$	inclination angle of dike inner slope	[°]
$\beta_0$	inclination angle of dike inner slope at $t_0$	[°]
$\beta_I$	critical value of $\beta$ and $\gamma$	[°]
$\chi$	impinging angle of jet flow in Stages II and III	[°]
$\phi$	soil internal friction angle	[°]
$\gamma$	inclination angle of breach side-slopes	[°]
$\gamma_{dry}$	soil dry unit weight	[(kg/m <sup>2</sup> )/s <sup>2</sup> ]
$\nu$	kinematic viscosity	[m <sup>2</sup> /s]
$\rho$	water density	[kg/m <sup>3</sup> ]
$\rho_{dm}$	maximum soil dry density	[kg/m <sup>3</sup> ]
$\rho_{dry}$	soil dry density	[kg/m <sup>3</sup> ]
$\rho_s$	soil density	[kg/m <sup>3</sup> ]
$\rho_{sat}$	soil saturated density	[kg/m <sup>3</sup> ]
$\rho_{solid}$	density of soil particles	[kg/m <sup>3</sup> ]
$\sigma$	normal stress	[N/m <sup>2</sup> ]
$\sigma_u$	soil compressive strength	[N/m <sup>2</sup> ]
$\tau_b$	bed shear stress	[N/m <sup>2</sup> ]
$\tau_c$	critical shear stress for erosion of soil	[N/m <sup>2</sup> ]
$\tau_j$	maximum shear stress acting on bed in jet impingement region	[N/m <sup>2</sup> ]
$\tau_s$	shear strength of soil	[N/m <sup>2</sup> ]
$\tau_t$	tensile strength of soil	[N/m <sup>2</sup> ]
$\omega$	water content	[-]
$\omega_{opt}$	optimum water content	[-]
$\zeta$	constant of soil erosion Equation (5.34)	[-]

<sup>1</sup> unit depends on value of  $\zeta$ , [s·m<sup>2</sup>/kg] if  $\zeta = 1.0$ , [s<sup>2</sup>·m<sup>2.5</sup>/kg<sup>1.5</sup>] if  $\zeta = 1.5$ .

## Acknowledgments

As a BSc in Civil Engineering, without the experience of writing an MSc thesis, I was lost when I just started this PhD research. Now looking back at the past five years of work that resulted in this thesis, I want to express my gratitude to all the people who have contributed directly or indirectly to this thesis.

First of all, I would like to thank my promoter, Han Vrijling, who gave me the opportunity to do this research. I thank him for trusting me, for his guidance, his constructive criticism and very valuable suggestions. From him I learned more than the research itself. I am also very grateful to my supervisor, Paul Visser, for his daily supervision, continuous encouragement, critical review of the manuscript and very valuable suggestions. I also appreciate very much his assistance during the laboratory experiments.

I want to thank my Chinese supervisor Wu Zhongru from Hohai University for his valuable support and suggestions to my research.

This PhD program is a part of the China-Netherlands cooperation project named "Strengthening of Education and Applied Research in Water Resources Engineering and Water Resources Management (China-DC/WRE)", funded by the Netherlands Directorate General for International Cooperation through the Royal Netherlands Embassy in Beijing, China. The financial support from the Project 02.02.02 "Breach Growth" of the Delft Cluster Strategic Research Programme under Theme 2 "Risk due to Flooding" and from the Section of Hydraulic Engineering of Delft University of Technology (DUT) is very much appreciated. My sincere gratitude is also due to the EC FLOODsite Project, which financially supported the last year of this PhD research.

I would like to thank Henk Verheij of Delft Hydraulics for providing the data of the EC IMPACT Project experiments on embankment breaching.

I thank all the staff members of the Fluid Mechanics Laboratory of DUT, especially Harry Fontijn, Arie den Toom, Hans Tas, Frank Kalkman, Jaap van Duin and Karel de Bruin, for their support and help during the experiments. I thank Luitze Perk for his assistance in making the artificial soil mixtures. My thanks also go to Wim Verwaal, Arno Mulder, Jacques Oostveen and Xiaohui Cheng from the Section of

Geo-Engineering of DUT for their help in conducting the tests characterizing properties of the soil mixtures.

I thank Walther van Kesteren for providing Illite for making the soil mixtures. I also thank Walter Jacobs for providing data on the particle size distribution of Illite and data on the mineralogical analysis of Polwhite E Kaolin and Illite.

Many thanks go to Krystian Pilarczyk, Bas Jonkman and Gijs Hoffmans from the Rijkswaterstaat for their concern about and support to my research.

I want to thank all the colleagues and friends of the Section of Hydraulic Engineering and the Section of Environmental Fluid Mechanics of DUT. Thank you all for your friendliness and kindness. I will never forget the tough but amusing and joyful cycling tour from Hoek van Holland to Den Helder, the hiking tour through the dune area near the Hague and attending conferences out of the Netherlands together with some of you. My special thanks go to Mark Voorendt, Adeeba Ramdjan, Chantal van Woggelum and Corine Franken for their support and assistance. The review of the propositions by Pieter van Gelder is highly appreciated.

I thank CICAT of DUT and the International Cooperation and Education Division of Hohai University for the management of the "China-DC/WRE" project. I owe a lot to Theda Olsder, Cees Timmers and Manon Post from CICAT for their kind help and facilitating my stay here. I thank them sincerely.

I am grateful to all my friends in Delft, with whom I shared so much good times. Because of you, my study and life here, though away from families, is still very pleasant.

I would like to thank Lou Jian and He Hai from Hohai University for their support to my research. My appreciation also goes to Yan Zhongming from Hohai University for his support during my stay at Hohai University in the middle of this research. I thank Gao Yufeng for the helpful discussion on the tests characterizing the soil mixture properties.

I am greatly indebted to my parents, for their support and understanding. My special thanks go to my parents in law and my sisters in law, for their support and taking care of my son when my wife and I were both in Delft. I owe a lot to my son Xuanyi, for being away from him for such a long time in his first four years of life. Finally, I want to express my deepest gratitude to my wife Liao Hongzhi, for her love, continuous support, encouragement and patience. Without these it would be impossible for me to finish this thesis.

## Curriculum Vitae

Yonghui Zhu was born on 9 September 1975 in Dao County, Hunan Province, China. He graduated from secondary school in July 1994. In September 1994 he continued his academic education at Hohai University in China and obtained the Bachelor of Science degree in Hydraulic and Hydropower Engineering in July 1998. His graduation project was "Design of Sha Xikou Hydropower Station". In 1997 he was awarded the Mao Yi-sheng Engineering and Education Student Prize that is financed by the Chinese Science and Technology Development Foundation. Due to his outstanding academic records, Zhu was recommended by Hohai University to continue with the MSc study (in Hydraulic Structure Engineering) in September 1998 by skipping the entrance examination. From then on to February 2000, Zhu finished all the courses required for the MSc study and again with outstanding academic records. Then in February 2000, he was selected by the university to go directly towards the PhD study in Hydraulic Structure Engineering by skipping the writing of the MSc thesis. During the period of 1998 - 2000, Zhu also took part in a few practical projects on safety monitoring of dams.

In February 2001, Zhu started a PhD study at the Section of Hydraulic Engineering of Delft University of Technology. Zhu's research mainly concerned modeling of breach growth in dikes constructed with cohesive soil, both experimentally and mathematically.